Experiments with a two-species Bose-Einstein condensate utilizing widely tunable interparticle interactions

by

Scott B. Papp

B.A. Physics, University of Colorado, 2001

A thesis submitted to the
Faculty of the Graduate School of the
University of Colorado in partial fulfillment
of the requirements for the degree of
Doctor of Philosophy
Department of Physics
2007

This thesis entitled:
Experiments with a two-species Bose-Einstein condensate utilizing widely tunable interparticle interactions
written by Scott B. Papp
has been approved for the Department of Physics

_____

Dr. Carl E. Wieman

_____

Dr. Deborah S. Jin

Date _____

The final copy of this thesis has been examined by the signatories, and we find that both the content and the form meet acceptable presentation standards of scholarly work in the above mentioned discipline.

Papp, Scott B. (Ph.D., Physics)

Experiments with a two-species Bose-Einstein condensate utilizing widely tunable interparticle interactions

Thesis directed by Distinguished Professor Dr. Carl E. Wieman

This thesis presents experiments with a quantum-degenerate gas of bosonic atoms where interparticle interactions can be precisely controlled using a magnetic-field tunable Feshbach resonance. Using our new apparatus, we have the capability to study either single species Bose-Einstein condensates of ^{85}Rb or ^{87}Rb, or a mixture of both species. With such a mixture we have created and studied the first ultracold heteronuclear Feshbach molecules. Further work with two-component gases includes the creation of a dual-species BEC in which the miscibility of the two quantum fluids can be controlled. Finally, with a single species ^{85}Rb condensate we have performed the first detailed measurements of the excitation spectrum of a BEC as a function of interaction strength. With strong interparticle interactions, we have observed that the excitation energy is smaller than that predicted by mean-field theory.

Dedication

This work is dedicated to my wife Cindy and to my family Ann Rae, Larry, and Jeff.

Acknowledgements

My long tenure as both an undergraduate and graduate student at JILA has been greatly enriched by the help and support of many people. Here I would like to take the opportunity to thank the people who have in no small way made the work in this thesis possible.

First and foremost, I thank Carl Wieman for providing me with an exceptional graduate education. Carl is a brilliant experimental physicist who is enthusiastic about even the most daunting challenges. Even with all of his other responsibilities, Carl has always been very generous with his time and thoughtful advice. I have profoundly benefited from my association with him. I can only hope that during the past several years I have been able to absorb some of his intuition for interesting physics.

As is always the case in the JILA ultracold atom groups, Eric Cornell and Debbie Jin played an important role in my thesis work. Debbie taught me how to work in a lab and how to understand and solve experimental problems. I gratefully thank Debbie for her guidance during my undergraduate days and throughout my graduate studies. Recently, Eric took over leadership of our ^{85}Rb BEC efforts and it has been a great pleasure working directly with him. I have benefited from his innovative ideas for research directions.

I had the privilege of working directly with several talented graduate students. Josh Zirbel has been a really good friend and colleague to me throughout my graduate career. Josh has a keen aptitude for physics and a good intuition for how to make things work in the lab. In the summer of 2001, we were the founding members of the "new" ^{85}Rb BEC project. Josh deserves my thanks for all the hard work he put in helping to design and construct the current version of the apparatus. Since those early days, Josh has gone on to build an even better apparatus to study K–Rb Feshbach molecules. My successors, Juan Pino and Rob Wild, both contributed significantly to the work in this thesis. Juan played an important part in both the construction and optimization of our apparatus. He has also been a good friend over the past few years. Rob only recently

joined our project, but with a few years of experimental BEC experience already under his belt, he immediately made significant contributions. His insights and pleasant nature were greatly appreciated. I look forward to hearing about all the wonderful experiments Juan and Rob perform with ^{85}Rb BECs.

All of the many (too many to list) current and former students and post-docs of the Wieman-Cornell-Jin supergroup deserve thanks. I would like to acknowledge the members of the original ^{85}Rb BEC project, graduate students: Jake Roberts, Neil Claussen, and Sarah Thompson and post-docs: Simon Cornish, Liz Donley, and Eleanor Hodby. Their work was the motivation for this thesis. Kurt Miller and Stephan Dürr worked on the other side of the curtain in our lab and they were a helpful source of advice. Wieman group visitors Andrew Wilson and Christine Steenkamp also provided useful advice and I thank them for their contributions. From my undergraduate days in the Jin Group I thank Brian DeMarco and Jon Goldwin.

I would like to acknowledge many useful interactions with the theoretical community at JILA. In particular, John Bohn has patiently helped me to understand various aspects of scattering theory and Feshbach resonances. More recently Shai Ronen has been instrumental in helping us to understand our Bragg spectroscopy data. I also enjoyed interacting with Murray Holland, Chris Greene, and Servaas Kokkelmanns.

I worked with a number of undergraduate students during my time in the Wieman group. Some students were participating in the REU summer program at CU or were visiting from other universities, while others were CU students. Each of them built valuable pieces of the apparatus. I would like to acknowledge the people that worked in our lab: Jason Smith, Tyler Powell, Christoph Kohstall, Jenelyn Amos, Jeff Giffin, and Joan Dreiling.

For good reason JILA is renown for its scientific support staff. The efforts of the JILA electronics and machining shops have been invaluable for the construction of our apparatus. In particular, I would like to thank Terry Brown, Mike Whitmore, Carl Sauer, Blaine Horner, Hans Green, Tracy Keep, Todd Asnicar, and Tom Foote for building critical parts for our apparatus. All the hardworking members of the supply office also deserve thanks for efficiently purchasing the equipment used in the experiments. I also want to thank Krista Beck for lots of assistance to me personally.

Finally, I would like to acknowledge my wonderful wife Cindy Regal. She is a gifted scientist from whom I have learned a great deal over the last several years. It is impossible to describe how important she is in my life. She is my best friend and a constant source of joy and support. The many times she cheered me up after a discouraging day in the lab kept me on track to complete this work.

Contents

Tables

Table

Figures

Figure

Chapter 1

Introduction

1.1 An overview of my work

My thesis work began during an exciting time in the Wieman group. After a few years of optimization, the first Bose-Einstein condensate (BEC) of ^{85}Rb was created in 2000, and right away their work was rewarded with the ability to study a condensate with tunable interactions. Atom-atom interactions in a ultracold gas of ^{85}Rb can be tuned using the experimentally convenient Feshbach resonance near 155 G. Initial studies included observations of the equilibrium condensate shape and density over a wide range of interaction strength [7] and a quantitative time-resolved analysis of the condensate collapse process for negative interactions [8, 9]. When I started in the group during the summer of 2001, the focus was on understanding the role of the bound molecular state associated with the ^{85}Rb Feshbach resonance. This focus led to the dramatic observation of coherent atom-molecule oscillations [10]. However, by 2001 the ^{85}Rb BEC apparatus was already old and it would need to be significantly upgraded to incorporate modern technologies like Bragg spectroscopy, optical trapping, etc. My thesis work started by designing and constructing a new apparatus. The goal of the new apparatus was to efficiently produce a quantum degenerate gas of ^{85}Rb for use in experiments studying the strongly interacting regime.

We had several design goals for the new ^{85}Rb BEC apparatus so that experiments could be performed in interesting new regimes. By 2001 the route to ^{85}Rb BEC via direct evaporative cooling had been optimized, but the overall efficiency of the cooling was low. Since the efficiency was low, the apparatus had to be well adjusted in order for condensates to be made. Therefore our goal was to robustly create ^{85}Rb condensates with a larger atom number. Since direct evaporation was difficult, we decided to pursue a new approach in which sympathetic cooling with ^{87}Rb would be used.[1] To perform experiments in new regimes, we would also need to include more technology than was feasible with the old apparatus. Techniques like optical trapping and Bragg spectroscopy are a main focus of the work presented in this thesis, but they were not available in the old apparatus where optical access was limited.

Our motivation for sympathetic cooling is that, in comparison to ^{85}Rb, evaporative cooling of ^{87}Rb is easy. By starting evaporation with a large number of ^{87}Rb atoms and a tiny ^{85}Rb number, we evaporate the ^{87}Rb gas while the ^{85}Rb gas cools due to thermal contact. This technique works well for lowering the temperature down

[1] By 2001 another group had attempted sympathetic cooling of ^{85}Rb with ^{87}Rb, but they were neither able to create a ^{85}Rb condensate nor access Feshbach resonances [11].

to 1 μK. To cool all the way to BEC, however, we switch from sympathetic cooling to simultaneous cooling of ^{85}Rb and ^{87}Rb. Especially in these last stages of evaporation we must be very careful to minimize ^{85}Rb density-dependent inelastic collisions [7, 12, 6]. In particular, we work with very weak trapping potentials to maintain a low density. We also take full advantage of the ^{85}Rb Feshbach resonance to optimize the elastic and inelastic collisions rates of ^{85}Rb. After spending a lot of time improving the evaporation efficiency, we were pleased to find that we could make ^{85}Rb condensates with up to 80,000 atoms, which is a factor of five improvement over the past results. Even better was the fact that condensate production was robust. Condensates could still be produced even if the apparatus was not perfectly optimized. Our system now has the unique ability to produce single-species condensates of ^{85}Rb and ^{87}Rb, as well as a two-species BEC.

Using both isotopes of Rb has advantages beyond an improvement of ^{85}Rb cooling efficiency. Experimentally accessible and interesting interspecies Feshbach resonances between the two isotopes were predicted to exist [13], but none had been observed experimentally. Once we were able to cool a gas of ^{85}Rb and ^{87}Rb to microKelvin temperatures in an optical dipole trap, we set out to find the predicted resonances. We discovered a total of four new Feshbach resonances, two of which were s-wave and two of which were p-wave. These Feshbach resonances not only allowed us to tune interactions between the two species, but also to create and study the first heteronuclear Feshbach molecules. Ultracold heteronuclear molecules in low-lying vibrational states are particularly interesting since they are predicted to exhibit a permanent dipole moment due to the unequal distribution of electrons. Although no significant permanent dipole moment is expected to exist in a ^{85}Rb–^{87}Rb molecule, our work demonstrates a first step toward the efficient production of ground-state ultracold heteronuclear molecules. In the future it may be possible to lower the vibrational state of our Feshbach molecule via, for example, stimulated two-photon Raman transitions. The molecule creation process allowed us to determine the location and width of Feshbach resonances in the two-species system; this information will be required for future studies of the ^{85}Rb–^{87}Rb system with a tunable interspecies interaction.

Prior to our work, the production of a two-species condensate with ^{85}Rb and ^{87}Rb had never been accomplished. Since the early days of dilute gas BEC, there has been great experimental and theoretical interest in multi-component condensates. While our system is not the first two-component BEC, it is unique due to our ability to control interactions. We are able to study the miscibility of two interacting quantum fluids as a function of the ^{85}Rb scattering length. The controllable spatial separation of the two components is observed due to interparticle interactions. Surprisingly, the immiscible condensates are observed to form multiple spatially-separated cloudlets.

As mentioned earlier, the main goal of our new ^{85}Rb BEC machine was to be able to make large, stable ^{85}Rb condensates in a system with plenty of optical access that would allow more sophisticated probes of a strongly interacting BEC. The final project of my thesis, in which we measured the excitation spectrum of a strongly interacting ^{85}Rb BEC, represents the realization of this goal. Bragg spectroscopy was used to record the excitation spectrum over a very wide range of scattering length. For a weakly interacting BEC, the excitation spectrum is given by the famous Bogoliubov formula. The Bogoliubov spectrum is valid only in the limit that the condensate is dilute ($n\,a^3 \ll 1$) and in the limit in which two-body scattering is independent of

momentum ($k\,a \ll 1$). With our apparatus we can achieve experimental conditions of density and scattering length under which neither of these conditions are met.

1.2 Historical overview

Lowering the temperature of a sample into a regime in which new physical effects can be observed has long been a goal of experimental physics. A great breakthrough occurred in 1911 with the discovery of superconductivity in a low-temperature sample of metallic mercury [14]. By monitoring the resistance of mercury as the temperature was lowered below 4.2 K, a dramatic transition to the superconducting state was observed. Years later, in 1938, careful studies of liquified ^{4}He at a temperature below 2.17 K revealed the appearance of viscosity-less fluid flow, the characteristic of a superfluid [15, 16]. The peculiar properties of this superfluid Bose liquid were discovered in the following decades. In particular, the elementary excitation spectrum of superfluid ^{4}He displays complicated behavior. The excitation spectrum refers to the energy required to add a single particle at a given momentum to the system.[2] Interparticle interactions tend to modify the excitation spectrum. In fact, the low momentum excitations of superfluid ^{4}He behave like phonons, and at larger momenta a so-called "roton-minimum" appears, at which the excitation energy has a local minimum. While the form of the excitation spectrum can be predicted from physical principles [17, 18], the physical interpretation of a roton is complicated [19].

In both of the examples given above, the temperature of the samples was lowered into a regime in which quantum-mechanical effects are important. Following these spectacular discoveries a strong experimental focus was to achieve ever lower temperatures in order to expose quantum-mechanical effects in a range of new systems. Of course, the effects of quantum mechanics are observed outside the regime of low-temperature physics. The electrons in a room-temperature metal behave quantum mechanically since the Fermi temperature of the system is so high. Likewise, a neutron star is a massive quantum degenerate gas due to the extreme density.

Jumping forward in time, in the 1990's a new superfluid system was realized in a dilute atomic vapor. The landmark experimental observation of dilute gas Bose-Einstein condensation (BEC) has opened the door to a wide range of new studies [20, 21, 22, 23]. If a low enough temperature is reached, then a phase transition occurs in which the ground state of the system is macroscopically occupied. There are several advantages to working with a dilute atomic vapor in comparison to a dense liquid like ^{4}He. Strong interactions in a ^{4}He superfluid severely deplete the number of particles in the lowest quantum state, while weak atom-atom interactions in atomic gas BEC result in a large ground-state occupation. The properties of a weakly interacting BEC may be accurately described by a mean-field theory. Finally, interactions in a quantum gas may be controlled via magnetic-field tunable Feshbach resonances. Some of the first work with condensates produced dramatic evidence for coherence via the interference of two condensates [24] and for superfluidity via the observation of quantized vortices [25]. More recently atomic BECs have been studied in trapping potentials where the dimensionality can be changed. This led to the observation of the Mott-Insulator phase

[2] For example, in a gas described by Maxwell-Boltzmann statistics the excitation energy of the condensate is $p^2/2\,m$, where p is the momentum and m is the mass.

transition in a 3D optical lattice potential [26] and the observation of a Tonks-Girardeau gas in a 1D optical lattice [27].

The experimental techniques used to create the first dilute gas BEC have also been applied to cool a Fermi gas of atoms to a low enough temperature that the effects of quantum mechanics are visible. Since fermions obey the Pauli Exclusion principle, at low temperature the particles stack up with one particle per quantum state. Without the macroscopic occupation of a single quantum state, ultracold fermions do not experience a phase transition, but the effects of Fermi statistics can be observed in the behavior of the energy in the gas as the temperature is lowered below the Fermi temperature [28, 29]. A degenerate Fermi gas has much more energy than a similar gas of Maxwell-Boltzmann particles at ultralow temperature [28].

A key theme of recent work in the field of ultracold quantum gases has been the exploration of the strongly interacting regime. There are two methods by which strong interactions can be achieved: by increasing the confinement or by using a Feshbach resonance to increase the interaction strength. Here we focus on experiments with tunable scattering length that are enabled by a Feshbach resonance. Much of the outstanding work during the last few years utilized Feshbach resonances in a Fermi gas of atoms. The culmination of these experiments with fermions was the realization of the BCS-BEC crossover in which pairing occurs between fermions in the gas [30, 31, 32]. On the side of the Feshbach resonance with attractive interactions the paired fermions resemble Cooper pairs. Whereas on the side of the Feshbach resonance with repulsive interactions, the paired fermions resemble Bose-condensed bound molecules [33, 34, 35]. A strongly interacting Fermi gas represents a single low-temperature system in which the quantum mechanical effects reminiscent of the physics of superconductivity and the physics of a Bose superfluid are observed.

In general, it is more difficult to study a Bose gas near a Feshbach resonance due to large losses associated with inelastic three-body recombination. Therefore studies of the strongly interacting regime with fermions dominated the field, since the rate of three-body processes is smaller [36, 37, 38, 39]. In spite of the strong losses, important results were also obtained with Bose gases. Coherent atom-molecule oscillations were observed in ^{85}Rb that helped elucidate the relationship between atom and molecule quantum states [10]. Later the efficient production of ultracold Feshbach molecules from an ultracold bosonic gas was demonstrated using a Feshbach resonance [40, 41, 42, 43]. The goal of my thesis is to continue this line of studies to develop a more detailed understanding of a strongly interacting Bose gas. An important long-term goal is to the explore the degree to which a strongly interacting quantum gas of bosons resembles a quantum liquid like superfluid ^{4}He.

1.3 Ultracold Bose gases

1.3.1 Thermodynamics of a non-interacting Bose gas

In this section we will briefly describe the thermodynamics of a trapped non-interacting Bose gas. The result of this analysis quantifies the temperature that we strive towards throughout this thesis to create a ^{85}Rb BEC. Based on a formulation using the Grand Canonical Ensemble we are able to calculate the transition temperature for the formation of a BEC, the phase-space density of the Bose gas, and the occupation

of the ground state.[3] This subject has been covered in detail in Refs. [44, 23, 45] and therefore only the most important results that are used throughout this thesis are recounted here.

We start with the Hamiltonian of a single particle in a harmonic trapping potential which is given by

$$H = \frac{p^2}{2\,m} + \frac{1}{2} m\,\omega_\rho^2\,r'^2 \tag{1.1}$$

where p is the magnitude of the total momentum, $r'^2 = x^2 + y^2 + Z^2$ is the (re-scaled) position coordinate, and m is the atomic mass. Here we define $Z = \lambda\,z$ and $\lambda = \omega_z/\omega_\rho$ where ω_ρ (ω_z) are the radial (axial) trap frequencies. In a harmonic potential the density of states is well approximated by [44]

$$\rho(\epsilon) = \frac{\epsilon^2}{2\lambda(\hbar\,\omega_\rho)^3}. \tag{1.2}$$

The statistics of a Bose gas are given by the Bose-Einstein distribution, which determines the occupation number of each quantum state n (with energy levels ϵ_n) in the system and it is given by

$$f(\epsilon_n) = \frac{1}{e^{\frac{1}{k_B\,T}(\epsilon_n - \mu)} - 1} \tag{1.3}$$

where T is the temperature of the gas, μ is the chemical potential, and k_B is Boltzmann's constant. In the following we assume that the energy levels can be treated as continuous. The chemical potential is determined by normalizing the distribution to the total number of particles, to find the chemical potential the following equation is solved implicitly for μ

$$N = \int_0^\infty \rho(\epsilon)\,f(\epsilon) d\epsilon. \tag{1.4}$$

For a non-interacting Bose gas the chemical potential reaches zero when the temperature is equal to the transition temperature. Therefore the transition temperature T_c of the non-interacting condensate is given by

$$k_B\,T_c = \hbar\,\omega_{ho}\left(\frac{N}{\zeta(3)}\right)^{1/3} \tag{1.5}$$

where $\zeta(3) = 1.202$ is the Riemann zeta function and $\omega_{ho} = (\omega_\rho^2\,\omega_z)^{1/3}$. In our experiments the transition temperature for ^{87}Rb is typically about 500 nK while the transition temperature for ^{85}Rb is approximately 100 nK. The difference lies in the efficiency of evaporative cooling, since many more ^{87}Rb atoms can be cooled. The fraction of the total number of atoms in the gas that are in the ground state is related to the temperature and the transition temperature by

$$\frac{N_0}{N} = 1 - \left(\frac{T}{T_c}\right)^3 \tag{1.6}$$

where N_0 is the number in the ground state and N is the total number. The peak phase space density D, which is the product of the density at the center of the trap and the

[3] In Chapter 4 we determine the density distribution of the trapped gas, from which the average density and mean-relative speed may be calculated.

thermal de Broglie wavelength ($\lambda_T = (\frac{2\pi\hbar^2}{m k_B T})^{1/2}$), is given by

$$D = \lambda_T^3 \times n_{BE}(0) \tag{1.7}$$

where the density of a harmonically trapped Bose gas (n_{BE}) is given by

$$n_{BE}(r') = \frac{1}{\lambda_T^3}\, g_{3/2}\left(e^{\frac{-1}{k_B T}\left(\frac{1}{2}m\omega_\rho^2 r'^2 - \mu\right)}\right) \tag{1.8}$$

where $g_{3/2}$ is the commonly tabulated Bose-Einstein function defined in Ref. [45].

1.3.2 An interacting Bose-Einstein condensate

In the absence of interactions the quantum-mechanical wave function of a fully condensed gas is given by the product of the single-particle wave functions [44]

$$\Psi(\vec{r_1}, \vec{r_2}, ..., \vec{r_N}) = \prod_{i=1}^{N} \phi(\vec{r_i}) \tag{1.9}$$

where N is the total number of particles in the gas and $\phi(\vec{r_i})$ are the single-particle wave functions which are normalized to one. Interactions require modifications to the total wave function. The total Hamiltonian of the system including interactions is given by

$$H = \sum_{i=1}^{N}\left(\frac{p_i^2}{2m} + V_{ext}(\vec{r_i})\right) + g\sum_{i<j}\delta(\vec{r_i} - \vec{r_j}) \tag{1.10}$$

where atom-atom interactions are specified by the contact interaction $g\,\delta(\vec{r_i} - \vec{r_j})$ in which $g = \frac{4\pi\hbar^2 a}{m}$ [44]. By minimizing the total energy of the system one finds the well known Gross-Pitaevskii (GP) equation for the ground state of the trapped condensate

$$\frac{-\hbar^2}{2m}\nabla^2\psi(\vec{r}) + V_{ext}(\vec{r})\,\psi(\vec{r}) + g\,|\psi(\vec{r})|^2\,\psi(\vec{r}) = \mu\,\psi(\vec{r}) \tag{1.11}$$

where $\psi(\vec{r})$ is the wave function of the condensed state, $|\psi(\vec{r})|^2$ is the density of the gas, and V_{ext} is the external confining potential. An important simplification of the GP equation can be made if the kinetic energy term is neglected. This simplification is known as the Thomas-Fermi (TF) approximation and its use is justified only when

$$N\frac{a}{a_{ho}} \gg 1 \tag{1.12}$$

where $a_{ho} = \sqrt{\frac{\hbar}{m\omega_{ho}}}$. In this limit the condensate size is large due to repulsive atom-atom interactions, therefore the kinetic energy is small. The density of the trapped condensate in the TF limit is given by

$$n(\vec{r}) = \frac{1}{g}\left(\mu - V_{ext}(\vec{r})\right). \tag{1.13}$$

In the TF limit the condensate chemical potential is $\mu = \frac{15^{2/5}\hbar\omega_{ho}}{2}\left(\frac{N\,a}{a_{ho}}\right)^{2/5}$ [23].

A major goal of the work presented in this thesis is to reach an experimental regime where the GP equation no longer accurately describes the properties of a condensate. The GP equation is valid in the dilute-gas regime in which the interparticle spacing in the gas is larger than the scattering length, *i.e.* $n\,|a^3| \ll 1$. The availability of magnetic-field Feshbach resonances in an atomic system allows access to strong atom-atom interactions. When the scattering length is large, corrections to the GP theory are expected to be important. These correction were initially studied during the 1950s for a homogeneous gas. For example, the first-order correction to the condensate chemical potential is $\mu_{LHY} = g\,n\left(1 + \frac{32}{3}\sqrt{n\,a^3/\pi}\right)$. This was first calculated by Lee, Huang, and Yang (LHY) [46, 47]. Strong interparticle interactions also tends to reduce the probability of an atom being in the ground state at zero temperature, the amount of this quantum depletion of the condensate is given by $\frac{N_{out}}{N} = \frac{8}{3\sqrt{\pi}}\sqrt{n\,a^3}$ where N_{out} is the total number of depleted atoms. Since quantum depletion is neglected in the GP equation, the size of the depletion is a good indicator of the validity of the GP theory [23].

1.3.3 Elastic and inelastic atomic collisions

A central theme in this thesis will be the differentiation between elastic and inelastic atomic collisions. Elastic collisions between atoms in the context of ultracold gas experiments can be considered good collisions. These collisions rethermalize the gas but do not change the internal state of the atoms. On the other hand a constant concern in ultracold gas experiments are inelastic collisions, often referred to in this thesis as bad collisions. In these collisions the products involve particles in different internal states, often of lower energy. These collisions lead to loss from the experiment, as the different internal states are often no longer detectable in our experiments. They also lead to detrimental heating because the difference in energy between initial atoms and the products of the collision must be released as kinetic energy. Inelastic collisions that are discussed in this thesis involve either two atoms (two-body collisions) or three atoms (three-body collisions). An excellent review of inelastic collisions in ultracold gases is found in Ref. [1].

To describe an elastic collision between a pair of atoms in an ultracold gas, the wave function is found by solving the time-independent Schrödinger equation. Scattering theory is described in great detail elsewhere [1, 6, 48, 49, 44, 50], here we give a few details that are used later in this thesis. The wave function Ψ for the relative motion of the two atoms is given by [48]

$$\Psi = e^{i\,k\,z} + f(\theta)\,\frac{e^{i\,k\,r}}{r} \tag{1.14}$$

where the first term represents the incoming wave function, which is a plane wave with relative motion along the z-axis. The second term represents the scattered wave function, which is a spherical wave with wave vector k. The factor $f(\theta)$ is the scattering amplitude where the angle θ describes the difference of the relative momentum wave vector before and after two-body scattering occurs. Important quantities that are used to characterize elastic collisions in our system are calculated from the scattering amplitude, for example the elastic collision cross section is $\sigma = 2\,\pi\int_{-1}^{1} d(\cos(\theta))|f(\theta)|^2$ [44].

The scattering amplitude is

$$f = \frac{1}{k\cot(\delta) - i\,k} \tag{1.15}$$

where δ is the scattering phase shift. This phase shift of the scattering wave function is calculated based on the interaction potential of the two colliding atoms [1]. The phase shift may also be determined from the effective range approximation; see Section 7.6.3 for more details. Note that in the limit of very low energy, the scattering amplitude is constant and equal to $-a$, then the wave function is [44]

$$\Psi = 1 - \frac{a}{r}. \tag{1.16}$$

Therefore the scattering length describes the asymptote of the wave function on the r-axis.

Another central theme is our ability to tune the interactions in our gas with a Feshbach resonance. At a Feshbach resonance simply by tuning a magnetic field B we can, through the differential Zeeman tuning, bring a bound state near the atomic scattering threshold. This leads to a divergence in the scattering properties of the system according to the following equation

$$a(B) = a_{bg}\left(1 - \frac{\Delta}{B - B_0}\right) \tag{1.17}$$

Here a_{bg} is the background (non-resonant) scattering length, B_0 is the magnetic field position of the Feshbach resonance, and Δ is the magnetic-field width of the Feshbach resonance, defined as the distance in magnetic field between B_0 and the magnetic field at which $a = 0$. Readers interested to know more about the physics of Feshbach resonance can consult a now very large literature on the effect [51, 52, 53, 54, 6, 32, 55, 56, 57]. It is important to recognize that near a Feshbach resonance inelastic collisions can be enhanced just as much as elastic collisions. For a discussion of the relationship between elastic and inelastic collisions near the ^{85}Rb Feshbach resonance see Ref. [12, 6].

1.4 Contents of this thesis

In the first half of this thesis I will concentrate on the apparatus and on the evaporative cooling sequence that we use to create condensates. We have the unique ability to produce a BEC with ^{85}Rb, ^{87}Rb, or a mixture of both species. The realization of this system was the culmination of several years work on building and optimizing our apparatus. The success of our apparatus is indicated by the significant improvement in the efficiency of ^{85}Rb condensate production that we achieved. For the benefit of future students using this apparatus, or a similar BEC machine at JILA, I have tried to make the description of the apparatus and cooling procedures as detailed as possible.

The main scientific results of this thesis are presented in Chapters five, six, and seven. Chapter 5 contains the results of experiments with a dual-species BEC of ^{85}Rb and ^{87}Rb. The miscibility of this system of two interacting quantum fluids was studied as a function of the ^{85}Rb scattering length. Chapter 6 describes the creation of the first heteronuclear Feshbach molecules. We studied two different methods to create the molecules, and using signatures of the molecule creation we precisely measured the position of two Feshbach resonances in our two-species system. Chapter 7 describes

our measurements of the excitation spectrum of a strongly interacting BEC. In particular, we have observed beyond mean-field corrections to the excitation energy of a condensate.

Chapter 2

The Apparatus

2.1 Chapter overview

This chapter describes the new apparatus that was used to obtain all the results detailed in the rest of this thesis. The overall goal for the new apparatus was to produce ^{85}Rb Bose-Einstein condensates in order to study a strongly interacting BEC. The motivation was the ground-breaking work done in the Wieman group using the apparatus detailed in Ref. [6, 58]. Despite the spectacular scientific results [7, 8, 9, 10], the original ^{85}Rb BEC machine had several shortcomings. Primarily it was quite old, built in 1994-1995 [59], and therefore not designed to incorporate modern technologies used in BEC experiments like Bragg spectroscopy, optical trapping, etc. Furthermore the original ^{85}Rb BEC machine relied on the difficult task of direct ^{85}Rb evaporative cooling. That task requires a very high quality vacuum, careful attention to nearly all experimental parameters, and precise optimization of the rf-evaporation trajectory. In this thesis, I will present an alternative approach that significantly relaxes the experimental requirements to produce ^{85}Rb BEC while also improving the efficiency of ^{85}Rb condensate production. We use sympathetic cooling with ^{87}Rb to reduce the difficulties associated with ^{85}Rb evaporative cooling. The evaporative cooling procedure we use is discussed in Chapter 4. Our apparatus has been specifically designed for this approach and the details of the apparatus are described in this chapter.

In the vast majority of quantum gas experiments two very different techniques are required to achieve ultralow temperatures: laser cooling and magnetic trapping with evaporative cooling. We use a standard three-dimensional, magneto-optical trap (MOT) to collect and cool room temperature Rb atoms from a background vapor. Unfortunately the lowest attainable temperatures in the MOT are not sufficient to create a BEC. Therefore the atoms are further cooled to ultralow temperature using forced evaporation in a magnetic trap. The primary obstacle in operating a MOT and evaporative cooling in the same vacuum system is the disparate vacuum conditions required. To efficiently collect atoms into the MOT, a relatively large vapor pressure of Rb is required, but evaporative cooling requires very low vacuum pressure. A now standard solution is to use physically separated MOT and evaporative-cooling chambers. The two chambers are connected by a long, thin tube through which laser-cooled atoms from the MOT chamber can be transported to the science chamber. The thin tube isolates Rb vapor in the MOT chamber from the evaporation chamber, however in the original ^{85}Rb apparatus it was determined that over several years a detrimental Rb vapor can build up in the evaporation chamber. Our apparatus is designed to overcome this problem by removing line-of-sight between the two chambers with a curved transfer

tube. Rb vapor that diffuses into the transfer tube sticks to the walls before reaching the evaporation chamber. A significant vapor pressure would have to develop in the transfer tube for much Rb to leak into the evaporation chamber. We prevent alkali buildup in the transfer tube by heating the tube to drive the vapor back towards the MOT chamber.

Essentially two techniques exist (with many variants) to transport cold atoms between the two chambers. The double MOT system where atoms are pushed by a resonant laser beam from a collection MOT through the transfer tube, then the atoms are caught in a second MOT [60]. The other technique is moveable magnetic trap transport, in which the atom trapping potential is translated to move the atoms [61, 62]. Our requirement of removing line-of-sight between the two chambers complicates the implementation of either technique. A significant portion of the early work in this thesis focused on testing new transport implementations that incorporate a curved transfer tube.

Once cold atoms can be delivered from the collection chamber to the science chamber evaporative cooling can begin. In a typical ultracold gas experiment the trapping potential is tightly compressed for evaporative cooling in order to increase gas density and enhance the collision rate. With ^{85}Rb this route is blocked since the elastic collision cross section is significantly lower at high temperature, and inelastic density-dependent loss rates are significantly larger [6]. Direct evaporation of ^{85}Rb is possible in a very weak trap, but the efficiency of the cooling is poor and long evaporation times are required. To improve efficiency of ^{85}Rb production, we implemented sympathetic cooling with ^{87}Rb. This required the added complexity of a dual-species MOT (described in Section 2.3) and simultaneous transfer of the two species, but it allowed significantly faster, more efficient, and more reliable production of ^{85}Rb BEC.

Evaporative cooling of the dual-species gas begins in a Ioffe-Pritchard-style magnetic trap. The design and construction of this magnetic trap is focused on satisfying two competing criteria. Evaporation requires an extremely stable and low noise trapping potential, while the science goals of our apparatus require the ability to quickly and precisely change the magnetic field value at the center of the trap. In Section 2.6 the magnetic trap used to obtain all the results of this thesis is described.

Due to several inherent limitations, sympathetic cooling in the magnetic trap is not able to produce a ^{85}Rb BEC. Finally, the solution is to use an optical trap and perform simultaneous cooling of ^{85}Rb and ^{87}Rb. The optical trapping setups that were used for the work in this thesis are described in Section 2.7. Our setups provide a very stable potential with low heating rate which is ideal for evaporation. With an optical trap, an arbitrary magnetic field can be applied to the atoms without significantly altering the confining potential. During evaporation the magnetic field is tuned near the ^{85}Rb Feshbach resonance in order to control both the elastic and inelastic collision rates in the ^{85}Rb gas.

Most of the data taken with our apparatus is obtained from absorption images. Section 2.8 gives a brief overview of our imaging setup. The procedure that we use for absorption imaging is now quite standard, therefore only a brief review of our work is provided and references are provided for further information.

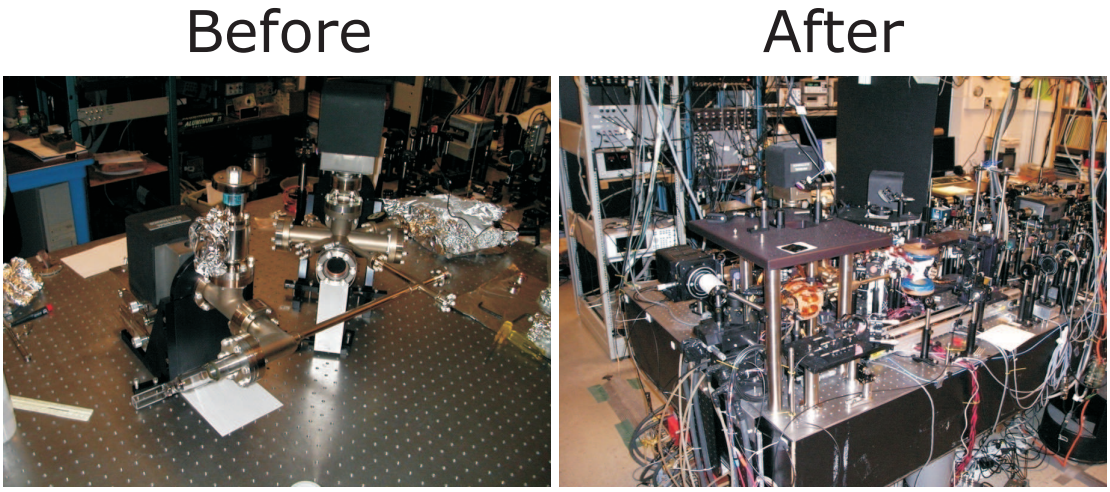

Figure 2.1: A photograph of the apparatus during vacuum assembly and a current photograph.

2.2 Vacuum system

Our vacuum system is constructed from ultrahigh vacuum (UHV) compatible components such as stainless steel and pyrex glass; joints are sealed with welds or with ConFlat-type copper compression fittings. A schematic of the vacuum system is shown in Figure 2.2. The system consists of two chambers separated by a long, thin tube. The collection MOT is a ten-way stainless-steel cross. Five ports have 2.75 inch Conflat (CF) fittings to which viewports with 1.5 inch clear aperture were attached; the MOT beams travel through these ports. Another 2.75 inch CF port is connected to a 2.75 inch tee in order to mount an ion pump and provide optical access for the remaining MOT beam. The remaining four ports are 1.33 inch mini-CF flanges; two have mini-CF viewports attached and allow for monitoring of the MOT fluorescence, one has a mini-CF viewport and a connection to the ampoule valve, the last port connects to the transfer tube. The collection chamber is pumped by a 20 L/s ion pump made by Physical Electronics (now Gamma Vacuum), the pumping element is a combination of tantalum and titanium to have a good pumping speed for noble gases and other gas loads. The collection MOT ion pump has been disabled for the last several years since the vacuum pressure in the collection chamber is dominated by Rb. In fact, the collection MOT ion pump is likely saturated with Rb vapor. It would have to be cleaned out before it could be used to pump on the collection chamber again.

The source of Rb for the collection MOT is an ampoule. A solid mass of Rb is enclosed in a glass ampoule tube sealed under nitrogen. The ampoule was placed inside a stainless-steel tube that was attached to the rest of the vacuum system. The ampoule was carefully broken under vacuum by pinching the steel tube prior to the first vacuum bakeout. An inexpensive valve was used to separate the Rb ampoule from rest of the vacuum system. We control the Rb vapor pressure in the collection MOT chamber by heating the steel ampoule tube. We choose to use a Rb ampoule instead of alkali dispensers ("getters") since the ampoule is guaranteed to produce Rb vapor and a significant amount of vapor is initially required to coat the steel walls of the collection MOT chamber.[1] Getters work very well in an all-glass chamber but in our experience their performance is marginal in a big stainless chamber like ours.

The science chamber is located at the other end of the transfer tube. The science cell is a commercially available glass fluorometer cell sold by Starna Cells, Inc. It is made of high optical quality pyrex glass and it is rectangular with dimensions: 10 mm tall, 20 mm wide, and 45 mm long. The cell is attached to a 1 inch diameter pyrex tube and then a 2.75 inch CF flange with a glass-to-metal seal. The science cell is quite small, basically only large enough so that a hot gas (800 μK) tightly confined in a magnetic trap fits inside. The small glass cell provides several advantages: magnetic trapping coils can be located close to the atoms, the optical quality is good across the entire cell, and induced currents from changing magnetic and rf fields are reduced.

On the science cell side of the transfer tube there are two vacuum pumps and an ultrahigh vacuum valve. The valve (made by Granville-Phillips, Model 203) is used to connect a turbopump for the initial pump down of the vacuum system from atmospheric pressure. There is another 20 L/s ion pump on the science cell side of the vacuum system which is identical to the collection MOT pump. Since there is little Rb vapor on science cell side of the system, this pump runs continuously to remove gas from the

[1] Alkali dispensers are sold by SAES Getters Inc.

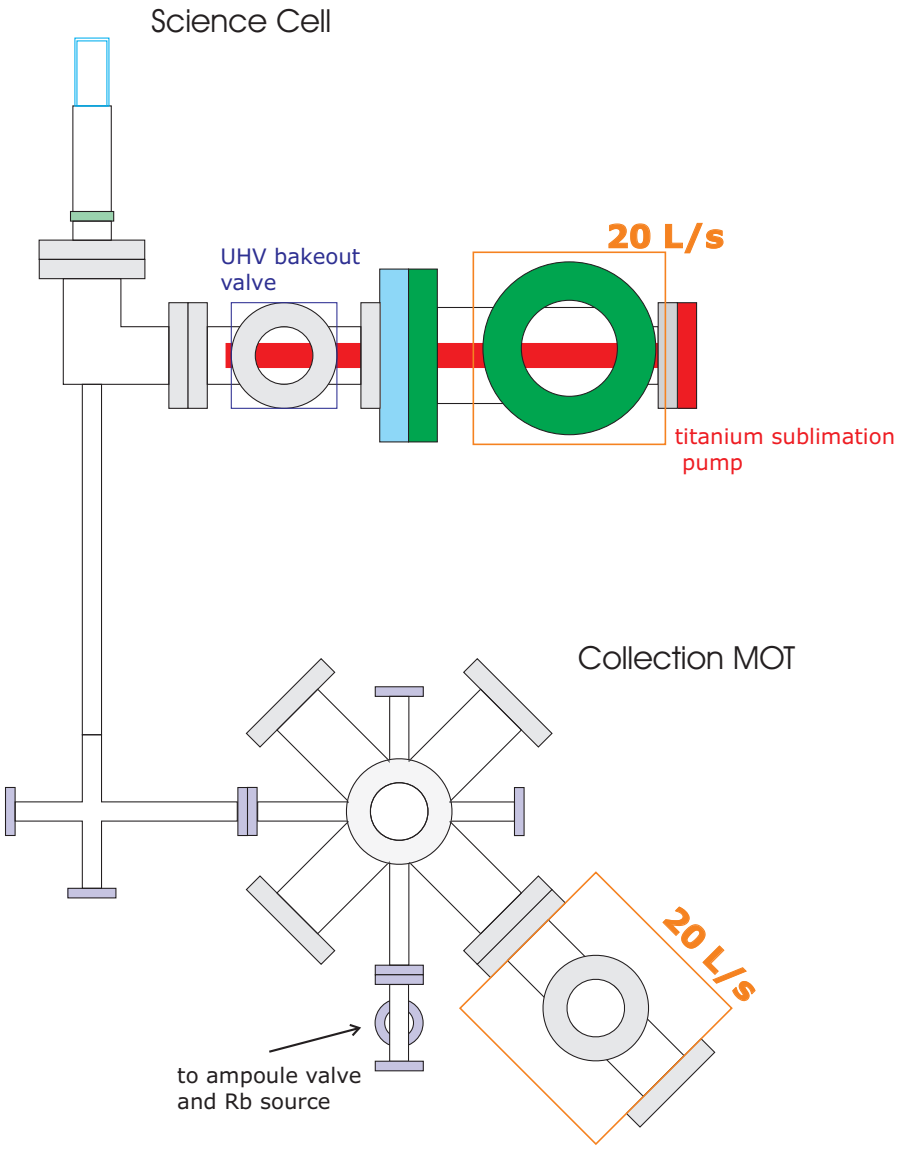

Figure 2.2: Schematic of the vacuum system used in this thesis. Atoms are laser cooled and trapped in the collection MOT chamber and evaporative cooling is performed in the science cell. The chambers are connected by a long thin transfer tube.

entire vacuum system. There is also a titanium-sublimation pump (TSP) on the science cell side of the system which is used to remove residual gas that diffuses out of the stainless-steel vacuum parts.

The transfer tube which connects the collection MOT chamber to the science cell is constructed from a long, thin stainless steel tube. It is composed of two segments welded at either end. The segments are connected in the middle with a mini-CF connection. The segment at the collection chamber end is about 4 inches long with an inner diameter of 9 mm and the segment at the science cell is 15 inches long with an 11 mm inner diameter. The conductance C in L/s of a long thin tube is $C = 12D^3/L$ where the diameter and length are in centimeters [63, 64]. The total conductance of the tube is 0.3 L/s for air, not including the effects of the 90^o bend which should lower the conductance by another factor of three for air [64].

The bend in the transfer tube has been successful at limiting Rb vapor from polluting the vacuum of the science cell. Since the first pump down of the vacuum system we have had consistently excellent vacuum conditions in the science cell. The only vacuum problems that we experienced were due to buildup of Rb in the collection chamber side of the transfer tube. The magnetic-trap transfer efficiency is an excellent indicator of the transfer tube pressure; we use it to diagnose the vacuum pressure in the transfer tube. We installed several heaters on this section of the tube; the heaters are constantly run to keep the tube temperature about 50-100° C above ambient. The heaters are designed to maintain a thermal gradient along the transfer tube. The collection chamber end is kept the coldest so that any vapor buildup on the tube walls is driven back towards the MOT area. We determined experimentally that the thermal gradient along the tube is important to maintain the best conditions.

Our vacuum system was designed with the minimum number of CF seals to make assembly of the system easier and to reduce the potential for leaks. Wherever possible we designed custom parts that were welded together instead of utilizing multiple commercial pieces. The welds in a custom part are typically easy to leak check after construction and are made reliably by the skilled machinists at JILA. In contrast, a large system with many CF seals can be awkward to leak check. Welded seals are also reliable to much higher temperature than a CF joint so that baking restrictions are relaxed. Unfortunately welded seals are sometimes magnetic, but in our experience it is more likely to find screws and nuts that are magnetic since they are made from lower quality steel.

Once the vacuum system was assembled and fully leak checked, we pumped the system down using a turbopump backed by a scroll pump. These pumps were connected through the UHV valve. We degassed the TSP by running each filament at 30 A for 20 minutes and then 40 A for 3 minutes. The vacuum system including the ion pumps was baked out for several days to reduce the outgassing rate. The stainless steel parts were wrapped in fiberglass heater tape, and aluminum foil was used for insulation. We constructed a fire-brick oven around the science cell, since heater tape could not be wrapped directly on the glass. The collection MOT chamber and ion pump were heated to 170 °C, but the ampoule temperature was kept below 90 °C. The transfer tube was heated to 225 °C and the science cell area was heated to 260 °C. The ion pump magnets were removed for the bake. We monitored the pressure at the turbopump during the bake, and a minimum pressure was reached after four days. At this point we closed the UHV valve and cooled the ion pumps so that they could be activated. The baking

continued into the ion pumps for another two days before we slowly cooled the system down. The TSP was fired at 47 A for 3 minutes and then 48 A for 1.5 minutes after the vacuum system was brought to room temperature.

There is some controversy about the effectiveness of titanium sublimation pumps. Some BEC machines in JILA (see Ref. [6]) have seen little reduction in the pressure after firing the titanium sublimation pump. Therefore we initially constructed our system without a titanium sublimation pump expecting that the ion pumps would be able to lower the vacuum pressure sufficiently. The most direct measurement of vacuum pressure in our system is the lifetime of magnetically trapped atoms. The population of atoms in the trap decays exponentially with a time constant that is related to vacuum pressure. Without a titanium sublimation pump, we measured a magnetic trap lifetime of 30 seconds. We performed a careful analysis of residual gas in the vacuum system using an SRS residual-gas analyzer; the results are shown in Figure 2.3. We found that the dominant contributions were from chemical species that typically desorbe and diffuse from stainless steel. We found no evidence of vacuum leaks to atmosphere. We installed a titanium sublimation pump to remove this residual gas, and we observed magnetic trap lifetimes greater than 500 seconds.

2.3 Two-species MOT

This section describes the two-species MOT used to collect and cool ^{85}Rb and ^{87}Rb from a room temperature vapor. The precise functioning of a MOT has been described elsewhere in detail [65, 6, 66] and will not be repeated here. A schematic of the MOT region is shown in Figure 2.4. Our MOT configuration has three orthogonal, retroreflected laser beams with σ^+-σ^- polarization; the laser beams are expanded to completely fill the vacuum system viewports.[2] A pair of anti-Helmholtz coils called the "MOT-coils" provide the magnetic-field gradient to establish the position of the MOT. These coils also provide the first quadrupole trap for our magnetic transfer sequence, and they will be discussed in more detail later. To load atoms into the MOT, 30 A is passed through the MOT coils to create a field gradient of 10 G/cm. The current in the MOT coils is controlled with an electronic servo, for details see Section 3.3. The reference voltage for the servo is supplied by an analog voltage from the computer. Three other utility coils are used to shim the MOT position, they are referred to by the direction of their axes "up/down", "east/west", and "north/south". The shim coils are made from 22 AWG magnet wire with about 100-200 turns per coil. The current through the coils is controlled with an analog voltage from the computer.

For both ^{85}Rb and ^{87}Rb trapping light for the MOT is derived from injection locked diode lasers (see Chapter 3 for more specific details) and delivered to the MOT region of the optical table with polarization maintaining optical fibers. The fibers provide very stable long-term pointing of the MOT trapping beams; in particular when the injection locked diode is replaced, only the input to the fiber need be realigned. In fact, since installing the fibers in 2004, the two-species MOT has not required serious realignment. Simultaneously collecting ^{85}Rb and ^{87}Rb into the MOT requires the combination of different laser beams at nearly the same frequency and with the same

[2] A MOT with a large number of atoms has a significant optical depth leaving a low-intensity shadow in the retroreflected beams. This typically results in a non-uniform MOT cloud shape which is not ideal but can be transiently corrected by reducing the optical thickness of the MOT.

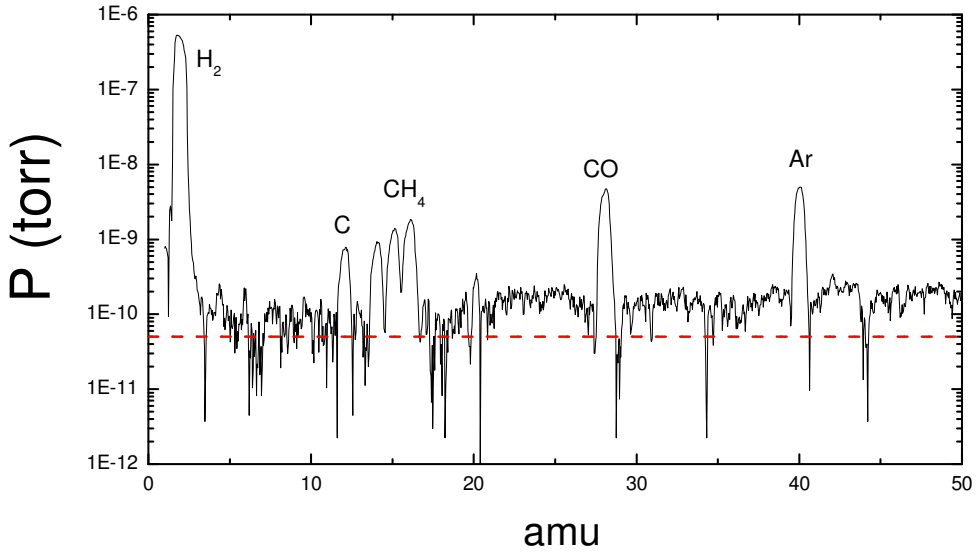

Figure 2.3: A plot of partial pressure as a function of mass showing the residual gases in our vacuum system without a titanium sublimation pump. The system was sealed and the ion pumps were left off for one hour for this measurement. The red dashed line indicates the sensitivity limit of the RGA.

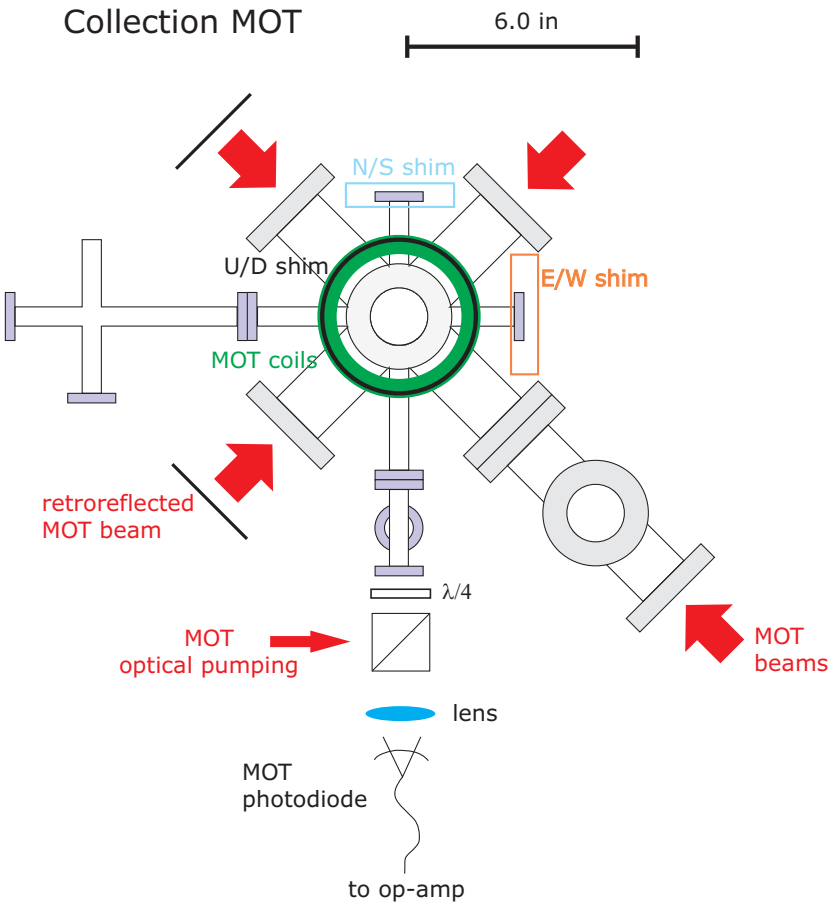

Figure 2.4: Schematic diagram of the MOT region including the anti-Helmholtz MOT coils, the three shim coils, and the lens used to collect MOT fluorescence onto the photodiode. Not shown: quarter-wave plates just before each MOT beam enters the vacuum system and the up/down direction MOT beams.

polarization. This is trivial with a non-polarizing beamsplitter as long as half the power in each beam can be sacrificed, but for our MOTs this is unacceptable. Approximately 65 mW of ^{87}Rb trapping light and 12 mW of ^{85}Rb trapping light is available after the optical fibers. We devised an optical system that combines the beams with the same polarization and no loss of power, but with a slight misalignment. The optical setup we use to combine the ^{85}Rb and ^{87}Rb MOT beams is shown in Fig. 2.5. The two beams are tightly focused with a 3 cm focal length achromatic lens very close to a dielectric mirror with a finely polished edge. The ^{87}Rb light passes by the edge of the mirror while the ^{85}Rb light is steered to reflect off the polished mirror into the same direction as the ^{87}Rb light. Both laser beams, now collinear and nearly completely overlapped, are expanded and collimated to the size of the MOT chamber viewports.

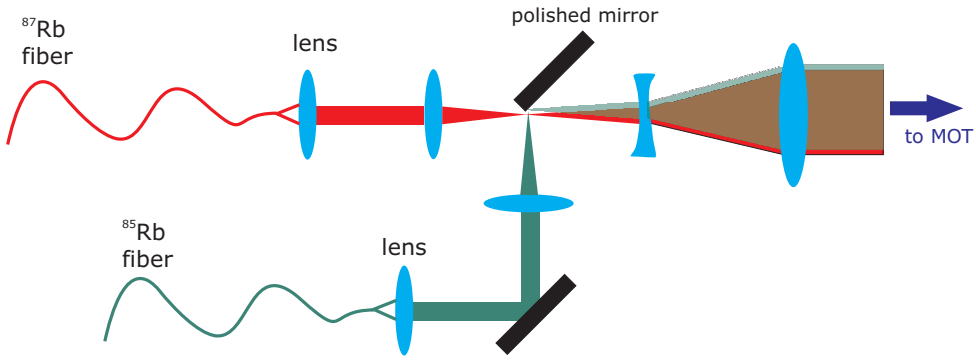

Figure 2.5: Optical arrangement used to combine MOT light with the same polarization for the two species. After the final lens the two beams are collinear with an offset less than 1 mm.

Repump light for both species is derived from diode lasers (see Chapter 3) and delivered to the MOT region. The ^{87}Rb repump light comes from an injection-locked diode laser, but it is not fiber coupled. The ^{85}Rb repump light comes directly from an external cavity diode laser; the light is fiber coupled to enhance the pointing stability. Approximately 15 mW of ^{87}Rb repump light and 4 mW of ^{85}Rb repump light is available for the MOT; this amount of power is more than enough to collect a large number of atoms into each MOT.

The trapping and repump beams for both species are combined using a polarizing beamsplitter cube since they do not require the same polarization. After combination the MOT light is split into three beams using a pair of polarizing beamsplitter cubes; each beam is aligned through a quarter-wave plate to produce circular polarization, then the beam is aligned into the MOT chamber with a pair of dielectric mirrors. A significant advantage of the stainless steel vacuum chamber is the ease of alignment of the all the MOT beams. Simply by verifying that the beams travel straight through the chamber, angular alignment of better than one degree is assured. The retroreflected beams are initially aligned to overlap the incoming beam as well as possible. With atoms collected into the MOT, the retroreflected beams are adjusted slightly to give the most compact and symmetric shaped cloud.

The absolute number of atoms trapped in the MOT can easily be determined within a factor of three by measuring the fluorescence emitted by the atoms. Fluores-

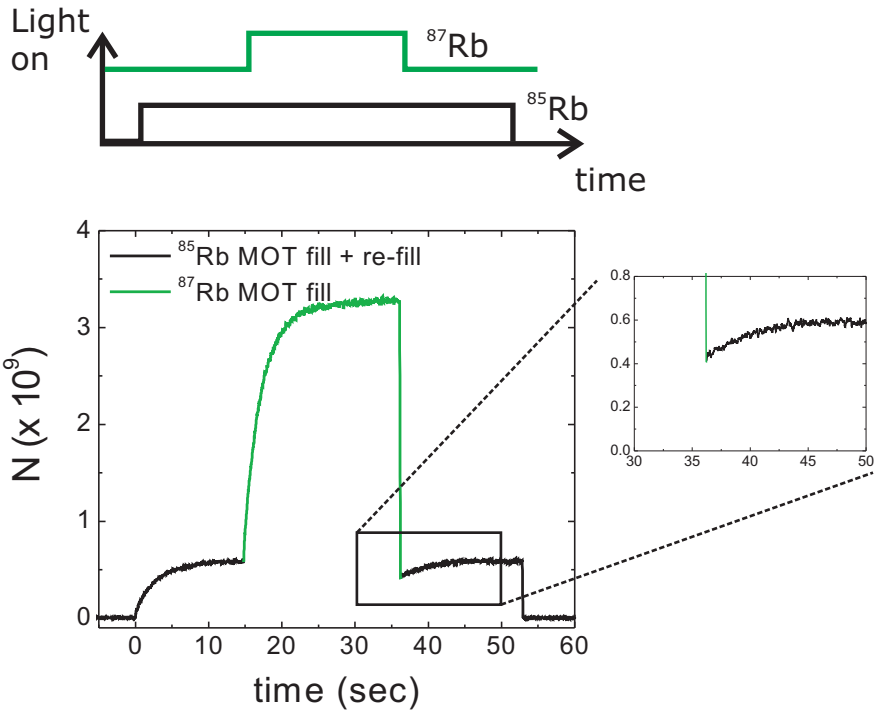

Figure 2.6: Number of atoms in the two-species MOT as a function of time. At t=0 the trapping and repump light for ^{85}Rb is applied and that MOT begins to fill. At the same time the trapping light for ^{87}Rb is switched on. At t=15 sec the repump light for ^{87}Rb is switched on so that atoms are loaded into that MOT. At t=37 sec the ^{87}Rb repump light is switched off and the atoms in the MOT are rapidly lost. After the ^{87}Rb MOT is switched off, the ^{85}Rb MOT refills to its initial number. Number loss occurs in the ^{85}Rb MOT due to light-assisted collisions as described in the main text.

cence from the MOT is collected onto a calibrated photodiode. The number of atoms is determined based on the expected scattering rate of a single atom given by [66]

$$\Gamma = \frac{1}{2}\gamma \left(\frac{1}{1 + s_0 + (\frac{2(\delta)}{\gamma\sqrt{1+s_0}})^2} \right) \tag{2.1}$$

where γ is the natural linewidth of the atomic transition, $s_0 = I/I_{sat}$ is the saturation parameter, and δ is the laser detuning from atomic resonance. The absolute number of atoms in the MOT as measured by the fluorescence depends on the MOT detuning, the MOT laser power, and the collection efficiency of fluorescence onto the photodiode. The absolute number also depends on the details of the atomic level structure, see Ref. [65, 67] for details. The MOT can be viewed through various vacuum ports but calibration of the solid angle is difficult since the inside of the vacuum system behaves as a light funnel. While loading atoms from the vapor in the collection chamber, the ^{87}Rb (^{85}Rb) MOT detuning is set to -21 MHz (-13 MHz) and both repump lasers are on resonance. We are typically able to collect approximately 3×10^9 ^{87}Rb atoms and a little more than 10^8 ^{85}Rb atoms based on the fluorescence signal. The fluorescence signal from the MOT is used to monitor the atom number during operation of the apparatus. For reproducible behavior of evaporative cooling in the science cell, we would like the MOT number to be stable to much better than 1%. However fluctuations in the parameters that determine the MOT number via fluorescence tend to limit the stability of MOT fluorescence to about 1%, meaning that we cannot measure the relative number better than this. To significantly improve our ability to measure the MOT number, we would need to stabilize the laser frequencies to better than 0.1 MHz and the MOT laser power to better than 1%.

Figure 2.6 shows the measured number in the two species MOT as a function of time during loading. For this experiment the ^{85}Rb MOT was loaded before the ^{87}Rb MOT was initiated. The presence of ^{87}Rb atoms tends to cause number loss in the ^{85}Rb MOT due to light assisted collisions between excited-state and ground-state atoms [68, 69, 70]. A pair of ^{85}Rb –^{87}Rb atoms can absorb a photon with energy $h\,\nu_1$ from the MOT light during a collision and interact via an attractive excited state potential. The pair emits a photon with lower energy $h\,\nu_2$ during the collision, due to the attractive potential. The energy difference between the two photons goes into the kinetic energy of the pair. If this kinetic energy is larger than the depth of the MOT, then the atoms are lost. This type of loss is evident in Figure 2.6, and we see a re-filling of the ^{85}Rb MOT after the trap for ^{87}Rb is switched off. We typically load a much larger number of ^{87}Rb atoms into the MOT and therefore light assisted losses are more severe in the ^{85}Rb MOT.

2.4 Quadrupole trap loading procedure

The two-species MOT collects atoms and cools them to approximately 100 μK, but this is not cold enough to make a BEC. Atoms from the MOT must be transferred to the science cell for evaporative cooling. In this section we describe the first step in the transfer process, atoms from the MOT are loaded into a quadrupole magnetic trap. Our goal is to load as many of the MOT atoms into the quadrupole trap (QT) as possible without raising the temperature significantly. If we simultaneously turned off

the MOT and switched on the QT, only a small fraction of the atoms would be loaded since the experimental conditions for collecting atoms into the MOT are different from the optimum conditions for loading the QT. Instead we use a multistep procedure to load atoms from the MOT into the QT. First, the shape and position of the MOT cloud are optimized for QT loading by initiating a compressed MOT (CMOT) stage [71]. The CMOT increases the density and tends to shape the cloud into a smooth ball. Next we use polarization-gradient (PG) cooling with the MOT light to remove as much kinetic energy from the atoms as possible. Following the completion of PG cooling, the MOT light is quickly switched off, and the atoms begin to expand and fall under gravity. We then quickly prepare all the atoms from the MOT into the correct spin state for QT loading. Finally the QT is rapidly switched on to catch the atoms.

Both species must be loaded into the QT from the MOT with reasonable efficiency. Although we can collect many more ^{85}Rb atoms into the MOT than are needed, we still must load ^{85}Rb efficiently or else stability is poor and a different number is loaded each run. Some experimental parameters can be set independently for the two species, but many parameters like the magnetic fields, laser polarizations, and duration of the loading procedure must be the same. The apparatus is first optimized to load ^{87}Rb from the MOT into the QT as well as possible. The remaining independent parameters for the ^{85}Rb MOT are then optimized.

The quadrupole trap potential is created with the same anti-Helmholtz coil pair used to produce the MOT field gradient. Each MOT coil is wound with 14 turns of square-shaped hollow copper tubing. The copper tubing is about 0.16 in. per side and it is insulated with a layer of kapton adhered to the copper with silicon. The copper tubing is hollow so that water can flow through the center of the conductor to remove the heat generated when the coil is energized with up to 300 A of current. In cross section there are three turns along the axis of the coil and five turns along the radius. The final turn of the coil is missing to make a total of 14 turns. The radius of the average MOT coil turn is 1.88 in, and the distance to the atoms is 2.0 in. The MOT coils provide a uniform magnetic field gradient of $0.37\frac{G}{cm\,A}$. The current running through the coil is controlled using our standard servo system discussed in Section 3.3. The reference signal for the MOT coil servo system is provided by an analog voltage from the control computer.

We use two diagnostic tools, MOT recapture and absorption imaging (see Section 2.8), to study the QT loading efficiency and the temperature of the gas in the QT. We perform MOT recapture during any stage of the QT loading procedure simply by switching all the MOT parameters to the values used during normal MOT operation. We record the MOT fluorescence immediately after the parameters are reset to exclude atoms loaded from the vapor. Of the two tools, MOT recapture is the most useful since it provides a direct measure of the fraction of the MOT loaded into the QT and it only requires a simple photodiode to record MOT fluorescence. However with MOT recapture it is difficult to get an accurate measure of temperature, when this information is required we resort to absorption imaging. There is an optical path available in the collection MOT for absorption imaging but the CCD camera must be moved from its normal location near the science cell.

2.4.1 Compressed MOT and polarization-gradient cooling

The density of atoms in a MOT is limited by number losses due to several processes like light-assisted collisions (see Refs. [72, 66]) and by effective repulsive atom-atom interactions through re-scattered light. The emitted photon from a trapped atom may be re-absorbed by another atom in the MOT before the photon leaves the trapping volume. Averaging this process over many absorption-emission events causes an effective repulsive interaction between atoms in the MOT that lowers the density.

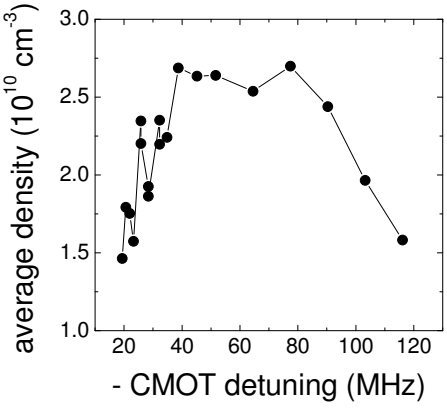

Figure 2.7: Measured density in the ^{87}Rb compressed MOT as a function of the CMOT laser detuning. We set the detuning to -35 MHz which gives the best performance. Here the detuning is measured with respect to the ^{87}Rb cycling transition.

One way to overcome this density limitation of the MOT is to quickly lower the rate of photon scattering by increasing the detuning of the trapping light and lowering the repump power. In this case, both the rate of light-assisted collisions and the rate of MOT light re-absorption are reduced and the density of the MOT is transiently increased. To realize a CMOT for ^{87}Rb (^{85}Rb) in our system, we change the trapping laser frequency detuning from -21 MHz (-13 MHz) to -35 MHz (-20 MHz) and we decrease the intensity of the repump laser from 4.8 mW/cm^2 (1.3 mW/cm^2) to 0.3 mW/cm^2 (0.15 mW/cm^2). We also change the MOT shim coil currents to new values in order to position the CMOT at the best location for QT loading. These conditions are maintained for approximately 40 ms until the maximum CMOT density is reached. Figure 2.7 shows the ^{87}Rb CMOT density as a function of the laser detuning. The best result is obtained near a -35 MHz detuning.

Following the CMOT we use polarization-gradient (PG) cooling to quickly lower the temperature of the gas. To initiate PG cooling the MOT magnetic-field gradient is switched off, the MOT shim coil currents are changed, and the laser detuning for ^{87}Rb (^{85}Rb) is tuned 103 MHz (60 MHz) red of the cycling transition. The shim coil settings during PG cooling are optimized by watching the real-time expansion of the MOT on a TV monitor after the PG cooling is initiated. The shim coils are tuned until the expansion is very slow and uniform as the cloud falls under gravity; we particularly

avoid any rapid center-of-mass jumps in the cloud position. The temperature after 40 ms in the CMOT was measured to be 150 μK, and after 3 ms of PG cooling the temperature was lowered to 50 μK. During the PG cooling the density drops by about 15%. Using MOT recapture we determined that only 5% of the atoms initially loaded into the MOT are lost during the CMOT and PG cooling stages.

Following the PG-cooling stage, the MOT light for each species is switched off quickly with a mechanical shutter made by Vincent Associates. The shutter is placed at the focus of the laser so that the switch off time is less than 0.1 ms. At this point in the loading procedure we have prepared a cold, dense two-species gas that is nearly ready to be loaded into the quadrupole trap. The only remaining step is to optically pump the atoms into the desired spin states before the QT is switched on.

2.4.2 Optical pumping and spin-state filtering

The CMOT and PG-cooling stages leave the atoms in a somewhat random mixture of all possible spin states. For magnetic trapping, all the atoms need to be spin-polarized into a low-field-seeking state, and for transfer to the science cell we need both species prepared into the stretched states with $F = 2, m_F = 2$ for ^{87}Rb and $F = 3, m_F = 3$ for ^{85}Rb where the magnetic moment is maximum. Figure 2.8 shows a level diagram for ^{87}Rb and the two laser frequencies required for optical pumping. Any ^{87}Rb atoms initially in the $F = 1$ lower hyperfine state are quickly repumped to the $F = 2$ state. Once there the atoms are optically pumped to the ^{87}Rb $F = 2, m_F = 2$ state which is a dark state due to polarization. The optical pumping scheme for ^{85}Rb is qualitatively identical, a diagram for ^{85}Rb is shown in Fig 2.9.

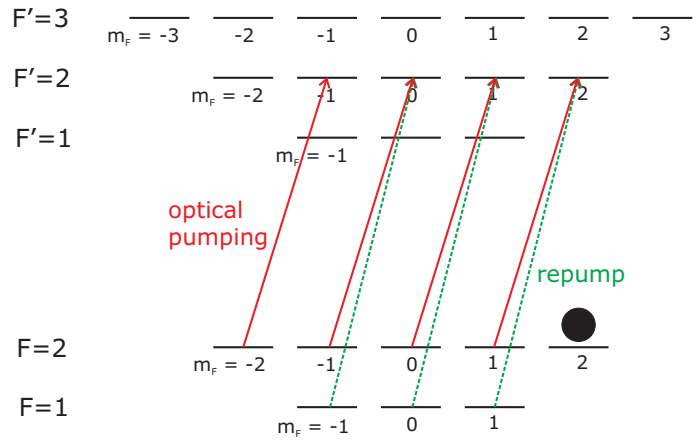

Figure 2.8: Level diagram for ^{87}Rb which shows the optical pumping scheme used to spin polarize the gas into the stretched state. The repump light (green dashed line) depopulates the lower hyperfine state quickly while the optical pumping light (red solid line) leaves atoms in the dark $F = 2, m_F = 2$ state.

A total of four optical pumping and repump laser beams for the two species enter the vacuum system along the north/south axis of the collection MOT chamber, as shown in Figure 2.4. The optical pumping light for ^{87}Rb (^{85}Rb) is tuned within a few MHz to

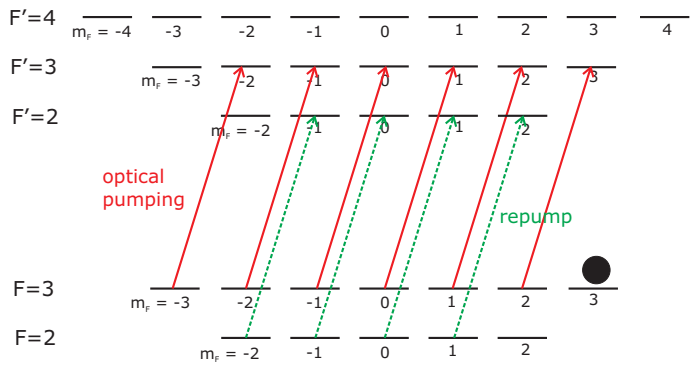

Figure 2.9: Level diagram for ^{85}Rb which shows the optical pumping scheme used to spin-polarize the gas into the stretched state. The repump light (green dashed line) depopulates the lower hyperfine state quickly while the optical pumping light (red solid line) leaves atoms in the dark $F = 3, m_F = 3$ state.

the $F = 2 \rightarrow F' = 2$ ($F = 3 \rightarrow F' = 3$) transition and the repump light for ^{87}Rb (^{85}Rb) is tuned on resonance with the $F = 1 \rightarrow F' = 2$ ($F = 2 \rightarrow F' = 2$) transition. Each laser beam is shuttered by an AOM so that short pulses can be created. Before the four laser beams enter the collection chamber, the light reflects off a polarizing beamsplitter cube which creates a clean linear polarization and then the light passes through a quarter-wave plate to create circular polarization. Both the repump and optical pumping beams are polarized to drive σ^+ transitions. The light is aligned parallel to the axis of the N/S MOT shim coil which provides a 2 G magnetic field that defines a quantization axis.

There are a number of parameters to optimize for the optical pumping including the laser frequencies, the polarization of the light, the intensity of the light, and the duration of the optical pumping stage. Since the density of the gas drops during the optical pumping stage, we set the total duration of optical pumping to be a little less than 1 ms. We experimentally optimized the remaining parameters by measuring the loading efficiency of the QT with MOT recapture. The polarization is clearly optimized when set to σ^+, and the best efficiency was obtained with the lasers tuned onto resonance. We were careful to keep the laser intensities as low as possible to avoid heating the sample with unnecessary photon scattering.

A reasonable question is: why does optical pumping work at all for a quadrupole trap? In the QT the magnetic-field vectors near the center of the potential do not all point in the same direction. Along the axis of the anti-Helmholtz coils the field vectors point inward, and along the radial direction of the coils the vectors point radially outward. Therefore if we perfectly spin-polarize the sample and load at the center of the trap, we should expect only about a third of the atoms to be loaded. The other two-thirds of the sample should be ejected from the trap since the spins are anti-aligned with the magnetic-field vector. We are definitely able to load much more than a third of the available atoms into the trap. There are likely two reasons for this unexpectedly high efficiency. The QT switch on is not instantaneous and there is enough time for the spins to rotate with the field vector. Also the experimentally determined optimum CMOT location likely includes a slight offset from the true trap center which tends to increase the efficiency of loading.

Our current best optical pumping efficiency is about 70% for ^{87}Rb and slightly less than that for the ^{85}Rb atoms. We studied the performance of the ^{87}Rb optical pumping stage and found that the high optical depth of the sample was the limiting factor. Re-absorption of a spontaneously emitted photon has the opposite effect of optical pumping. Keeping all parameters of the apparatus fixed and simply lowering the number of atoms loaded into the MOT, we observe greater than 90% of the available atoms are loaded into the QT. We are further able to directly check that the degree of spin polarization is higher for a sample with low optical depth. We directly measured the fraction of the atoms in the QT that were properly spin polarized into the ^{87}Rb $F = 2, m_F = 2$ state; this data is shown in Figure 2.10. If the MOT is fully loaded then only 70% of the atoms are successfully optically pumped. But that percentage increases toward 100% if a smaller number is loaded into the MOT.

The fact that the optical pumping stage in our system does not work perfectly is unfortunate. Some of the atoms are left in magnetically trappable spin states other than the stretched state. The fraction of the sample in the wrong state is usually about ten percent. This would hardly be a problem except for the presence of ^{85}Rb. Since the ^{85}Rb number in the MOT is so small, the population of ^{87}Rb in bad spin states

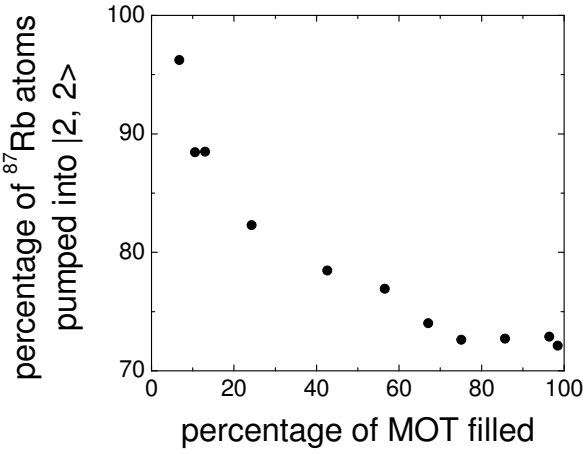

Figure 2.10: Fraction of the ^{87}Rb MOT that is optically pumped into the stretched state as a function of the MOT fill. When there are a large number of atoms in the MOT the optical depth of the gas is large and the efficiency of optical pumping is limited by re-absorption of spontaneously emitted photons. When we decrease the optical depth of the MOT by lowering the number of atoms, the optical pumping efficiency rises due to the reduction in photon reabsorption.

can actually be greater the total ^{85}Rb number. The rate of spin exchange collisions and inelastic collisions between ^{85}Rb and the bad ^{87}Rb spins is large. This leads to a rapid depletion of the ^{85}Rb population once the gases are loaded into the QT. We have observed an unacceptable factor of ten loss of ^{85}Rb number during the transfer to the science cell.

We devised a method to selectively remove only the unwanted spin states from the QT. The magnetic-field gradient of the QT must be large enough to support an atom against gravity. The required gradient β to balance gravity is given by $\beta = \frac{m\,g}{\mu}$ where μ is the magnetic moment of the atom and $m\,g$ is the force due to gravity. We can filter out the ^{87}Rb atoms in the bad spin states by holding the sample in a QT with a field gradient only large enough to hold the stretched state. Since the masses of ^{85}Rb and ^{87}Rb are nearly the same and the magnetic moments are identical, the stretched state of ^{85}Rb is also trapped. Figure 2.11 shows the results of an experiment designed to test the QT as a spin state filter. We loaded the QT with ^{87}Rb atoms from the MOT with a large enough QT current so that any magnetically trappable state is held. The QT current was then slowly decreased to different values, and the number of atoms remaining in the trap was recorded with MOT recapture. In the figure there are two distinct levels as the QT current is decreased. The highest level corresponds to trapping all ^{87}Rb spin states, and the slightly lower level corresponds to trapping only the stretched state. Below a certain current no atoms are held in the trap.

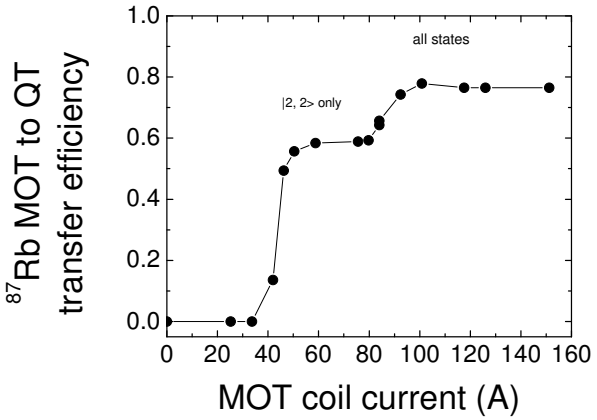

Figure 2.11: Fraction of the ^{87}Rb MOT loaded into the QT as a function of the QT current. At the smallest currents the trap is too weak to hold any atoms. Based on the calculated magnetic fields of the QT, a current of 42 A is required to trap atoms in the stretched state. Twice as much current is required for the other states that have a magnetic moment of $\mu = 1/2\,\mu_B$. If we hold the trap current at about 60 A all the atoms in unwanted spin states slowly fall out of the trap.

We use the QT as a spin state filter during normal operation of the apparatus. Immediately after the optical pumping stage terminates, the quadrupole trap is rapidly switched on with a current designed to only hold the stretched spin states of ^{85}Rb and

^{87}Rb. This current is maintained for 250 ms to allow all the bad spin states to fall out of the trap. Then the current is increased in 150 ms to provide a field gradient of 100 G/cm. At this point the atoms in the QT are ready for transfer to the science cell. The QT loading efficiency is approximately 70% (65%) for ^{87}Rb (^{85}Rb) with a total ^{87}Rb (^{85}Rb) number of approximately 10^9 (4×10^6). The two gases are in thermal equilibrium with a temperature in the range 180-200 μK in the fully compressed QT. We estimate the temperature is about 70 μK when the atoms are loaded into the weak QT.

2.5 Magnetic trap transfer to the science cell

After loading the two-species spin-polarized atomic sample into the quadrupole trap, the transfer to the science cell begins immediately to minimize number loss due to collisions with background gas. To transfer the sample between the two vacuum chambers, we translate the center of the quadrupole trapping potential. Atoms in the trap will precisely follow the translating potential and the temperature of the gas will not rise as long as the trap center does not move too quickly. The trapping potential is translated in two stages: along the transfer tube and around the 90° bend. In the first stage the currents running through a series of spatially overlapped anti-Helmholtz coil pairs are varied as a function of time. The currents are optimized so that the trapped atoms are smoothly passed between each pair of the overlapped coils from the center of the MOT chamber to the transfer tube corner. The final pair of overlapped coils is centered exactly at the corner; this coil pair is mounted on a sliding, motorized translation stage, and the motion of the stage is controlled via computer. The final coil pair and the trapped atoms are physically translated from the corner to the science cell.

2.5.1 Multi-coil transfer

The first stage of our magnetic transfer, which we refer to as the multi-coil transfer (MCT), is described here. This method was first demonstrated by the Munich group, and their implementation is described in Ref. [61]. An undergraduate student in our lab also helped with the MCT, see Ref. [73]. The partially overlapped anti-Helmholtz coil pairs are aligned in a row along the transfer tube. The combined magnetic fields of the coils create a quadrupole-like trapping potential. Due to the symmetry of our setup, the center of the trap always lies somewhere along the axis of the transfer tube. The remaining degrees of freedom are the trap center position along the tube and the three magnetic field gradients near the trap center. Only two of the field gradients are truly independent since $\nabla \cdot B = 0$ must be satisfied. We only energize three of the coil pairs, out of a total of six coils pairs, at a single time; these three currents allow us to pick the trap center position, the field gradient against gravity, and the field gradient perpendicular to the axis of the tube.

Figure 2.12 shows a side-view diagram of the collection MOT chamber, the transfer tube, and the six coil pairs involved in the MCT. As shown in the figure our coordinate system is aligned so that the x-direction points along the axis of the transfer tube and the y-direction points against gravity. The location and other properties of the coils are listed in Table 2.1. Atoms from the MOT are loaded into the QT provided by the MOT coils; see Section 2.4 for details. The coil pairs labeled a, b, c, d, and T are sequentially energized to transfer the trapped atoms to the corner. Coil pairs a-d

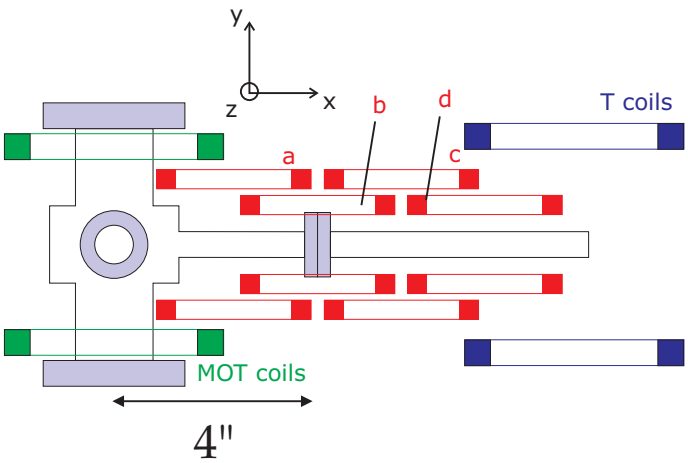

Figure 2.12: A schematic of the transfer tube region and the magnetic-field coils for the multi-coil transfer. The length from the center of the MOT chamber to the tube corner is 8 in. The T coils are mounted on a motorized translation stage to move the coils in and out of the page.

Table 2.1: Physical parameters of the coils used for the multi-coil transfer to the science cell. The radius and spacings listed here are for the average turn of the coil.

Coil	radius (in)	spacing (in)	turns	x position (in)
MOT	1.875	4	14	0
a	1.3125	3	64	2.325
b	1.3125	2	64	3.95
c	1.3125	3	64	5.575
d	1.3125	2	64	7.2
T	1.75	4.5	19	8

(shown in red) are composed of 64 turns of solid 18 AWG magnet wire.[3] These coils are air cooled since they are only energized for a few hundred milliseconds during the transfer. The fact that water cooling is not required represents a significant advantage of our system. To simplify alignment of the coils with respect to the tube, the coils are all glued onto an aluminum plate. The plate is referenced to the transfer tube for easy alignment and it is rigidly mounted to the optical table. The construction of the T-coil pair is very similar to the MOT coils.

The currents running through all the coils for the MCT are controlled by a simpler version of the servo electronics described in Section 3.3. To minimize heating of the gas during the MCT, the current noise must be kept below about 0.1%, which is easily obtainable. There is a servo setup for each coil and the reference voltages come from the control computer. To minimize the number of analog voltages required for the MCT, we use three digital lines from the computer boards to multiplex three analog signals. The digital lines program electronic that route the analog signals to the proper coil. Coils pairs a-d are powered by an HP power supply with an output current up to 50 A. The MOT coil pair and the T coil pair are powered by the main Agilent power supply which can output up to 440 A.

We numerically optimized the time-dependent currents that flow through all six of the MCT coils. The objective is to find current settings that smoothly translate the combined trapping potential from the center of the MOT chamber to the transfer tube corner. The three-dimensional magnetic field of each coil pair is modeled using Eqn. 2.5, which is discussed later in this chapter. The field components of each coil pair are summed together to find the total quadrupole trapping potential. There are several methods that can be used to optimize the coil currents for the transfer. We found a particularly simple and efficient approximate solution to the problem which is described here. For simplicity we consider only the first three of the MCT coil pairs. Our optimization procedure is run at every location along the axis of the tube at intervals of 0.005 in. Since there are three currents, we can constrain three parameters of the trapping potential. We choose to constrain the sum of the x-direction magnetic-field components of the coils, the sum of the z-direction magnetic-field gradients of the coils, and the sum of the y-direction magnetic-field gradients. The x-direction magnetic-field

[3] We ordered these custom-designed coils from Custom Coil Inc. The price per coil was only about $20. The construction quality of the coils is excellent. Each coil is securely glued with high-quality epoxy that can withstand a temperature close to 200°C

components and the two field gradients need only be calculated at the center of the tube for a given x location. Essentially we have the following three linear equations in the three unknown currents

$$B_{m,x}(x)\, I_m(x) + B_{a,x}(x)\, I_a(x) + B_{b,x}(x)\, I_b(x) = 0 \tag{2.2}$$

$$\beta_{m,z}(x)\, I_m(x) + \beta_{a,z}(x)\, I_a(x) + \beta_{b,z}(x)\, I_b(x) = \beta_z \tag{2.3}$$

$$\beta_{m,y}(x)\, I_m(x) + \beta_{a,y}(x)\, I_a(x) + \beta_{b,y}\, I_b(x) = \beta_y \tag{2.4}$$

where $I_m(x)$, $I_a(x)$, and $I_b(x)$ are the currents in the coils as a function of x, respectively. The calculated x-direction magnetic field per amp is labeled $B_{m,x}(x)$, $B_{a,x}(x)$, and $B_{b,x}(x)$ for the MOT, a, and b coils. The calculated y-direction and z-direction magnetic-field gradients per amp of current in the MOT, a, and b coils are labeled by, for example, $\beta_{m,z}(x)$. The constants β_y and β_z fix the strength at the center of the composite trapping potential provided by the three coils. These gradients are set to be 58 G/cm and 100 G/cm, respectively, for the transfer. By solving this simple linear system of equations for the currents I_m, I_a, and I_b at every point along the transfer tube, we are guaranteed that the field gradients of the trapping potential will be nearly constant throughout the MCT. We verify that the approximate solution works by calculating the full trapping potential with I_m, I_a, and I_b.

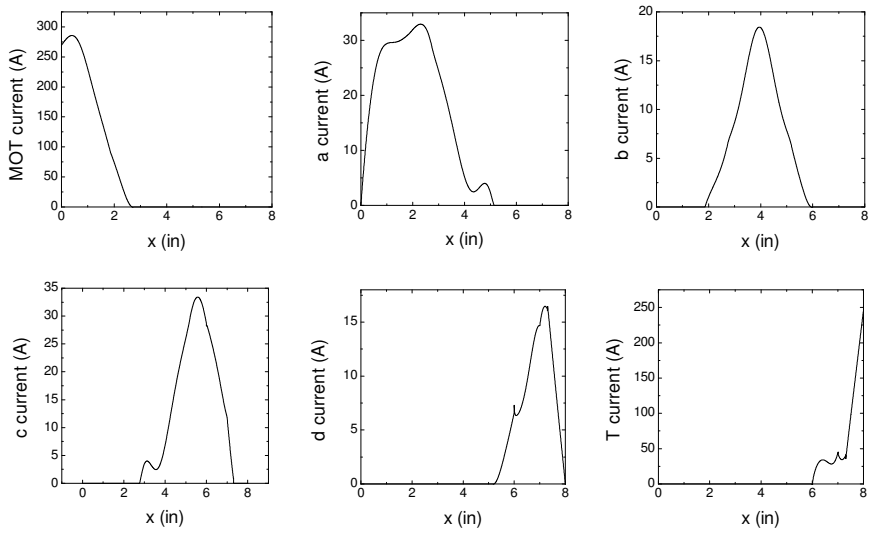

Figure 2.13: Optimized currents for the mulit-coil transfer as a function of location along the axis of the transfer tube. At peak current each coil pair provides a field gradient of approximately 100 G/cm in the direction against gravity.

The optimized currents for the MCT transfer are shown in Figure 2.13 as a function of location along the tube. The atoms start at the center of the MOT chamber where only the MOT coil is energized. To move the potential toward the corner, the

MOT-coil current is slowly lowered while the a-coil current is ramped up.[4] This general trend continues until only the T coil is energized and the atoms are trapped at the corner. The transition at which one coil is switched off and a new coil is switched on occurs "on-the-fly" as the atoms are being transferred, *i.e* the motion of the atoms is not stopped when a switch-over between coils is necessary. For example, at $x = 2.75$ in. the MOT coil current is zero and current begins to flow in the c coil. The physical placement and degree of overlap between the coil pairs is critical in making these transitions smooth.

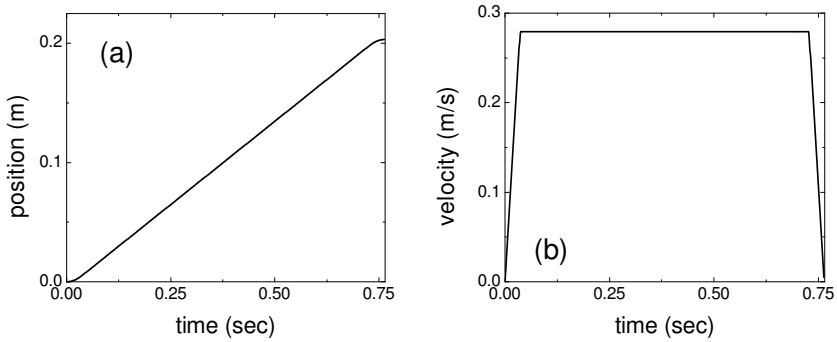

Figure 2.14: (a) The calculated position of the atoms as a function of time. (b) The velocity versus time. The velocity starts from zero so that the beginning of the transfer is smooth. Likewise, near the corner the velocity is slowly reduced to zero. Number loss and heating are observed if the atoms are violently accelerated to the 0.3 m/s top speed of the transfer. If the start of the transfer is too slow, atoms are lost due to collisions with the Rb vapor in the collection chamber.

Using our optimization procedure we found the required currents as a function of x along the transfer tube. Based on this information, we can generate any desired time-dependent trajectory $x(t)$ for the atoms to follow. We picked the trajectory that is shown in Figure 2.14. The acceleration out of the MOT chamber was experimentally optimized, as well as the maximum speed of the transfer. Since there are no mechanical pieces in the MCT, the maximum speed is limited to the rate at which the currents can be ramped. Our electronic control system for the MCT coil currents is capable of smoothly moving the trapping potential from the center of the MOT chamber to the transfer tube corner in approximately 10 ms.

The multi-coil transfer works well. We are able to transport at least 75% of the atoms loaded into the QT to the corner. We test the transfer efficiency by moving atoms to the corner and bringing them back to the MOT for MOT recapture. The limitation in the efficiency is due to the short vacuum lifetime in the collection MOT chamber. One useful diagnostic of the MCT is to vary the distance that the atoms are transferred into the tube, and then bring them back to the MOT. It allows us to pinpoint the specific

[4] For the first bit of the MCT we actually only use two coils due to the details of our system.

location of any number losses. In particular, this diagnostic helped us to characterize and understand the optimized current ramps. The MCT setup is quite reliable and robust. Since ironing out several problems during the initial testing of the setup, we have observed good performance and the setup has required little maintenance. As long as the computer control sends out the proper signals to the MCT electronics, we can expect that the transfer will work.

2.5.2 Moving coil transfer and science cell optical pumping

Once the atoms reach the transfer tube corner, the second stage of magnetic transfer can begin. Atoms are transferred to the science cell using the quadrupole trap provided by the T coils. The coils are physically moved with a motorized translation stage. As long as the stage does not move too fast the atoms remain trapped and they are delivered to the science cell. This method of magnetic transfer, via a physically moving coil pair, was developed by the Cornell group at JILA; For further information see Refs. [62, 74].

We use a motorized translation stage made by Parker-Daedal Automation. The moving platform on the translation stage is driven by a precision ballscrew and it is guided by a pair of steel rails. The ballscrew is rotated by a small motor and an internal rotary encoder precisely determines the location of the moving platform. There is an external controller that powers the motor and processes the signal from the rotary encoder. The controller also accepts external TTL signals so that the motion of the platform can be precisely timed. The hardware controller communicates with one of the experiment control computers to program the motion of the platform.

We mounted an aluminum structure on top of the moving platform that holds the T coils. The structure was designed to take up as little space around the science cell as possible, making it easier to align light into the science cell for optical trapping and Bragg spectroscopy. To accomplish this goal, the T coils are suspended well off the axis of the motorized translation stage. The structure is rigid enough to create a stable magnetic trap for the atoms.

The transfer efficiency from the transfer tube corner to the science cell is very good. We estimate that the transfer efficiency must be greater than 75% based on the measured atom numbers in the MOT and the science cell. There also appears to be little or no heating that occurs during this stage of the transfer. It takes about three seconds to transfer the atoms a distance of 19 in from the corner to the science cell. The translation stage delivers the atoms to the exact center of the Ioffe-Pritchard trap. The atoms are released from the T coils by switching off the current in less than 0.1 ms.

Before the IP trap currents can be switched on, the atoms must be spin polarized into the desired spin state for evaporation. During the transfer we want the ^{85}Rb and ^{87}Rb atoms in the stretched states to take advantage of the larger magnetic moment. For evaporation in the IP trap we want the ^{87}Rb (^{85}Rb) atoms in the $F = 1, m_F = -1$ ($F = 2, m_F = -2$) state. As will be seen in later chapters, these are the states that have magnetic-field Feshbach resonances. To prepare the atoms into the desired spin states we perform another iteration of optical pumping similar to the one described in Section 2.4.2.

Figure 2.15 shows a level diagram for ^{87}Rb and the two laser frequencies required for optical pumping. During optical pumping in the science cell, any ^{87}Rb atoms initially

in the $F = 2$ upper hyperfine state are quickly de-pumped to the $F = 1$ state. On average only two photons must be absorbed on the de-pumping transition for an atom to get to the lower hyperfine state. Once in the lower hyperfine state, the atoms are optically pumped until they reach the ^{87}Rb $F = 1, m_F = -1$ state which is dark to all the applied light due to the polarization of the light. The optical pumping scheme for ^{85}Rb is qualitatively identical.

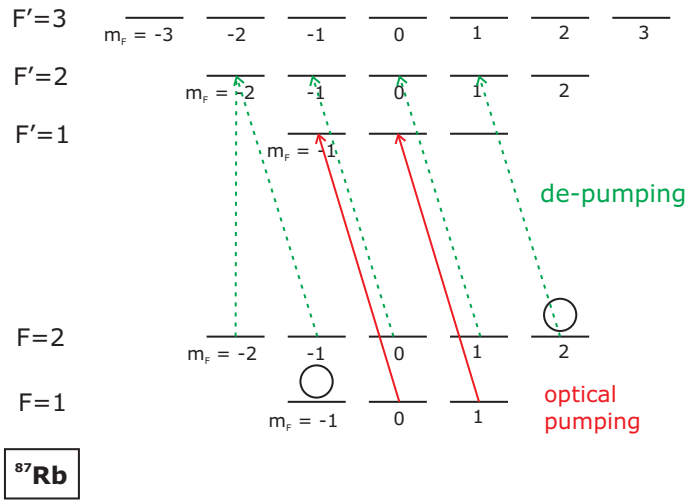

Figure 2.15: Level diagram for ^{87}Rb that shows the optical pumping scheme used to spin-polarize the gas into the $F = 1, m_F = -1$ state. The atoms all start in the $F = 2, m_F = 2$ state. The de-pumping light (green dashed line) depopulates the upper hyperfine state quickly while the optical pumping light (red solid line) leaves atoms in the dark $F = 1, m_F = -1$ state.

A total of four optical pumping and de-pumping laser beams for the two species enter the vacuum system along the east/west axis of the science cell, as shown in Figure 7.2. The optical pumping light for ^{87}Rb (^{85}Rb) is tuned within a few MHz to the $F = 1 \rightarrow F' = 1$ ($F = 2 \rightarrow F' = 2$) transition and the de-pumping light for ^{87}Rb (^{85}Rb) is tuned on resonance with the $F = 2 \rightarrow F' = 2$ ($F = 3 \rightarrow F' = 3$) transition. Each laser beam is shuttered by an AOM so that short pulses can be created and the intensity can be varied with a computer-controlled voltage. Before the four laser beams enter the collection chamber, the polarization is set to be circular by a quarter-wave plate, and the four beams reflect off a dichroic beamsplitter plate that combines the optical pumping beams with the optical trapping beam. The light is aligned parallel to the axis of the E/W science cell shim coil which provides about a 2 G magnetic field to provide a quantization axis for the atoms.

The absolute efficiency of the science cell optical pumping stage is somewhat difficult to measure. Since there is no MOT at the science cell we cannot perform MOT recapture. Moreover, absorption imaging is inaccurate for the spatially large clouds at this point in the experiment. We estimate that the optical pumping efficiency is better than 50% based on a comparison of absorption images of the gas in the quadrupole trap and in the IP trap. To optimize this stage of optical pumping we measure the

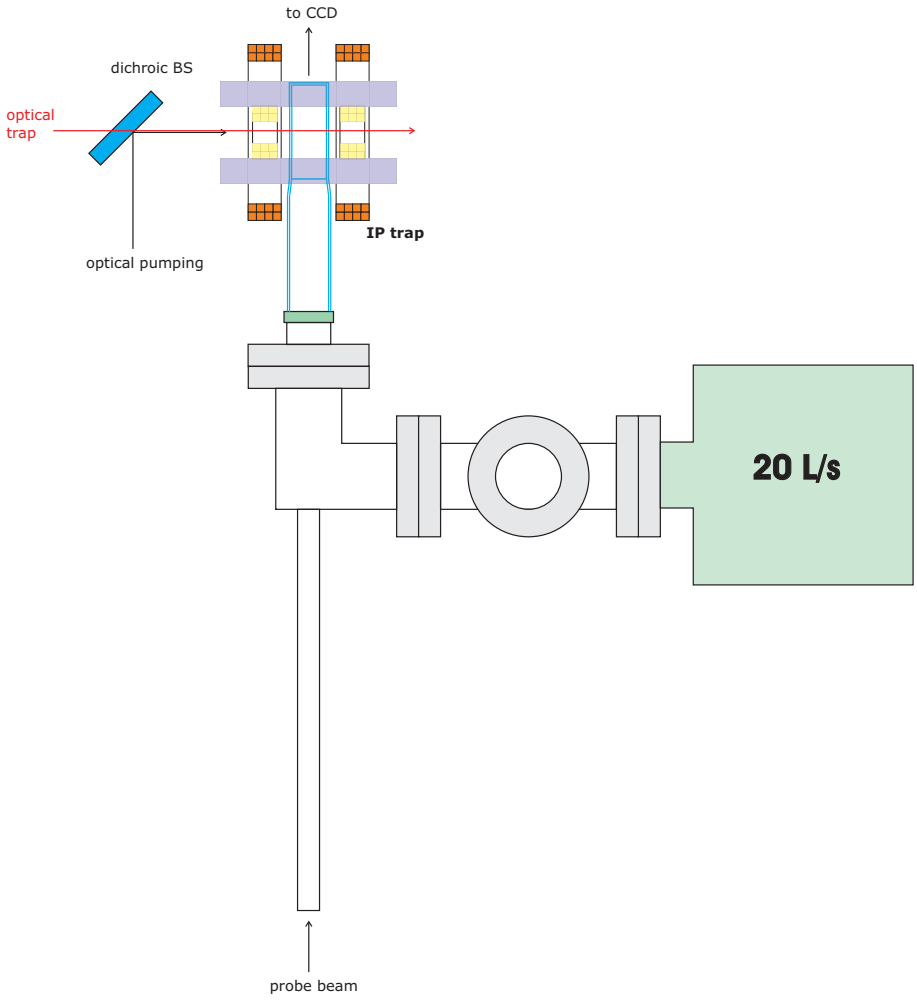

Figure 2.16: Top-view schematic showing the science cell portion of the vacuum chamber. The positions of the IP trap coils are shown. Along the east/west direction of the science cell, optical pumping light and the optical trap beam are combined on a dichroic beamsplitter. Probe light for both species resonant with the cycling transition is aligned down the transfer tube, through the atoms in the science cell, and onto the CCD camera for absorption imaging.

number of atoms after some evaporation in the magnetic trap where accurate number determination is possible. The parameters of optical pumping (*e.g.* laser power, laser detuning, etc.) are systematically varied to produce the largest number of atoms after evaporation.

2.5.3 Concluding thoughts on magnetic transfer

We are in a unique position to evaluate the relative advantages of the two magnetic-trap transfer techniques, the multi-coil transfer (MCT) method and the motorized translation stage (track) method. Our decision to use both methods was based on our desire to have a bend in the transfer tube.[5] Both methods can transfer atoms with about the same efficiency. Both methods take up about the same amount of valuable space in the science cell area. Based on our experience, the motorized track system is significantly faster to implement.

2.6 Ioffe-Pritchard trap

The Ioffe-Pritchard (IP) trap is the most critical single piece of equipment in the apparatus. We use the IP trap to create a harmonic potential suitable for evaporative cooling of the ^{87}Rb and ^{85}Rb gases. A pair of Helmholtz coils that are a part of the IP trap are used to provide the magnetic bias field for all of our Feshbach resonance work. A good deal of time went into the design of our magnetic trap; the design was guided by several criteria related to producing ^{85}Rb condensates, and performing experiments near a Feshbach resonance. We require excellent optical access to the condensate from multiple different angles for imaging and to perform measurements like Bragg spectroscopy. The size and placement of the trapping coils must be optimized to provide the necessary fields without taking up too much space. Likewise the holder pieces that mount the coils to the optical table must be rigid, but not take up too much space. For evaporative cooling we require that the magnetic fields be very stable. In contrast, for many experiments we need the ability to quickly change the magnetic field. This section describes our trap design, which satisfies all of these requirements.

The term Ioffe-Pritchard trap refers to a particular arrangement of coils that produce a harmonic trapping potential as compared to the linear potential of a quadrupole trap. A typical arrangement is shown in Fig. 2.17 where a set of four current carrying wires (called Ioffe bars) placed along the z-direction, provide a strong radially-oriented magnetic-field gradient. A pair of coils (pinch coils) with axes placed parallel to the z-direction are optimized to produce a field curvature, but they also create a large magnetic field near the center of the trap. A second pair of Helmholtz coils (bias coils) are optimized to produce a uniform field that opposes that of the pinch coils and eliminates the large field at the trap center. With this arrangement tight confinement is achieved along the radial direction of the trap, while relatively weak confinement exists along the axis of the trap. The trapping potential is harmonic and is characterized by a radial and an axial frequency.

[5] We could have used the MCT to transport atoms all the way to the science cell, but that would require a lot of coils near the science cell. Those coils would take up a lot of space around the science cell, limiting the optical access and add mutual inductance to the other coils which slows the rate at which the magnetic field can be changed. Coils mounted on the track can be moved away from the science cell area after the atoms are dropped off, therefore the inductance of the coils is irrelevant.

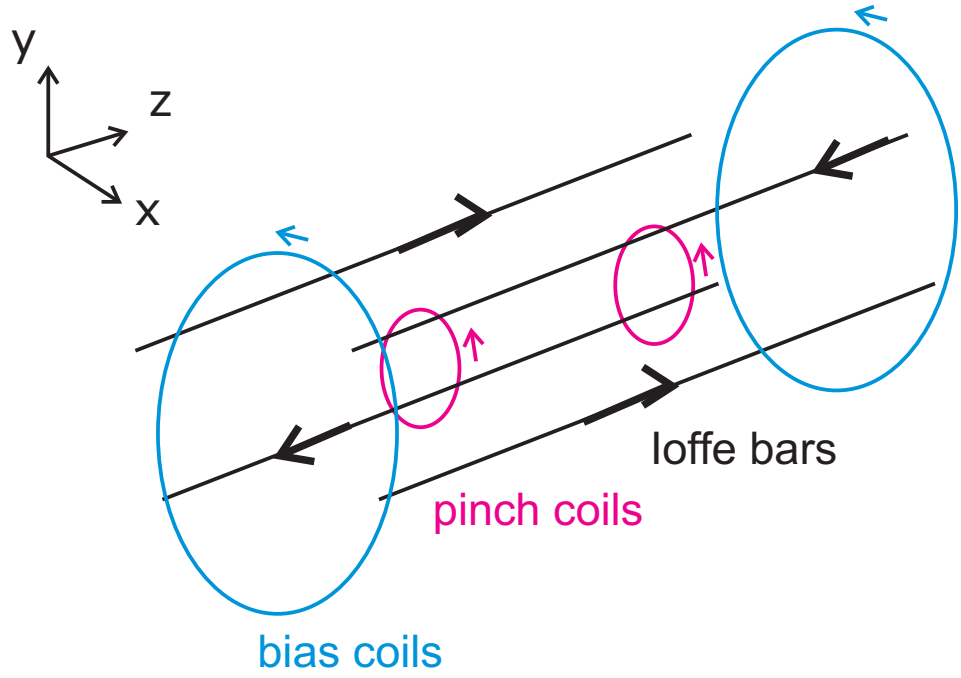

Figure 2.17: Schematic drawing of a Ioffe-Pritchard trap. Radial confinement is supplied by the magnetic fields of the four parallel wires (purple) and axial confinement comes from the pinch coils (yellow) along the axial direction. In order to get stronger confinement along the radial direction, the bias coils (orange) are set to oppose the field from the pinch coils. Since the field of the bias coils is uniform, the axial curvature provided by the pinch coils is not modified.

There are a number of different coil arrangements that can create a harmonic potential. At JILA there are examples of a "TOP" trap [75], a "baseball-style" trap [59], a "cloverleaf" trap [76], and a couple of different IP-style trap designs. We chose a design which closely mimics the diagram shown in Figure 2.17, since the coils are relatively easy to fabricate and the physical size of the complete trap can be small.

The design of the IP trap is broken into two tasks. First we determine what coil shapes, sizes, and placement are required to give the desired magnetic fields. The main factor in designing the coils is a desire to keep the number of turns N small, since the coil self-inductance scales as N^2. This decision means that the coils have to be close to the atoms to create the desired field with a reasonable amount of current. After deciding on the coils, we have to figure out how to hold all the pieces together in a rigid manner without sacrificing too much optical access. The coil holder pieces must be electrically insulating so that induced fields due to eddy currents are avoided. Since a drift in the coil positions will significantly change the magnetic field, the holder pieces must have a small coefficient of thermal of expansion.

We modeled the magnetic fields of our IP trap using standard electromagnetic theory. Here we review the three dimensional magnetic-field formulae necessary for the model. The fields of a coil placed at the Cartesian coordinates $(x',\, y',\, z')$ with radius R are given by [77]

$$B_x(x,y,z) = \frac{\mu_0\, I}{2\,\pi\,\rho}\frac{z-z'}{\sqrt{(R+\rho)^2+(z-z')^2}}\frac{x-x'}{\rho} \times\left(-E_K(k_s)+\frac{R^2+\rho^2+(z-z')^2}{(R-\rho)^2+(z-z')^2}E_E(k_s)\right) \tag{2.5}$$

$$B_y(x,y,z) = \frac{\mu_0\, I}{2\,\pi\,\rho}\frac{z-z'}{\sqrt{(R+\rho)^2+(z-z')^2}}\frac{y-y'}{\rho} \times\left(-E_K(k_s)+\frac{R^2+\rho^2+(z-z')^2}{(R-\rho)^2+(z-z')^2}E_E(k_s)\right) \tag{2.6}$$

$$B_z(x,y,z) = \frac{\mu_0\, I}{2\,\pi\,\sqrt{(R+\rho)^2+(z-z')^2}} \times\left(E_K(k_s)+\frac{R^2-\rho^2-(z-z')^2}{(R-\rho)^2+(z-z')^2}E_E(k_s)\right) \tag{2.7}$$

$$\rho(x,y) = \sqrt{(x-x')^2+(y-y')^2} \tag{2.8}$$

$$k_s(x,y,z) = \frac{4\,R\,\rho}{(R+\rho)^2+(z-z')^2} \tag{2.9}$$

where E_K and E_E are commonly tabulated elliptic integrals, I is the current, and $\mu_0 = 4\pi\times 10^7$ N/A^2. To accurately model the field gradient produced by the Ioffe bars we note that the field at the Cartesian coordinates (x, y, z) due to a finite length L piece of wire located at $(x',\, y')$ carrying a current I is given by

$$B_x = -\frac{\mu_0\, I\,(y-y')}{4\pi((x-x')^2+(y-y')^2)} \times\left(\frac{L-2z}{\sqrt{4((x-x')^2+(y-y')^2+(L-2z)^2)}}+\frac{L+2z}{\sqrt{4((x-x')^2+(y-y')^2)+(L+2z)^2)}})\right) \tag{2.10}$$

$$B_y = \frac{\mu_0 I (x - x')}{4\pi((x-x')^2 + (y-y')^2)} \times \left(\frac{L-2z}{\sqrt{4((x-x')^2+(y-y')^2+(L-2z)^2)}} + \frac{L+2z}{\sqrt{4((x-x')^2+(y-y')^2)+(L+2z)^2)}}) \right). \quad (2.11)$$

To find the total magnetic field of the trapping coils we sum together the three components of each coil and calculate the magnitude $B_{tot} = \sqrt{B_x^2 + B_y^2 + B_z^2}$. The trapping frequencies are related to the second derivative of the total field and they are given by $\omega_i = \sqrt{\frac{\mu}{m}\frac{d^2B}{dx_i^2}}$, where the i subscript indicates the different Cartesian directions, μ is the magnetic moment of the atoms, and m is the mass. Since the above equations are valid anywhere in space, they can be used to estimate the effects of anharmonic terms in the trapping potential.

Our IP trap is composed of three coil pairs. For each coil we specify the parameters of the "average" turn. In our calculation of the fields, we assume that each turn is located at the average location. We verified that this approximation is accurate at the few percent level for our system by comparing to a calculation of the fields that includes the individual turns. The bias coils are in approximately Helmholtz configuration, in which the coil radius is equal to the coil pair separation. The bias coils have a radius of 1.5 in., a separation of 1.875 in., and are composed of 8 turns per coil. The measured resistance of the bias coils is 7.23(1) mΩ. The pinch coils are designed to provide a large field curvature so their radius is small compared to the pair separation. The pinch coils have a radius of 0.4375 in., a separation of 1.87 in., and are composed of 6 turns per coil. The measured resistance of the pinch coils is 2.119(4) mΩ. The Ioffe bars are 4 in long and each bar has seven conductors. The Ioffe bars are placed along the radial direction with coordinates $x' = 0.625$ in. and $y' = 0.656$ in; the zero of the coordinate system is at the center of the bias coils. The measured resistance of the Ioffe bars is 7.61(2) mΩ.

With the above coil dimensions the magnetic fields of our trap can be calculated. For the pinch and bias coils we characterize the coils by the field generated per amp of current and the field curvature per amp. The model predicts that the bias coil field is 1.61 G/A with a curvature of 0.097 G/cm^2/A. The pinch coil supplies 0.515 G/A and a curvature of 0.695 G/cm^2/A. The Ioffe bars are characterized by the radial field gradient, which is 1.04 G/cm. During evaporation we pass about 312 A through the Ioffe bars and pinch coils, and about 90 A flows through the bias coils. The model indicates that these currents provide a radial (axial) trap frequency of about 210 Hz (13 Hz) for ^{87}Rb at a bias field of about 1.6 G. Tighter confinement is possible with a smaller bias field at the center of the trap.

Each of the six IP trap coils are wound from square, hollow copper tubing that is about 0.16 in. per side and is insulated with a layer of kapton. The resistance of the tubing is 1.73 mΩ/m. This is the same tubing that is used for the MOT and T coils. The hollow core of the tubing allows us to water cool the coils.[6] [7] The IP

[6] It is important to interlock the high current power supply against flow of the cooling water. We use a TTL based flow switch and the interlock feature of the power supply.

[7] We have a simple model for the water flow rate required to cool the coils. The flow rate is $\frac{P_{coil}}{\rho_w V c_w \Delta T}$ where P_{coil} is the power dissipated in the coil, ρ_w is the density of water, $c_w = 4187 J/kg\,K$ is the heat capacity of the water, V is the volume of water in the coil, and ΔT is the temperature increase of the cooling water between the entrance and exit of the coils. We observed excellent agreement between this model and the observed temperature increase of the water.

coils were wound around custom-machined forms made of aluminum and plastic. The gaps between different turns of a coil were filled with two-ton epoxy to keep the coil from unraveling when it is removed from the form. For simplicity, the upper and lower pairs of Ioffe bars are actually wound as racetrack-shaped coils. The section of the these racetrack coils near the center of the trap is straight.

With all the parameters of the coils picked out, we focus on the design of the IP trap mounting structure. All the coil holder pieces are made from phenolic which is basically layers of cotton cloth held together with epoxy and compressed to form a rigid, machinable material. Phenolic is an excellent electrical insulator and it has a reasonably small coefficient of thermal expansion. A machine drawing of the coil holder pieces is shown in Figure 2.18. All the coils are mounted onto a central phenolic form. We started with a solid block of phenolic and removed material in the shape of the coils until they fit snugly. The coils are held in compression against the central form by various phenolic clamp pieces. We use titanium screws to attach the clamps; titanium is used since it is non-magnetic. Any eddy currents generated in these screws should be small. The central phenolic form is supported from below by the attachment piece as shown in the figure. This piece is bolted to a solid aluminum structure which in turn is attached to the optical table. Figure 2.19 shows a machine drawing of the complete IP trap setup along with the aluminum structure. The IP trap coils and holder piece are carefully positioned near the science cell with a sliding dovetail mount. The overall clearance between the science cell and the IP trap setup is only about 2 mm. The dovetail structure assures that the trap slides into the correct position around the cell.

We tested the IP trap by directly measuring its magnetic fields, the results are shown in Figure 2.20. A FW Bell calibrated gaussmeter was used to measure the field. We recorded the field as a function of position along the axial and radial directions of the trap. We extracted from the data a radial magnetic-field gradient of 99.0(1) G/cm and an axial curvature of 34.0(5) G/cm^2; these measurements agree with our calculations to within 5% and 2% respectively. We measured the magnetic field at the center of the bias coils and found it to be 1.618 G/A, in excellent agreement with our calculations.

We measure the trapping frequencies of the IP trap by monitoring the motion of cold, trapped atoms. To measure the radial trap frequency, we transiently change the center position of the trap by lowering the bias coil current for about 5 ms. Then, as a function of time, we record the center-of-mass position of the gas. We extract the trap frequency with a fit to the oscillating position. In the axial direction of the trap we transiently change the position by applying a field from the E/W science cell shim coil.

We have also characterized the stability of the IP trap magnetic fields over the past several years. On a many-week timescale or shorter we have measured that the trap fields are stable to a little better than 10 mG. Over many months we sometimes observe drift in the field by about 50 mG. We have not characterized this drift very carefully, but it seems to be correlated to seasonal changes in the water temperature. The excellent long terms stability of the IP trap is due to the mechanical design of the setup as well as active stabilization of the coil currents. In order to realize these levels of stability, we put a great deal of effort into the electronics used to control the current in the IP trap coils. Section 3.3 is devoted to those details.

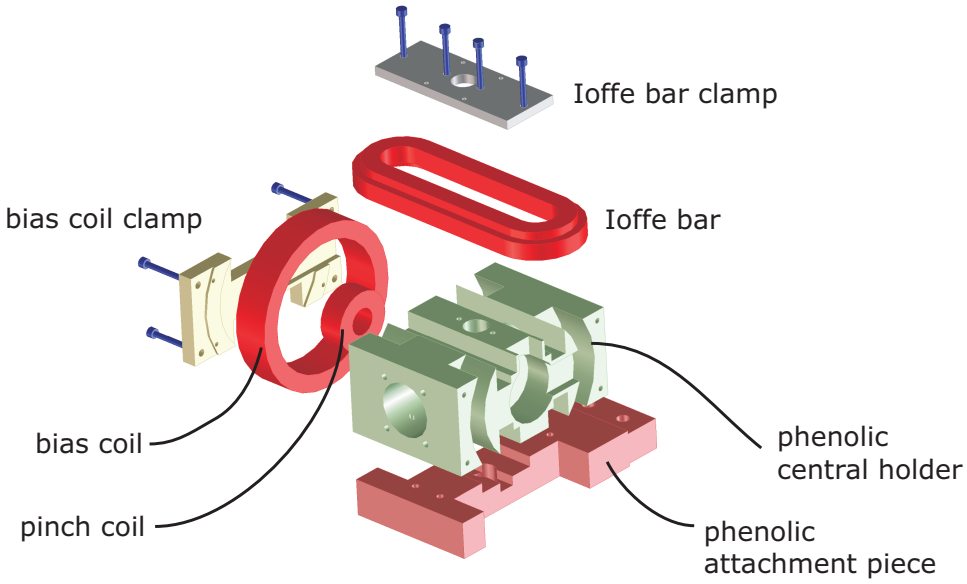

Figure 2.18: An exploded view of the IP trap coils and the phenolic holder pieces. The central phenolic holder was shaped so that all the coils fit snugly against it. The coils are held in compression against the central holder by the phenolic clamp pieces shown. The bottom attachment piece connects the central holder to the optical table mount.

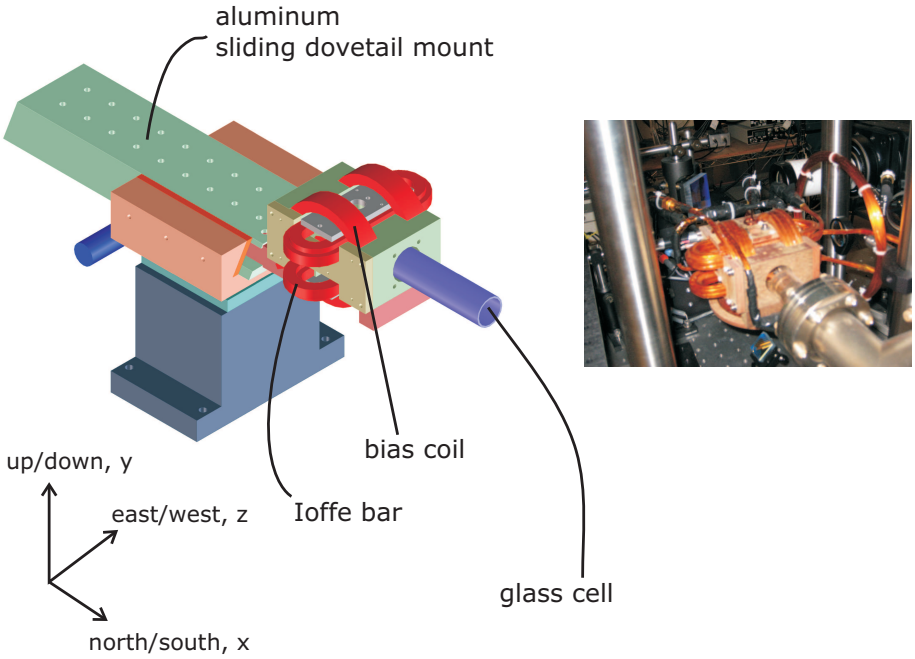

Figure 2.19: A machining drawing of the IP trap setup and a recent photograph of the IP trap. The six trap coils are rigidly attached to a main holder piece made of phenolic. The Ioffe bars and the bias coils are visible from the outside of the holder. The pinch coils are not visible. The IP trap is mounted on a sliding dovetail mount so that the trap can be easily positioned near the science cell. Below the dovetail is a large aluminum block that mounts the trap to the optics table.

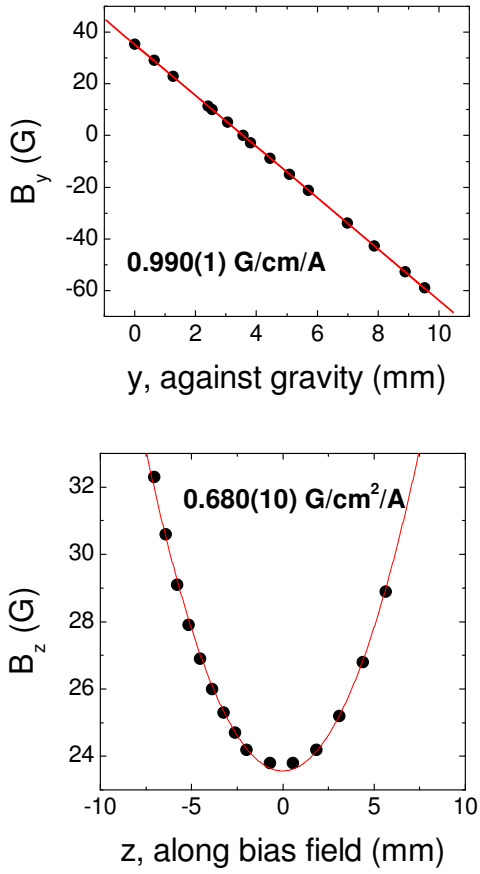

Figure 2.20: Magnetic fields of the IP trap as a function of position. The data was acquired with a calibrated gaussmeter. A stable current of 50 A was used to generate the fields. These measurements are in excellent agreement with the prediction of our model.

2.6.1 Driving radiofrequency transitions in the science cell

There are a few other small coils in the vicinity of the IP trap that have not been discussed yet. These coils are used to drive radiofrequency atomic transitions in the gases confined to both the magnetic trap and the optical trap. Driving rf transitions between internal Zeeman states of ^{85}Rb and ^{87}Rb is critical for both evaporative cooling (see Chapter 4) as well as precise calibrations of the magnetic-fields used in our experiments. This section describes how we deliver rf to the trapped atoms and our procedure for calibrating the magnetic-field. The key to delivering a large enough radiofrequency field to the trapped atoms is the impedance match between the broadcasting coil and the 50 Ω transmission line that connects the rf coil to a high power amplifier.

To calibrate the magnetic fields that are applied to the trapped atoms we excite Zeeman transitions. Here we only describe what was done in the optical trap since all the data presented in later chapters was obtained in an optical trap. Following evaporation to a temperature less than 1 μK, a short pulse (5 μs - 100 μs) of rf is applied to the initially spin-polarized gas in order to excite Zeeman transitions. We then release the atoms from the optical trap and let the gas expand. During the expansion we apply a magnetic-field gradient of approximately 30 G/cm with a coil mounted directly below the IP trap; the axis of the coil is oriented vertically. This field gradient spatially separates the expanding gas into clouds corresponding to the different Zeeman states. To calibrate the magnetic field, we measure the fraction of the gas that makes an rf transition as a function of the drive frequency. The frequency that excites the largest fraction of the gas corresponds to the magnetic field at the center of the trap.

We use rf (Agilent E4400B and E4420B) synthesizers to generate the signals that we need. The output of the synthesizers is amplified (ZHL-1-2 made by Mini-Circuits) with 5 W total output, gain of 40 dB, and a nominal 50 Ω impedance. Since we operate the magnetic-trap bias field in the range 1 G to 500 G, the frequencies that are needed range from 1 MHz to 350 MHz. The rf coil used in the experiment is two turns of 18 AWG magnetic wire with a diameter slightly larger than 1 inch. The coil is placed along the axis of the transfer tube which is perpendicular to the bias magnetic field and it sits within approximately 2 cm from the atoms. We optimized the impedance match between the rf coil and the 50 Ω output impedance of the amplifier over this frequency range. Coaxial cable is used to bring the rf close to the magnetic trap but for the last 4 inches the leads are untwisted magnet wire. Note that several standard rf cable types are magnetic (RG-174) and should not be placed close to the magnetic trap. In order to drive rf transitions between the magnetic sub-levels only the magnetic field of the radiated power is relevant, and so the axis of the rf coil is placed perpendicular to the magnetic-field direction of the trap.

The rf coil in our experiment is matched to the transmission line using a single 1/2 Watt 50 Ω resistor. This provides the most broadband impedance match possible and is only limited by the parasitic inductance of the resistor and the inductance of the coil. The amplitude of the rf signal that is delivered to the atoms is adequate for our requirements. For example, it takes approximately 5 μs to drive a "π-pulse", which transfers 100% of the atoms, in a magnetic field of 165 G.

Since the rf coil is just a loop of wire it basically looks like a short to the amplifier. The rf coil could also be matched to 50 Ω by using a lumped LC network. Following the useful analysis of Pozar [78] the rf matching network is easily designed. Construction of

the rf coil and the matching network is critical but straightforward. Stray capacitance and inductance is avoided by keeping lead lengths as short as possible. In the ideal case the rf from the amplifier is carried through coax right up to the rf coil. The matching network is soldered This impedance match is resonant at a frequency which is easily tuned *in-situ* with either a variable inductor or capacitor. A distinct feature of this technique is that the impedance match is performed with reactive components with little resistance; therefore the current flowing in the coil is large and a large oscillating magnetic field is produced.

We have also developed the ability to efficiently impedance match coils into the GHz frequency range. In this case we construct the coil directly on a small piece of high quality microwave circuit board (free samples are available from Rogers Corporation). The circuit board has spatially uniform dielectric constant that does not vary significantly with frequency. A track in the shape of a coil can be easily patterned onto the board either with a circuit board routing machine or the tracks can be cut by hand with a razor blade. The coil shaped track is matched to 50 Ω using a technique called stub tuning; see Ref. [78] for details. The JILA electronics shop can make and stub tune coils over a very wide range of microwave frequencies. In particular, coils have been made that are centered at 3 GHz and 7 GHz; these coils have a useable range of at least a few hundred MHz. Using a microwave amplifier with an output power of a few Watts, Rabi frequencies of $2\,\pi \times 50$ kHz have been attained.

2.7 Optical dipole trap

It is in the optical dipole trap that the final stages of the experiment occur. As discussed previously in this thesis, the main advantage of the optical trap for our experiments is its ability to hold the two species in the same spatial location independent of the spin states. Another important feature is that an arbitrary magnetic field can be applied; we use this feature to access various Feshbach resonances. Optical traps have become standard technology in BEC experiments so we will not describe the concept of an optical trap in detail. For a useful review article on the concept see the review in Ref. [79]. Three useful JILA theses by Kristen Corwin [80], Kurt Miller [81], and Cindy Regal [32] discuss optical traps in great detail.

The trap we use is a far red-detuned optical dipole trap formed at the focus of a single laser beam at 1030 nm. The trapping potential is related to the gaussian shape of the laser beam and is given by [79]

$$U_{dip}(r,z) = \frac{3\pi c^2}{2\,\omega_0^3}\frac{\Gamma_a}{\Delta} \times \frac{2P_L}{\pi w^2(z)} \exp(-\frac{2r^2}{w^2(z)}) \tag{2.12}$$

where ω_0 is the atomic transition frequency, Γ_a is the linewidth of the atomic transition, Δ is the detuning of the optical trap from the atomic resonance, and the waist $w(z)$ of the laser along the axis of the beam is given by

$$w(z) = w_0\sqrt{1+\left(\frac{z}{z_R}\right)^2} \tag{2.13}$$

with w_0 equal to the waist at the focus and z_R is the Rayleigh range. These formulae are relevant in the case that the optical trap laser detuning from the atomic resonance is

large compared to the fine structure splitting, the polarization of the trap laser is linear, and the rotating wave approximation ($|\Delta| \ll \omega_0$) can be made. In our experiments we use a waist w_0 of either 23 or 46 microns. This waist size is important to the evaporation process as discussed in Chapter 4, since a trap with larger waist will hold a gas at lower density. One must also consider the role of gravity; the main effect of gravity on an optical dipole trap potential is to lower the trap depth, but the radial trap frequency in the direction against gravity is also modified. These effects become important in the very weakest traps during the final stages of evaporative cooling.

For efficient evaporation in the optical trap, we require both a very low heating rate as well as a smooth potential that maintains the expected depth at the end of the evaporation. To maintain a low heating rate, both good intensity stability and good beam pointing stability must be achieved. For our optimized setup described below, we realize a heating rate of 1 nK/sec, which is even better than we achieve in our magnetic trap.

The optical trap laser is installed on a second optical table in a room next to the main experiment. It is nice to have the higher power laser away from the main apparatus for safety reasons, and since we do not have space on the main table. We typically run the optical trap laser with an output power of about 5 W. The light is sent through an AOM that is used for intensity stabilization and then the light is aligned into a polarization maintaining (PM) optical fiber. This fiber is made by Oz Optics, and it is the same as the other PM fibers in our laboratory except it has a stainless steel protective layer to prevent damage to the fiber and to contain the light if the fiber breaks. The fiber carries the light over to the main optical table where it is collimated and then focused into the science cell. The optimized optics to collimate and focus the light from the fiber are discussed below. After exiting the science cell, the light is collected and a small fraction is sent to a calibrated photodiode. The signal from this photodiode is used to feedback to the AOM to stabilize the intensity of the trap. The reference signal for the servo system comes from the computer, so that the intensity of the optical trap can easily be controlled.

Laser light for the optical trap is derived from a diode-pumped solid state Yb:YAG Versadisk laser sold by ELS. Currently this laser is adequate for our needs but it has a long and troubled history in our lab. As specified on paper the Versadisk system is an excellent laser, however in our experience few of the specifications are met in reality. We have measured that neither the output power stability or the frequency stability of the laser are as good as they should be. There appears to be significant frequency noise in the 10's of Hz range that gives the laser a linewidth of about 40 MHz. The source of this noise seems to be related to water cooling of the cavity and the gain medium. It may be possible to remove this noise by stabilization of the frequency to an external cavity. We should point out that on a millisecond timescale the linewidth of the laser is 100 kHz. The pointing stability of the Versadisk laser appears to be adequate since the coupling efficiency into our PM fiber remains high for many weeks at a time.

We have constructed a diffraction-limited optical system to take the optical trap light from the polarization maintaining fiber and focus it onto trapped atoms in the science cell. A schematic drawing of the optics used in our experiments to make a 46 micron waist is shown in Figure 2.21.[8] The first two optics collimate the light exiting

[8] The optics for our 23 micron waist optical trap include the following elements to collimate the

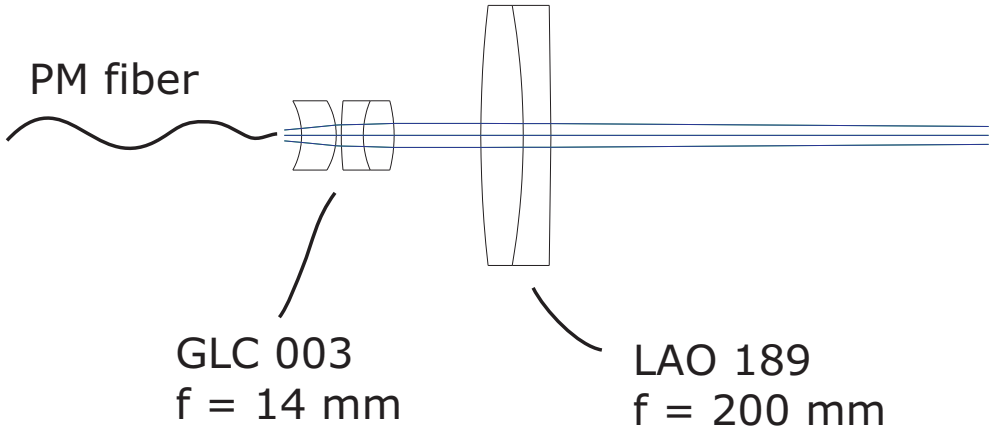

Figure 2.21: The optical setup used to create a 46 micron waist trap. Both lenses are made by Melles Griot and have good AR coatings near 1030 nm. Light for the trap comes over an optical fiber from the Versadisk laser that is mounted on a second optical table. To focus the trap light on the atoms we translate the position of the fiber output facet with respect to the first lens assembly. Not shown are the mirror for trap alignment and the dichroic beamsplitter.

the fiber, and the last lens focuses the light. Not shown in the figure are a mirror to steer the beam and a dichroic beamsplitter plate to combine the optical trap light with light at 780 nm. These optics are between the collimating lenses and the focusing lens. The fiber output is mounted on a translation stage to move the location of the focus. For beam-pointing stability, we specially machined the holders for all the optics and mounted the entire setup on a stable, raised platform. The Thorlabs cage assemblies are useful for mounting the optics; we machined custom lens holders from blank cage plates. We tested the optics using a beam profiling CCD camera to make sure the focus size is what we expect and to make sure that astigmatism is minimized.[9] Astigmatism is induced by off-center and tilted optics, so we built a special mounting jig so that lenses could be properly mounted in the Thorlabs cage assemblies.

The most important parameter of the optical trap is the focused waist size, which is given by $w_0 = \frac{\lambda f}{\pi w}$, where f is the focal length of the focusing lens and w is the size of the laser beam at the lens. We change the optical trap waist by using different collimation lens systems to give a different beam size entering the focusing lens. Melles Griot sells a variety of high quality, diffraction-limited lenses suitable for collimating the 1030 nm light that exits the PM fiber. The GLC series lenses are convenient since different focal lengths come in the same package size so that switching between different lenses, and different waists, is easy. Matched pairs of achromats and meniscus lenses like the one shown in Figure 2.21 are also available.

We align the optical trap onto the position of the Ioffe-Pritchard trap by translating the focus in three dimensions. To enhance the stability of the optical trap setup we have only one knob for each direction. It can be somewhat difficult to align the two traps from scratch, but once atoms can be held in the optical trap the three knobs are independently tuned to maximize the initial number in the trap.[10]

In the most recent experiments with ^{85}Rb condensates, the 46 micron waist optical trap is used. It is important to note that with such a large waist the confinement along the axial direction of the trap is very weak when the trap power is low. With the current apparatus, the axial confinement is enhanced by the curvature of the magnetic-field produced by the bias coils. The harmonic trapping frequencies of the magnetic-field potential and the optical trap add in quadrature so that the magnetic-field curvature is the dominant effect. Since the magnetic moments of ^{85}Rb and ^{87}Rb are different, the two species have slightly different axial trap frequencies. Near the ^{85}Rb Feshbach resonance at 155 G the axial frequency of ^{85}Rb was measured to be $2\,\pi \times 2.9$ Hz, which is in good agreement our expectations.

---

light from the optical fiber: a plate of BK7 glass with 12 mm thickness, a Melles Griot LAM-059/077 meniscus lens, and a Melles Griot LA0-059/077 achromat lens. Otherwise the 23 micron and 46 micron optical trapping setups are identical.

[9] The WinCamD CCD camera made by www.dataray.com was used for testing. It has small 4.7 micron pixels for excellent spatial resolution and good dynamic range. The software for the WinCamD is useful since it performs online gaussian fits to extract the beam waist.

[10] We have only had to align the optical trap from scratch once even though we have changed the optics multiple times. Before changing the optics, we image the trap laser beam after it exits the science cell onto the beam profiling CCD camera and mark the pixel coordinates. We then switch the optics and position the focus of the new trap onto the CCD camera pixel mark.

2.8 Absorption imaging

Nearly all of the data in this thesis comes from absorption images of gases expanded either from the magnetic trap or the optical trap. Absorption imaging is such a standard technique in the ultracold gas community that it will only be discussed briefly here. There is an excellent discussion of absorption imaging in Jake Robert's thesis [6] and in the review article by the Ketterle group [82]. For reference we present the formulae for the number and temperature of an expanded Maxwell-Boltzmann gas given by

$$N = \frac{2\,\pi}{\sigma_0}\, pkOD\, \sigma_x\, \sigma_y \left(1 + 4\,\frac{\Delta^2}{\Gamma^2}\right) \tag{2.14}$$

$$T = \frac{m}{k_b}\frac{(2\pi f_r)^2\,\sigma_r^2}{(1 + (2\pi f_r)^2\, t_{exp}^2)^2} \tag{2.15}$$

where $\sigma_0 = 3 \times 780nm/2\pi$, $pkOD$ is the optical depth at the center of the cloud, σ_i are the cloud widths, t_{exp} is the expansion time, Δ is the detuning from atomic resonance, and Γ is the linewidth of the atomic transition, and f_r is the radial trapping frequency. For a classical gas described by Maxwell-Boltzmann statistics, we fit the absorption image to a gaussian. We neglect any corrections to the atom number due to saturation of the probe transition, because we keep the intensity low.

Since we take up to several hundred absorption images per day we have developed automated image processing software. The software is written in Visual Basic 6 and communicates directly with the camera controller hardware. It automatically sets all the parameters of the camera and receives the raw data when an image is acquired. The data are automatically saved and organized. The absorption images can be fit via a reduced χ^2 algorithm to a variety of two-dimensional trial functions like a gaussian, double gaussian, or an inverted parabola. The software is also able to acquire images using the kinetics mode of operation of the camera.

We use a CCD camera from Roper Scientific (Model 1024B) with 1024×1024 square pixels each about 13 microns per side. The CCD is back-illuminated for the best quantum efficiency. This camera is completely adequate for our needs but two things might be improved. The CCD array suffers from a larger than normal amount of etaloning compared to other models. Etaloning comes from reflections between the front and back surfaces of the CCD array. The particular CCD model used in our camera has particularly severe etaloning in the near-IR. The etalon fringes that we observe are quite stable and therefore they are subtracted from the absorption images. Also, the charge shift rate from row-to-row could be faster so that images could be acquired more rapidly. The readout noise of the camera appears to meet the specification and is low enough to not degrade the signal-to-noise of our images.

We acquire absorption images along the north/south direction of the science cell with an optimized two lens imaging system. The first lens is an achromat (Melles Griot model LAI-009) optimized specifically for near-IR wavelengths. It has a focal length of 8 cm and is located about one focal length from the atoms. The second lens (LAI-015) is also optimized for the near-IR and has a focal length of 18 cm. This lens is placed about a focal length from the camera so that the magnification of the imaging system is about 2.25. In off-line tests we verified that the imaging system spatial resolution was diffraction limited by taking pictures of a calibrated test target. The size of a camera

pixel is approximately 5.8 microns and that is about the resolution limit of the first optic. It would be helpful for several of our experiments to increase the magnification so that the image is spread over a larger number of pixels, but we would likely have to also lower the resolution limit of the imaging system.[11] The imaging system is focused by translating the first lens and imaging a small sized gas. The magnification is calibrated by observing the acceleration of atoms released from either the magnetic trap or the optical trap.

We acquire an absorption image of the gas after releasing the atoms from either the magnetic trap or the optical trap. The gas is allowed to expand for at least a few ms, and typically 20 ms, to lower the optical depth and increase the size. Since both ^{85}Rb and ^{87}Rb are trapped in the lower hyperfine state, we apply a short and intense pulse of repump light just before the probe to pump the atoms into the upper state. The probe beam is circularly polarized to drive either σ^+ or σ^- transitions, so that the atoms are optically pumped into a stretched state. We apply a 2 G bias field with a coil placed along the imaging axis. This field is switched on immediately after the atoms are released from the trap. To obtain the best signal to noise in the absorption images we set the probe beam intensity to about 0.15 times the saturation intensity and the duration of the probe pulse is 50 μs.

Since a single measurement of a condensate with absorption imaging is destructive, experiments are performed with multiple runs of the apparatus. Ideally each identical run would yield the same number of atoms and temperature, but fluctuations in the apparatus cause noise. Even if we could produce exactly the same number of atoms at the end of each run, some noise is generated during absorption imaging. The biggest source of the number noise is laser frequency fluctuations. We spent a good deal of time optimizing our laser frequency stabilization electronics to lower number noise from the imaging. The shot-to-shot imaging noise is usually about 5% for ^{87}Rb and slightly higher for ^{85}Rb, see Chapter 3 for details on the laser system.

Our best diagnostic test on the accuracy of absorption imaging is a comparison of the calculated BEC transition temperature with experimental observations. In the absorption images it is straightforward to observe when the transition temperature is reached, a strong OD peak in the center of the cloud appears. We can observe a condensate fraction of only a few percent and extract the temperature of the gas precisely from the thermal component. Based on a knowledge of the trapping frequencies and the number of particles, we can calculate the transition temperature. To estimate the accuracy of the absorption images, we calculate the number of atoms, N_{calc}, based on the measured BEC transition temperature. We compare N_{calc} with the number of atoms, N_{abs} determined from the total absorption of the gas. When the imaging system is reasonably tweaked-up, the accuracy is better than 10%.

2.9 Chapter conclusion

This concludes the chapter on our apparatus. Throughout the remainder of the thesis we will refer back to this chapter concerning some of the experimental details of our measurements. In particular, this chapter is related to the work that is presented in

[11] It might be possible to improve the resolution of our imaging system without inducing aberrations, by using a meniscus lens to lower the f-number of the first lens.

the chapters that cover experimental components of the apparatus and the chapter that describes the evaporative cooling that is performed in the magnetic and optical traps.

Chapter 3

Components of the apparatus

Ultracold gas experiments do not require any state-of-the-art technology, but rather combine an impressive array of advanced techniques that must all work together seamlessly. In this chapter various components of the apparatus are described including the diode laser system, the computer control system, and the magnetic trap current stabilization electronics. The role of this chapter is to give a brief technical overview of these different systems since they are not documented elsewhere. The main focus here is on technology that we worked on which might be useful for the other quantum gas experiments at JILA. In particular, we will discuss a new external cavity diode laser design with low sensitivity to optical table vibrations, a simplified offset frequency stabilization setup, and our low-noise low-drift electronics for current stabilization.[1]

3.1 Diode laser system

Currently ten separate laser systems are required to operate the experiment. Nine of those are low power diode lasers; the tenth is a high power solid-state laser for optical trapping. The optical dipole trap laser has already been described in Section 2.7. We require a large number of diode lasers for laser trapping and cooling of both ^{85}Rb and ^{87}Rb, and to probe the quantum gases after evaporative cooling. Keeping all the lasers in the apparatus stabilized to the desired frequencies is challenging. A further complication is that the frequency of each laser must be tunable over a wide range. We use a frequency offset stabilization technique ("offset lock") to control the frequency of our lasers. The offset lock allows us to precisely tune the laser frequency over several hundred MHz and to stabilize the frequency to better than 1 MHz. We will also describe a mechanically stable diode laser setup that we developed. This "stable laser" system is significantly less sensitive than previous designs to mechanical vibrations present in our laboratory. The stable laser design is currently in use throughout the ultracold gas laboratories at JILA, with at least ten setups in use today.

3.1.1 Laser system

A diagram of the entire laser system is shown in Figure 3.1. There are five external cavity diode lasers (ECDLs), each laser is in the Littrow configuration. We refer to the lasers in our apparatus by their function; for example the ECDL that is closest to the

[1] Detailed mechanical diagrams and electrical circuit diagrams for much of the work described in this chapter are available from the JILA shops.

^{87}Rb $F = 2 \rightarrow F'$ transitions is called the ^{87}Rb trap laser. The fifth ECDL is called the ^{85}Rb master, and it is discussed below in more detail. The frequency of the ECDLs is tuned by changing the length of the cavity. The frequency is stabilized via feedback to a piezoelectric transducer (PZT) placed on the diffraction grating, and it is further stabilized by feedback to the diode laser current. The source of the stabilization signal either comes from saturated absorption (only for the ^{85}Rb master laser), or from our offset locking scheme that is described below. There are three injection locked diode lasers. The frequency of these lasers is stabilized with a low power seeding laser beam from one of the ECDLs. The arrows in the figure indicate the source of the stabilization signal for each laser.

The most important laser in our system is the ^{85}Rb master. It is the only laser stabilized directly to a Rb saturated absorption line.[2] All the other lasers in the system are stabilized with respect to the frequency of the ^{85}Rb master. Since the frequency stability of this laser is critical, its design is of the "stable laser" variety described in Section 3.1.3. The laser is locked to a derivative of the saturated absorption spectrum. To generate the derivative signal, we modulate the current of the master laser diode at 300 kHz, and we detect the modulation via a lock-in amplifier. The gain bandwidth of both the photodetector that acquires the modulation signal and the lock-in detector were carefully optimized to increase the size of the derivative signal. We estimate that the RMS frequency noise on the laser is approximately 0.3 MHz. The frequency noise is measured by monitoring fluctuations in the atomic absorption when the laser frequency is tuned onto the side of a saturated absorption line. The frequency noise is limited by the shot noise in the saturated absorption spectrometer photodiode.[3]

In our apparatus there is an ECDL for both the trapping and repump transitions for each species. These lasers give us flexibility in the frequencies of the trapping and repump light. The frequencies of these ECDLs are stabilized via an offset lock (see Section 3.1.2) with respect to the ^{85}Rb master laser. Typically we can tune the frequencies of these lasers over all the hyperfine lines in a particular saturated absorption manifold. The ECDLs do not provide enough laser power to collect a large number of atoms into the MOTs. To increase the available MOT laser power we use injection locked diode lasers. A small amount of light from the ^{87}Rb trap laser, the ^{85}Rb trap laser, and the ^{87}Rb repump laser is used to stabilize the associated injection locked lasers. The injection locking light for each ECDL is aligned into the laser to be locked with an optical isolator that has a "feedback" port. In the injection locked laser setups we use either a 120 mW Sharp laser diode or a 80 mW Sanyo diode. The performance of the Sharp diode is not as good as the Sanyo diode. Therefore the Sharp diode is only used in the case that the largest available optical power is required. We monitor the frequencies of the injection locked lasers using a confocal scanning Fabry-Perot (FP) interferometer. We have constructed a low-cost confocal FP cavity using a pair of curved mirrors and Thorlabs cage components. One of the mirrors is placed on a PZT to scan the length of the cavity over a free spectral range. The cost of this setup is significantly less than a commercial FP cavity and the performance is comparable.

Most of the light used for laser cooling and trapping in the MOTs is delivered

[2] The ^{85}Rb master is locked to the peak of the $F = 3 \rightarrow F = 2'/F = 4'$ crossover transition

[3] A significant improvement to the frequency stability of this laser would be attained if an electro-optic modulator were used to increase the amplitude of the frequency modulation sidebands in the locking setup.

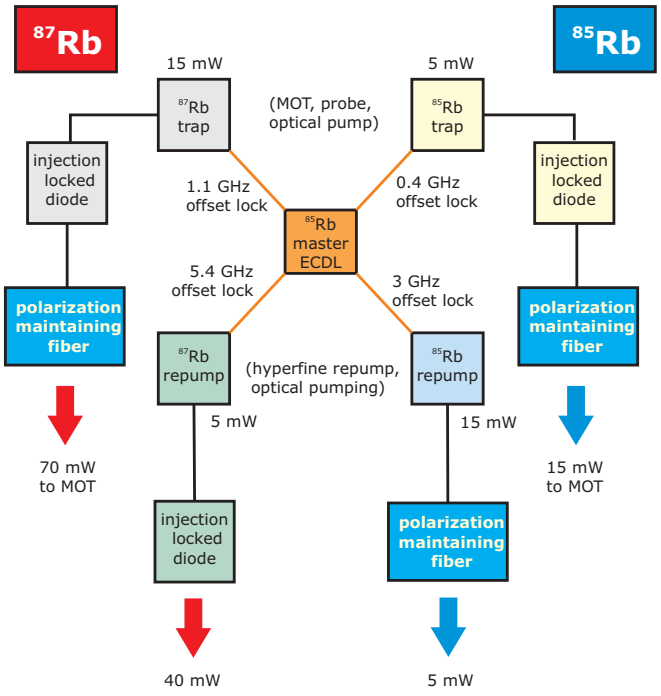

Figure 3.1: Schematic diagram of the laser system for both ^{85}Rb and ^{87}Rb. The lines indicate the source of the frequency stabilization signal for each laser. The ^{85}Rb master is locked via saturated absorption to a Rb line. The other laser frequencies are stabilized using the offset lock technique. There is an injection locked laser to amplify the power for the two MOTs. There is also an injection locked laser for the ^{87}Rb repump light in order to increase the available power.

with polarization maintaining optical fibers in order for the MOT beams to have good pointing stability. Only the ^{87}Rb repump light is not fiber coupled. We typically achieve 75% fiber coupling efficiency using optical fibers in which the distance from the fiber facet to the coupling lens can be optimized. We have up to 70 mW available for the ^{87}Rb MOT. This is plenty of laser power to collect more than 10^9 atoms.

As we described in Chapter 2, a number of different laser beams are required for absorption imaging and optical pumping in our experiments. We send a total of four beams into the north/south (N/S) axis of the collection MOT chamber, the four beams consist of repump and trap light for both species. We also send the same set of four laser beams into the east/west (E/W) port of the science cell. For absorption imaging we send trapping light for the two species along the transfer tube into the N/S direction of the science cell. Figure 3.2 shows the source of all these laser beams for imaging and optical pumping. In each case the light is passed through an 80 MHz AOM, the function of which is to generate short pulses and to control the optical power in the beams. The frequency of the laser beams for probing and optical pumping is set exclusively by the offset locking setups, we never tune the AOM drive frequency.

There is one more ECDL that has not yet been discussed. This laser is of the "stable" design variety and it is used for Bragg spectroscopy. The laser is locked to the peak of a saturated absorption feature in the ^{87}Rb trapping manifold. Therefore the laser is approximately 4.2 GHz detuned from the ^{85}Rb atomic resonance. This detuning is one of the parameters that determines the two-photon Rabi frequency for Bragg spectroscopy. Further details of this laser are given in the Bragg spectroscopy chapter.

3.1.2 Widely tunable laser frequency stabilization

Precise absolute frequency control of laser light is critical for many of the experiments described in this thesis. The natural linewidth of Rb is approximately 6 MHz. Therefore the laser frequency must be controlled to less than 1 MHz in a bandwidth of 100 kHz. The laser frequency must also be continuously tunable in order to reach the different atomic transitions in ^{85}Rb and ^{87}Rb, which are separated by a few hundred MHz. Therefore direct stabilization to a single atomic line is impractical. A large body of literature exists detailing numerous methods to stabilize and tune the frequency of a laser [83]. For an excellent review of different stabilization techniques see Ref. [84]. Several techniques exist which are low-cost and are simple to implement, see for example Refs. [85, 86]. Recent start-of-the-art results have been described in Refs. [87, 88, 89]. One technique used extensively at JILA is the DAVLL [90]. The DAVLL provides a wide tuning range since the signal is derived from the Doppler broadened absorption features of Rb. There are a few disadvantages to the DAVLL including a large temperature dependence of the locking signal and a lack of absolute frequency calibration. In this section we describe the offset locking scheme that we use to precisely stabilize and tune the frequency of our lasers. Our scheme has a frequency tuning range that is larger than that of the DAVLL, a negligible temperature dependence, and an absolute calibration of the laser frequency is readily available. Offset frequency stabilization of a slave laser with respect to a master laser is a well-known technique; see Ref. [83] and citations therein. The offset locking scheme described here uses cheap and easily accessible components and it provides all the flexibility and performance required for

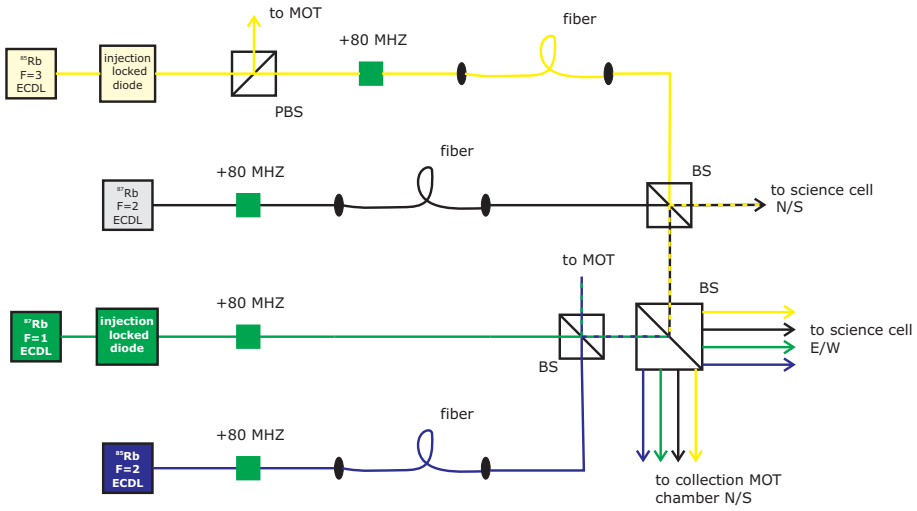

Figure 3.2: Schematic of laser system layout to generate the probing and optical pumping light for each species. AOMs (shown as green squares) are used in each beam path to generate short pulses and to control the intensity of the beams. There is also a mechanical shutter (not shown) in each beam path to block light that leaks through the AOMs. A large number of mirrors, which are not shown in the schematic, are required to get all the beam paths aligned. The long term stability of the setup is good since most of the light is fiber coupled. The beamsplitter cubes are labeled either BS for a non-polarizing model or PBS for a polarizing one.

our quantum gas experiments.

The scheme is based on determining the frequency of a slave laser by measuring the heterodyne beat between that laser and a calibrated master laser. The phase of the beatnote frequency is compared to a stable rf source by an electronic phase detector to produce an error signal. Using standard JILA electronics the error signal is filtered and amplified and then used as feedback for the slave laser.[4] In principle this system is capable of stabilizing the difference between the slave laser frequency and the master laser frequency to approximately the level of the rf source. The absolute frequency stability of the slave laser is then given by the stability of the master. To meet our requirements all that is needed is a cheap voltage controlled oscillator (VCO). Tuning of the unknown laser frequency is accomplished simply by changing the rf from the VCO.

A schematic diagram of our stabilization scheme is shown in Fig. 3.3. There are four separate realizations of this scheme with offset frequencies of approximately 400 MHz, 1.2 GHz, 3 GHz, and 5.4 GHz respectively. These provide the four different laser frequencies needed for our experiments. The heterodyne beatnote between the master and slave lasers is measured with a fast photodiode. We use a digital phase-frequency detector made by Analog Devices (AD9901).[5] This chip has two digital inputs into which a reference rf source and the rf beatnote are applied and two digital outputs that report the phase difference. There are two automatically selected modes of operation of the chip. When the two rf input signals are nearly in phase the output of the chip is a voltage which is linear in phase. When the two lasers are exactly in phase the output of the chip is zero. When the two rf inputs are far out of phase, therefore not at the same frequency, the output of the chip is a constant positive or negative output of approximately 1 V. The sign of the constant signal depends on the relative frequency difference of the two lasers. The AD9901 can only accept rf input frequencies of about 100 MHz. Therefore higher beatnote frequencies must be reduced. Up to a frequency of 3 GHz commercial VCOs are readily available (Mini-circuits) and are used with a double-balanced mixer to reduce the beatnote frequency into the proper range for the AD9901. VCOs above 3 GHz are more difficult to obtain (although they have recently become available from Hittite Microwave) so an ultrafast digital prescaler (Hittite Microwave) is used to downconvert the beatnote from 5.5 GHz to 690 MHz.[6] The signal from the phase detector is the error signal that the servo electronics uses to control the frequency of the ECDL.

A typical error signal produced by the AD9901 phase detector is shown in Fig. 3.4 (top) as a function of the beatnote frequency between the two lasers. For comparison the Doppler broadened absorbtion signal is also shown by the black line (bottom) in the figure. The slave laser is locked to one of the sharp transitions where the output signal crosses zero. The sharp transition occurs when the phase of the rf reference signal is the same as the beatnote phase after the down-conversion. The frequency of the slave laser is tuned by changing the down-conversion frequency. Effectively this changes the frequency at which the sharp transition occurs. The two sharp transitions each correspond to a different sign of the beatnote signal. The width of a sharp transition is

[4] Most of the components in our system are available from the JILA electronics shop.

[5] This phase detector chip is used in the JILA circuit WC061A2.

[6] A circuit board from the electronics shop exists for these Hittite prescaler chips. The board number is WC065B1.

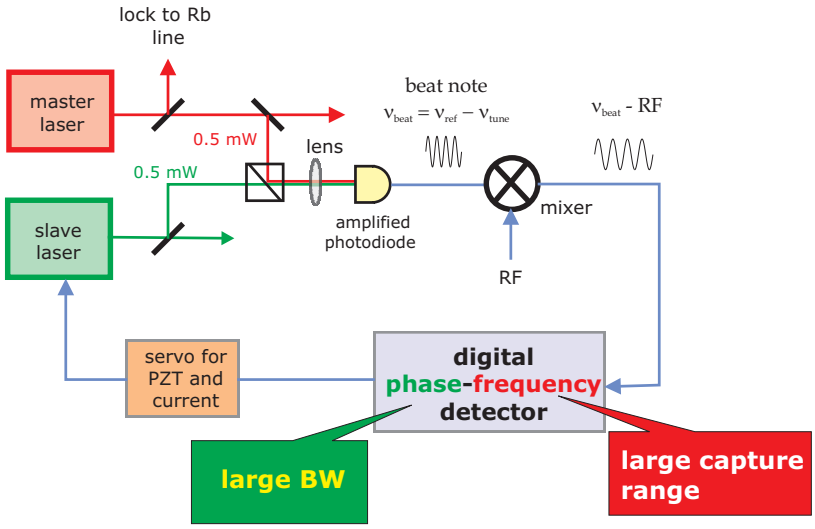

Figure 3.3: Schematic diagram of the offset locking system used in our experiments. Light from two separate lasers is superimposed onto a fast photodetector. The radiofrequency beatnote signal is amplified and then downconverted to approximately 50 MHz using a mixer. The phase of the downconverted signal is compared to a stable 50 MHz source by a digital phase-frequency detector (Analog Devices AD9901) from which an error signal is derived. A servo uses the error signal to stabilize the frequency of the slave laser by feeding back to the current and PZT of the slave laser.

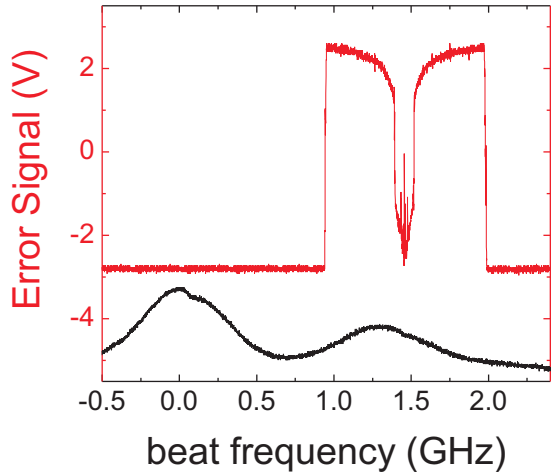

Figure 3.4: The red curve (top) is a typical output voltage signal from the digital phase-frequency detector as a function of beatnote frequency between the slave laser and master laser. The frequency of the reference laser was stabilized for this data and the frequency of the unknown was swept over a wide range. For comparison the black curve shows the Doppler broadened Rb signal that was simultaneously acquired. With respect to the lower trace, a larger absorption is up in this figure.

only about 1 MHz. This is significantly more narrow than any available Rb absorption line. The capture range of the offset lock is at least several hundred MHz. In order for the slave laser to lose lock, the frequency of the slave laser must deviate from the master laser by a significant amount comparable to the capture range of the system. A slave laser stabilized using our offset locking setup can routinely remain locked for an entire day. A typical level of vibration on the optical table, for example the movement of the motorized translation stage during transport from the vacuum system corner to the science cell, does not cause the laser to lose lock. The most common reason for a loss of lock is a diode laser mode-hop.

3.1.3 Stable external cavity diode laser design

We developed a new mechanical design for a stable external cavity diode laser (ECDL) using the Littrow configuration.[7] For an excellent review of diode lasers and applications to ultracold gas experiments see the review article in Ref. [84]. Like all lasers, an ECDL is extremely sensitive to mechanical vibrations of the cavity since the frequency is set by the length of the cavity. The goal of our "stable laser" design is to reduce the sensitivity of the laser frequency to the mechanical vibrations present in the laboratory. Figure 3.5 shows a photograph of the design with labels indicating some of the components. Our design builds on previous work at JILA by including a few new features. The most important feature is the monolithic design of the mechanical pieces that hold the laser diode and the diffraction grating. This reduces the effects of laboratory vibrations on the laser frequency. Other measures described below were taken to further reduce vibrations. Another feature of our design is that it can be rapidly duplicated by the JILA shop.

All the components of the laser are made from standard 6061 aluminum. The cavity is formed around a solid metal block (main cavity block) to which the diffraction grating and the laser diode holder are mounted. The grating sits on a mirror mount that is incorporated into the main cavity block for stability. Since the main cavity block is rigid, it is difficult for the cavity length to change quickly. Therefore, the main components of noise on the laser frequency are at low frequency where our servo is most effective. Below the cavity block is a large heat sink that also raises the block off the surface of the optical table. The cavity block is surrounded by a commercial Al box. A large fraction of the heat sink was hollowed out so that lead shot could be added to further reduce vibrations. The entire laser assembly is vibration isolated from the optical table with rubber o-rings.

A feature of the stable laser design is that all the pieces are machined on a CNC milling machine by the JILA shop. This helps to guarantee that each new system will have the same characteristics. This also allows several laser systems to be made all at the same time. It takes about two weeks of shop time to build and assemble ten entire laser systems. To date at least ten of these setups are in use at JILA.

We have tested the performance of the stable laser setup. We characterize the frequency noise of the laser by monitoring fluctuations of atomic absorption when the laser frequency is tuned near resonance. Figure 3.6 shows the measured spectrum of

[7] A second stable laser design currently exists that is much more compact. It is a little smaller than a New Focus Vortex laser head. Only two setups with this compact design have been tested, but the performance is similar to what is described here. See the JILA machine shop for more details.

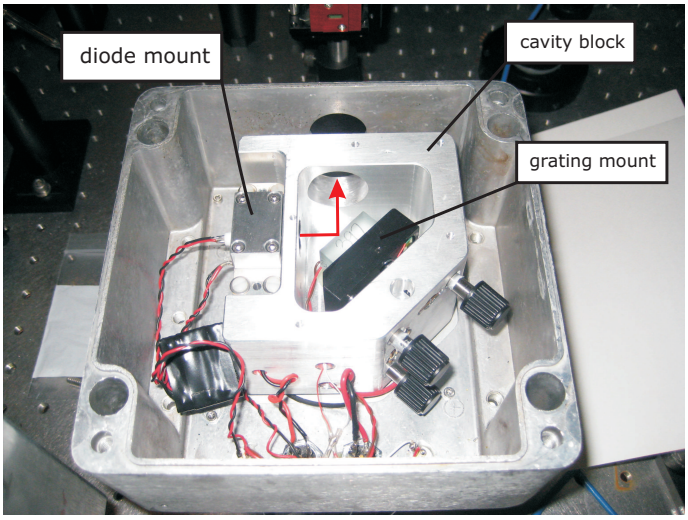

Figure 3.5: Photograph of the stable laser setup. The red arrow indicates the path of the laser light. The diode mount, the grating mirror mount, and the cavity block are indicated in the picture. The main cavity block is made from a solid piece of aluminum. In this design the cavity block is extremely thick to provide rigidity. The main cavity block sits within a hermetically sealed box to help keep water from condensing on the temperature controlled laser parts. The entire assembly rests on a hollowed out block of aluminum.

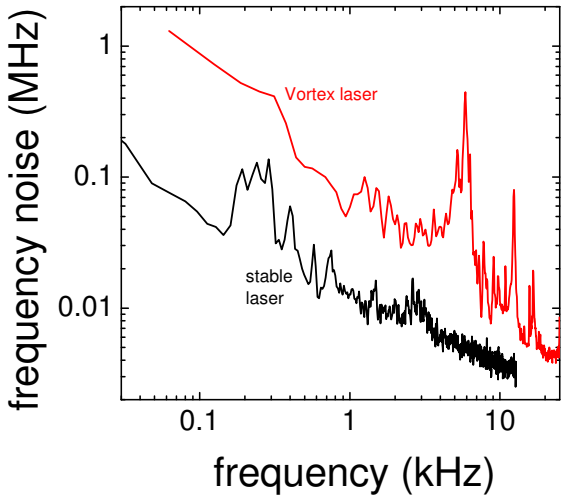

Figure 3.6: Measured laser frequency noise as a function of frequency. The frequency noise is determined by monitoring fluctuations in an atomic absorption signal. The red trace (top) shows the results for a New Focus Vortex laser and the black trace (bottom) is the results for the stable laser design. The stable laser has approximately ten times lower frequency noise and the noise occurs predominantly at low frequency where our servo is most effective. The large feature at 5 kHz in the red trace is a PZT resonance in the Vortex laser.

laser frequency noise for the stable laser design and for a New Focus Vortex laser. The frequency noise of the stable laser is significantly less than that of the Vortex, particularly at 1 kHz and above. The un-stabilized RMS noise of the stable design is 0.2 MHz measured in a bandwidth of 100 kHz. The un-stabilized RMS frequency noise of a Vortex laser is 1-2 MHz. Other homemade laser designs used in our lab typically have 1 MHz of frequency noise. The un-stabilized frequency noise of the other homemade lasers is dominated by mechanical vibrations. The fact that the frequency noise of the stable laser is a factor of five smaller is due to the more rigid design. To further characterize the frequency noise, two identical stable laser setups were constructed in the same laboratory by the Jin group. The outputs of the lasers were heterodyned together and a linewidth of less than 100 kHz was measured on a few ms timescale. We have also characterized the frequency drift of the stable laser design over several hours and found it to be approximately 50 MHz/hour. This level of drift is comparable to other homemade lasers in our apparatus.

3.2 Computerized control system

We built a computerized system to control the various pieces of equipment that make up the apparatus. The computer system is capable of controlling the apparatus with precise timing (at the few microsecond level) and high resolution (typically at the 1 part in 10,000 level or better). Our goal was to produce a computer code that is highly flexible and reliable. The ability to quickly change the parameters of an experiment or to switch to an entirely new set of timings is extremely important. The current computer control apparatus is based on a combination of commercial output boards and homemade electronics. All of the software to program these boards is written in the graphical language of LabView. A schematic of the computer control system is shown in Figure 3.7. In this section we briefly describe the various elements of the computer system.

The most important hardware board is the DIO-128 by Viewpoint Systems which provides 64 programmable digital output lines. The central feature of the DIO-128 is a digital signal processor which changes the output level of the digital lines only when required. Complex digital patterns can be generated with precise time resolution (1 μs) without the need to specify the output state of every digital line at every clock cycle. The DIO-128 has an onboard clock that seems to be stable at the few ppm level but operates at 1.000490 MHz. Since this offset from 1 MHz is well within the timing resolution of the board, it is corrected in software. Each output line from the DIO-128 is buffered and opto-coupled in an attempt to shield the experiment from electrical noise in the computer and to protect to DIO-128 from accidental short-circuits.

Seventeen digital lines from the DIO-128 are multiplexed to control a set of 16 independent digital-to-analog converter chips (AD767) with 12-bit resolution (5 mV resolution). Twelve of the sixteen lines provide data for the AD767 DAC chips. Another four digital lines are encoded with the address of a single DAC chip. Based on the address lines a signal from the seventeenth digital line is routed to update the DAC. Only three clock cycles are required to update any single DAC out of the sixteen; one cycle to load the data and address lines and two cycles to arm and trigger the chip. In practice 160 μs are required to change the analog output value of all the DACs. This homemade DAC system has proved to be very useful. Nearly all the laser frequencies

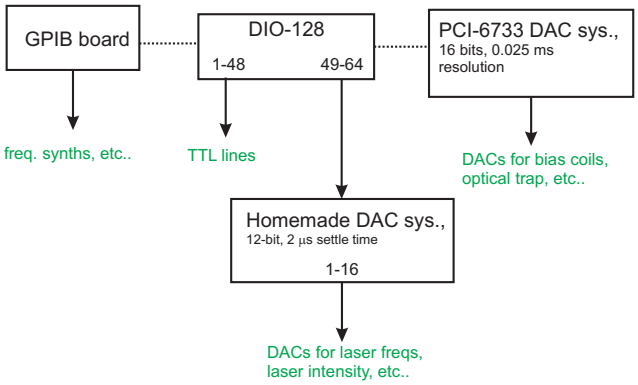

Figure 3.7: Schematic of the computerized control system of the experiment. The DIO-128 generates TTL signals on 64 different lines. Most of the lines go directly to equipment in the apparatus. The final 16 digital lines are used to create 16 analog voltage with our homemade DAC system. The DIO-128 also controls the timing of GPIB command execution and it triggers the PCI-6733 board.

and the laser powers as well as many of the magnetic coil currents are controlled with voltages from this system. The system is also quite flexible since the AD767 chips can be replaced with a different part number if better specifications or different features are required.

We also use a National Instruments PCI-6733 (16-bits, 0.3 mV resolution, 8 lines) analog output board when computer controlled voltage ramps of long duration or more precise resolution are required. For example the multi-coil transfer, optical-trap evaporation, and B-field ramps near the Feshbach resonance are controlled with this board. The 6733 board utilizes an on-board clock (40 kHz update rate) for precise timing and is always triggered to start from the DIO-128 so that the two boards remain synchronized at the 10^{-5} level. Output lines from the 6733 board are buffered by op-amps for protection against short circuit. A significant disadvantage of the 6733 board is that data is required to be output at each clock cycle.

Several instruments in the experiment are controlled via a GPIB board in the computer. These include rf synthesizers for the magnetic trap evaporation and Bragg spectroscopy and arbitrary waveform generators that produce rf sweeps. The timing of GPIB signals is synchronized to the DIO-128 clock with a few ten's of millisecond precision via software written in LabView. This level of time resolution is adequate since it can take several hundred milliseconds for the GPIB instruments to execute a command.

3.3 Magnetic-field coil current control electronics

Precise control of magnetic fields at the few milliGauss level is required for the experiments described in this thesis. For evaporative cooling in the Ioffe-Pritchard (IP) trap, the magnetic-field at the center of the trap must be constant throughout the cooling. Noise on the currents that produce the magnetic field leads to inefficient evaporation since the noise reduces the energy selectivity of the RF knife. In addition, for our Feshbach resonance experiments we need the ability to create complicated magnetic-field waveforms in which the field is rapidly changed. This section describes the electronic feedback system which satisfies both of these requirements, see Refs. [91, 6] for further information on magnet coil servos. The electronics are optimized to produce long-term stability as well as the ability to quickly change the magnetic fields. Here we describe the electronics for only the IP trap bias coils; this particular system is representative of the techniques used to control other magnetic-field coils used in the apparatus. A large current is passed through the bias coils to create up to 700 G and the amount of current can be controlled with a field-effect transistor (FET). The servo electronics feedback to the FET based on a real-time measurement of the current.

Figure 3.8 shows a schematic drawing of the bias-coil high-current circuit. Current flows from the Agilent power supply, through the bias coils, into a set of four field-effect transistors (FETs) connected in parallel, through a precision current probe, and then the current is returned to the power supply. The current probe generates a voltage signal which is proportional to the current flowing in the bias coils.[8] The 20 Ω resistor

[8] We initially used a Hall effect current probe from FW Bell. Unfortunately the response of this type of probe depends on temperature at the 0.01% level, in our system this large temperature coefficient is unworkable. We switched to current probe made by Danfysik with a temperature coefficient that is 1000 times smaller. The temperature response of the Danfysik probes is so much lower since they are

for the currents probe has a very low temperature coefficient of resistance of 2 ppm/° C. Any drift in the value of this resistor would cause a drift in the coil current. We use high power FETs from Advanced Power Technology. The FETs have a capacitance of about 10 nF between the gate and the source and between the drain and the source.[9] It is important to have a small FET capacitance since this capacitance in series with the trap coils' inductance forms a resonant circuit. The presence of this resonance limits the useful bandwidth of our servo system. The voltage signal at the FET gate connection comes from the servo electronics, which are described below. The return of the Agilent power supply is grounded to a connection from the regular room AC ground in only a single location. It is critical that ground be attached only once for the entire system to avoid ground loops.

To stabilize the current flowing through the bias coils, an electronic servo monitors the difference between current probe signal and a reference signal. Based on the difference of these signals, the servo regulates the current flowing through the bias coils with feedback to the FET gate. The goal of the servo is to make the difference between the reference signal and the current probe signal zero. A simple schematic of our servo electronics is shown in Figure 3.9. The servo electronics reside in a grounded box that has many inputs and outputs. All signals that enter the servo box are buffered by an instrumentation amplifier to avoid ground loops.[10] For simplicity we will assume that the servo has two inputs and a single output that is connected to the FET gates. The input signals come from the current probe and from the computer control so that the reference voltage can be adjusted. For maximum flexibility, the total reference voltage is the sum of a stable DAC signal which is generated inside the servo box and several signals from the control computer. All these signals are combined with a single summing amplifier.[11] The servo works by comparing the current probe voltage to the total reference voltage. The difference of these two signals is amplified and used as feedback at the FET gate to control the amount of current flowing through the bias coils. During normal operation of the servo the sum of the current probe voltage and the total reference voltage is zero.

The highest current stability is attained when the gain of the servo is as large as possible. A large gain allows the observation of a small voltage difference between the reference signal and the current probe signal. Of course the servo gain is limited by the delay in the response of the current to a change in the servo output. If the delay time is too long the servo will provide positive feedback instead of negative feedback at

based on a fluxgate whereas the FW Bell probes are based upon a Hall effect sensor.

[9] Note that the actual FET arrangement in our system is different. An H-bridge configuration is used so that the current in the bias coils can be reversed via a digital signal from the computer. It is important to be able to reverse the current of the bias coils so that a wide range of magnetic fields can be achieved in the IP trap. A simple digital switching circuit routes signals from the servo electronics to the FET gates based on the desired direction of current flow.

[10] Commercial instrumentation amplifiers (IAs) have several nice features including a high input impedance, low temperature drift, and excellent common-mode rejection. In our experiments we have found it necessary to improve the IA common-mode rejection for MHz frequencies, see the Analog Devices Application Note AN-671 for details. Commercial IAs do have a downside which is large noise for a gain of only one.

[11] For the best long-term stability and low noise, a large fraction of the reference voltage comes from the stable DAC. The computer signals are much smaller and therefore do not need to be as stable. For the best immunity to rf signals in the lab we found it necessary to low-pass filter all the op-amps in the servo at about 100 kHz.

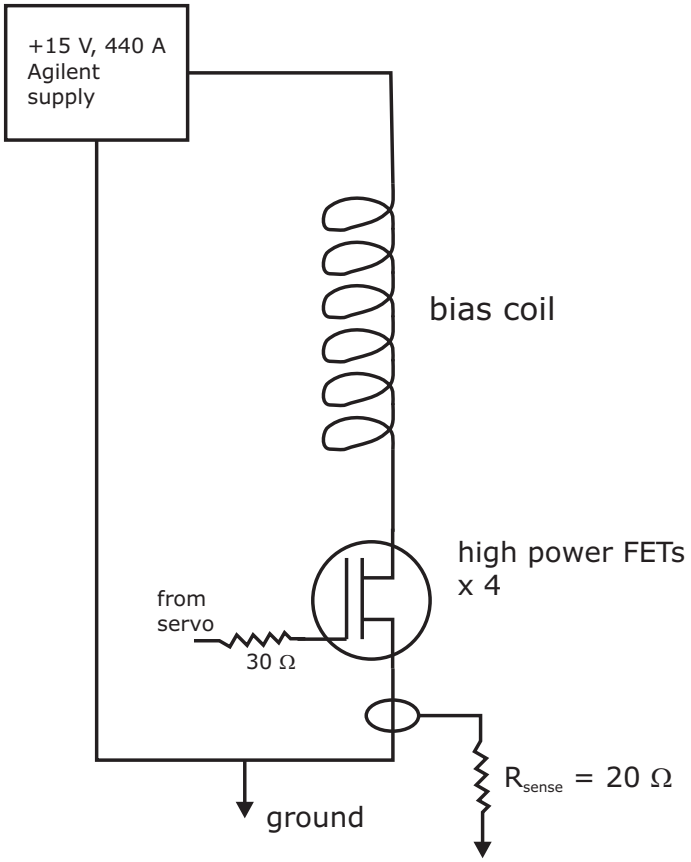

Figure 3.8: A schematic of the high current circuit for the bias coils. Current flows from a 15 V, 440 A power supply through the coils, a set of four parallel FETs, and a current probe. The return of the power supply is grounded to the AC wall ground. Note that the actual FET arrangement in our system is different. An H-bridge configuration is used so that the current in the bias coils can be reversed via a digital signal from the computer. It is important to be able to reverse the current of the bias coils so that a wide range of magnetic fields can be achieved in the IP trap. A simple digital switching circuit routes signals from the servo electronics to the FET gates based on the desired direction of current flow.

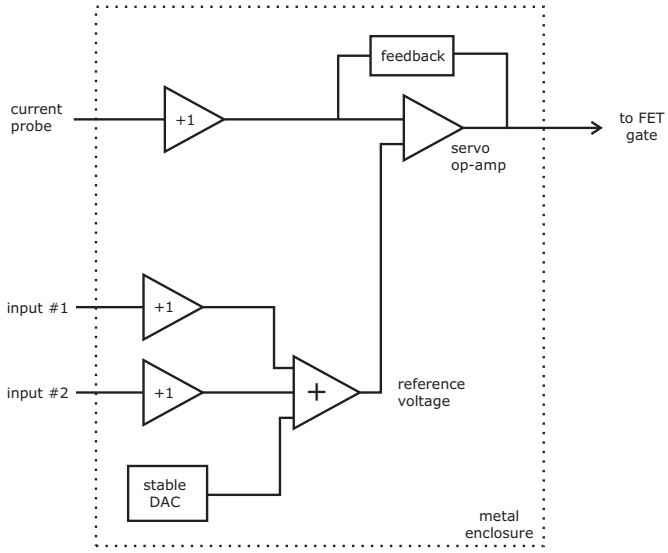

Figure 3.9: Simple schematic of the bias coil servo. The complete set of diagrams is available from the JILA electronics shop under file WC063A1. The dashed box indicates the grounded box; all external inputs entering the grounded box are buffered to avoid ground loops. In this simple schematic only the current probe signal and the reference voltage signals are shown. The servo works by comparing the current probe voltage to the total reference voltage. The output of the servo is sent to the FET gates.

some frequency, and the bias coil current will oscillate. Therefore we reduce the gain of the servo to prevent positive feedback. Figure 3.10 shows a plot of the servo loop filter response as a function of frequency. In order to realize the best DC stability of the current we use an integrator. Since the response of the coil and FET system is not perfect at every frequency (see below for details) we must switch to proportional gain at a frequency of about 0.25 kHz. At even larger frequencies we use a differentiator to extend the useable frequency range of the servo. The differentiator turns on at about 11 kHz. At frequencies beyond about 90 kHz our servo cannot possibly control the current effectively because of the delay between a change in the servo output and the corresponding change in current. Therefore we low-pass filter the loop filter response at 90 kHz. This complicated loop filter arrangement is not necessary for good DC current stability. For good stability only the integrator and first proportional section are needed. The differentiator and second proportional sections of the loop filter are necessary to provide good dynamic current stability. For example, the coil current should accurately follow a rapid change in the reference voltage signal without any overshoot or oscillation. The high frequency sections of the loop filter response are critical in eliminating unwanted overshoots and oscillations after a rapid change in the reference voltage.

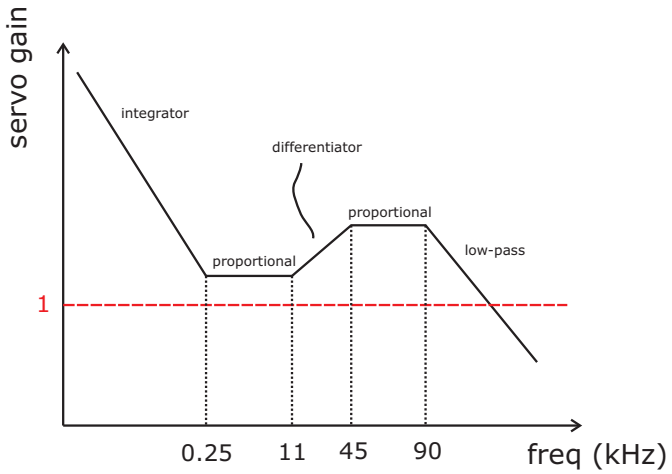

Figure 3.10: A schematic of the feedback network (loop filter) response of the servo as a function of frequency. The calculated corner frequencies of the bias coil servo are shown for reference. This loop filter provides excellent long-term stability of the current and it guarantees the currents accurately tracks rapid changes in the reference signal without overshoots.

The bias coil loop filter parameters (*i.e.* the frequency at which we switch from an integrator to proportional, etc.) were primarily determined based on measurements of the response of coil and FET system.[12] The parameters of the servo are shown in Figure 3.10. We directly measured the transfer function of the bias coils and FET

[12] A small amount of trial and error was used to set the highest frequency parameters in the loop filter since accurate measurements of the bias coil and FET system response are difficult at high frequency.

circuit using a network analyzer. The measured response and phase shift of the circuit is shown in Figure 3.11 as a function of frequency. The network analyzer output signal was directly attached to the FET gate and the current probe signal was fed into the input of the network analyzer. To obtain this data we use a servo to control the DC current flowing in the circuit. The servo gain bandwidth was limited to approximately 200 Hz. We choose 200 Hz since it is much lower than the expected bandwidth of the coils and FET system. Based on our measurements we can accurately predict the optimum parameters of the servo loop filter. For example the phase shift of the coils and FET system is around 90 degrees at 1 kHz, this means that with an integrator the current will oscillate at 1 kHz. Therefore the gain of the servo would have to be sufficiently low (*i.e* a closed loop gain of less than one is required) at 1 kHz to eliminate the oscillation.

We characterize the success of the servo electronics by both the short-term (a timescale of milliseconds) and long-term (a timescale of seconds or more) DC stability attained and the rate at which we can change the coil currents and thus the magnetic field. Based on measurements of the field using rf transitions between Zeeman levels we have determined that the short-term (100 μs) magnetic-field noise is only a few mG. Over a timescale of weeks the magnetic field appears to be stable to better than 10 mG. For longer times it appears that seasonal variations do effect the magnetic field at the 50 mG level. However the source of this drift has not been carefully analyzed. Finally, with our servo system we are able to change the magnetic-field at a maximum rate of 6 μs/G without any overshoot or any substantial field oscillations following the change.

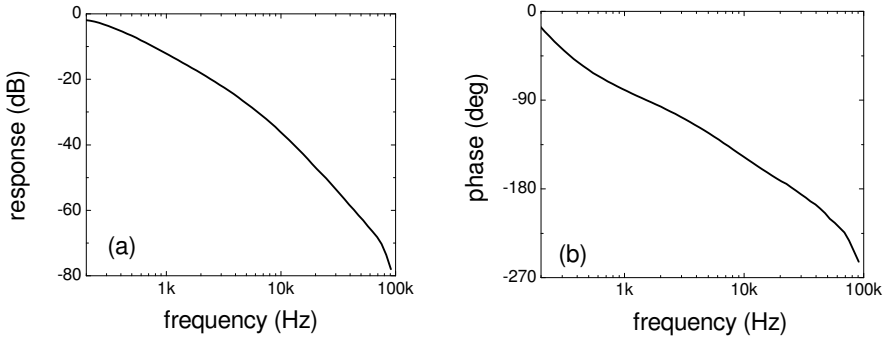

Figure 3.11: Measured open loop response (a) and phase shift (b) of the bias coil and FET system obtained with a network analyzer. The network analyzer driving signal was attached directly to the FET gate and the response was determined from the current probe signal. A slow integrator was used to keep a stable current running through the system. Beyond 200 Hz the data displays the response of the coil and FET system. Since an integrator requires a phase shift of less than 90°, our measure response indicates that the servo loop filter must be switched to proportional gain at a frequency of 1 kHz or less. Based on the measured phase shift we can accurately predict the required servo electronics parameters.

Chapter 4

Evaporative cooling of ^{85}Rb to BEC

4.1 Introduction

The main goal of our apparatus is to create a ^{85}Rb BEC near the Feshbach resonance at 155 G. Using a Feshbach resonance the two-body scattering length may be tuned to access new physical regimes in a quantum degenerate gas. In particular we would like to study the properties of a condensate in the strongly interacting regime where beyond mean-field effects are expected to be important. In the previous two chapters we described the process of collecting atoms into a MOT, transferring the atoms to the science cell, and loading the atoms into the IP trap. This chapter describes our new approach to evaporative cooling of ^{85}Rb, in which the ^{85}Rb gas is sympathetically cooled via thermal contact with a ^{87}Rb gas in both a magnetic trap and an optical dipole trap. The results presented here are different from previous work in which a ^{85}Rb gas was cooled to BEC using direct evaporation [7, 6] and ^{85}Rb was sympathetically cooled to 1 μK via collisions with ^{87}Rb [11]. Our evaporative cooling approach represents a significant improvement over this previous work since we can produce larger number ^{85}Rb condensates than ever before, and since production of ^{85}Rb condensates is robust in the sense that condensates can be produced even if the apparatus is not perfectly optimized.

The intent of evaporative cooling is to lower the temperature of a trapped gas while simultaneously increasing the phase-space density of the gas. The requirements for the formation of a condensate were discussed in Chapter 1. The efficiency of evaporative cooling is determined by the ratio of the elastic collision rate to the rate of inelastic collisions that cause number loss and heating. Both the elastic and inelastic collision rates for ^{85}Rb have been carefully studied and are documented in Refs. [8, 92, 12]. Since the collision properties of ^{85}Rb are quite poor, efficient evaporation is extremely difficult to implement. In comparison, ^{87}Rb suffers little loss or heating due to inelastic collisions and this represents a key feature of our system. We verified the ability of our apparatus to perform evaporative cooling (*i.e.*, stability of the trapping potential, background gas in the science cell, etc.) with ^{87}Rb since its collision properties are nearly ideal. The performance with regard to ^{87}Rb is excellent and condensates with a few million atoms can be produced. Of course our goal is to make ^{85}Rb condensates and the achievement of that goal is the main focus here.

There are two central roadblocks to efficient evaporative cooling of a ^{85}Rb gas: a zero in the s-wave elastic collision cross section near 0.4 mK and large two- and three-body inelastic collisions that lead to atom loss and heating. At high temperature the elastic collision cross section of ^{85}Rb is suppressed causing evaporation to be inefficient

(see Section 4.2.3 for more information). As the temperature is lowered the elastic cross section sharply increases and evaporation can proceed more rapidly. However in efficient evaporation lowering the temperature of the gas will also increase the density. Since the rate constants of density-dependent inelastic collisions in ^{85}Rb are large, an increased density leads to more rapid number loss from the gas, which causes evaporation to be inefficient. These two sources of inefficiency in the cooling process are the roadblocks that must be avoided. At the beginning of evaporation we use sympathetic cooling with ^{87}Rb which circumvents the first roadblock (small collision cross section). Once inelastic number loss becomes significant during the cooling, we load the atoms (^{85}Rb and ^{87}Rb) into an optical trap in which we are able to apply a magnetic field to reach the ^{85}Rb Feshbach resonance. Using the Feshbach resonance elastic and inelastic collision rates in the ^{85}Rb gas can be controlled; in particular we tune the magnetic field to minimize inelastic collisions and this capability allows us to circumvent the second roadblock. In the optical trap we simultaneously evaporate the two gases; the ^{85}Rb gas rethermalizes primarily through collisions with the ^{87}Rb gas. The combination of the control afforded by the Feshbach resonance and the presence of ^{87}Rb for sympathetic cooling represents a significant advantage for cooling ^{85}Rb in our system.

The optimized evaporation procedure we currently utilize to cool a gas of ^{85}Rb to ultralow temperature can be summarized by the following steps. The evaporative cooling process begins with sympathetic cooling in a magnetic trap. We load approximately 5×10^8 ^{87}Rb atoms and 4×10^6 ^{85}Rb atoms into the IP trap. We directly evaporate the ^{87}Rb gas to a temperature of 8 μK; the ^{85}Rb gas is cooled due to thermal contact. This evaporation in the IP trap takes 44 seconds and approximately 3×10^6 atoms of each species remain in the IP trap. To further cool the mixed species gas we load into an optical trap. Both species are simultaneously cooled by lowering the depth of the optical trapping potential. The duration of the optical trap evaporation is 11.5 seconds. During the first few seconds of the optical trap evaporation the magnetic field at the center of the trap is tuned to 168.8 G. At this field ^{85}Rb inelastic collisions are minimized. In order to create a BEC of only ^{85}Rb, prior to the last two seconds of the cooling, we ramp the magnetic field to 163 G and increase the speed of evaporation. With these settings ^{87}Rb the efficiency of ^{87}Rb cooling is low and a significant fraction of the gas is lost from the trap. At the end of evaporation we can produce ^{85}Rb condensate with up to 80,000 atoms and a condensate fraction of greater than 80%. A residual non-condensed gas of ^{87}Rb with approximately 10,000 atoms remains in the trap.

While our cooling procedure currently works well and can be summarized in the short paragraph above, arriving at this final, complex procedure required a long series of experiments and studies. In our first work towards cooling ^{85}Rb we worked to optimize sympathetic cooling in our IP magnetic trap. In this trap we carried out many experiments that, while they never allowed us to fully reach ^{85}Rb BEC, were essential to identifying the techniques we use to circumvent the roadblocks to cooling ^{85}Rb. In the end these careful studies led us toward our current use of an optical trap for the final cooling. Readers interested in an understanding of the intricacies of ^{85}Rb cooling via ^{87}Rb should follow our historical discussion of our cooling work presented in the entire chapter, while readers mostly interested in our current experimental procedure should skip towards the end of the chapter where the optical trap cooling is described.

This chapter is organized into several sections. We begin with a discussion of a model for the evaporation process that we use to understand our cooling results. The

results of the simulations motivate our route to ^{85}Rb BEC using sympathetic cooling. Next evaporation of ^{87}Rb to BEC in both the magnetic and optical traps is discussed. This information provides a baseline for the best performance we could hope to observe in ^{85}Rb. Unfortunately this just sets our hopes far too high. Then the results and limitations of sympathetic cooling of ^{85}Rb with ^{87}Rb in the magnetic trap are discussed. Finally evaporative cooling of both ^{85}Rb and ^{87}Rb in the optical trap is discussed including cooling into the quantum-degenerate regime. Efficiently producing a ^{85}Rb BEC in the optical trap required a very weakly confining potential to maintain low density as well as detailed control of the ^{85}Rb collision rates during the evaporation.

4.2 Simulations of ^{85}Rb evaporative cooling

The concept of evaporative cooling in a trapped gas is straightforward but very powerful [93, 94, 95, 96, 97, 98, 99]. To lower the temperature of an equilibrium atomic gas, a small fraction of the most energetic atoms are selectively removed. The remaining non-equilibrium gas has a smaller total energy and elastic collisions tend to rethermalize the gas to a lower temperature. By repeating the process many times the temperature can be lowered by many orders of magnitude. Evaporative cooling can be a very efficient process. In an extreme case a large fraction of the energy in a gas can be contained in a small fraction of the atoms. By removing just those energetic atoms, the total energy in the gas drops significantly but the total particle number is nearly unchanged. This extreme situation can only occur, however, if very low loss and heating of the gas are maintained.

We have performed a simulation of the evaporation process based upon a simple model. These simulations serve as a guide in understanding the most efficient route to BEC with ^{85}Rb. The model includes the removal of energetic atoms from trap and the rethermalization of the gas to lower temperature. It is critical to include sources of atom loss and heating in the model. During the rethermalization process atom loss and heating can occur due to inelastic density-dependent collisions as well as collisions with the background vapor in the science cell. The best route to BEC must balance the atom loss due to inelastic collisions against a more efficient slow evaporation. Unfortunately our initial attempts at cooling ^{85}Rb were an abject failure for a variety of reasons. Comparison of the experimental data to our simulations allowed us to pinpoint the failure and devise an improved strategy. In this section our simple model is developed based on calculations of the collision rate in the gas including the energy dependence of the elastic cross section. Truncated distributions of the energy in a gas are used to model energy removal. Based on this information we lay out our strategy for evaporative cooling.

4.2.1 Simple model of evaporative cooling

There is a significant body of theoretical work on evaporative cooling (for example see [96]) including non-trivial effects due to the quantum statistics of the particles [100]. This is particularly evident in evaporation of a Fermi gas into the quantum-degenerate regime, where suppression of collisions due to the quantum statistics of the particles changes the efficiency of evaporative cooling [101]. Our simulations draw from Refs. [96, 6, 102] and always assume that the gas behaves classically since for our Bose gas

changes to thermodynamic quantities like heat capacity due to quantum statistics should be small compared to the effects of inelastic losses. The elastic collision rate per atom in the gas sets the timescale for rethermalization and it is given by the following expression

$$\Gamma = 2\langle n\rangle \, \sigma \, \langle v_{rel}\rangle \tag{4.1}$$

where $\langle n\rangle$ is the average density, $\langle v_{rel}\rangle$ is the mean relative speed, and σ is the elastic cross section (see Section 4.2.3). The factor of 2 represents an increase in the collision rate of identical non-condensed bosons due to atom-atom correlations. We will calculate the average density and mean relative speed from the gas density distribution. We will consider the elastic cross section later in this chapter (see Section 4.2.3). For a cylindrically symmetric harmonic trap with radial (axial) frequency ω_ρ (ω_z) the potential is

$$U = \frac{1}{2} m(\omega_\rho^2 \rho^2 + \omega_z^2 z^2) \tag{4.2}$$

and the distribution function is given by

$$n(\vec{r},\vec{p}) = n_{pk} e^{-\frac{1}{k_b T} H(\vec{r},\vec{p})} = n_{pk} e^{-\frac{1}{k_b T}(\frac{p^2}{2\,m} + U(\vec{r}))} \tag{4.3}$$

where n_{pk} is the density at the center of the trap and the normalization is given by $N = \int n(\vec{r},\vec{p})\, d^3\vec{r}\, d^3\vec{p}$. It is useful to re-scale the coordinate system with $Z = \lambda\, z$ where $\lambda = \omega_z/\omega_\rho$ to obtain a spherically symmetric potential $U = \frac{1}{2} m\omega_\rho^2(\rho^2 + Z^2) = \frac{1}{2}\, m\, \omega_\rho^2\, r'^2$ with $r'^2 = \rho^2 + Z^2$. For a Bose gas with temperature above the transition point, the momentum integral is easily calculated to obtain the spatial density distribution of the gas

$$n(\vec{r}) = n_{pk} e^{\frac{-m\,\omega_\rho^2\, r'^2}{2\, k_b\, T}} \tag{4.4}$$

where $n_{pk} = N\omega_\rho^2\, \omega_z \left(\frac{m}{2\pi k_b T}\right)^{3/2}$ is the density at the center of the trap. The average density is

$$\langle n\rangle = \frac{1}{N}\int n(\vec{r}) d^3\vec{r} = \frac{N}{8}\omega_\rho^2\omega_z \left(\frac{m}{\pi k_b T}\right)^{3/2} = n_{pk}/\sqrt{8} \tag{4.5}$$

and the mean relative speed is [6]

$$\langle v_{rel}\rangle = \sqrt{\frac{16\, k_b\, T}{\pi\, m}}. \tag{4.6}$$

For our simulations of evaporative cooling it is useful to determine the occupancy of a particular quantum state of the system with energy ϵ_n. Each quantum state is labeled by the quantum number n, and the occupancy is

$$f(\epsilon_n) = e^{\frac{-1}{k_b T}(\epsilon_n - \mu)} \tag{4.7}$$

where we have assumed a Maxwell-Boltzmann (MB) gas with a chemical potential μ. For the remainder of this discussion we will assume the energy takes on a continuous range of values.[1] The density of quantum states in the three-dimensional harmonic potential is

$$\rho(\epsilon) = \frac{\epsilon^2}{2\lambda(\hbar\omega_\rho)^3}. \tag{4.8}$$

[1] For a MB gas this is a reasonable assumption since the temperature of the gas is larger than the spacing of a quantum states with $k_B\, T \gg \hbar\, \omega_\rho$.

For a classical (MB) gas the chemical potential is easily determined by normalizing the energy distribution to the number of total number of trapped particles

$$N = \int \rho(\epsilon) f(\epsilon) d\epsilon \rightarrow e^{\mu/k_b T} = \lambda N \left(\frac{\hbar\,\omega_\rho}{k_b\,T}\right)^3. \tag{4.9}$$

In our simulations we assume that the evaporation process truncates the distribution of energies in the gas at some maximal value η. It is convenient to scale the truncation energy to the temperature of the gas as $\eta = \frac{\epsilon_{cut}}{k_b T}$. We can find the number of particles lost and the total energy lost in the gas by truncating the distribution at η by performing the following integrals

$$N_{lost} = \int_\eta^\infty \rho(\epsilon) f(\epsilon) d\epsilon = \frac{N}{2}(e^{-\eta}(2 + 2\eta + \eta^2)) \tag{4.10}$$

$$E_{lost} = \int_\eta^\infty \epsilon\,\rho(\epsilon) f(\epsilon) d\epsilon = \frac{N k_b T}{2}(e^{-\eta}(6 + 6\eta + 3\eta^2 + \eta^3)). \tag{4.11}$$

In Fig. 4.1 these quantities are plotted as a function of η. In our simulation the value of η is set to 5.5 so that only a small fraction of the atoms and energy in the gas is removed. In our calculations we assume that the time scale for removal of atoms from the trap is very fast compared to the rethermalization rate of the gas.

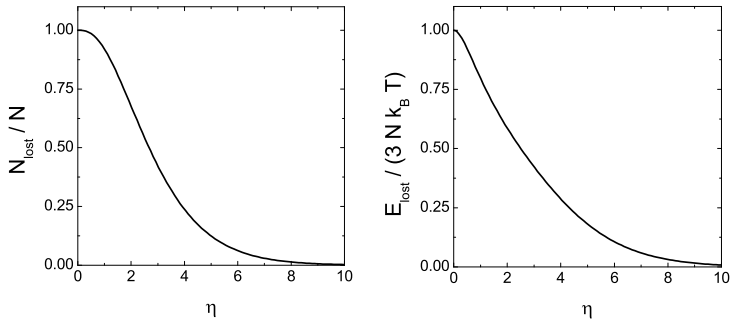

Figure 4.1: Number of particles lost and energy lost in a gas as a function of the truncation parameter η. Forced evaporation typically utilizes $\eta \approx 4 - 6$ so that only a small fraction of the gas is lost in each cooling iteration.

To simulate the forced evaporation process in our experiments, we break the process into a large number of iterations. At each iteration a small fraction of the atoms in the gas are removed and therefore a small fraction of the total energy is lost. We then estimate the rethermalization time based on the collision rate in the gas. For a specific value of η and initial temperature T and number N we calculate the number of atoms (N_{lost}) and energy (E_{lost}) removed as well as the time required to repopulate the high-energy trap states. This required time represents the relevant rethermalization time for evaporation and is approximated by [96]

$$\frac{1}{t_{evap}} = \Gamma \times b \exp -\eta. \tag{4.12}$$

where we have added a scale factor b that is described below. Our model significantly underestimates the time required for evaporation as compared to the observed time in our experiments. The model predicts that efficient ^{87}Rb evaporation can occur ten times faster than we observe in our experiments. We account for this underestimation by changing the scale factor $b \approx 0.1$ to set the total duration of many iterations to roughly coincide with our experimental observations. The likely cause of the underestimation is that full thermodynamic equilibrium throughout the gas is required for efficient evaporation. For the duration of this rethermalization time, loss of atoms and heating can occur due to density-dependent inelastic collisions and collisions with background gas. A value for the heating rate, R_{heat}, is obtained from experimental data since we lack an adequate model of this process. We simulate the number loss using the following differential equation

$$\frac{dN}{dt} = -K_2\langle n\rangle N - K_3\langle n^2\rangle N - \frac{N}{\tau_{bg}} \tag{4.13}$$

where the terms with K_2 and K_3 represent two and three-body loss and τ_{bg} is the exponential lifetime due to background gas. For a non-condensed gas of bosons in a harmonic potential we find

$$\langle n^2\rangle = \frac{8}{\sqrt{27}}\langle n\rangle^2 \tag{4.14}$$

For now we consider single species ^{87}Rb cooling. The temperature T' and number N'_{87} after a single iteration of the evaporation simulation is approximated by

$$T' = \frac{3Nk_BT - E_{lost}}{3N'k_B} + R_{heat}\,t_{evap} \tag{4.15}$$

$$N'_{87} = N - N_{lost} - K_3\,\langle n^2\rangle\,N\,t_{evap} \tag{4.16}$$

where we have neglected two body losses since K_2 for ^{87}Rb is small. The next iteration of the simulation begins with these values and a new rethermalization time is calculated. The simulation runs until no atoms remain in the gas or a minimum temperature has been reached.

We have performed simulations using our model under a variety of different conditions, and we find qualitatively reasonable behavior. Figure 4.2 shows the result of our simulation for single species ^{87}Rb evaporation under the typical conditions of our experiments. The radial (axial) trapping frequency is $2\pi \times 215$ Hz ($2\pi \times 12.5$ Hz). In the absence of loss and heating, as η is increased the number of atoms lost is lower and the duration of evaporation is expected to be longer. Also increasing the elastic cross section or the trap frequencies shortens the duration of the cooling because these changes increase the elastic collision rate. As expected, starting the evaporation with a larger number of atoms or a lower temperature tends to increase the final number. When loss and heating are included we also observe reasonable behavior. In particular as the value of K_3 increases, the atom number remaining after evaporation decreases.

So far our model is limited to single-species evaporation but including a second species is straightforward. In our simulations the magnetically trapped ^{85}Rb gas will always be sympathetically cooled by the ^{87}Rb gas. In order for sympathetic cooling to be effective there must be good thermal contact between the two species; *i.e* the ^{85}Rb and ^{87}Rb gases must be spatially overlapped so that collisions occur between the two species, and the elastic collision cross section must be sufficiently large. In our

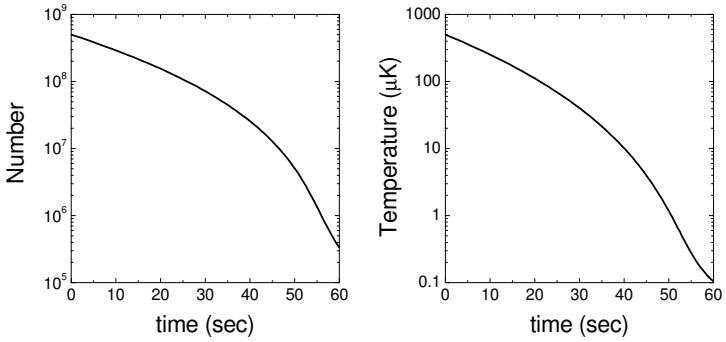

Figure 4.2: Results of our single species ^{87}Rb evaporative cooling simulation. The number of particles in the ^{87}Rb gas (left) and the temperature of the ^{87}Rb gas (right) is shown as a function time. For this simulation we used $K_3 = 4 \times 10^{-29}$ cm^6/s, and the heating rate was 10 nK/s.

Table 4.1: Various relevant parameters that are used in our simulations of evaporative cooling are collected here. For each parameter the relevant magnetic field or range of fields is indicated.

Parameter	B (G)	Value	units	Reference
K_3 ^{87}Rb	all	4×10^{-29}	cm^6/s	[104]
K_2 ^{87}Rb	all	$\approx 10^{-18}$	cm^3/s	[13]
K_3 ^{85}Rb	2	$5 - 10 \times 10^{-25}$	cm^6/s	[6]
K_2 ^{85}Rb	2	3×10^{-14}	cm^3/s	[6]

simulation we assume good thermal contact since the elastic cross section is large (the interspecies scattering length is 213 a_0 [103, 11]) and our IP trap assures spatial overlap between the two gases. To include sympathetic cooling in our model, we modify the temperature T' and number N' after a single iteration of the evaporation simulation to be

$$T' = \frac{3(N_{85} + N_{87})k_B T - E_{lost}}{3(N'_{85} + N'_{87})k_B} + R_{heat}\, t_{evap} \tag{4.17}$$

$$N'_{87} = N_{87} - N_{lost,87} - K_{3,87}\langle n^2_{87}\rangle N\, t_{evap} \tag{4.18}$$

$$N'_{85} = N_{85} - K_{3,85}\langle n^2_{85}\rangle N\, t_{evap} - K_{2,85}\langle n_{85}\rangle N\, t_{evap}. \tag{4.19}$$

Here we have included separate rates of inelastic atom loss for each species. Loss from inelastic interspecies collisions is ignored since the rate constants are known to be small [13, 1]. The actual rate constant values used in the model are listed in Table 4.1. These values were derived from previous work in the Wieman group (see the table for references). In our model, the time required for a single iteration does not change with the addition of ^{85}Rb. This is because we have assumed good thermal contact between the two species so that thermal equilibrium is maintained, therefore the timescale for rethermalization is the same for both species. Energy is only directly removed from the ^{87}Rb gas. Sympathetic cooling works best in the limit that the number of ^{87}Rb atoms is much larger than the number of ^{85}Rb. When the number in each species is roughly the same the ^{87}Rb cooling becomes inefficient. The inefficiency is characterized by the large fraction of the ^{87}Rb gas that has to be evaporated in order to lower the temperature of the two-species gas by an appreciable amount. When the cooling is inefficient, the number of ^{87}Rb atoms is rapidly depleted and no further reduction in temperature occurs. The specific results of a sympathetic cooling simulation based on this model will be presented later in conjunction with experimental data (see Fig. 4.11).

4.2.2 Analytic model of sympathetic cooling

To conclude the discussion of evaporation models, we briefly mention an analytic model of the sympathetic cooling process that is based on an energy budget. As described in Ref. [102], the model takes into account the finite heat capacity of the gas that is used as the coolant during sympathetic cooling. This model is useful for understanding the limitations of sympathetic cooling when the number of particles in the two gases are nearly equal. The key result of Ref. [102] is a prediction for the temperature of the

two-species gas as a function of particle number of each species during the cooling. This prediction will be compared to our experimental observations of sympathetic cooling presented in Section 4.5.1. In a two-species gas with particle numbers N_1 and N_2 the total energy is $E = 3(N_1 + N_2)k_BT$ and the change in total energy for a single step of evaporation is $dE = dN_1(\eta\, k_b\, T)$.[2] After rethermalization the temperature of the gas may be found from $E + dE = 3(N_1 + N_2)k_b(T + dT)$. We define $\alpha = \eta/3 - 1$, and then the temperature as a function of particle numbers N_1 and N_2 during the evaporation is

$$T = T^i \left(\frac{N_2}{N_1^i}\right)^{\alpha} \times \left(\frac{N_1}{N_2} + 1\right)^{\alpha}. \tag{4.20}$$

Here T^i is the initial temperature of the two gases prior to evaporative cooling and N_1^i is the initial number of that species. During sympathetic cooling the number N_1 decreases as atoms from that gas are evaporated, the number N_2 remains constant, and the temperature of the two-species gas drops. When the number N_1 reaches zero, the cooling ceases and the final temperature is $T_{min} = T^i \times \left(\frac{N_2}{N_1^i}\right)^{\alpha}$.

4.2.3 Motivation for sympathetic cooling based on elastic collision cross sections

With the theoretical results obtained in the previous section in mind, in particular the scaling of evaporation rate with collision rate, several conclusions about the expected performance in our system can be drawn. The traditional route to efficiently producing alkali-atom BEC involves increasing the trap frequencies as much as possible since the elastic collision rate scales as w_ρ^2. The temperature of the gas also increases with increasing ω_ρ but only fractionally as $\left(\frac{\omega'_\rho}{\omega_\rho}\right)^{2/3}$ so an overall increase in collision rate is still obtained. With a larger elastic collision rate the evaporation process is faster compared to the loss caused by collisions with background gas in the vacuum system, and therefore evaporation can be quite efficient. In fact a highly desirable "runaway" process can occur where evaporative cooling actually increases the elastic collision rate despite significant loss of atom number [99, 105, 97]. In this condition as the gas is cooled to lower temperature the collision rate rises and the efficiency of the process increases. Runaway evaporative cooling is quite easily achieved for many different species but this route assumes no negative side-effects of the increased density or initial temperature. Unfortunately achieving runaway evaporation with ^{85}Rb is difficult since increasing the trap frequencies actually leads to a decrease in the elastic cross section and an overall loss of collision rate. Large inelastic collision rates for ^{85}Rb further preclude the increase of trap frequencies.

The elastic collision cross section is calculated from the energy-dependent scattering amplitude in a partial-wave expansion [49, 48]

$$f_l = \frac{1}{k\cot(\delta_l) - ik} \tag{4.21}$$

where l is the angular momentum of the collision, k is related to collision energy by $k = \frac{\sqrt{2\mu E_{coll}}}{\hbar}$, μ is the reduced mass, and δ_l is the two-body scattering phase shift. The

[2] In this model N_1 and N_2 would correspond to the number of ^{87}Rb and ^{85}Rb atoms respectively.

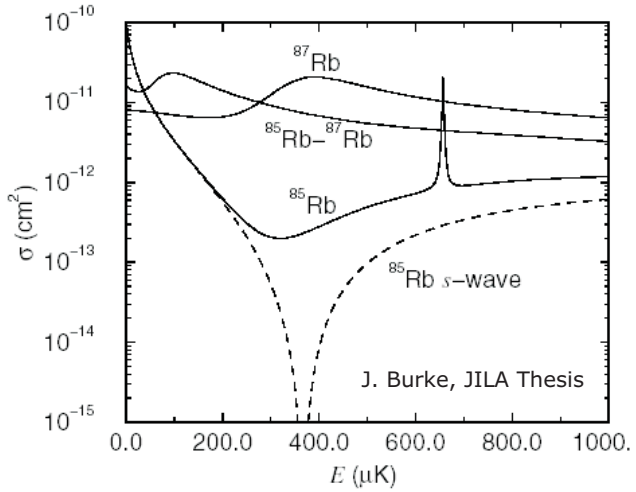

Figure 4.3: The elastic collision cross section for ^{85}Rb, ^{87}Rb, and collisions between the two species as a function of the collision energy. The total cross section for ^{87}Rb and interspecies collisions is roughly flat over a very wide range of temperature. In contrast, near 375 μK the ^{85}Rb s-wave cross section suffers a Ramsauer-Townsend type minimum. This figure was reproduced from Ref. [1].

term with $-ik$ represents the unitarity limit since kf_l cannot exceed 1. At unitarity the elastic cross section is not larger than $\frac{4\pi}{k^2}$. The cross-section is then [49, 48]

$$\sigma_{tot} = \frac{4\pi}{k^2}\sum_{l=0}(2l+1)\sin^2(\delta_l). \tag{4.22}$$

At low temperature only s-wave scattering is relevant and the total cross section is well approximated by $\sigma = 4\pi a^2$. In Fig. 4.3 a plot of the elastic cross section as a function of collision energy from Jim Burke's PhD thesis is shown to illustrate several advantages and challenges in our system (see Refs. [13, 1]). The elastic cross section for both ^{87}Rb and interspecies collisions is constant and large over the range in temperature relevant for our experiments (0-1 mK). In contrast the ^{85}Rb cross section, the solid line is the total cross section for all partial waves and the dashed line is for s-wave scattering only, is small over much of that range due to the presence of a Ramsauer-Townsend type minimum near 0.4 mK. To understand the origin of this suppression in the cross section, consider only $l = 0$ scattering for which the cross section is $\frac{4\pi}{k^2}\sin{\delta_0}^2$. When the phase shift approaches π the cross section is minimized. If the higher partial waves are suppressed by the low temperatures attained in our experiments, then the total cross section is also small. This represents a significant challenge in cooling ^{85}Rb into the quantum regime and has been the subject of discussion in Refs [7, 6].

There are two strategies for overcoming the small elastic cross section of ^{85}Rb. In the first strategy direct evaporation is performed with reasonable efficiency as long as the cooling is initiated from a low temperature. In the initial Wieman group experiments with ^{85}Rb great care was taken to load a very cold gas into the magnetic trap and compression of the trap was avoided. This resulted in a low but manageable initial collision rate so that evaporation could proceed slowly. Another strategy indicated by Fig. 4.3 and first proposed in Ref. [13] is to utilize the large elastic cross section between ^{85}Rb and ^{87}Rb. The ^{87}Rb gas is then cooled by direct evaporation while the ^{85}Rb is cooled through thermal contact. Sympathetic cooling is the strategy that we use, and therefore in principle we only need to worry about cooling ^{87}Rb efficiently.

4.3 RF for evaporation in the Ioffe-Pritchard trap

In the magnetic trap the most energetic atoms are selected by driving radio-frequency (rf) transitions between different magnetic sub-levels. Figure 4.4 shows a schematic diagram of the rf transitions leading to evaporative cooling in ^{87}Rb. The evaporation frequency is set to $\nu_{rf} = \nu_0 + \eta\, k_b\, T/h$ where η sets the fraction of the gas that is removed and ν_0 represents the bottom of the trap given by $\nu_0 = g_F\, m_F\, \mu_B\, B_0/h$ where g_F depends on the hyperfine state of the atom and B_0 is the field at the center of the trap. Since the g-factor of ^{85}Rb is smaller than that of ^{87}Rb, the frequency to remove atoms at a given energy is higher. Therefore if the two gases are in thermal equilibrium only ^{87}Rb atoms will be evaporated.

An Agilent E4400B rf synthesizer is used to generate the rf for evaporative cooling. This signal is sent to an amplifier (ZHL-1-2 made by Mini-Circuits) with 5 W total output, gain of 40 dB, and a nominal 50 Ω impedance. The frequency and output power of the synthesizer are set by the control computer over the GPIB interface. Since the timing precision of the GPIB interface is poor the rf is turned on and off with microsecond precision using an rf switch. The amplified signal is broadcast to the

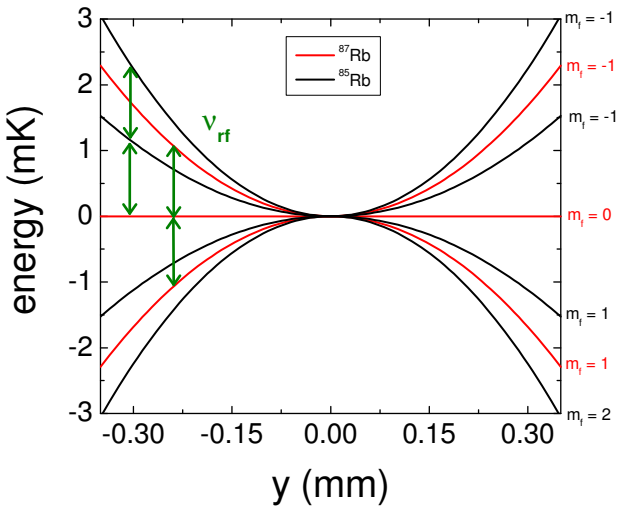

Figure 4.4: Energy level diagram for evaporative cooling as a function of the distance y from the center of our magnetic trap. The plot shows the level diagram of the ^{85}Rb $|f = 2, m_f = -2\rangle$ and ^{87}Rb $|f = 1, m_f = -1\rangle$ states. We can selectively evaporate only ^{87}Rb atoms since the g-factors of the two species are different.

atoms with a simple coil that is placed as close to the atoms as possible. The coil is approximately 2 cm from the atoms and it has a radius slightly larger than 1 inch. See Section 2.6.1 for more details on our rf setup.

It might seem advantageous to continuously sweep the rf source to obtain the most efficient evaporation, but this is both technically very challenging and in practice unnecessary since the synthesizer frequency can be changed on a timescale roughly equal to the rethermalization time in the gas. In our experiments the rf is swept discontinuously with a frequency change every 50-100 ms.

The evaporation frequency sweep is broken into several stages in which the parameters of the sweep are separately optimized. Typically we choose the start and stop frequencies to break the evaporation into stages in which the temperature of the gas is lowered by a factor of 2-4. The rf power and time constant τ_{stage} of each stage are varied over a wide range to optimize the atom number after the cooling. If the evaporation is reasonably efficient the temperature is determined by the rf, and the temperature will not change for different values of the rf power and time constant. In general, the rf power and time constant for evaporation are only sensitive at approximately the 30% level and tend to behave smoothly. The parameters for the magnetic trap evaporation currently used in the experiment are shown in Table 4.2.

Table 4.2: Evaporation parameters optimized for ^{87}Rb in the magnetic trap. The frequency of the final stage sets the final cut which changes slightly and is near 1.25 MHz. The power referenced here is what is programmed into the synthesizer and does not include the gain of the amplifier or loss through various rf components.

Stage	f_{start} (MHz)	f_{stop} (MHz)	τ_{stage} (sec)	f_{offset} (MHz)	rf power (dBm)
1	50	20	20	1.4	-18
2	20	7	15	1.4	-21
3	7	3	6	1.4	-24
4	3	1.8	3	1.3	-24
5	1.8	x	6	1.05	-24

The pattern of the sweep is an exponential function given by

$$f(t) = (f_{start} - f_{stop}) \exp \frac{-(t - t_{start})}{\tau_{stage}} + f_{offset} \tag{4.23}$$

with start, stop, and offset frequencies. The offset frequency can be used to vary the speed of evaporation. If the offset is far below the final frequency of a stage, then the time it takes to reach the stage end frequency is shorter. To maintain the best possible timing accuracy the frequency is calculated by the control computer "on-the-fly" during the evaporation using the internal Windows clock. This suppresses the accumulation of unknown timing lags during the evaporation.

4.4 Evaporation of ^{87}Rb to BEC

This section describes our ^{87}Rb single species evaporative cooling procedure in both the magnetic trap and the optical trap. The focus of this section is to document

the excellent performance of evaporative cooling that we observe with the ^{87}Rb gas. This information is important for two reasons. First, it allows us to verify and monitor the proper functioning of our apparatus.[3] With a baseline for ^{87}Rb performance established, when poor evaporation of ^{85}Rb is observed, we can eliminate many possible technical malfunctions of the apparatus as the cause of the poor ^{85}Rb cooling performance. With this knowledge we can focus our efforts on improving the ^{85}Rb cooling by minimizing inelastic collisions. Secondly, the information in this section provides a useful comparison to our observations of the efficiency of sympathetic cooling. During sympathetic cooling, we monitor the number of ^{87}Rb atoms that remain in the magnetic trap in order to understand the heat load due to the ^{85}Rb gas. If the number of ^{85}Rb atoms in too large, a large fraction of the ^{87}Rb gas must be evaporated and a low enough temperature after cooling may not be reached. We compare the final number of ^{87}Rb atoms after the cooling with and without ^{85}Rb to understand whether a large number of ^{85}Rb atoms may be cooled.

4.4.1 Forced rf-evaporation in the magnetic trap

Prior to evaporative cooling in the magnetic-trap, atoms are delivered to the science cell from the MOT located in the collection chamber. Typically the number of ^{87}Rb atoms delivered to the science cell is in the range of $5-10\times10^8$ and the temperature is 220 μK. The atoms are optically pumped into the $|f=1, m_f=-1\rangle$ state and loaded into the Ioffe-Pritchard magnetic trap. The magnetic trapping frequencies are slowly increased over 3 seconds to $\omega_\rho = 2\pi \times 215$ Hz and $\omega_z = 2\pi \times 12.5$ Hz just before evaporative cooling begins. This adiabatic compression raises the temperature of the gas according to $\frac{T'}{T} = \left(\frac{\omega'_\rho}{\omega_\rho}\right)^{2/3}$ so that cooling begins from approximately 700 μK. It is also the case that atoms are lost due to contact with the science cell walls during the compression. We made efforts to minimize this loss such as increasing the physical size of the glass cell along the weak direction of the trap. But the residual loss of these energetic atoms does not significantly hinder the performance of evaporation.

To characterize the efficiency of the cooling, we measure the number of atoms and temperature of the gas at different values of the rf-cut; we refer to this data as an evaporation trajectory. The term rf-cut (or simply cut) describes the final frequency used to cool the atoms. If the evaporation is working reasonably well then the cut will be proportional to the temperature of the gas. An important indicator of bad evaporation is a large mismatch between the cut and temperature. Figure 4.5 shows a trajectory that represents nearly our best evaporation results. We characterize the efficiency of the cooling by the slope of the data points in Fig. 4.5 (a), this slope is defined as

$$\alpha_{evap} = \frac{d(\ln T)}{d(\ln N)} \tag{4.24}$$

and the data were fit to a line to extract $\alpha = 1.60(5)$. For every factor of ten loss in atom number the temperature of the gas drops by a factor of fifty. This result is in good agreement with other examples of excellent evaporation performance such as that

[3] For example, good evaporation performance of ^{87}Rb indicates that the magnetic-trap currents are stable. Good performance is also an indication that the transfer from the MOT to the science cell is functioning properly.

described in Ref. [106]. In Fig. 4.5 (b) the measured peak phase space density calculated based on a Maxwell-Boltzmann distributions is shown as a function of temperature. The BEC transition is reached when the peak phase space density reaches $\zeta(1.5) \approx 2.612$. The solid black lines in Fig. 4.5 (a) and (b) are the result of our previously discussed simulation with $\eta = 5.5$ and are in reasonable agreement with the data. The total duration of the simulated evaporation was set to be equal to the 50 seconds used in the experiment. A three-body loss rate with $K_3 = 4 \times 10^{-29}$ cm^6/s and heating rate of 20 nK/s were used in the simulation. Two-body losses are expected to be small and the agreement between our data and the simulations confirms this is true. Since there is good agreement with the simulation we can safely conclude no other factors significantly contribute to the evaporation efficiency.

The number of ^{87}Rb atoms cooled to microKelvin temperatures depends on the initial number at the beginning of evaporation. In Fig. 4.6 we show a plot of the number at a fixed rf-cut in which we varied the initial number by changing the MOT fill. The temperature of the gas after evaporation is constant over the data except for the two points with lowest number. For these points that evaporation was very inefficient. The data in the figure suggests that we could increase the performance of the experiment by loading more atoms in the MOT or delivering a greater fraction of the MOT to the science cell. Increasing the MOT number might be accomplished by adding more trapping laser power or delivering more number to the science cell, which requires improving the transfer tube vacuum or the optical pumping. Given the current performance of the experiment, none of these improvements seem necessary.

The results shown in Figure 4.5 reflect the baseline performance of our apparatus under typical experimental conditions. On a daily basis we measure the number of ^{87}Rb atoms at an rf cut of 2.5 MHz. Under these conditions the temperature is 8–9 μK and the number of particles is 21 million. When the apparatus is not functioning properly a drop in the number of atoms at this cut is observed. It is of course important to understand the causes of poor evaporation performance. In particular, it is important to understand the difference between poor evaporation that is caused by the unfavorable collision properties of the gas and poor evaporation which is caused by technical malfunctioning of our apparatus. A good example of a technical malfunction is noise on the magnetic-trap currents, which leads to an effective broadening of the rf knife for evaporation since the magnetic field at the center of the trap is rapidly changing. A broad rf knife indiscriminately removes atoms from the trap over a wide range of energy. As the temperature of the gas drops the rf knife does not have adequate energy selectivity for efficient evaporation. This results in a reduced efficiency of the cooling and a reduction in the final number of atoms. Figure 4.7 shows a comparison of two evaporation trajectories for different values of the magnetic-trap current noise amplitude. When the rf-knife is too broad (large noise amplitude) a dramatic loss of number occurs. As shown in the figure, when we decrease the amplitude of the noise by a factor of ten, we are able to cool the gas to a temperature approximately ten times lower.

4.4.2 Cooling ^{87}Rb in the optical trap

This section describes the single-species evaporation of the ^{87}Rb gas in an optical trap. It represents the baseline performance of our apparatus with respect to ^{87}Rb cooling efficiency. The work described in the later chapters of this thesis was performed

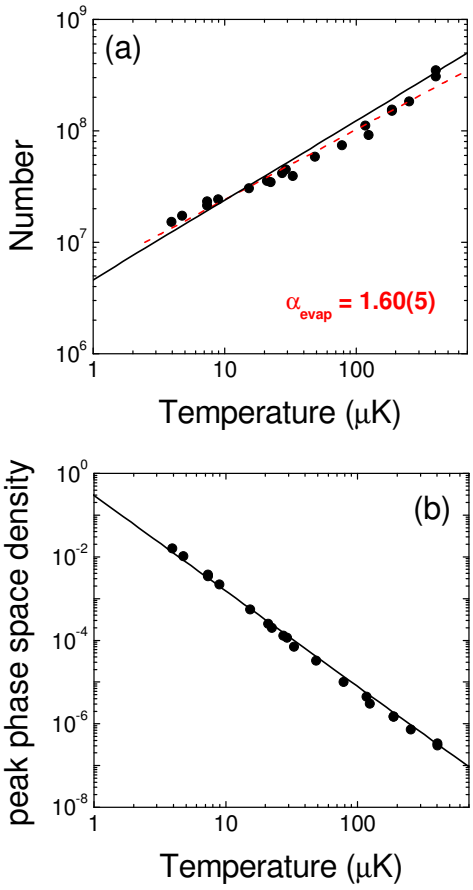

Figure 4.5: (a) Single-species evaporation trajectory of ^{87}Rb plotted as Log-Log. The points are the measured atom number at each temperature, the red dashed line is a linear fit to the data to extract $\alpha_{evap} = 1.60(5)$, and the black solid line is the result of our simulation. (b) The points are the measured phase space density for a classical gas extracted from the number and temperature of the gas. The black line is the calculated peak phase space density from our simulation. These data represent the current best performance of the ^{87}Rb evaporation.

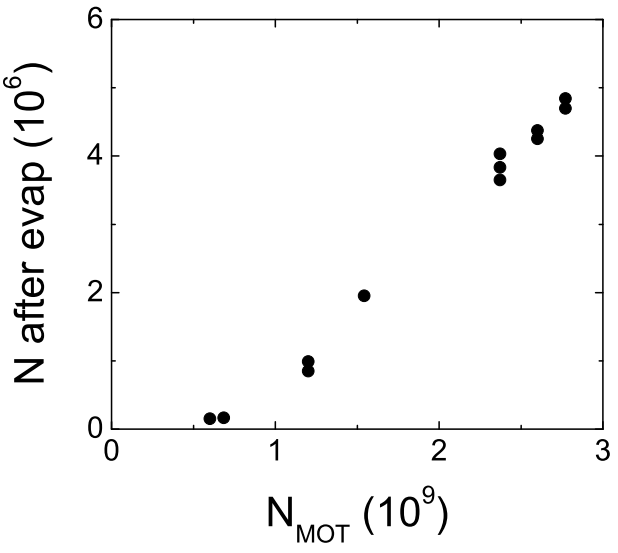

Figure 4.6: Measured ^{87}Rb number after evaporation to a fixed rf-cut as a function of the number of atoms loaded into the MOT. The evaporation is run with the same rf ramps for each value of N_{MOT}. Roughly 25% of the atoms from the MOT are delivered to the magnetic trap for evaporation.

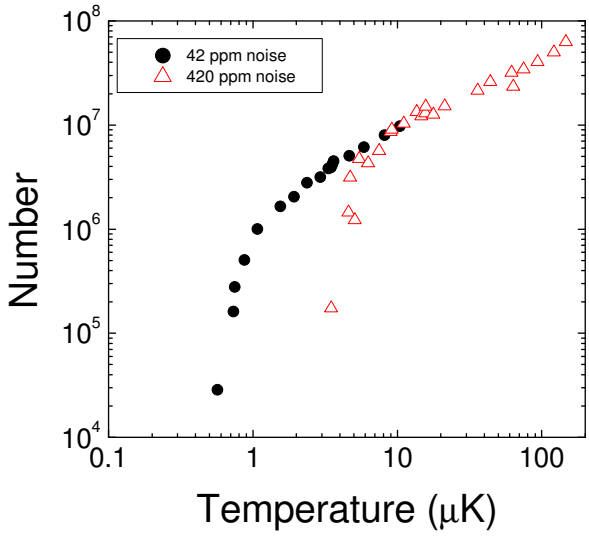

Figure 4.7: Evaporation trajectory of ^{87}Rb with two different amplitudes of magnetic-trap current noise. Here the noise amplitude is the total integrated AC signal from 10 Hz to 100 kHz. During normal operation the current noise is 6 ppm on the IP trap coils. When the amplitude of noise on the trap current was decreased, thelowest achievable temperature also dropped by a similar amount. This data is an example of poor evaporation due totechnical limitations in the apparatus. The noise here is limited by the inherent current instability of the commercial power supply we used at the time.

with two different optical trapping setups: the "tight" trap with a 23 micron waist and the "weak" trap with a 46 micron waist. We attain a very similar efficiency for single species ^{87}Rb evaporation in both traps. To avoid confusion, in this section we only discuss evaporation in the tight trap. To begin single-species ^{87}Rb cooling in the tight optical trap, we pre-cool a gas in the magnetic trap and then we load the atoms into an optical dipole trap for further cooling. We perform evaporative cooling in the optical trap by slowly lowering the depth of the potential to let the most energetic atoms spill out. Then the remaining atoms in the gas rethermalize to lower temperature just as in the magnetic trap. After several seconds of optical trap evaporation we are able to create a condensate with more than a million atoms.

After evaporation in the magnetic trap to 3-30 μK, we load the optical trap as described in Section 2.7. The final temperature in the magnetic trap is chosen to maximize the number of atoms remaining in the optical trap after evaporation to 1 μK. Figure 4.8 shows the number of atoms remaining in the optical trap after evaporation to 1 μK as a function of the final temperature in the magnetic trap. The rf evaporation was stopped at different frequencies in the range 1.8 - 5 MHz, and then the optical trap evaporation sequence was performed. Loading the optical trap with a higher temperature gas is inefficient since only a fraction of the atoms fit into the finite initial depth of the trap. Starting the optical trap evaporation with a colder gas is slightly less efficient, since more atoms are consumed by the magnetic trap cooling than are consumed by the optical trap evaporation. Optimum performance is obtained for a final magnetic trap temperature of approximately 10 μK.

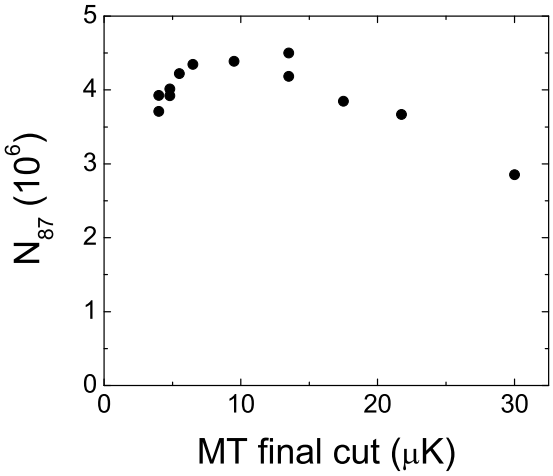

Figure 4.8: Measured ^{87}Rb number after evaporation in the optical trap as a function of the final cut temperature in the magnetic trap. The optical trap has a finite depth so the best loading will occur at lower temperatures. But evaporation in the optical trap evaporation is likely a little more efficient than the magnetic trap so loading the coldest atoms does not produce the best result.

Table 4.3: Evaporation parameters used for the tight optical trap. There are four stages in the tight trap evaporation each with an initial power, final power and ramp rate. Powers here are listed as the control voltage entered into the control computer. The calibration is roughly 1.2 W / 1.7 V. Listed in the last column is the calculated radial trap frequency at the end of the stage.

Stage	P_{start} (V)	P_{stop} (V)	rate (V/sec)	ν_{radial} (Hz)	ν_{axial} (Hz)
1	1.7	0.3	5	1900	18
2	0.3	0.1	0.2	780	8
3	0.1	0.03	0.01	451	4
4	0.03	0.02-0.018	0.004	~ 200	~ 2

To evaporate in the optical trap we linearly decrease the power as a function of time.[4] The only input parameters are the initial power, final power, and the ramp rate. The power of the optical trap is continuously monitored with an amplified photodiode. The photodiode signal is used as feedback to an acousto-optic modulator in order to stabilize the trapping power. An analog voltage from the experiment-control computer supplies the reference voltage for the servo electronics that stabilize the trapping power. The optical trap evaporation is broken into several stages each with a different ramp rate. The start and stop powers are chosen to give a change in temperature of approximately a factor of two. The ramp rate is optimized to give the largest number of atoms remaining after evaporation as long as the target temperature is achieved. In Table 4.3 we have listed the parameters for each stage of evaporation in the tight trap. The entire evaporation takes nearly 11 seconds. The optical trap evaporation is straightforward to optimize since there is only one parameter per stage to set, the ramp rate. The ramp rate is varied over a wide range to find the largest number of atoms after evaporation. Since we are searching for the largest number at a fixed temperature and a fixed optical power, the ramp rate that optimizes the number also corresponds to the highest phase space density.

We have recorded an evaporation trajectory of ^{87}Rb in the tight optical trap; the data is shown in Figure 4.9. The optical trap power is lowered from 1.2 W to 0.035 W in 11 seconds. The first two stages of the cooling are fast and take only 1 sec while the last two stages take much longer. The BEC transition temperature is reached with at least two million atoms, and we are routinely able to produce condensates with a large atom number. Since the gas cools by adiabatic decompression as well as evaporation, extracting an efficiency from the data is complicated. The adiabatic decompression also complicates a comparison of the data and our evaporation model, since our model does not account for the decompression. Our data indicates that the evaporation in the optical trap is efficient since the final number of atoms after the formation of a condensate is comparable or slightly better than what we observe in the magnetic trap. In Figure 4.10 three absorption images of ^{87}Rb after 20 ms of expansion from the optical trap are shown. The images were acquired at different temperatures near the

[4] We have verified that exponential ramps do not improve the performance of ^{87}Rb evaporation in the optical trap.

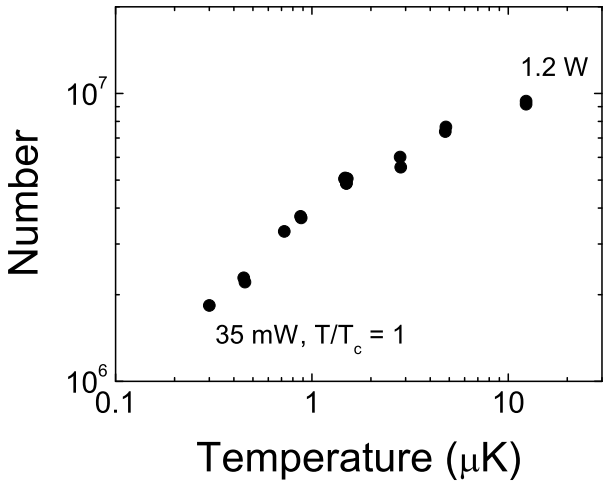

Figure 4.9: ^{87}Rb evaporation trajectory in the tight optical trap demonstrating efficient evaporation. This data represents the baseline performance in the optical trap and is useful for comparing the simultaneous evaporation efficiency of ^{85}Rb and ^{87}Rb.

BEC transition point. The last image is a good representation of the appearance of a ^{87}Rb BEC after expansion from the optical trap. The vertical direction of the images correspond to the radial direction of the gas. In this direction the images represent the momentum distribution of the trapped gas. Since confinement along the axis of the gas is weak, the images in this direction are to be interpreted as the spatial distribution of the atoms in the trap. Further, given the typical expansion times used in our experiments (3-100 ms) and the weak axial confinement, we do not observe anisotropic expansion of the Bose condensed gas. However, the appearance of a condensate is readily observed through the appearance of a bi-modal distribution in both the axial and radial directions of the absorption images when the temperature falls below T_c.

4.5 Sympathetic cooling of ^{85}Rb in the magnetic trap

The remainder of this chapter describes our work cooling a gas of ^{85}Rb atoms into the quantum degenerate regime. In this section we discuss sympathetic cooling of ^{85}Rb in the magnetic trap using a ^{87}Rb gas as the coolant. In particular we will describe our successful sympathetic cooling results in which a temperature of 5 μK is achieved. The cooling is judged to be successful since no ^{85}Rb atoms are lost from the trap as the temperature is lowered from an initial value of nearly 1 mK. The achievement of this low temperature represents a solution to the first roadblock on the path to ^{85}Rb BEC, namely the zero in the elastic cross section at 0.4 mK.

However, a temperature of 5 μK is not cold enough to form a BEC. Therefore we have explored the limitations of sympathetic cooling in the magnetic trap in order to understand the coldest attainable temperatures in our system. One limitation is the finite heat capacity of the ^{87}Rb gas; in Section 4.5.1 we show that sympathetic cooling becomes inefficient when the number of ^{85}Rb atoms is nearly equal to the number of ^{87}Rb atoms. This observation is consistent with the predictions of the evaporation models previously discussed. Another limitation is ^{85}Rb inelastic collisions; in Section 4.5.2 we directly demonstrate the effect of inelastic collisions on the cooling efficiency. Below a temperature of 5 μK in the magnetic trap, sympathetic cooling is difficult since ^{85}Rb inelastic collisions occur frequently and they lead to significant ^{85}Rb number loss. This loss of number limits the phase-space density of the gas to a value less than that required for BEC. In Section 4.5.3 we investigate the possibility of improved ^{85}Rb cooling efficiency by lowering the density of the two-species gas in the magnetic-trap. With a lower density the frequency of ^{85}Rb inelastic collisions decreases, therefore ^{85}Rb number losses are also decreased and a larger phase-space density is achievable. However, this phase space density in our magnetic trap experiments doesn't quite reach the values required for BEC. Our experiments in which we do achieve BEC by doing the final cooling in an optical trap will be described in subsequent Section 4.6.

The general concept of sympathetic cooling is rather simple. A hot substance with small heat capacity is placed in thermal contact with another substance at colder temperature and larger heat capacity. Sympathetic cooling in ultracold neutral atom gases was first demonstrated by the Wieman group with two different hyperfine states of ^{87}Rb in Ref. [106]. Since then the technique has been used with a variety of different species, in particular Bose-Fermi mixtures (^{6}Li and ^{7}Li [29, 107], ^{6}Li and Na [108], K and Rb [109, 110, 111]). Sympathetic cooling of a mixture of ^{85}Rb and ^{87}Rb was first reported in Ref. [11], but ^{85}Rb BEC could not be reached due to severe inelastic number

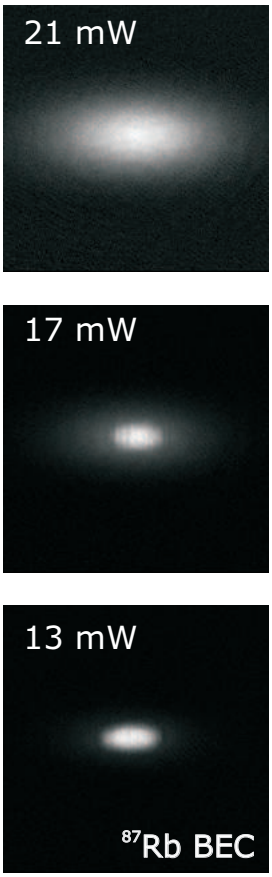

Figure 4.10: Standard three absorption images of ^{87}Rb BEC formation in the tight optical trap. Since the axial trap frequency is very low, the image represents the spatial distribution in that direction and anisotropic expansion is not observed. The first signature of condensation in the optical trap is the appearance of a bi-modal density distribution.

loss and the negative background scattering length. A significant amount of theoretical work has also been reported including predictions for our system in Ref. [13, 112].

There are two critical prerequisites for sympathetic cooling. First we must spin-polarize the gases into the ^{85}Rb $|f = 2, m_f = -2\rangle$ and ^{87}Rb $|f = 1, m_f = -1\rangle$ states since loss due to spin-exchange collisions is large. As described earlier we spin polarize the gases quite well before loading into the magnetic trap for evaporation, and hereafter we ignore this type of loss. Another critical issue in the magnetic trap is the difference in magnetic moments of the two states. At low field the magnetic moment in the ^{85}Rb $|f = 2, m_f = -2\rangle$ state is $2/3\mu_B$ while the moment in the ^{87}Rb $|f = 1, m_f = -1\rangle$ state is $1/2\mu_B$. In the tight trap initially used for evaporation, the ^{85}Rb radial (axial) trap frequency is $2\pi \times 250$ Hz ($2\pi \times 14$ Hz). In a magnetic trap with harmonic confinement gravity tends to "sag" the central position of the trapped gases by an amount equal to g/ω_ρ^2. Since the trap frequencies of each species are different, there is an offset in the center position of each gas given by the difference

$$\Delta y = g\left(\frac{1}{\omega_{\rho,87}^2} - \frac{1}{\omega_{\rho,85}^2}\right). \tag{4.25}$$

In the magnetic trap this difference is only a few μm. We expect good thermal contact between the two species until the temperature is lowered to approximately 100 nK. At this temperature the difference between the central locations of two species is on order of the trapped size of the two gases.

4.5.1 Effects of ^{87}Rb heat capacity on sympathetic cooling

Sympathetic cooling is only efficient as long as the ^{85}Rb number is smaller than the ^{87}Rb number. Once the number of particles is roughly equal the coolant gas does not have sufficient heat capacity and rapid loss of the coolant occurs. This effect sets either a maximum number of ^{85}Rb atoms that can be cooled, a minimum number of ^{87}Rb atoms required, or a minimum achievable final temperature of the two gases. In this section we demonstrate the limitation of sympathetic cooling due to the heat capacity of the ^{87}Rb gas.

We begin sympathetic cooling by loading ^{85}Rb and ^{87}Rb into the magnetic trap. To evaporate, the same radio-frequency ramps that were optimized for single-species ^{87}Rb cooling are applied to the mixed species gas. We optimized the rf ramps specifically for sympathetic cooling, but we only found a slight improvement in the final number of atoms. In Fig. 4.11 several evaporation trajectories for sympathetic cooling are shown. The dashed lines in the figure show the BEC transition temperature for the ^{85}Rb (black) and ^{87}Rb (green) gases. Therefore the line represent our goal for evaporative cooling. This data demonstrates successful sympathetic cooling of the ^{85}Rb gas to 5 μK, since no atoms are lost while the temperature is decreased by more than two orders of magnitude. While we could not cool into the quantum-degenerate regime, this data was the first demonstration of sympathetic cooling in these spin states and represented a significant milestone in our efforts to reach ^{85}Rb BEC. Finally we note that the temperatures reached with sympathetic cooling are sufficient to provide a large elastic cross section for direct ^{85}Rb evaporation, lifting the first roadblock to ^{85}Rb BEC.

The solid lines in Fig. 4.11 are a fit to the data using the analytic model of sympathetic cooling from Ref. [102] that is described in Section 4.2.2. In each case the

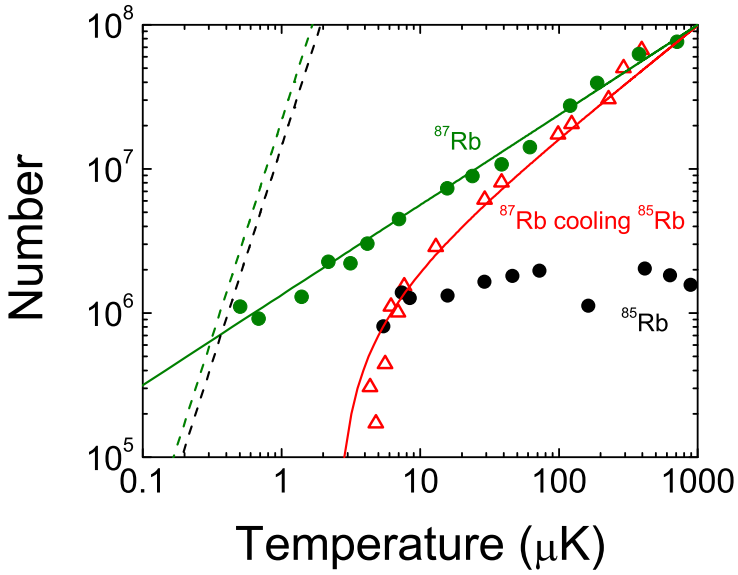

Figure 4.11: Evaporation trajectories for sympathetic cooling of ^{85}Rb (black points) via collisions with ^{87}Rb (red open triangles). For comparison the data points with filled green circles are the single-species ^{87}Rb evaporation trajectory. Sympathetic cooling is successful since the observed ^{85}Rb number does not change while the temperature drops more than a factor of 100. Below 10 μK the number of each species is roughly the same and cooling of ^{87}Rb is very inefficient. The inefficiency is characterized by the large fraction of the ^{87}Rb gas evaporated in order to lower the temperature.

only fitting parameter α is related to the overall efficiency of evaporation. We first fit the single-species ^{87}Rb data to extract a value of $\alpha = 1.6$ which is consistent with the results discussed previously (Sec. 4.4.1).[5] Rapid loss of ^{87}Rb occurs while cooling ^{85}Rb when the number of atoms in each gas is roughly equal. We fit the ^{87}Rb data to the model with $N_{85} = 10^6$ and extracted $\alpha = 1.3$ which indicates less efficient cooling. The qualitative agreement between the data and the analytic model indicates that no other effects play a significant role in the rapid loss of ^{87}Rb number.

4.5.2 Effects of inelastic collisions on ^{85}Rb evaporation

In this section we consider the effect of inelastic collisions on the efficiency of ^{85}Rb cooling. To demonstrate the effects of these bad collisions, we have obtained an evaporation trajectory during sympathetic cooling in which the number of ^{85}Rb atoms is always significantly less than the number of ^{87}Rb. Under these conditions (Fig. 4.12) sympathetic cooling is not limited by the heat capacity of the ^{87}Rb gas, and therefore the temperature of the two-species gas can be lowered much further than what had previously been possible.[6] In fact a temperature significantly below 1 μK is attained, but at these temperatures a rapid loss of ^{85}Rb atoms from the trap is observed. The focus of this section is to demonstrate that this behavior is consistent with inelastic collisions.

The data shown in Fig. 4.12 demonstrate efficient sympathetic cooling, with no loss in the ^{85}Rb number, until a temperature of approximately 3 μK. Below this temperature rapid ^{85}Rb number loss occurs. Also shown in Fig. 4.12 is the measured peak phase-space density of the two gases. This quantity is calculated based on the measured number and temperature of the gas along with a knowledge of the trap frequencies. Our goal is to increase the peak phase-space density of the ^{85}Rb gas to 2.612 but the largest phase-space density achieved here is still a factor of 100 too small. The data covers a very wide range of temperature. We purposely continued to cool the ^{87}Rb gas until BEC was reached, in spite of the fact that only a few thousand ^{85}Rb atoms remain. We are able to continue cooling ^{87}Rb since the number in the two species is never equal. For the lowest temperatures it is likely the case that the gases were no longer in perfect thermal contact due to gravitational sag. Therefore the two species are not in thermal equilibrium. For reference, we note that at a temperature of 5 μK the average density of the ^{85}Rb gas is 7×10^{11} cm^{-3}.

In order to understand the the poor ^{85}Rb evaporation performance, we have compared the measured evaporation trajectory to the predictions of the simple model described in Section 4.2.1. Number loss and heating occur during the time required for evaporative cooling, and as the density increases this loss worsens and eventually the gas cannot be cooled fast enough. The solid lines in Fig. 4.12 are the results of a

[5] We point out that this agreement is interesting since the two sets of data were taken under very different conditions in the experiment and separated in time by more than a year. The data in Sec. 4.4.1 has nearly an order of magnitude more atoms yet the efficiency of evaporation is the same.

[6] Note that the number of ^{85}Rb and ^{87}Rb atoms at the beginning of evaporation is significantly higher in the data shown in this section. Following our initial demonstration of sympathetic cooling, we increased the efficiency of the transfer to the science cell allowing a larger initial number for cooling. We were also able to increase the efficiency of optical pumping from the MOT into the quadrupole trap. This increase in atom number was carried throughout the cooling to produce a larger final atom number.

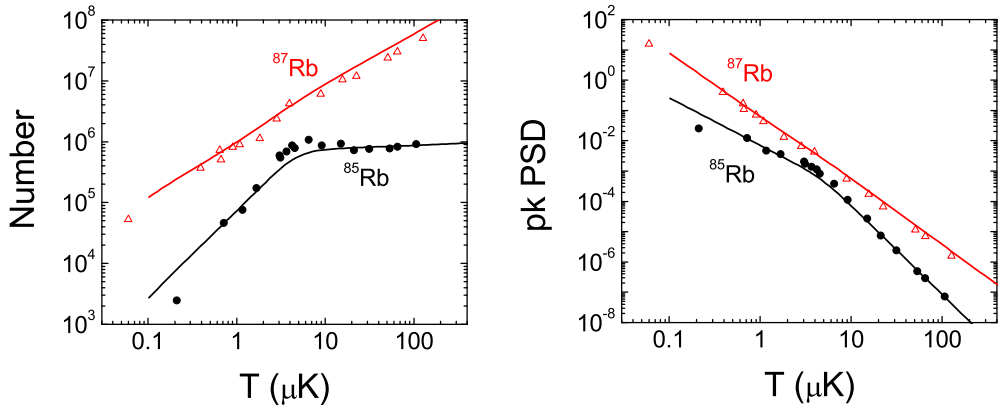

Figure 4.12: Evaporation trajectories of ^{85}Rb (black filled points) and ^{87}Rb (red open triangles). The solid lines are the result of our simple model for evaporation. The lines are in good qualitative agreement with the data. The efficiency of ^{87}Rb cooling remains high throughout the entire evaporation indicating that the heat-capacity limit was not reached. The coldest ^{87}Rb point is below the BEC transition temperature. Frequent inelastic collisions cause poor cooling efficiency in the ^{85}Rb gas.

simulation based on our model. The predictions of the model are in good qualitative agreement with the data. Simulations were performed using the values for inelastic loss coefficients (K_2 and K_3) shown in Table 4.1. The model roughly predicts the temperature at which loss of ^{85}Rb begins and it predicts how many atoms will be lost during the evaporation. Furthermore the model predictions of the phase-space density during sympathetic cooling are also in qualitative agreement with our observations. Our results strongly indicate that ^{85}Rb condensate formation is highly unlikely under these conditions. Based on the agreement between the simulation and our data we are able to conclude that ^{85}Rb inelastic collisions are the primary limitation of the sympathetic cooling.

We have performed experiments to directly characterize the ^{85}Rb inelastic collisions in our system by measuring the ^{85}Rb population decay as a function of time. From this data we can extract an estimate for the two-body inelastic rate constants and compare this with the values derived from previous experiments and used in our simulations (Table 4.1). Lifetimes of the gas were acquired at two different temperatures near the end of evaporation, one at a temperature just as the evaporation begins to fail and the other well into the poor cooling regime. The evaporation is stopped either at 3.5 μK or 1 μK, and the number of atoms and temperature of the gas is monitored as a function of time. We calculate the average density of the gas using the trapping potential parameters. The results for 1 μK and 3.5 μK are shown in Fig. 4.13 in a log-log plot as a function of time. In each plot the data were fit to a exponential function (red line) with two time constants. The second time constant was fixed to the previously measured background lifetime in the trap of 300 s. At 1 μK the first time constant was only 2.2 s, a factor of five shorter than at 3.5 μK. The data in Fig. 4.13 have also been fit to extract the values of the inelastic rate constants K_2 and K_3; the rates that we extracted are given in the figure. The atom loss in the magnetic trap is primarily due to two-body collisions with a measured rate constant of $K_2 \approx 5 \times 10^{-13}$ cm^3/s. There is reasonable agreement between this measured rate and previous work [6]. Our data does not allow us to determine the rate of three-body collisions. From the measured temperature as a function of time we also extract the heating rate. It was 70 nK/s for both data sets. We do not have a detailed understanding of this heating rate; in the following section we will discuss experimentally exploring its origin.

For future reference we present an evaporation trajectory (Fig. 4.14) during sympathetic cooling in the magnetic trap that demonstrates the best evaporation results obtained to date with our apparatus. We are able to cool several million ^{85}Rb atoms without loss to a temperature of several microKelvin. At this temperature nearly 10 million ^{87}Rb atoms remain in the trap. These conditions are the starting point for further cooling in an optical dipole trap in which ^{85}Rb condensates are formed. As discussed above, the heat-capacity limit is never reached in this data indicating that even more atoms could be cooled. We have measured the heating rate of the two-species gas after stopping the evaporation at a temperature of 9 μK. We observe a single-species ^{87}Rb heating rate of 80 nK/s. When ^{85}Rb is also present in the trap the rate soars to 400 nK/s. The two-species heating rates are significantly larger than the 70 nK/s reported above and the likely cause is the increase in overall ^{85}Rb number.

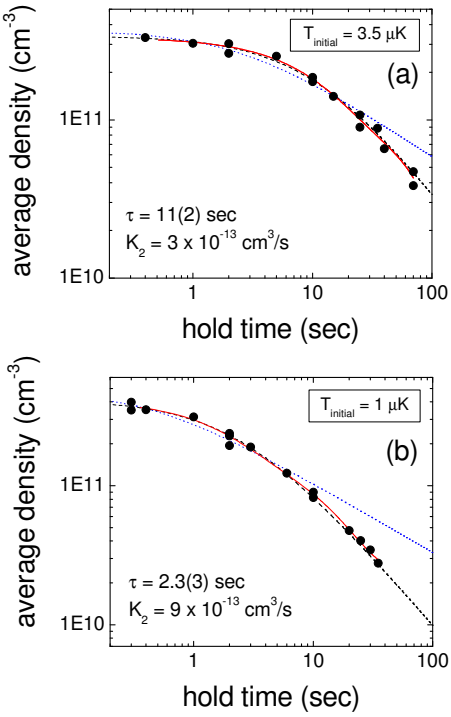

Figure 4.13: Measured average density as a function of time after the completion of evaporation to a final temperature of (a) 3.5 μK and (b) 1.0 μK. The filled circles are our data points and the lines are fits to the data. The red solid line is a double exponential function with a fast decay time of 11 sec in (a) and a fast decay time of 2.3 sec in (b). In both (a) and (b) the second time constant was fixed to 300 sec according to the measured background lifetime. The dashed line (black) and dotted line (blue) are fits to two- and three-body inelastic collision rates, respectively. We extract a value of $K_2 \approx 5 \times 10^{-13}$ cm^3/s from the fit. The three-body fit does not agree with our data.

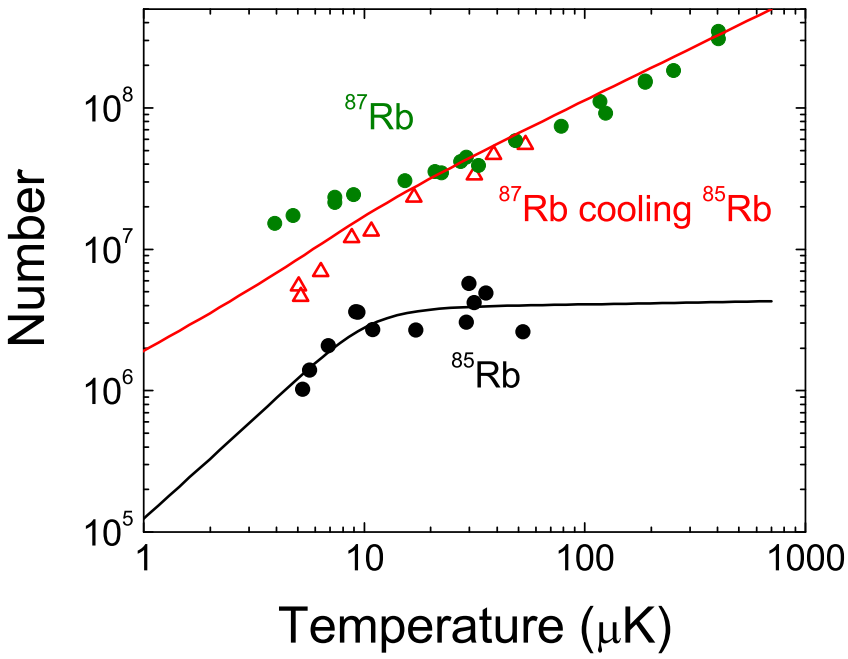

Figure 4.14: Our most efficient evaporation trajectory during sympathetic cooling in the magnetic trap. The filled black circles are ^{85}Rb, the open red triangles are ^{87}Rb while cooling ^{85}Rb. The ^{87}Rb single species trajectory (green) is shown for comparison. Below approximately 5 μK ^{85}Rb atoms are rapidly lost due to inelastic collisions as indicated by the results of our simulation. The experimental conditions of number and temperature shown here represent an excellent starting point for cooling in an optical trap.

4.5.3 Toward ^{85}Rb BEC in the magnetic trap

In the previous section we established inelastic collisions as the limitation to cooling ^{85}Rb in the magnetic trap. In this section we will focus on work we did to lower the inelastic collision rate in our sympathetic cooling experiments. Specifically we have explored evaporative cooling in a magnetic trap with a significantly lower radial trapping frequency. To avoid confusion, hereafter we refer to the magnetic trap with reduced radial frequency as the "weak" trap. The magnetic trap with higher frequency, that has been used in all previous experiments, is now called the "tight" trap. The density of the ^{85}Rb gas is reduced in the weak trap; therefore the rate of inelastic collisions is also reduced. Under these conditions a low heating rate in the trapped gases is critical, so we added a second radio-frequency source to remove energetic ^{85}Rb atoms generated during inelastic collisions. We first discuss our experimental setup to control the magnetic trap heating rate, and then we present an improved evaporation trajectory in the weak magnetic trap. With a lower ^{85}Rb density, we are able to improve the ^{85}Rb phase-space density at the end of evaporation.

4.5.3.1 RF shielding to lower the magnetic trap heating rate

We characterized the heating rate in the tight magnetic trap by applying an rf-shield to a ^{87}Rb gas. A radio frequency is applied just above the temperature of the gas in much the same way as evaporation. Heating can either occur internally in the gas or as a result of elastic collisions with a low density, high temperature secondary gas sometimes called an "Oort cloud" [59, 113]. The source of this secondary gas is typically from incomplete evaporation, in which a small fraction of the atoms removed during the evaporation do not leave the trap. An Oort cloud may also be created from the remnants of inelastic collisions. The Oort cloud is only in weak thermal contact with the much colder gas at the center of the trap. Infrequently an energetic atom from the Oort cloud collides with the cold gas depositing a lot of energy. In the tight trap we test the shield by holding the ^{87}Rb gas immediately after evaporation stops. During this holding time the gas heats up at a known rate. We characterize the effect of different shield frequencies by measuring the temperature after the hold; the data are shown in Figure 4.15. As long as the shield frequency is larger than 3.5 MHz, no heating occurs during the hold and no number loss is observed. The fact that similar shielding of the gas is observed for a wide range of frequencies is a clear indication that the heating rate is mostly due to the external Oort cloud. This is because the temperature of the Oort cloud is much larger than the temperature of the gas at the center of the trap. Using the rf shield we were able to reduce the ^{87}Rb heating rate in the tight trap to approximately 30 nK/s from 80 nK/s and the heating rate of the two-species gas to approximately 100 nK/s from 400 nK/s.

By applying an rf-shield to the atoms in the weak trap, the heating rate of the gas is even smaller. We cool a two-species gas in the tight magnetic trap to a temperature of 8 μK with nearly 10^7 ^{87}Rb atoms and 2×10^6 ^{85}Rb atoms. We reduce the density in the magnetic trap by slowly lowering the current in the bias coil over a few seconds until the radial trap frequency for ^{87}Rb (^{85}Rb) is $2\pi \times 45$ Hz ($2\pi \times 53$ Hz) while the axial frequencies remain unchanged. The bias field at the center of the trap is set to 31.6 G. The trap frequencies are chosen to give a low density, but still maintain thermal overlap between the two species. We verified that the phase space density of the gas

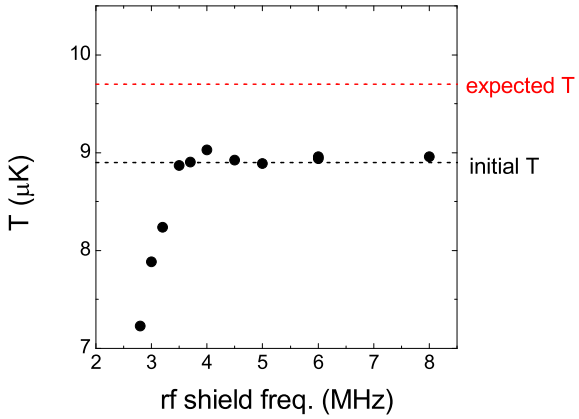

Figure 4.15: Measured temperature following a 10 sec hold in the tight trap as a function of rf-shield frequency. The red line indicates the expected temperature of the gas due to the known heating rate. The black line is the initial temperature just after evaporation stops. When the rf-shield is too low a fraction of the gas is evaporated. No number loss or heating occurs for a shield frequency of more than 3.5 MHz.

does not change during the trap decompression, meaning that the ramp is adiabatic. Using the rf shield we were able to reduce the ^{87}Rb heating rate in the weak trap to approximately 3 nK/s from 35 nK/s.

Since the spin states of ^{85}Rb and ^{87}Rb that we use have different magnetic moments, in the weak magnetic trap it is possible to place an rf shield in-between the two species. Figure 4.16 shows a diagram of the trapping potential for the two species and the location of the two rf shields. The rf transition between the ^{85}Rb $|2,-2\rangle \rightarrow |2,-1\rangle$ is sufficiently different from the ^{87}Rb $|1,-1\rangle \rightarrow |1,0\rangle$ transition that each gas can be accessed separately. The field rf_1 is used to evaporate the ^{87}Rb gas, and it is used as a shield after the cooling. We place the field rf_2 just above the ^{85}Rb gas but far below the bottom of the ^{87}Rb trap. The only use of this shield is to protect the ^{87}Rb gas against energetic atoms generated inside the ^{85}Rb cloud. Without the second shield, ^{85}Rb atoms are trapped with energy up to 0.4 mK before possible removal by the ^{87}Rb rf knife. If the shield were not present then the ^{87}Rb cloud absorbs a lot of energy from this Oort-like ^{85}Rb gas. Using both the rf_1 and rf_2 shields the heating rate of the two-species gas is reduced to approximately 15 nK/s from the original 100 nK/s. This heating rate is a factor of 27 better than the rate observed in the tight trap, see Figure 4.14.

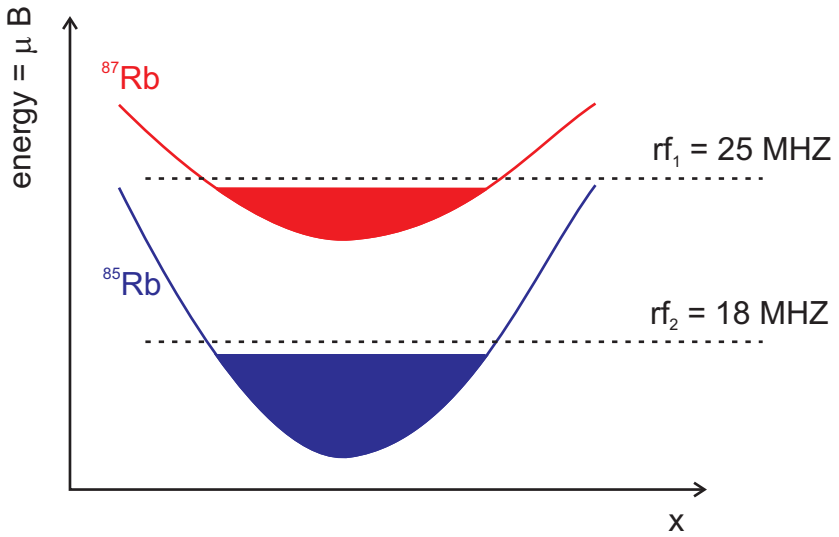

Figure 4.16: Schematic of the two rf shields used to control the heating rate in the magnetic trap. The solid red and blue curves represent the trapping potential for ^{87}Rb and ^{85}Rb and the fill is the surface of the trapped cloud. The ^{87}Rb gas is evaporated by rf_1 and rf_2 is the tunable shield for ^{85}Rb.

4.5.3.2 Evaporation in the weak magnetic trap

Here we describe the results of sympathetic cooling of the ^{85}Rb gas in the weak magnetic trap. In particular we identified two critical parameters of our system that primarily determine the efficiency of the cooling. The first critical parameter of our system is the relative number of atoms of the two species that are loaded into the

magnetic trap for evaporation. The second critical parameter is the rf shield (rf_2) that is placed above the the ^{85}Rb gas but below the ^{87}Rb gas. This shield is particularly effective at protecting the ^{87}Rb gas from energetic ^{85}Rb atoms generated during inelastic collisions. We optimized these two parameters in order to achieve the best evaporation results.

Evaporation of ^{87}Rb in the weak trap is very similar to all the discussion in the previous sections of this chapter. We modified the radio-frequency sweeps to account for the different magnetic field at the center of the trap (see Table 4.4). Since the collision rate in the gas is lower the optimum duration of the sweeps is approximately five times higher than in the tight trap. We verified that the efficiency of cooling ^{87}Rb is still good. For every factor of two reduction in number the temperature drops by a factor of 3.4. The BEC transition temperature is reached with 3×10^6 atoms.

Table 4.4: Evaporation parameters optimized for ^{87}Rb in the weak magnetic trap. The parameters are optimized by searching for the largest ^{87}Rb phase space density. The power referenced here is what is programmed into the synthesizer and does not include the gain of the amplifier or loss through various rf components (see Section 4.3).

Stage	f_{start} (MHz)	f_{stop} (MHz)	τ_{stage} (sec)	f_{base} (MHz)	rf power (dBm)
1	26.5	25	20	24.7	-27
2	25	24.73-24.8	15	24.7	-27

The results of sympathetic cooling in the weak magnetic trap are shown in Fig. 4.17. The figure is a compilation of three different data sets that demonstrate the two critical parameters of our system. The first set of data at the highest temperatures (filled circles and triangles) is an evaporation trajectory immediately following the decompression into the weak trap. The ^{85}Rb gas is cooled below 1 μK, but inelastic collisions are constantly removing atoms from the trap. We do not use the rf_2 shield yet so the heating rate is still large. Therefore much of the ^{87}Rb gas is evaporated. By 500 nK nearly all the ^{87}Rb number has been evaporated in order to reach that temperature, and cooling cannot continue.

Since we are constantly losing ^{85}Rb atoms to inelastic collisions there is no benefit to starting the evaporation (*i.e* the initial cooling in the tight trap) with a large number of ^{85}Rb atoms. To maximize the number of ^{85}Rb atoms at the end of evaporation we vary the number of that species loaded into the MOT. We have directly measured the final number of each species after evaporation (Fig. 4.18) to 600 nK as a function of the initial ^{85}Rb number. In this experiment the initial number of ^{87}Rb atoms was fixed. Interestingly the final ^{85}Rb number is unchanged as the ^{85}Rb MOT number varies by a factor of two. In contrast the ^{87}Rb number dramatically increases if there are fewer ^{85}Rb atoms to cool in the magnetic trap. There is a significant advantage to starting the evaporation with fewer ^{85}Rb atoms. The limitation to the trajectory with filled points in Fig. 4.17 is the large fraction of the ^{87}Rb cloud that is evaporated to reach only 500 nK. By starting the cooling with fewer ^{85}Rb atoms a lower temperature is reached. The trajectory with open data points in the Fig. 4.17 has an optimized initial ^{85}Rb MOT load allowing that gas to be cooled significantly closer to BEC without evaporating away the entire ^{87}Rb cloud.

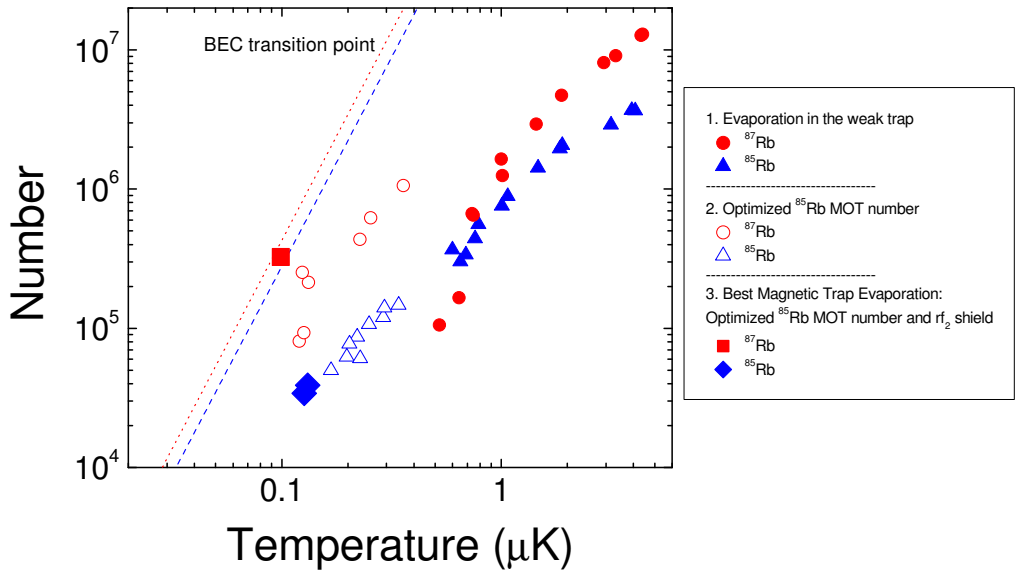

Figure 4.17: A compilation of three evaporation trajectories in the weak magnetic trap. (1) The filled data points are a continuation of the cooling from Figure 4.14 after decompression to the weak trap. (2) To reach even lower temperature (open data points) we optimized the initial number of ^{85}Rb atoms at the start of cooling. (3) The larger solid points represent our best results in the magnetic trap.

Based on the data in Fig. 4.18, we developed a physical picture to understand the results of evaporative cooling in our system. In order to create a ^{85}Rb BEC the peak phase-space density of the gas much reach 2.612. Therefore our goal is to evaporate the largest possible number of ^{85}Rb atoms to the corresponding temperature for BEC. Since we can cool ^{87}Rb with high efficiency, the final temperature achievable is only set by the heat load of ^{85}Rb. Here the heat load is a combination of the atom number plus any heating due to ^{85}Rb inelastic collisions. Therefore a colder temperature can be obtained by starting the evaporation with slightly less ^{85}Rb. Of course this assumes good thermal contact so that the two gases are in thermal equilibrium. The final number of ^{85}Rb atoms will depend on many factors including trap strength, the ^{87}Rb cooling rate, and ^{85}Rb inelastic rate constants but the key point is that sufficiently low temperature for condensation may be obtained.

In order to further improve the evaporation we used the rf_2 field to shield the ^{87}Rb gas from energetic ^{85}Rb atoms generated during inelastic collisions. This is the second critical parameter of our system. In conjunction with an optimized ^{85}Rb MOT number, the rf_2 shield improves the phase-space density after evaporation. The results with the rf shield are shown in Fig. 4.17 as the filled square and diamond points. The large diamond-shaped points with 30,000 ^{85}Rb atoms near 100 nK indicate the highest peak phase-space density (0.1) of ^{85}Rb achieved in the magnetic trap. This phase space density is a factor of 500 improvement over our best tight magnetic trap result. The transition temperature for ^{87}Rb is reached, but at this temperature we believe thermal contact between the two species is no longer adequate to establish thermal equilibrium due to gravitational sag. At the lowest rf-cuts we perform we still observe ^{87}Rb cooling but the ^{85}Rb temperature has stopped changing. The temperature at which cooling stops is roughly consistent with the known sag.

To be certain that only ^{85}Rb inelastic collisions are responsible for the poor evaporation, we have measured the lifetime of the ^{85}Rb gas with and without a ^{87}Rb gas present at a temperature of 0.9 μK. The results of this experiment are shown on a log-log plot in Figure 4.19. The initial number of atoms was slightly different since some ^{85}Rb loss occurred during the removal of ^{87}Rb. From the plot it is clear that the decay rate of the two data sets is the same, meaning that ^{85}Rb inelastic collisions are primarily the source of the observed atom loss from the trap.

In conclusion, we have sympathetically cooled a gas of 30,000 ^{85}Rb atoms to a peak phase-space density of 0.1 in our weak magnetic trap. The limitation of the sympathetic cooling is poor thermal contact with the ^{87}Rb cloud. Further improvements to the sympathetic cooling might be possible if thermal contact of the two species could be achieved. One possibility might be to use an optical dipole laser beam in conjunction with the weak magnetic trap in order reduce the relative gravitational sag of the two clouds. If such an arrangement could be implemented, in might be possible to tune the magnetic field at the center of the trap to the ^{85}Rb Feshbach resonance at 155 G. There the ^{85}Rb inelastic collision rate can be tuned in order to optimize the conditions for sympathetic cooling further.

4.6 Simultaneous evaporation of ^{85}Rb and ^{87}Rb

This section describes the simultaneous evaporation of ^{85}Rb and ^{87}Rb in an optical dipole trap to create a ^{85}Rb BEC. The evaporation of both species is performed

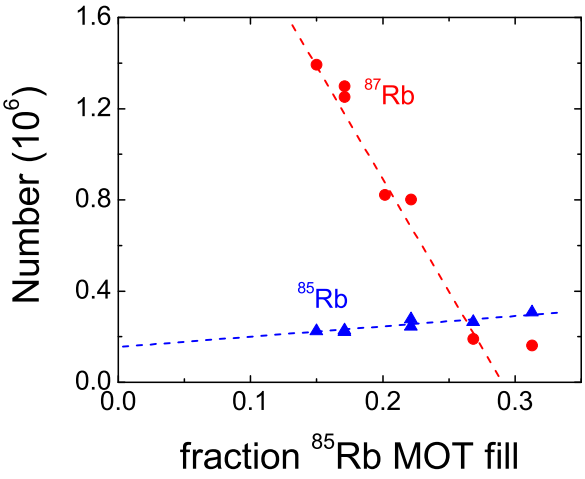

Figure 4.18: Dependence of the ^{85}Rb and ^{87}Rb atom number near the end of evaporation at 600 nK in the weak trap as a function of the number loaded into the ^{85}Rb MOT. The MOT number is changed by varying duration of the MOT fill time. Due to inelastic collisions, the final ^{85}Rb number is not very sensitive to the ^{85}Rb MOT number. In contrast the ^{87}Rb number is very sensitive to the ^{85}Rb MOT.

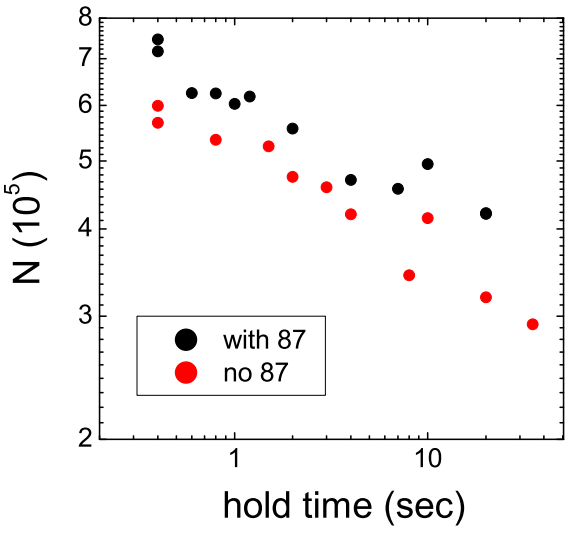

Figure 4.19: A comparison of the ^{85}Rb population decay as a function of time with and without ^{87}Rb present. Since the decay rate is roughly the same for the two cases we conclude that interspecies inelastic loss is negligible.

simultaneously since the depth of the trapping potential for the two species is nearly the same and it is not independently tunable. The work described in the later chapters of this thesis was performed with two different optical trapping setups: the "tight" trap with a 23 micron waist and the "weak" trap with a 46 micron waist. We note that the evaporation efficiency of ^{85}Rb is very different in the tight and weak traps. The differences will be described in the later sections of this chapter. To put these sections into context, we point out that the heteronuclear molecule work (Chapter 6) was performed with the tight trap in which cold enough gases could be obtained to make Feshbach molecules with ^{85}Rb and ^{87}Rb. The dual BEC work (Chapter 5) and the Bragg spectroscopy work (Chapter 7) were performed in the weak trap where evaporative cooling is more efficient and ^{85}Rb condensates can be produced.

After understanding the difficulties inherent in producing a ^{85}Rb condensate in the magnetic trap via sympathetic cooling, we switched to evaporation in an optical trap which has several advantages. The optical trap holds each species in the same location without significant relative gravitational sag of the two species. The depth of the optical trap during evaporation is held only slightly above the maximum energy of the gas. Therefore any hot atoms produced via density-dependent loss are naturally lost and the heating rate in the gas is significantly reduced. Another advantage is that simultaneous cooling in the optical trap is straightforward since the depth of the trap is nearly the same for both species. Finally, the biggest advantage is that any arbitrary magnetic field may be applied to the atoms while in the optical trap without changing the trapping potential significantly. This allows us to tune near the ^{85}Rb Feshbach resonance where we can suppress inelastic collisions and we can control the elastic collision cross section.

Our goal is to overcome the limits of evaporation that were encountered in the magnetic trap. To evaporate we simply lower the depth of the optical trapping potential on a timescale set by the rethermalization rate of the two-species gas. Since both species are cooled simultaneously the heat capacity of ^{87}Rb is no longer a limitation. As the depth is lowered by reducing the optical power, the trap frequencies are also reduced. The optical trap evaporation simultaneously lowers the temperature of the gas by removing the most energetic atoms and by decompression of the trap. A simple model was presented in Ref. [114] which includes both of these effects and agrees reasonably well with experiments. From our experience cooling in the magnetic trap, we can qualitatively understand the results in the optical trap without comparison to an evaporation model.

During our initial work in the tight optical trap (Section 4.6.1), our cooling routine resembles the routine that is used in the magnetic trap. Apart from the trapping potential there are only two fundamental changes. First, since both species are simultaneously evaporated, we begin the cooling with roughly equal atom numbers. Second, the ^{85}Rb Feshbach resonance is used to minimize inelastic collisions as much as possible. With that setting the ^{85}Rb elastic collision cross section is small. Therefore during the cooling, the ^{85}Rb gas primarily rethermalizes via collisions with the ^{87}Rb gas. This is feasible since the cross section for interspecies elastic collisions is large.[7] In fact, assuming that the number of particles in each gas is the same and the trapping potential is identical for both species, the timescale for rethermalization of the two-species gas is

[7] The interspecies scattering length is approximately 213 a_0. The rate of inelastic ^{85}Rb -^{87}Rb collisions is expected to be small and we have verified this fact experimentally (see below).

limited by the rate of ^{87}Rb collisions. During the simultaneous evaporation each trapped ^{85}Rb atom should behave very much like a ^{87}Rb atom since we purposely suppressed ^{85}Rb collisions. Therefore the cooling routine during the simultaneous evaporation in the tight optical trap is optimized for the ^{87}Rb gas.

Unfortunately the ^{85}Rb evaporation in the tight optical trap is not efficient enough to produce BEC. But from our experience with the tight trap, we were able a gain insights into the best procedures for cooling ^{85}Rb. In particular, we learned that ^{85}Rb inelastic collisions still preclude the formation of a ^{85}Rb BEC. We have applied this knowledge to cooling in a weaker optical trap (Section 4.6.2) where the density of the gases can be lower. In this weak trap we are able to cool the ^{85}Rb gas with a high enough efficiency to create a condensate for the first time. Soon after making our first ^{85}Rb BEC, we discovered that the shape and atom number of the condensed ^{85}Rb gas depends sensitively on the co-existence of a ^{87}Rb condensate in the optical trap. This is because the two quantum fluids are immiscible (they spatially separate) under the typical conditions of our experiments; see Chapter 5 for more details. Fluctuations in the shape of the ^{85}Rb condensate cause a significant experimental uncertainty in density of the gas. In order to perform meaningful experiments with a single-species ^{85}Rb condensate, we modified the cooling routine in the weak optical trap to suppress the formation of a ^{87}Rb BEC. We now use an improved evaporation routine that not only produces a ^{85}Rb BEC, but the new routine also suppresses the ^{87}Rb atom number by making the evaporation inefficient for that species.

4.6.1 Evaporation in the tight optical trap

Simultaneous cooling of ^{85}Rb and ^{87}Rb in the tight optical trap is performed in much the same way as the single-species ^{87}Rb optical trap evaporation described in Section 4.4.2. After evaporative cooling in the tight magnetic trap to approximately 9 μK the atoms are loaded into the optical trap following the procedure outlined in Section 2.7. The optical trap power is decreased in several stages using the ramps listed in Table 4.3. After the optical trap is loaded we ramp the bias-coil current in 100 ms to provide a magnetic-field near 168.8 G, where $a \approx -100\,a_0$. The optical trap evaporation is initiated during this ramp of the magnetic field. The efficiency of the ^{85}Rb evaporation depends strongly on magnetic field as expected. To optimize the evaporation, the total number of ^{85}Rb atoms after cooling is measured as a function of the magnetic field; the results are shown in Figure 4.20. For this data we cooled until a ^{87}Rb condensate with $T/T_c = 0.75$ was formed. The temperature of the ^{85}Rb gas was 110 nK and $T/T_c \sim 2.5$. The best results are obtained near 168.8 G where the ^{85}Rb scattering length is $a \approx -90\,a_0$, suggesting that the minimum of inelastic losses does not coincide with the exact point that $a = 0$.[8] Anywhere near the peak of the Feshbach resonance and above 185 G the entire ^{85}Rb gas is lost before 110 nK is reached. Unfortunately we were not able to form a ^{85}Rb condensate in this trap even though we could access the Feshbach resonance.

We characterized the optical trap cooling by recording an evaporation trajectory;

[8] In fact we have repeatedly determined that simultaneous cooling with ^{87}Rb works best near 168.8 G. Later in this section we present evidence that the elastic cross section is minimized at 165.7 G as expected. This effect has been previously observed in the measurements of ^{85}Rb inelastic loss presented in Ref. [6].

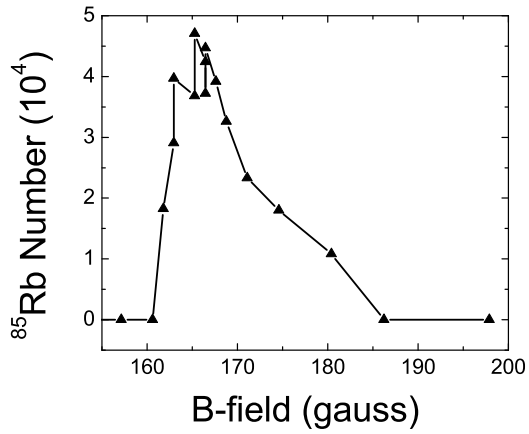

Figure 4.20: Number of ^{85}Rb atoms after evaporation to 110 nK as a function of magnetic field. The peak of the ^{85}Rb Feshbach resonance is 155 G where inelastic losses are expected to be severe. Near 166 G both elastic and inelastic collisions are suppressed and we expect the best evaporation performance.

the data are shown in Figure 4.21 (a). The calculated phase space density of each gas is shown in Fig. 4.21 (b). Following the same color coding used previously the black points are ^{85}Rb, the red open triangles are ^{87}Rb while cooling ^{85}Rb, and the green points are single-species ^{87}Rb cooling shown for comparison. There are several interesting aspects to the data. Using the single-species ^{87}Rb trajectory as a guide, at the beginning of evaporation we observe good cooling efficiency for both ^{85}Rb and ^{87}Rb, and it continues well below 1 μK. Near 300 nK a rapid decline in the ^{85}Rb number begins and the phase space density does not exceed a value of 0.1. As the cooling begins to fail, the average density is approximately 10^{12} cm^{-3} and the poor evaporation performance is consistent with our observations in the magnetic trap where inelastic loss was the limitation. The measured lifetime of the ^{85}Rb gas at 300 nK is less than the time required to cool, a clear indication that the efficiency will be poor. At this temperature we systematically varied both the evaporation rate and the magnetic field in search of better performance, but we were not able to find a more favorable combination. Since the gas is still far from the BEC transition temperature, condensate formation and subsequent collapse due to the negative scattering length is not the problem.

Since the optical trap evaporation starts at such a low temperature, in principle we have the ability to directly cool ^{85}Rb without any ^{87}Rb present. As a last-ditch effort to produce a ^{85}Rb BEC in the tight optical trap we attempted single-species ^{85}Rb evaporation. This experiment is also a nice check on our understanding of number loss during evaporation, as we can test that interspecies inelastic collisions are unimportant. The cooling was optimized by varying both the ramp rates and the magnetic field independently. The first step was to locate a favorable range of magnetic field to perform the cooling. Since there is no ^{87}Rb gas to rely on, the ^{85}Rb scattering length was set to provide a large elastic cross section. In Figure 4.22 the measured number and temperature after running the evaporation to a fixed cut are shown as a function of magnetic field. For each point we used the same cooling ramps so that the data roughly indicate the difference in collision properties. Near 166 G the temperature of the gas is high since a low elastic cross section inhibits cooling. Another consequence of the higher temperature at 166 G is that fewer atoms fit in the trap. There is a small range on either side of 166 G where the evaporation works reasonably well, but closer to the peak of the Feshbach resonance and above 170 G the cooling is less efficient. This data is a coarse measurement of the elastic collision rate. The points with largest temperature give an estimate of 165.7 G for the magnetic field where $a = 0$, which is in good agreement with the precise determination of 165.75 G found in Ref. [5].

After optimization of the entire single-species evaporation trajectory, we found that our largest peak phase space density was a factor of two smaller than that achieved using simultaneous cooling of ^{85}Rb and ^{87}Rb. Even though the cooling is not quite as efficient, we were encouraged that a further reduction in the optical trap strength might finally provide the conditions to make BEC. We also confirmed that interspecies inelastic collisions do not hinder the efficiency of evaporation.

4.6.2 Creation of ^{85}Rb BEC in the weak optical trap

In this section we describe evaporative cooling in the weak optical trap, in which we are able to produce either a single species ^{85}Rb or ^{87}Rb condensate or a dual BEC of both species. To control what species remain in the optical trap after evaporation,

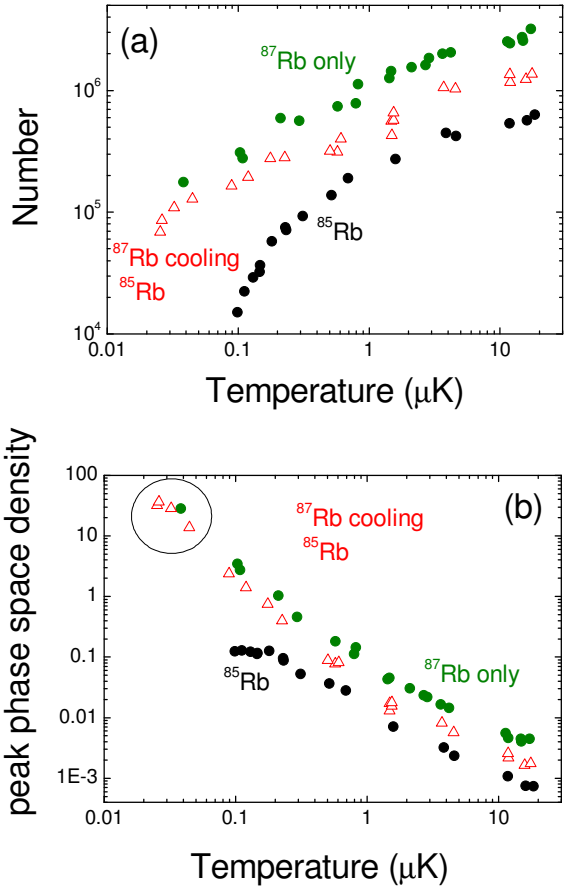

Figure 4.21: (a) Evaporation trajectory in the tight optical trap demonstrating our best results. (b) Peak phase space density at the center of the trap calculated from the number and temperature during evaporation. The ^{85}Rb cooling saturates at a phase space density of 0.1, which is less than the requirement for BEC. Note that the circled points are for condensates and the phase space density is not known very accurately.

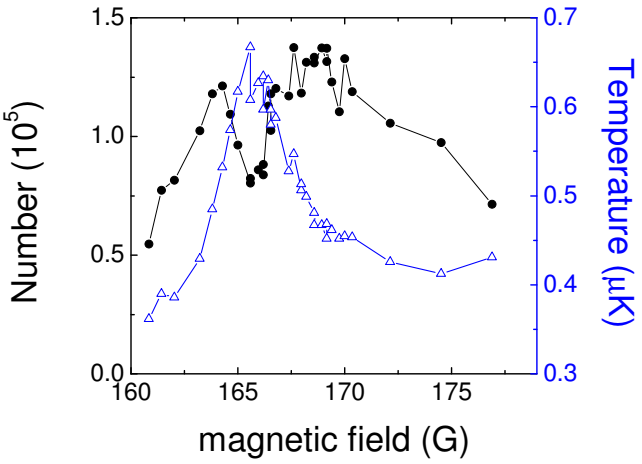

Figure 4.22: The number (black, left side) and temperature (blue, right side) as a function of magnetic field during single-species ^{85}Rb evaporative cooling. The elastic cross section is minimized near 165.7 G and evaporation is inefficient.

we vary the relative number of each species in the MOT. The evaporation in the weak optical trap is quite successful. Condensates with up to 80,000 ^{85}Rb atoms are routinely created under the best conditions. This represents a significant improvement over the previous record of 17,000 [6, 58]. The production of ^{85}Rb BEC is robust; for example we can tolerate significant loss of number in either species' MOT and still make condensates. The production of condensates is also stable, with atom number reproducibility of 10%. We note that this level of stability is inferior to the previous Wieman group ^{85}Rb apparatus [6, 58].

In order to achieve this ^{85}Rb evaporation performance, two critical changes have been made to our system. First, we lowered the confinement of the trapped gas by increasing the waist of the optical trapping beam by a factor of two. This was done to maintain a low density during evaporation. In this new optical trap a ^{85}Rb condensate can be produced by simultaneously cooling the two-species gas. During the cooling the magnetic field was tuned to 168.8 G where ^{85}Rb collisions are minimized and the optical trap power ramps were optimized for the best ^{87}Rb evaporation. The presence of a ^{87}Rb condensate in the optical trap distorts the ^{85}Rb condensate so much that the ^{85}Rb condensate is not usable for some of our experiments (*i.e.* Bragg spectroscopy). We can minimize the number of ^{87}Rb atoms at the end of evaporation by starting with the appropriate relative numbers of ^{85}Rb and ^{87}Rb in the MOT. However, as we have already discussed the ^{87}Rb number after the cooling is extremely sensitive to the relative number in the MOT. Although the shot-to-shot stability of the relative MOT number in our system is less than 1%. This is not stable enough to guarantee a ^{87}Rb condensate does not form. Therefore, the second critical change to our system was a new evaporation routine that suppresses ^{87}Rb atom number near the end of the cooling. In the new routine the ^{87}Rb cooling efficiency at the end of evaporation is low and severe ^{87}Rb number loss occurs. This has the effect of dramatically reducing ^{85}Rb condensate fluctuations. Only the combination of these two critical changes has allowed us to robustly produce ^{85}Rb condensates with larger atom number.

4.6.2.1 A weak optical trap

We have experimentally verified the performance of the weak optical trap setup by performing single species ^{87}Rb evaporative cooling. Evaporation of ^{87}Rb in the weak trap is very similar to what is described in the previous section, except the optical power ramps were optimized to slightly different values. We can produce single-species ^{87}Rb condensates with two million atoms, but since the trap is so weak the duration of the cooling is close to 30 seconds. Evaporation can still be efficient despite the long time required since the heating rate in the weak trap is very low. The measured heating rate in our trap is 1 nK/sec. Inelastic number losses are also minimized due to the low density. The average density of a gas with 10^5 atoms at the transition temperature is 10^{12} cm^{-3}. For comparison, in the tight magnetic trap with a radial (axial) frequency of 215 Hz the density is approximately five times larger.

We have performed simultaneous cooling of ^{85}Rb and ^{87}Rb in the weak optical trap using optical trap power ramps that were optimized for single-species ^{87}Rb cooling; the ramps are documented in Section 4.4.2. By taking advantage of the low densities offered in the weak optical trap and by tuning the magnetic field to 168.8 G where ^{85}Rb inelastic collisions are minimized, we were able to observe our first ^{85}Rb condensates. In

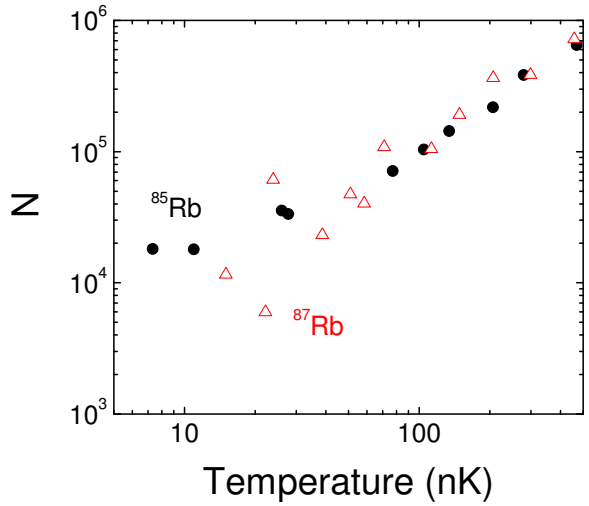

Figure 4.23: Our first evaporation trajectory that makes a single-species ^{85}Rb BEC. The key to efficient cooling was very weak confinement to reduce losses. Near the end of evaporation the ^{87}Rb number fluctuates wildly shot-to-shot causing large instability in the ^{85}Rb condensate shape and density. This makes quantitative measurements such as Bragg spectroscopy with the ^{85}Rb BEC impossible.

our experiments, just prior to the formation of a condensate we ramp the magnetic field to 164.4 G so that the scattering length was $60\,a_0$. With a positive scattering length, interactions in the condensate are repulsive and collapse does not occur. In order to acquire an absorption image of the condensate we expand from the optical trap. The magnetic field remains on for the first 10 ms of the expansion to keep the condensate from collapsing due to the negative scattering length when the magnetic-field is switched off.

For many experiments we desire a BEC of only ^{85}Rb atoms. The presence of even a small ^{87}Rb condensate distorts the shape and atom number in the ^{85}Rb gas so dramatically that measurements cannot be performed. We have studied the evaporation in the weak optical trap (Fig. 4.23) to understand the optimal conditions with which to make pure ^{85}Rb condensates. Until the the vary end of evaporation when the magnetic field is ramped to 164.4 G, rethermalization of the ^{85}Rb gas occurs primarily due to collisions with ^{87}Rb. Therefore the evaporation routine used to obtain the trajectory shown in Fig. 4.23 is optimized to obtain the best results for ^{87}Rb. The trajectory in the figure demonstrates the creation of a pure ^{85}Rb condensate. To create this quantum gas we optimized the relative number of atoms in the MOT so that the ^{87}Rb gas was mostly evaporated away. In order to reliably create a ^{85}Rb condensate in this way the MOT number must be stable to better than 0.5% on every run of the experiment. When our apparatus is well optimized the stability reaches that level, but obtaining a significant amount of data under this stability requirement is challenging. The observed stability of the MOT number is typically only slightly better than 1%.

MOT number stability of 0.5% is required because number of ^{87}Rb atoms at the end of the cooling is very sensitive to the relative number of ^{85}Rb and ^{87}Rb in the MOT. The sensitivity results from that fact that the ^{87}Rb gas acts as a coolant throughout the evaporation; more ^{87}Rb atoms are consumed during evaporation when the ^{85}Rb atom number in the MOT is increased. Figure 4.24 shows the steep dependence of the ^{87}Rb number after cooling on the ^{85}Rb MOT number. To inhibit the formation of a ^{87}Rb condensate, we choose the ^{85}Rb MOT number to suppress the *final* ^{87}Rb number. However, the ^{85}Rb MOT number cannot be too large or else a low enough final temperature is not reached. In order to produce single-species ^{85}Rb condensates using the routine described in this section, shot-to-shot fluctuations in the MOT number must be smaller than 0.5%. In the next section we describe a new evaporation routine that relaxes the MOT number stability requirements to reliably make ^{85}Rb condensates.

4.6.2.2 Achieving reproducible evaporation performance

We have developed a new evaporation routine that suppresses the formation of a ^{87}Rb BEC. The ^{85}Rb Feshbach resonance is used to make the optimal rates of the two-species evaporation significantly different. By evaporating at a rate that is unfavorable for the ^{87}Rb gas, we suppress the final number of that species. First we present a physical picture of the cooling procedure. Later on in this section the experimental details of the cooling routine are documented and our most efficient ^{85}Rb evaporation results are presented.

The timings of the evaporation optical power ramps described in the previous section have been modified in order to make ^{87}Rb cooling *inefficient* so that a large fraction of that gas is lost. We simultaneously cool a gas of ^{85}Rb and ^{87}Rb with roughly

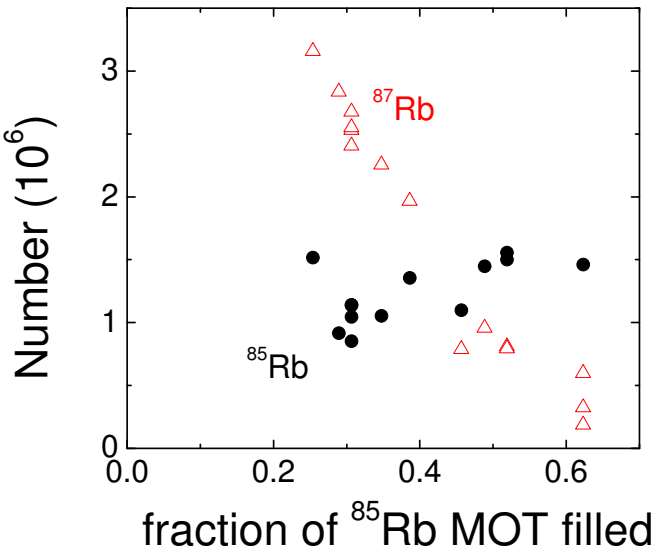

Figure 4.24: Dependence of the ^{85}Rb and ^{87}Rb atom number at 900 nK in the weak optical trap as a function of the number loaded into the ^{85}Rb MOT. The MOT number is changed by varying duration of the MOT fill time. These data are very similar to what we observe in the magnetic trap (for example see Figure 4.18).

Table 4.5: Evaporation parameters used for the weak optical trap. There are six stages in the weak trap evaporation each with an initial power, final power and ramp rate. Powers here are listed as the control voltage entered into the control computer, the calibration is roughly 1.2 W / 1.7 V. The parameter t_{end} is the end time of each stage measured from the start of evaporation. Listed in the last two columns are the calculated trap frequencies at the end of each stage.

Stage	P_{start} (V)	P_{stop} (V)	rate (V/sec)	t_{end} (sec)	ν_{radial} (Hz)	ν_{axial} (Hz)
1	1.7	0.7	1	1	1900	3
2	0.7	0.35	0.1	4.5	780	3
3	0.35	0.2	0.06	7	451	3
4	0.2	0.15	0.014285	10.5	~ 200	~ 2.9
5	0.15	0.11	0.025	12.1	~ 150	~ 2.9
6	0.11	0.100 - 0.107	0.014285	12.52	~ 100	~ 2.9

equal number to 250 nK. At this temperature, the magnetic field is ramped from 168.8 G to 163.05 G which changes the scattering length from approximately -85 a_0 to 150 a_0. At the lower magnetic field the ^{85}Rb elastic collision cross section is approximately a factor of three larger. Therefore the timescale for rethermalization of the ^{85}Rb gas is shorter. Slightly after the field ramp, we speed up the evaporation rate in the optical trap to a value that is optimized with respect to the efficiency of ^{85}Rb cooling. Since the ^{87}Rb elastic cross section has the same value at 169 G and 163 G, that gas does not rethermalize fast enough and a significant loss of atoms from the trap occurs. This preferential loss of ^{87}Rb atoms suppresses the formation of a ^{87}Rb condensate, and the final number of ^{85}Rb atoms is larger than the final of ^{87}Rb atoms by a factor of 5-10. In fact, using our new routine the final ^{85}Rb number can be as large as 80,000.

The suppression of final ^{87}Rb number moderates our sensitivity to the relative number of ^{85}Rb and ^{87}Rb atoms in the MOT. This fact represents an important feature of our new routine. With this new evaporation routine the required stability of the MOT number is 4%, which is much better than the previous requirement of 0.5%. The 4% requirement is well within the capabilities of our system.

Table 4.5 lists the parameters of the weak optical trap power ramps that are used in our new cooling routine. The evaporation is broken into a series of consecutive stages; each stage lowers the temperature of the gas by approximately a factor of two. In each stage the power decreases linearly as a function of time. Unlike all the other sets of optical trap power ramps described in this chapter, this one is *not* optimized for the best ^{87}Rb performance. A plot of the ramps is shown in Figure 4.5 (a) and (b) shows the time derivative of the ramps, which is related to the cooling rate of the gas. The increase in cooling rate occurs at 10.5 seconds when the temperature of the gas in the optical trap is 250 nK. The first three stages of evaporation are similar to what was used in the tight optical trap except the cooling rate is slower. The magnetic-field is set to 168.8 G so that the ^{85}Rb inelastic losses are minimized. Before the end of the fourth stage, we ramp the scattering length to 150 a_0 in 500 ms by changing the field to 163.05 G. The fifth (sixth) stage of evaporation is then performed a factor of five

(three) faster than optimum for ^{87}Rb. The parameters of the evaporation ramps listed in Table 4.5 are optimized to produce the largest number of ^{85}Rb atoms at the end of the cooling. To optimize the evaporation ramp rates, we varied the rates and recorded the number of ^{85}Rb atoms after the cooling. The total time of the two stages is about 1.5 seconds. The measured lifetime of a ^{85}Rb condensate is about 3 seconds, which is a little bit longer than the formation time. After the cooling ends, we linearly increase the depth of the optical trap from the final cut to 1 μK in a fixed time of 50 ms.

The value of the magnetic-field during the evaporation has also been optimized. Of course the optimum value of this field depends on the temperature of the gas. During the first few weak optical trap stages, the field must be set to 168.8 G to minimize inelastic collisions. We have systematically optimized the evaporation ramps during the first few stages of the cooling for different values of the ^{85}Rb scattering length; the data are shown in Fig. 4.26. As we had demonstrated previously (Fig. 4.20), the best performance occurs when the scattering length is set near -85 a_0. During the final few stages of evaporation, the magnetic field is tuned to 163.05 G to produce ^{85}Rb condensates with the largest atom number. We studied the range of magnetic fields suitable for the final evaporation stages and we determined that the field must be within $\pm$0.5 G of the optimum value.

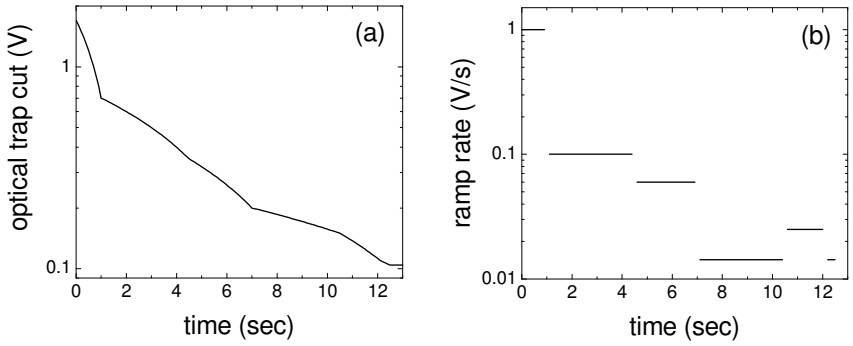

Figure 4.25: (a) Log plot of the optical trap power as a function of time during evaporative cooling to make ^{85}Rb BEC. (b) The cooling rate during evaporation which is related to the time derivative of (a). The increase in cooling rate at the end of evaporation is used to suppress the final ^{87}Rb atom number in the trap. When the ^{87}Rb number is suppressed a pure ^{85}Rb condensate can be repeatedly created over consecutive runs of the apparatus.

We have developed an understanding of how the final ^{87}Rb atom number depends on the relative number of ^{85}Rb and ^{87}Rb atoms in the MOT. In particular, a procedure has been developed to lower the final ^{87}Rb number sensitivity to the relative MOT number. For each run of the apparatus the loading time of the ^{87}Rb MOT is the same. The optimum value of the relative atom number in the two species MOT is determined by varying the ^{85}Rb MOT loading time and observing the number of atoms in each species after the cooling. Our goal is to produce a ^{85}Rb BEC and a small non-condensed

gas of ^{87}Rb. The minimum value of the ^{85}Rb MOT loading time is set by the initial ^{85}Rb number required to suppress the final ^{87}Rb atom number. In contrast, the ^{85}Rb MOT number cannot be too large or else a low enough final temperature will not be reached. By studying the evaporation performance at the very end of the cooling, we found a dependence between the lowest optical trap power of the evaporation (the final cut) and the final ^{87}Rb sensitivity to the relative MOT number. Our measurements showed that the ^{87}Rb final number suppression can be enhanced (*i.e* less ^{87}Rb atoms) by the combination of an *increased* ^{85}Rb MOT number and a *lowered* final cut. We note that the number of atoms in the ^{85}Rb condensate tends to be smaller.

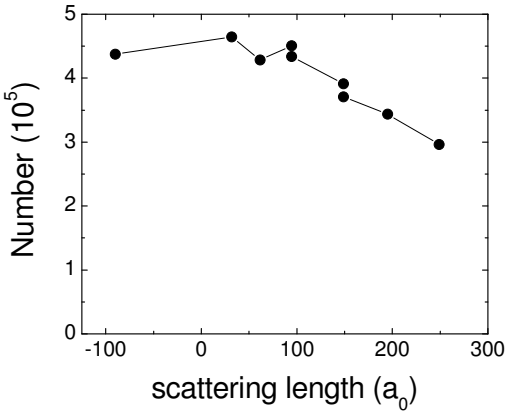

Figure 4.26: The optimized number of ^{85}Rb atoms cooled in the optical trap as a function of the scattering length. Each point represents a separate optimization of the evaporation ramps for a different value of a. The gas was cooled to a temperature of 200 nK. While performance may not appear to vary significantly the temperature must be lowered by another factor of five so that a small advantage here is more important at lower temperature.

Figure 4.27 shows an evaporation trajectory typical of our current experimental setup. To obtain these data the evaporation was performed using the optical trap power ramps of Table 4.5. For these data the initial number ratio in the two-species MOT was set to reproducibly create a ^{85}Rb condensate with 60,000 atoms and a non-condensed ^{87}Rb gas with approximately 10,000 atoms. In the weak optical trap we actually begin with a slightly larger number of ^{85}Rb than ^{87}Rb; this helps suppress the ^{87}Rb number after cooling. At the start of evaporation the efficiency for both species is roughly the same and equal numbers from each gas are evaporated. If this trend were to continue, we would end up with a dual BEC. But as the temperature of the gas reaches 250 nK, which is equivalent to $T/T_c \approx 1.5$ for ^{85}Rb, the cooling rate is increased and the steep loss of ^{87}Rb begins. Since the ^{87}Rb number is low at the end of the cooling, small fluctuations are much less likely to cause random ^{87}Rb condensate formation. The results here with a suppressed final ^{87}Rb number should be compared against the

results shown in Fig. 4.23 where the ^{87}Rb fluctuated wildly at the end of the cooling. By varying the relative number in the two-species MOT, we have measured that the stability of the MOT number must be better than 4%, *i.e* fluctuations larger than 4% cause random shot-to-shot condensate formation.

We lack a detailed theoretical model to completely understand the cooling process at the end of the evaporation routine. It is likely that the different gravitational sag of the two species plays a role in the final stages of evaporation. Since ^{87}Rb is slightly heavier it tends to spend more time near the evaporation surface at the lower lip of the optical trap potential in the direction parallel to gravity. There may also be a non-negligible mean-field repulsion between the two species which leads to a preferential loss of ^{87}Rb from the optical trap. Given the scattering lengths in our system a two-species superfluid is immiscible and tends to spatially separate (see Chapter 5). Spatial separation of the two species might explain some suppression of the final ^{87}Rb number but, we have not been able to systematically study this possibility since reproducibility in the experiment is poor.

It may be possible to further improve the production of ^{85}Rb condensates via evaporation in our system. Possible improvements include an increase in the ^{85}Rb final number and an enhanced suppression of the ^{87}Rb number. Condensates of ^{87}Rb with two million atoms can be made with our system, but to date we have been limited to ^{85}Rb condensate with at most 80,000 atoms due to inelastic collisions. Performing the optical trap evaporation in a still weaker trap might increase the final number of atoms in the ^{85}Rb condensate.[9] It may be possible to further suppress the final ^{87}Rb number by utilizing either resonant light or resonant radio-frequencies. Since the atoms are primarily confined in the axial direction of the weak optical trap by the curvature of the ~ 160 G magnetic field, only magnetically trapable spin states are confined. By driving rf transitions ^{87}Rb atoms may be removed from the trap. One complication of this technique is that the atoms exit the trap in only the axial direction. Therefore they can collide with trapped atoms and heat up the trapped gas.[10]

4.7 Chapter conclusion

In this chapter we described the evaporative cooling routine that is used to produce a ^{85}Rb BEC. Our system is also capable of robustly producing a ^{87}Rb condensate as well as a dual BEC of the two species. Evaporation begins in a magnetic trap where sympathetic cooling of ^{85}Rb is performed using the ^{87}Rb gas as a coolant. We have thoroughly investigated the limitations of ^{85}Rb sympathetic cooling in the magnetic trap. The limitations include the finite heat capacity of the ^{85}Rb gas and inelastic collisions between ^{85}Rb atoms. In the magnetic trap these ^{85}Rb inelastic collisions have so far limited the maximum obtainable phase space density to a value of 0.1, a factor of 25 smaller than that required for BEC. In the magnetic trap it might be possible

[9] We tried an optical trap with an 83 μm waist, but single species evaporation of ^{87}Rb was not efficient since only a fraction of the atoms from the magnetic trap could be transferred into this weak optical trap.

[10] We have observed a slight decrease in the final ^{87}Rb number by using a fixed frequency resonant with atoms near the bottom of the trap. The time during evaporation at which the rf drive is applied is critical; the ^{87}Rb atoms cannot be removed prematurely or else a low enough final temperature is not reached. The optimum time was determined to be at the end of stage 5. It is likely that sweeping the frequency from the edge of the gas inward toward the center may provide better results.

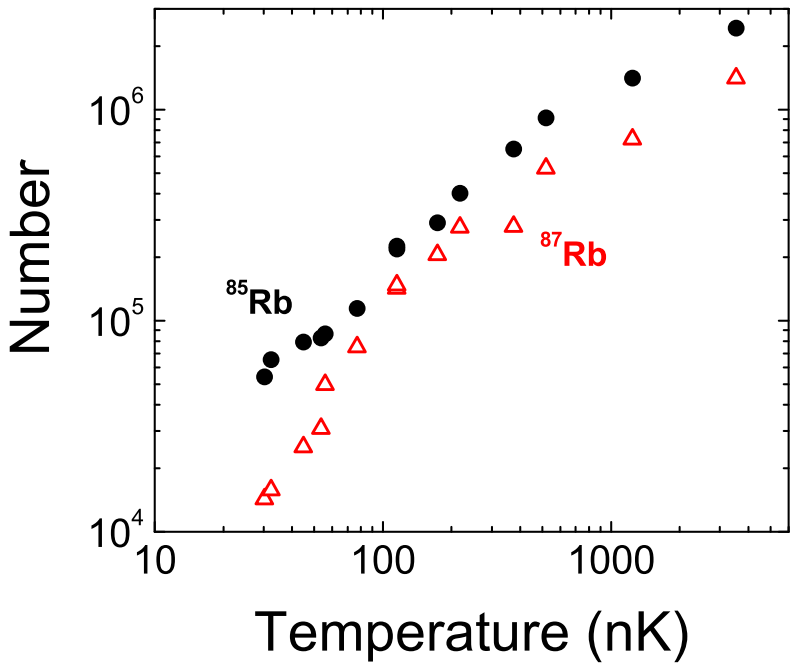

Figure 4.27: Evaporation trajectory in the weak optical trap to create a pure BEC of ^{85}Rb with a large number of atoms. In these data the temperature is always determined from the ^{87}Rb gas since it does not form a condensate. The final ^{85}Rb number is small enough that if a small fluctuation in the number ratio at the start of cooling occurs it is unlikely to lead to ^{87}Rb BEC.

to improve the ^{85}Rb sympathetic cooling efficiency if the field at the center of the trap can be tuned to the ^{85}Rb Feshbach resonance. But some method must be found to compensate for the relative gravitational sag of the two gases.

In order to create a ^{85}Rb condensate in our system, we pre-cool a two-species gas in the magnetic trap. Those atoms are then loaded in an optical trap for further cooling. In the optical trap an arbitrary magnetic field may be applied in order to control ^{85}Rb elastic and inelastic collisions. We are able to produce ^{85}Rb condensate with up to 80,000 atoms and this represents a factor of five increase in performance over the previous best results [6, 58]. This work opens the door to a variety of new experiments. In particular, we now have access to a condensate in which the interactions may be tuned over a very wide range. By tuning the magnetic-field at the center of the optical trap toward the peak of the Feshbach resonance the strongly interacting regime may be reached.

Chapter 5

Tunable spatial separation in a two-species BEC

5.1 Introduction

Two-component quantum fluids have long been known to exhibit rich physics as a consequence of access to new parameter regimes [115]. The miscibility of two quantum fluids represents a fundamental property of a two-component system and is partially controlled by interparticle interactions. Building on the achievement of dilute-gas Bose-Einstein condensation [23], mixtures of ultracold quantum gases provide a unique system for the study of interacting quantum fluids. Moreover resonant control of two-body interactions in ultracold gases is possible via magnetic-field Feshbach resonances [56] and provides a parameter which directly alters the miscibility of the dual-species BEC.

The first two-component condensate was produced with different hyperfine states of ^{87}Rb, and evidence for repulsive interspecies interactions was reported [106]. Further work with different hyperfine states of ^{87}Rb studied the dynamics of interpenetrating quantum fluids [116]. In spinor condensates of Na both miscible and immiscible two-component condensates were observed for the first time [117]. More recently a dual-species BEC of ^{41}K and ^{87}Rb was reported in Ref. [118] where scissors-like collective oscillations were observed as a result of off-axis collisions. Two-component quantum gases have long been the subject of significant theoretical interest; topics of study include the density pattern and phase separation of the components [119, 120, 121, 122, 123, 124] and the spectrum of collective excitations [125, 126]. Spatial separation of two immiscible quantum fluids in a trap is typified by a ball-and-shell structure [119] in which one fluid forms a low density shell around the other and it depends on the relative strength of interspecies and single-species interactions. Other structures are expected as well and a general classification of all possible spatial structures has been presented in Ref. [127].

A mixture of ^{85}Rb and ^{87}Rb has long been considered a promising system for studying the miscibility of quantum fluids and a route to dual-species BEC with ^{85}Rb –^{87}Rb was proposed in Ref. [13]. Applying the analysis of Refs. [128, 129], in which the Thomas-Fermi limit is utilized, to the case of a ^{85}Rb –^{87}Rb mixture, we define $\Delta = u_{85}\, u_{87} - u_{85-87}^2$ where $u_i = \frac{4\,\pi\,\hbar^2\,a_i}{m_i}$ and m_i is the mass. In the case where a_{85-87} is always positive two regimes emerge: one with $\Delta > 0$ in which the two condensates can overlap in space and one with $\Delta < 0$ in which overlap is restricted due to the strong interspecies repulsion. Since the masses of ^{85}Rb and ^{87}Rb are nearly identical the parameter Δ can be re-scaled to depend only on the three scattering lengths in the

system

$$\Delta' \equiv \frac{\Delta}{u_{85-87}^2} = \frac{a_{85}\, a_{87}}{a_{85-87}^2} - 1; \tag{5.1}$$

the quantity Δ' compares the strength of single-species and interspecies interactions. Finally we note that gravitational sag is predicted to cause nontrivial modifications to the expected ball-and-shell structures [128].

In this chapter I focus on experiments with a dual-species BEC of ^{85}Rb and ^{87}Rb near the ^{85}Rb Feshbach resonance, where the ^{85}Rb interaction can be tuned. Immiscibility of the two-component quantum gas was observed as a dramatic departure in the gas density distribution from that expected due to the observed symmetry of the potential. The shape and size of the gases depended on the influence of gravitational sag and the external trapping potential. Surprisingly we observed the robust formation of multiple, non-overlapped, single-species "cloudlets". Furthermore we found that the degree of spatial separation between the two species can be controlled with a tunable ^{85}Rb scattering length. This information will be important for further studies of this rich dual-species system with widely tunable single-species and interspecies interactions.

5.2 Spatial separation measurements

The work in this chapter was performed after our success in creating ^{85}Rb and ^{87}Rb dual-species BEC as described in Ch. 4. By precisely controlling the evaporation rate and the number ratio of the two species at the start of evaporation, we are able to create in our optical trap a single species ^{87}Rb BEC with 3×10^6 atoms, a ^{85}Rb BEC with up to 8×10^4 atoms, or a BEC of both species. Unless otherwise noted, for this work, after evaporation the depth of the optical trap is raised in 50 ms to approximately 1 μK with a measured ^{85}Rb radial (axial) trap frequency of $2\pi \times 130$ Hz ($2\pi \times 2.9$ Hz). While the ^{87}Rb radial frequency is nearly the same, the axial frequency that is $2\pi \times 2.6$ Hz is smaller due to a different magnetic moment. In the entirety of this work the interspecies scattering length is +213(7) a_0 [103] and the ^{87}Rb scattering length is +99 a_0 [130].

One way in which we can demonstrate the different dual-species density patterns that are observed is by varying the number of particles in each Rb species. Figure 6.3 shows absorption images of both ^{85}Rb and ^{87}Rb condensates immediately after evaporation without recompression of the optical trap. The ^{85}Rb scattering length was set to 81 a_0 with $\Delta' = -0.82$. Prior to imaging, the gas is released from the optical trap and expands for 20 ms; the magnetic field remains on for the first 10 ms of expansion to prevent collapse of the ^{85}Rb gas [8, 9]. In each image a different condensate is shown since the measurement process is destructive. The elongated axial direction of the images is interpreted as the spatial density of the gas since the trapping frequency is small; the radial direction is interpreted as the momentum density.

When a condensate of each species is present in the trap we observe"holes" in the ^{87}Rb image that correspond to "spikes" at approximately the same location in the ^{85}Rb image (Fig. 6.3 (a)-(d)). This behavior is consistent with spatial separation of two immiscible quantum fluids since the density distributions no longer display the symmetry of the trapping potential. However the images are not consistent with a typical ball-and-shell phase-separation structure. Surprisingly, the ^{85}Rb gas is observed to split into multiple separated cloudlets that appear as distinct holes in the ^{87}Rb gas. In

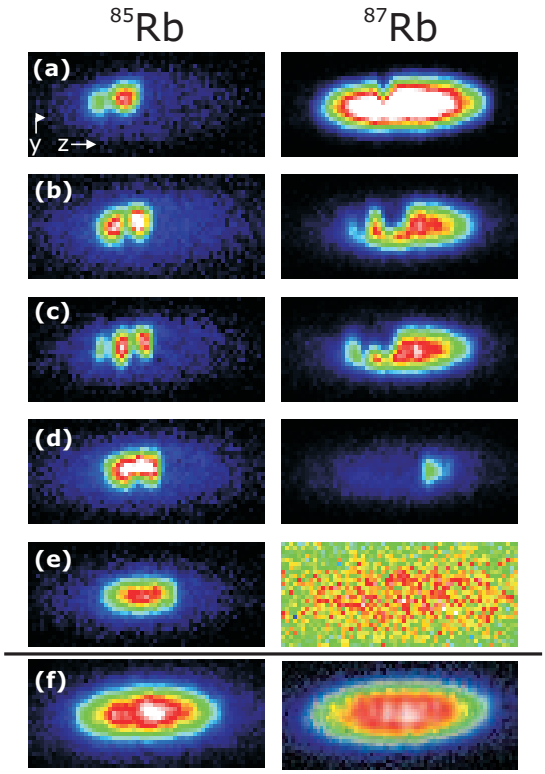

Figure 5.1: Absorption images of ^{85}Rb (left column) and ^{87}Rb (right column) condensates demonstrating the immiscibility of the quantum gases. For clarity the intensity of each ^{87}Rb image was scaled by a factor of 0.5. The size of each image is 330 μm $\times$ 150 μm. The number of ^{85}Rb particles varies from approximately 12,000 in (a) to 22,000 in (e); the ^{87}Rb number varies from 140,000 in (a) to 3,000 in (e). Since the trap frequency in the elongated axis is low this direction of the image is interpreted as the spatial density of the gas. For comparison (f) shows single-species condensates.

Fig. 6.3 (a) and (b) two ^{85}Rb cloudlets are observed, and three cloudlets are observed in image (c). If the initial number of ^{85}Rb atoms at the start of evaporation is too large, the ^{87}Rb gas cannot be cooled into the quantum degenerate regime; in this case (Fig. 6.3 (e)) the ^{85}Rb condensate shape is unperturbed and well approximated by a Thomas-Fermi model. For comparison absorption images of single species ^{85}Rb and ^{87}Rb condensates are shown in Fig. 6.3 (f).

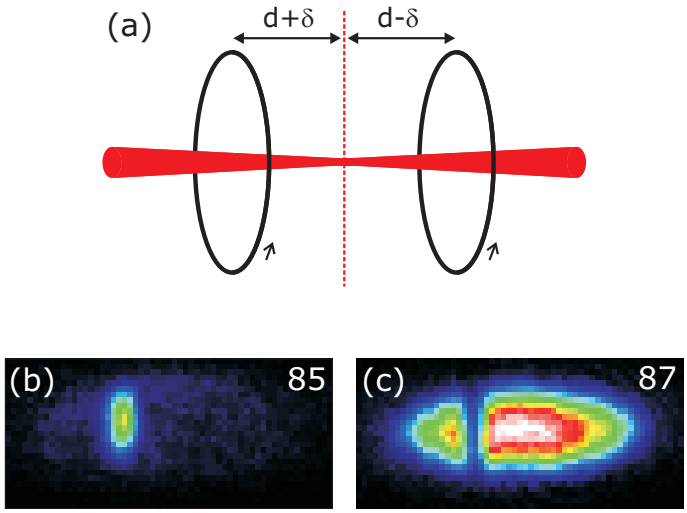

Figure 5.2: (a) A schematic drawing of the optical trap laser beam and the magnetic-field coils. The relative position of the minimum of the trapping potential for each species can be adjusted by changing the position of the optical trap focus with respect to the center of the bias field coils. Here δ indicates the relative difference between the focus of the optical trap beam and the center of the bias field coils. Absorption images of immiscible ^{85}Rb (b) and ^{87}Rb (c) condensates demonstrating a symmetric density pattern in the radial direction after recompression of the optical trap.

The immiscible gases shown in Fig. 6.3 are not symmetric with respect to either the radial or axial directions of the trap. These asymmetries are caused by gravitational sag of the trap and can be corrected by recompression of the optical trap to increase the depth or compensated for by careful alignment of the optical trap focus with respect to the magnetic-field center. In Fig. 5.2 (a) and (b) absorption images of immiscible gases were acquired after recompression of the trap; in the images symmetry in radial direction was restored but spatial separation is still clearly observed along the axial dimension. Similarly we have verified that offsets in the center-of-mass axial position of each species can be controlled via alignment of the optical trap. Although the precise shape, size, and position of the immiscible gases is affected by details of the trapping potential, the observation of spatial separation and the formation of separated ^{85}Rb cloudlets is repeatable under a variety of experimental conditions. By monitoring the total number of atoms in each gas as a function of time at a ^{85}Rb scattering length of 144 a_0, we find that the lifetime of the dual species BEC is approximately 1 sec. This decay is predominantly due to loss of ^{85}Rb atoms, the likely cause of which is inelastic density-dependent collisions [12]. During the decay, the dual-species BEC remains spatially separated and individual cloudlets of ^{85}Rb do not coalesce even after many radial and

a few axial trap periods.

We lack a detailed understanding of ^{85}Rb cloudlet formation in our experiments. The geometry of our system is complicated by the elongated axial direction of the trap, with a trap aspect ratio near 50, and the presence of gravitational sag. In an analysis of the favorability for cloudlet formation, the energy cost of forming and maintaining extra boundary surface area must be weighed against the cost of all particles residing in the same cloud [122]. These questions appear to require the solution of coupled Gross-Pitaevskii equations for the dual-species BEC wave-functions which is beyond the scope of this thesis [121].

5.3 Tuning the spatial separation with ^{85}Rb interactions

The ability to tune interactions between ^{85}Rb atoms in the gas represents a significant feature of our system. We have investigated the degree of spatial separation between the two species as a function of the ^{85}Rb scattering length. After preparation of a dual species BEC, the magnetic field was swept from 163.1 G to a value in the range of 164.6 G to 158.6 G in 400 ms; the sweep covers a range in Δ' of approximately -1 to +1. The rate of this sweep was measured to be slow with respect to the response of the gases in the radial and axial directions of the trap. Absorption images of each gas were acquired following release from the trap as before, the results of which are shown for $\Delta' = -0.89$ [Fig. 5.3 (a) and (b)] and $\Delta' = 0.72$ [Fig. 5.3 (c) and (d)]. The measured two-dimensional optical density (OD) was summed in the remaining radial direction to produce the cross sections shown in Fig. 5.3. As expected, spatial separation of the two gases is observed primarily when the parameter Δ' is negative. In addition to the coexistence of each species throughout the axial direction, separated cloudlets with sharp density spikes give way to a smooth overall density. Spatial separation was observed to return when an initial magnetic-field sweep to $\Delta' > 0$ was immediately followed by a second field sweep in the opposite direction. The penetration distance in the axial direction over which the two gases overlap is estimated to be approximately 30 μm when $\Delta = -0.89$. Note that this penetration was measured for an expanded cloud. All of the mean-field energy is released during expansion and this effect must be accounted for in a comparison to this measured penetration depth.

To characterize the degree of spatial separation as the parameter Δ' is varied we have extracted the axial center-of-mass location of each species from images similar to those shown in Fig. 5.3. In this experiment an offset between the axial trap centers for each species was intentionally introduced to favor the spatial separation in the center-of-mass location. The offset causes the two immiscible quantum gases to separate primarily in the axial direction with each species preferring a well-defined side of the trap. The results of this experiment are plotted in Fig. 5.4 as a function of Δ'. The axial position of each species in the trap gradually approach eachother as Δ' is increased from -0.9 toward zero. Once $\Delta > 0$ is attained, the center-of-mass position of each gas depends only weakly on the ^{85}Rb scattering length. This is consistent with the expectation that the two species can coexist throughout the axial direction of the trap. In this case, the measured difference in the position of each gas is in good agreement with that expected for single-species condensates. With our current imaging system, we are not able to quantify the spatial overlap of the two gases throughout the entire trapping volume, and residual gravitational sag likely induces incomplete spatial overlap.

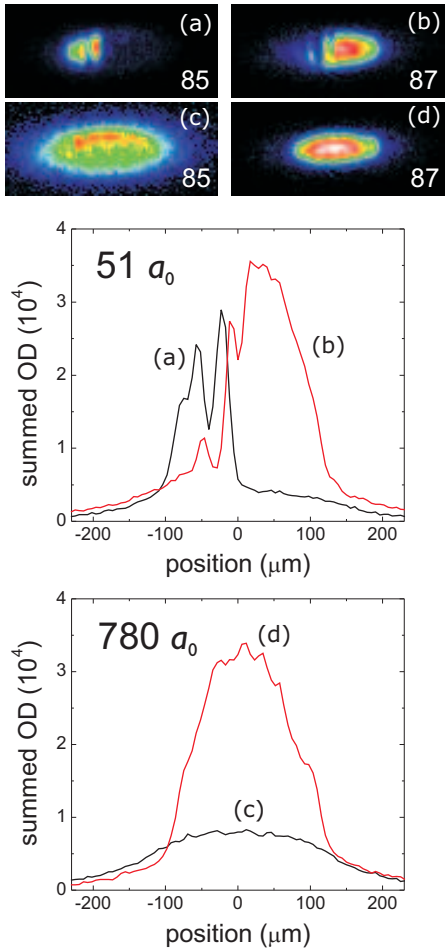

Figure 5.3: Absorption images (a-d) and corresponding axial cross sections at two different ^{85}Rb scattering lengths with significantly different spatial separation. The number of ^{85}Rb (^{87}Rb) atoms is approximately 40,000 (90,000).

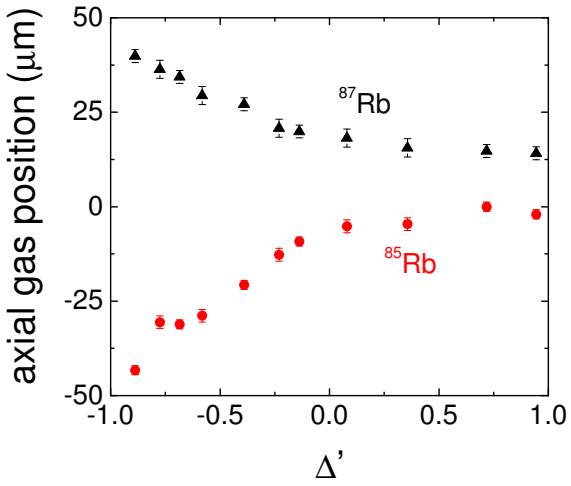

Figure 5.4: Measured axial position of the ^{85}Rb and ^{87}Rb gases as a function of the parameter Δ'. Here we have varied Δ' by tuning the ^{85}Rb scattering length from 50 a_0 to 900 a_0. The uncertainty in the position reflects the shot-to-shot reproducibility of our measurements.

5.4 Conclusion

In summary, we have observed immiscibile behavior in a dual-species BEC of ^{85}Rb and ^{87}Rb with tunable interactions. Surprisingly, immiscible condensates are observed to form multiple spatially-separated cloudlets, the exact cause of which remains unknown.[1] By varying the ^{85}Rb scattering length, the degree of spatial separation was characterized. In the future studies of the collective-excitation spectrum of a two-component BEC may be possible [126]. Numerous Feshbach resonances are available in the ^{85}Rb –^{87}Rb system making it possible to study a two-component condensate with a tunable interspecies interaction (see Ch. 6). In addition, the dynamics of single-species condensate collapse may be modified by the presence of a second condensate component.

[1] Shai Ronen and John Bohn have performed numerical simuilations of our system using a pair of coupled GP equations. They find qualitative agreement between our data and the simulations.

Chapter 6

Creation of heteronuclear Feshbach molecules

6.1 Introduction

In this chapter I present our work on ultracold heteronuclear Feshbach molecules. Starting with a ^{87}Rb BEC and a cold atomic gas of ^{85}Rb, we utilized previously unobserved interspecies Feshbach resonances to create up to 25,000 molecules. Even though in these experiments the ^{85}Rb gas was non degenerate, we observed a large molecular conversion efficiency due to the presence of a quantum degenerate ^{87}Rb gas; this represents a key feature of our two-species system. Using signatures of the molecule creation, we precisely measured the positions of two Feshbach resonances in our two species system to be 265.44 ± 0.15 G and 372.4 ± 1.3 G. We compared the molecule creation at these two different Feshbach resonances with different magnetic-field widths. We also directly measured the small binding energy of the molecules through resonant magnetic-field association.

The creation of ultracold molecules from ultracold atoms is currently a topic of great experimental and theoretical interest [10, 131, 132, 56]. Ultracold heteronuclear molecules in low-lying vibrational states are particularly interesting since they are predicted to exhibit a permanent dipole moment due to the unequal distribution of electrons. Numerous proposals for utilizing polar molecules exist, including quantum computation [133] and the search for the electron electric dipole moment [134]. Although no significant permanent dipole moment is expected to exist in a ^{85}Rb–^{87}Rb molecule, our work demonstrates a first step toward the efficient production of ground-state ultracold heteronuclear molecules.

Furthermore we note that the data presented in this chapter may be useful for understanding possible non-adiabatic corrections to the Born-Oppenheimer potential that describes atom-atom interactions in our system [135]. In the limit that beyond Born-Oppenheimer corrections can be neglected, the two-body Hamiltonian which describes the interaction of two atoms can be written as $H = \frac{p^2}{2\,M_r} + V_{BO}(r)$ where M_r is the reduced mass and $V_{BO}(r)$ is the interaction potential of Rb. This interaction potential does not depend on the mass of the Rb atoms in question, *i.e.* the same potential describes ^{85}Rb–^{85}Rb , ^{87}Rb–^{87}Rb , and ^{85}Rb–^{87}Rb interactions. In the theoretical analysis of Refs. [136, 103, 135] it was shown that beyond Born-Oppenheimer effects did not need to be included to accurately describe available experimental data on the Rb potential. In this chapter we present a precise experimental determination of several new interspecies Feshbach resonances. It would be interesting to understand whether our experimental data can also be described without including corrections to the Born-Oppenheimer potentials. We note that beyond Born-Oppheimer effects have previously

been observed through precise spectroscopic studies of H_2, HD, and D_2 spectral lines [137].

To date, cold heteronuclear molecules in high-lying vibrational levels have been created using photoassociation [138, 139, 140]. These molecules can then be pumped toward low-lying vibrational levels by exciting bound-bound molecular transitions [132] via, for example, stimulated Raman-type transitions [133] that enhance the probability of populating the lowest vibrational level. The initial photoassociation step used in this process is inefficient, and many final vibrational levels of the molecule are occupied. An alternative to this initial photoassociation step is the direct conversion of two free atoms into a molecule in the highest vibrational levels using a Feshbach resonance [10, 131, 41, 43, 141, 142, 143, 144]. High conversion efficiency using a Feshbach resonance has been demonstrated in single-species gases via adiabatic magnetic-field sweeps across the resonance [40, 56], three-body recombination [142], resonant magnetic-field association [144], and non adiabatic magnetic-field sweeps [10, 145]. Feshbach resonances between two different atomic species [146, 147] have previously been reported. Our work has built upon these observations by demonstrating stable heteronuclear Feshbach molecules.

6.2 Experimental setup

The previous chapters of this thesis have described in detail the experimental apparatus used to create an ultracold mixture of ^{85}Rb and ^{87}Rb. Here we will briefly describe a few details of the experimental setup relevant to the results in this chapter. The optical trap for these measurements is formed at the focus of a Yb:YAG laser beam with a $1/e^2$ radius of 23 μm. A Helmholtz pair of coils provides a magnetic field up to 700 G; the magnetic field is calibrated using rf-driven Zeeman transitions with a systematic uncertainty of 0.01%. We perform the optical trap evaporation slightly above the ^{85}Rb Feshbach resonance at 155 G where density-dependent ^{85}Rb–^{85}Rb loss is minimized [12]. We typically produce a ^{87}Rb BEC with 300,000 atoms and 50% condensate fraction and a non degenerate ($T/T_c = 2.4$) gas of ^{85}Rb with 40,000 atoms. Measurements are performed in an optical trap with a radial trap frequency of $\omega_r = 2\pi \times 200$ Hz and an aspect ratio of approximately 70. Both the optical trapping potential and the curvature of the magnetic field contribute to the confinement of the atoms in the axial direction. Confinement in the radial direction of the trap is primarily provided by the optical trap.

For the measurements presented in this chapter, we create a BEC of ^{87}Rb but only a thermal gas of ^{85}Rb. There are two reasons for this choice. Away from the Feshbach resonance at 155 G, a ^{85}Rb condensate is not stable against collapse due to the attractive atom-atom interactions. If we attempt to set the magnetic field above 165.7 G or below 155 G, we measured that the ^{85}Rb condensate would collapse in less than 0.1 ms [8]. The other reason for working with a ^{85}Rb thermal gas is that phase separation can occur in a dual BEC system, this was demonstrated in the previous chapter.

6.3 Discovery of heteronuclear Feshbach resonances

Our work on heteronuclear molecules follows from our discovery of two heteronuclear s-wave Feshbach resonances in the ^{85}Rb $|f = 2, m_f = -2\rangle$ state and ^{87}Rb $|f = 1, m_f = -1\rangle$ state, one near 265 G and the other near 372 G. These resonances

were predicted theoretically in Ref. [13] and were first located in our lab by detecting the enhanced inelastic collision rate near the resonance position. For both of the resonances the binding energy of the bound molecular state increases with magnetic field above the position of each Feshbach resonance. Figure 6.1 shows data used to locate the s-wave Feshbach resonance at 265 G. In this measurement we also discovered a p-wave ($l = 1$) resonance (left feature). Because the ^{85}Rb loss only occurs in the presence of ^{87}Rb, we can clearly see that the features are due to heteronuclear collisions.

We have looked more closely at the structure of the p-wave resonance (Fig. 6.2). The doublet feature is due to the magnetic dipole-dipole interaction between the atoms [148]. This effect results in two distinct peaks characterized by their partial-wave projection onto the magnetic field axis, $m_l = 0$ or $|m_l| = 1$. Such a resonance could provide a way to tune anisotropic interactions in a two-species BEC.

6.4 Creating Feshbach molecules with magnetic-field sweeps

To create heteronuclear molecules we adiabatically (450 μs/G) sweep [131] the magnetic field from low to high field through one of our s-wave Feshbach resonances. Figure 6.3b shows an absorption-image cross section of the ^{85}Rb gas following a sweep through the resonance. Prior to imaging, the gas is released from the optical trap and expands for 3 ms; at the same time as the optical trap release is initiated, the magnetic field is switched off within 50 μs. A significant fraction ($\sim 60\%$) of the atoms disappear as compared to an absorption-image cross section without sweeping the magnetic field (Fig. 6.3a). When we reverse the molecule creation process by applying a second field sweep in the opposite direction less than 100 μs after the first sweep ends, (Fig. 6.3c), a large fraction of the atoms reappear [131]. The atoms that reappear represent reversible heteronuclear molecule formation. The small fraction of atoms that do not return are lost to ^{85}Rb–^{87}Rb inelastic collisions that remove atoms from the trap. We verified this by sweeping across the resonance at the same rate in the opposite direction. At a typical ^{87}Rb density of 0.5×10^{14} cm^{-3} we observe approximately 15% ^{85}Rb number loss during a sweep. By monitoring the reappearance of atoms as a function of time before the second sweep, we find that the molecules decay with a lifetime of approximately 1 ms. This decay is due to a combination of inelastic collisions with the ^{87}Rb gas and a one-body spontaneous process [149, 150].

The dependence of molecule conversion efficiency on sweep rate was measured in Ref. [40] and is well characterized by a Landau-Zener model. For our two-species gas we observe a factor of 5.3 ± 1.9 decrease in the ramp rate required to create molecules at the 372 G Feshbach resonance as compared to the 265 G resonance (see Fig. 6.4) for a similar number and temperature. This factor is consistent with the ratio of the predicted widths of the two resonances, which is in the range of 6–8 [13, 151, 152]. This directly verifies the predicted inverse relationship between the Feshbach resonance width and the sweep rate required to create molecules.

6.5 Determination of the Feshbach resonance locations

We precisely located the Feshbach resonances with an experimental technique that avoids the need for rapid magnetic-field sweeps. At the lower (higher) field resonance, we sweep the magnetic field from 269 G (397 G) downward toward the resonance stopping

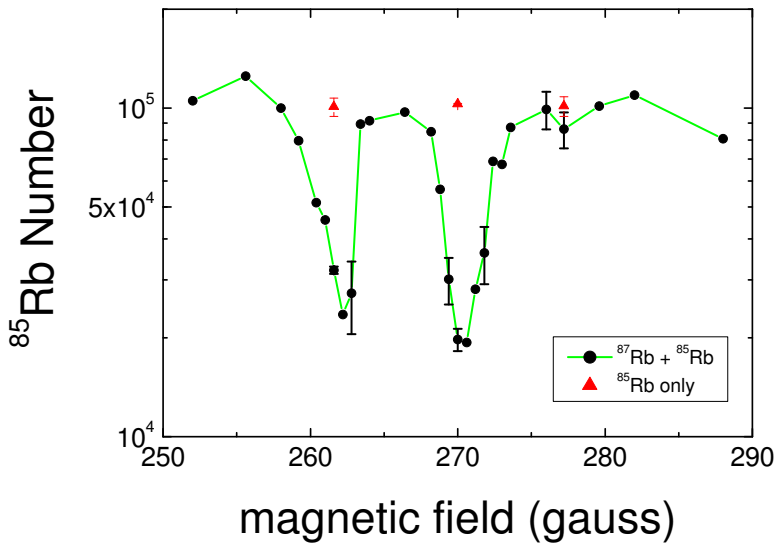

Figure 6.1: Investigation of Feshbach resonances in the ^{87}Rb and ^{85}Rb system via the enhanced inelastic number loss at the resonances. The asymmetric nature of the left peak is characteristic of higher partial-wave Feshbach resonances. The right peak corresponds to a heteronuclear s-wave resonance. The temperature of the two species gas was 1000 nK for this data.

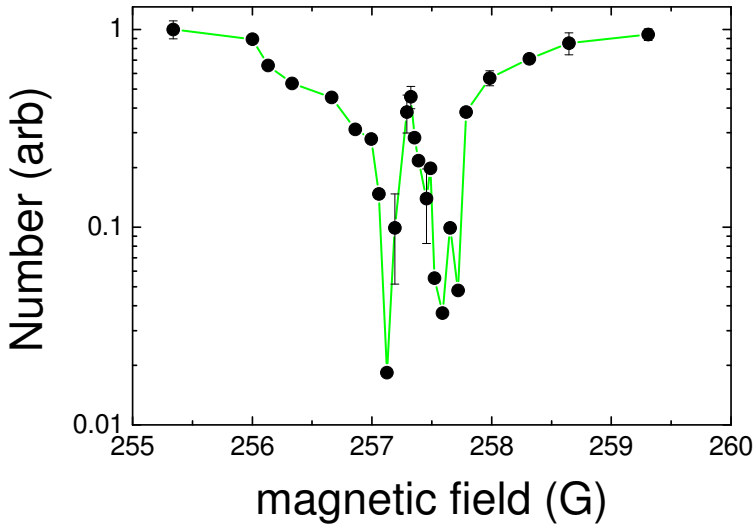

Figure 6.2: Doublet structure of a heteronuclear p-wave Feshbach resonance observed via inelastic losses at the Feshbach resonance. The temperature of the two species gas was 100 nK for this data.

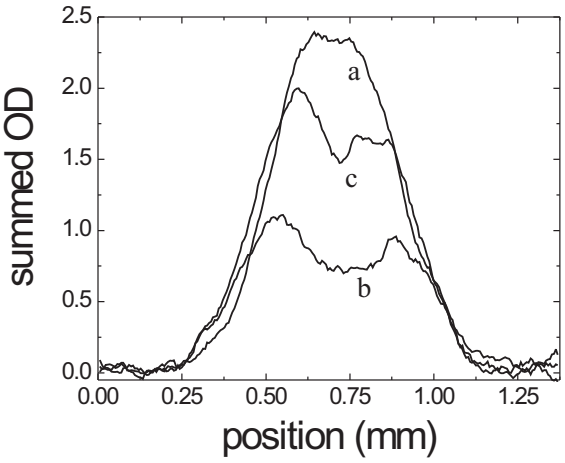

Figure 6.3: Absorption-image axial cross sections of the ^{85}Rb gas demonstrating reversible molecule creation. The measured two-dimensional optical density (OD) was summed in the remaining radial direction of the absorption image. (a) Prior to sweeping the magnetic field the atom number is 26,500. (b) After sweeping through the resonance 53% of the gas is converted to molecules. (c) By reversing the molecule creation process approximately 85% of the initial atom number is observed to reappear. Note that most of the ^{85}Rb loss occurs in the center of the gas where the ^{87}Rb BEC density is largest.

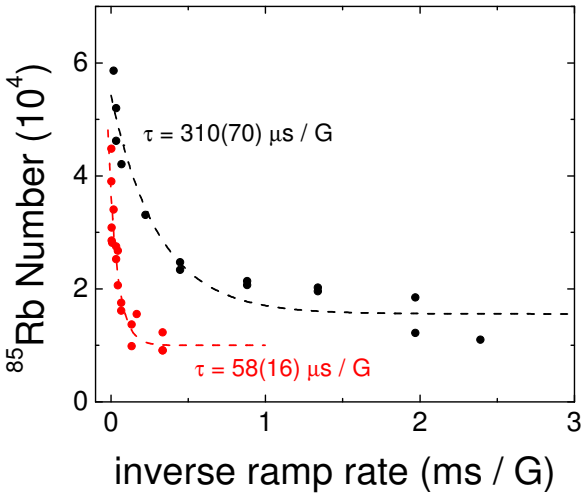

Figure 6.4: Molecule conversion efficiency as a function of sweep rate. The black points show the rate required for conversion at the 265 G resonance, while the red points show the required rate at the wider 372 G resonance. Both datasets were taken starting with similar atom number and temperature. This data has not been corrected for the effects of atom loss not due to molecule formation, therefore the number of molecules created in these data is less than the total atom loss.

at various final values. The rate of this magnetic field sweep is fast compared to both the timescale for molecule creation and atom loss due to inelastic collisions. The field is held at the final value for 0.3 ms and then returns to 269 G (397 G) at a rate of 450 μs/G (70 μs/G) which is slow compared to the molecule creation rate. The magnetic field remains here for 5 ms to ensure that any molecules made during the second sweep decay and are lost from the optical trap [149, 150]. We then simultaneously turn off the magnetic field and the optical trap to let the gas expand for 6 ms and measure the number of ^{85}Rb atoms remaining. In Fig. 6.5 we show the atom number remaining as a function of the final magnetic field for the two Feshbach resonances. The key to this method is that if the field passes through the Feshbach resonance on the first sweep, then a fraction of the atoms will be converted into molecules by the second sweep. The rapid onset of atom loss due to molecule creation when the magnetic field is swept below 265.44 G (372.4 G) represents crossing the peak of the Feshbach resonance.

6.6 Heteronuclear molecule creation efficiency

6.6.1 Experiment

We have investigated the adiabatic conversion efficiency from atoms to molecules. We begin by sweeping the magnetic field upward through the 265 G Feshbach resonance at a rate that is slow with respect to the molecule conversion rate. It is then held at 269 G for 5 ms to allow the molecules to decay and be lost from the trap. The number of molecules formed is simply the difference in ^{85}Rb number before and after the sweep with a small correction applied to account for measured inelastic atom loss during the field sweeps. The conversion efficiency to heteronuclear molecules is shown in Fig. 6.6 as a function of ^{87}Rb T/T_c. We varied T/T_c by either changing the number of ^{87}Rb atoms or the temperature. The ^{85}Rb gas had a T/T_c in the range of 2.2 to 4. The number of ^{85}Rb atoms was always less than or equal to the number of ^{87}Rb; the ^{85}Rb number ranged from 28,000 to 55,000 and the ^{87}Rb number ranged from 30,000 to 400,000. We observe up to 60% conversion of the ^{85}Rb gas into molecules even when the ^{85}Rb gas is far from quantum degeneracy. The largest conversion efficiency is observed when ^{85}Rb is least quantum degenerate, indicating that the conversion efficiency primarily depends on ^{87}Rb T/T_c.

6.6.2 Theory

In a single-species gas the molecule conversion efficiency for an adiabatic field sweep was shown to depend only on the degree of quantum degeneracy [40, 153]. A molecule is formed during an adiabatic sweep if two free atoms are sufficiently close in phase space so that their wavefunction can smoothly evolve to a bound molecule as the Feshbach resonance is crossed. This model also explains the behavior we observe here. Each particle of the less degenerate species is surrounded in phase space by particles of the more degenerate ^{87}Rb gas with which molecules can be formed. We used a Monte-Carlo simulation to model the observed conversion efficiency. Phase space distributions of position and momenta of ^{85}Rb and ^{87}Rb are generated based on the number and temperature of each gas and the trap frequencies. For the ^{87}Rb gas at temperatures above T_c a Maxwell-Boltzmann (MB) distribution is used. Below T_c we use a combination of a Thomas-Fermi distribution for the BEC and a Bose-Einstein

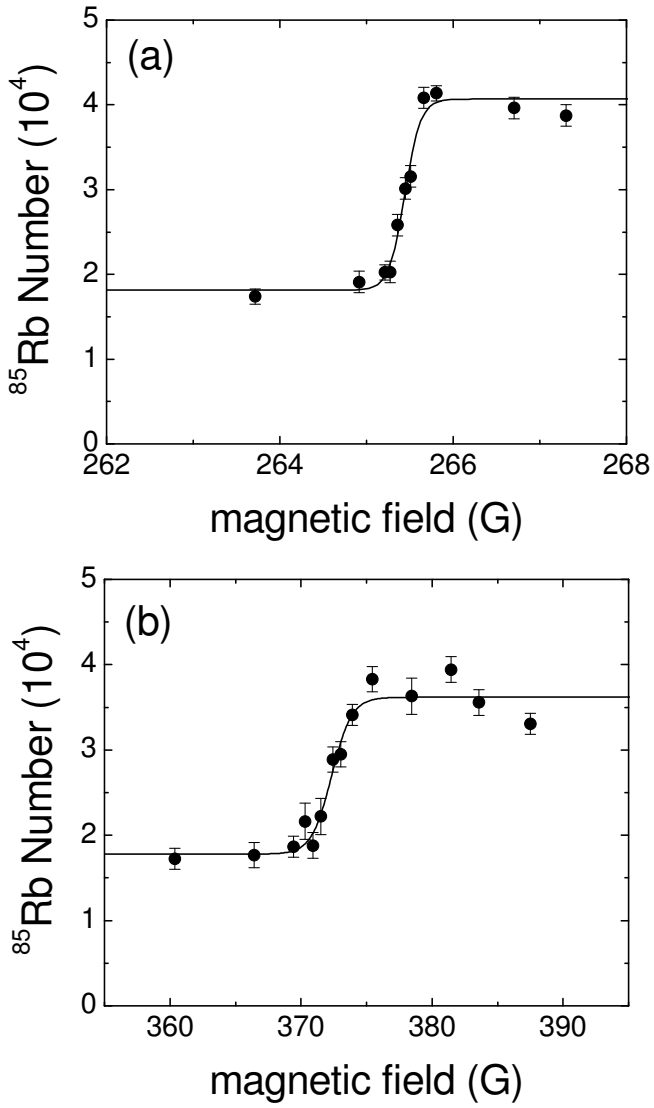

Figure 6.5: Atom loss after magnetic-field sweeps through a Feshbach resonance. The number of ^{85}Rb atoms is a function of the final magnetic field during the sweeps near the (a) 265 G and (b) 372 G Feshbach resonances. Initially there are $2.1 - 2.3 \times 10^5$ ^{87}Rb atoms at T/T_c between 0.82 and 0.84. The data are fitted to an error function to extract the center position and width. The resulting positions of the two transitions are 265.44 ± 0.15 G and 372.4 ± 1.3 G with the uncertainty given by the fitted RMS width.

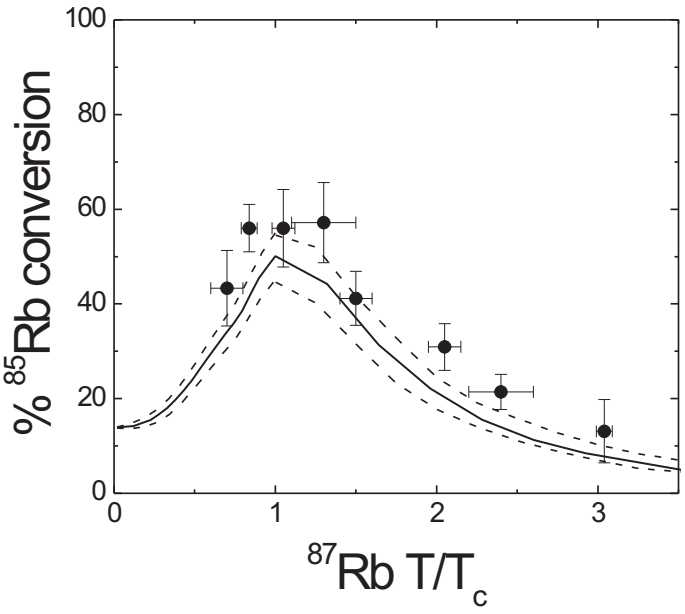

Figure 6.6: Heteronuclear molecule conversion efficiency at the 265 G Feshbach resonance as a function of ^{87}Rb T/T_c. At our largest conversion efficiency the ^{85}Rb gas has $T/T_c = 2.6$. The solid line shows a simulation based on our conversion model, and the dashed lines represent the uncertainty. The conversion drops below $T/T_c = 1$ since the BEC is spatially smaller than the thermal ^{85}Rb gas and the conversion process depends on the proximity of two atoms in phase space. Some of the data for this figure has been averaged together. The error bars represent the weighted average of the points.

distribution for the thermal component. A MB distribution is always used for the ^{85}Rb gas since the temperature of the gas does not fall below $T = 2.2\,T_c$. For each ^{85}Rb atom the simulation searches the ^{87}Rb gas to find a mate that is sufficiently close in phase space. After a pairing occurs, the two atoms are removed from the simulation.[1]

Two atoms are considered sufficiently close in phase space if either of the following conditions is met: (1) If a BEC is present, any ^{85}Rb atoms inside the Thomas Fermi radius of the condensate form a molecule, or (2) outside the BEC, an ^{85}Rb atom and a partner ^{87}Rb atom must satisfy the relation found in Ref. [40]: $|\delta r_{rel}\, m\, \delta v_{rel}| < \gamma\, h$, where δr_{rel} is the separation of the pair, m is the atomic mass, δv_{rel} is the relative velocity, and $\gamma = 0.44 \pm 0.03$.

The results of our simulation are shown by the solid line in Fig. 6.6. For $T/T_c > 1$ each gas has roughly the same spatial size in the optical trap, and therefore molecule conversion can occur anywhere in the gas as long as the local phase space criterion is met. At $T/T_c = 1$ and below, a significant fraction of the ^{87}Rb atoms are part of the condensate, which is spatially small compared to the extent of the ^{85}Rb gas. Therefore the conversion efficiency of atoms into Feshbach molecules drops in this regime since the spatial overlap of the two species decreases. If the ^{85}Rb gas were a BEC, the two species would have a better spatial overlap, and our simulation would predict that the molecule conversion efficiency quickly approaches 100% as the T/T_c of each gas drops below one. There is good agreement between the experiment and simulation in both the non degenerate and quantum degenerate regimes, suggesting that the pairing model in Ref. [40] is also applicable to heteronuclear molecule creation.

6.7 Feshbach molecule binding energy

We have found that a useful way to spectroscopically characterize the Feshbach bound state is to create heteronuclear molecules using a small oscillating magnetic field. The oscillating field causes two atoms to bind together and form a molecule [144, 154]. We first ramp the magnetic field from 269 G to a selected value between 266.2 and 267 G in 0.3 ms. The field modulation is then applied using the Helmholtz coil pair for 20 ms with a peak-to-peak amplitude between 0.6 and 1.0 G at a frequency up to 40 kHz. Next the field is returned to 269 G and held there for 5 ms, allowing any molecules made during the modulation to decay. Finally we determine the number of atoms remaining as described previously in this Chapter. As in Ref. [144], we observe strongly enhanced atom loss at certain frequencies, and the loss depends on the duration and amplitude of the modulation. A typical loss spectrum is shown in the inset of Fig. 6.7; the frequency at which we observe maximum atom loss gives a measure of the binding energy of the molecules [155].[2]

[1] The results of our simulation for the molecule conversion efficiency depend on the absolute number of atoms in the two gases. The predicted molecule creation efficiency increases as the total number of particles in the simulations is increased. We study the behavior of the number dependence by running our simulations over a very wide range of particle number. It takes several hours to run the simulation at a single T/T_c for a number of particles similar to what is used in our experiments. Therefore we determine the number dependence at only the single value $T/T_c = 1.22$, and we use that information to scale the simulation results when a smaller number of particles is used in the simulation. The correction factor we use is approximately 10%.

[2] The atom-loss spectrum was recorded for a ^{87}Rb gas with 50% condensate fraction and two non-condensed gases with temperatures of 130 and 190 nK. Over this range in temperature, the measured

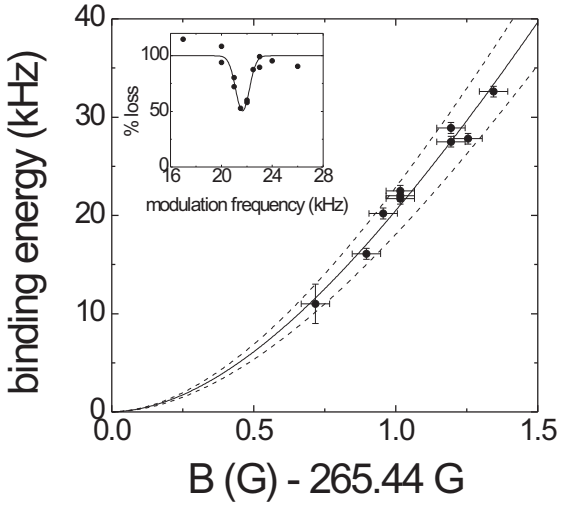

Figure 6.7: Resonant frequency of atom loss as a function of magnetic field. The solid line is a fit to the data based on the universal binding energy of s-wave Feshbach molecules and the dashed lines represent the uncertainty in the Feshbach resonance width. (Inset) An atom-loss spectrum at 266.5 G as a function of the modulation frequency. The modulation converts roughly 50% of the gas to molecules. The loss is centered at 21.7 kHz with a width of 0.6 ± 0.2 kHz. The solid line is a gaussian fit to the data. We report the uncertainty in the binding energy as the width of the loss spectrum because we lack a detailed understanding of the lineshape.

The resonant frequency of maximum atom loss is shown in Fig. 6.7 for various magnetic fields near the Feshbach resonance. For each loss curve the amplitude used converted roughly half the ^{85}Rb gas into molecules. The solid line is a fit to the data based on the universal form of the molecular binding energy near an s-wave Feshbach resonance [56]. In the fit the background scattering length is fixed to the value $213 \pm 7\ a_0$ [103], and the Feshbach-resonance peak position and width are varied; the best fit finds the peak position and width to be 265.42 ± 0.08 G and 5.8 ± 0.4 G, respectively. These results are consistent with our previously discussed determination of the Feshbach-resonance peak position and with the predicted width of the Feshbach resonance in Refs. [13, 152, 151].

Resonant association of free atoms into Feshbach molecules has recently been used in an atomic ^{40}K gas to create stable p-wave molecules [156]. Two-body scattering at p-wave Feshbach resonances has also been studied in ^{40}K [148, 157]. Due to the higher angular momentum of the p-wave molecules, the binding energy scales *linearly* as opposed to the quadratic dependence of the s-wave molecules. In our system, the resonant modulation technique that has already been described was extended to spectroscopically study the binding energy (Fig. 6.8) of p-wave heteronuclear ^{85}Rb–^{87}Rb Feshbach molecules. The data presented here represents only a preliminary study of this interesting new system, and it might be useful as a starting point for future experiments.

The molecules are associated at the p-wave Feshbach resonance that we discovered near 257.5 G; earlier in this chapter we investigated the doublet structure of this Feshbach resonance. To begin our experiments we ramped the magnetic field to a selected value in the range of 256.7 G to 258.2 G. The field modulation is then applied using the Helmholtz coil pair for 20 ms with a peak-to-peak amplitude between 0.1 and 0.7 G at a frequency up to 50 kHz. Finally we determine the number of atoms remaining in the trap with absorption imaging. As in the case of s-wave molecules, the frequency of the modulation at which maximum atom loss corresponds to the binding energy of the molecules. We acquired resonant modulation spectra at a few different magnetic fields near the p-wave Feshbach resonance; the measured binding energies at these fields is shown in Fig. 6.8. We have extracted a preliminary value for the slope of the binding energy at the p-wave Feshbach resonance, the slope is 58(4) kHz/G.

6.8 Conclusion

In this Chapter I have discussed how we created heteronuclear Feshbach molecules from an ultracold gas of ^{85}Rb and ^{87}Rb. We demonstrated that molecules can be produced with two methods, magnetic-field sweeps and resonant-field modulation. The conversion efficiency of ^{85}Rb into molecules can reach 60% even when that gas is not quantum degenerate. For this measured conversion efficiency the number of ^{87}Rb atoms was a factor of five larger than the number of ^{85}Rb atoms. The presence of two species with different quantum degeneracy provides a rich system for testing our understanding of the conversion efficiency from atoms to molecules. The heteronuclear molecules described here are ultracold and are stable for at least 1 ms. These conditions may provide a first step toward the efficient production of ground-state heteronuclear molecules. Furthermore, the molecule creation process allows us to determine the location and width

resonant frequency shifts by only 5(2) Hz/nK.

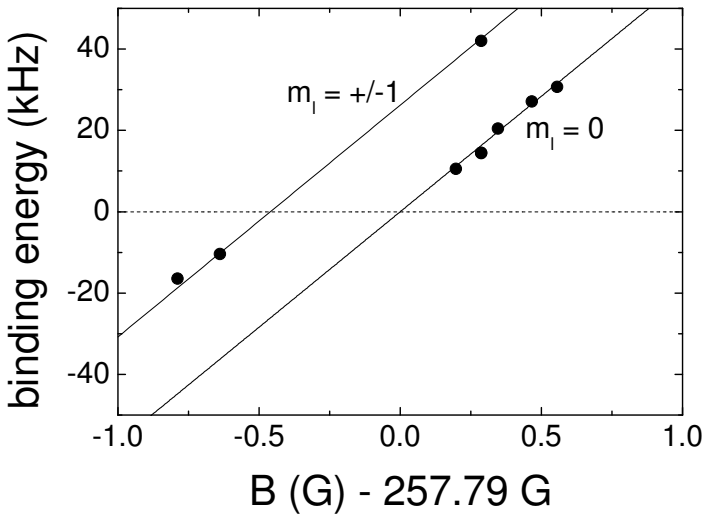

Figure 6.8: Preliminary measurements of the binding energy of p-wave heteronuclear Feshbach molecules. Each binding energy measurement represents the resonant frequency of atom loss. The solid lines are a linear fit to the data with slope 58(4) kHz/G. The splitting between the two m_l resonances is approximately 0.5 G.

of Feshbach resonances in the two-species system; this information will be required for future studies of the ^{85}Rb–^{87}Rb system with a tunable interspecies interaction.

Chapter 7

Bragg spectroscopy of a strongly interacting BEC

7.1 Introduction

Many physical properties of a Bose-Einstein condensate can be described within the framework of a mean-field theory [23]. In the mean-field theory the Hamiltonian of the system is composed of three terms, a term for the kinetic energy, a term for the energy due to the external confining potential, and a mean-field term that describes the energy due to interparticle interactions in the condensate. The kinetic energy of a trapped condensate is very small and is typically ignored. The mean-field term depends on the condensate density and the s-wave scattering length a. The total energy of the condensate and its physical properties like size and shape are determined by the trapping potential and the strength of interactions. Mean-field theory is remarkably successful at describing experimental observations of a BEC with weak atom-atom interactions. However as the strength of interactions increases, the observed physical properties of a condensate are expected to deviate from the predictions of mean-field theory.

As a particular example of predicted beyond mean-field effects, consider the chemical potential of a condensate. In a mean-field theory the chemical potential is proportional to the product of density and scattering length. If the scattering length is increased, a beyond mean-field correction to the chemical potential is expected; the correction scales as $\sqrt{n\,a^3}$. The exact form of this correction was first calculated by Lee, Huang, and Yang (LHY) in the 1950s [47, 46, 158]. Beyond mean-field corrections also show up in other physical properties of a condensate with strong interactions. Recently, a beyond mean-field shift in the collective oscillation frequency of a Fermi gas on the BEC-side of the BCS-BEC crossover was observed [159]. The shift in the oscillation frequency is related to the LHY correction. But to date, efforts to observe the effects of this beyond mean-field correction have not been successful in a Bose gas [6].

Measuring the excitation spectrum is an another important way of revealing the effects of inter-particle interactions in a condensate. Here the excitation spectrum refers to the energy required to add a particle or quasiparticle with a given momentum. In a classical gas, which obeys Maxwell-Boltzmann statistics, the excitation spectrum is free-particle-like for all values of momentum. A key characteristic of a superfluid is the presence of phonon excitations at small momenta. The energy of a phonon scales linearly with momentum and the slope is given by the sound velocity in the gas. In the case of superfluid ^{4}He, measurements of the excitation spectrum not only revealed the existence of phonons at small momentum, but the presence of a local minimum in the spectrum at larger momentum due to rotons. The current physical understanding of the origins of the roton minimum is complicated, see Ref. [19] for details.

In this Chapter the excitations of a BEC are studied. The excitation spectrum of a condensate with no interactions scales quadratically with momentum since the quasiparticles behave as free particles. Atom-atom interactions modify the character of this spectrum; at low momentum the spectrum is linear due to phonon-like excitations, while at large momentum the spectrum is free-particle-like with a shift in energy due to interactions. The excitation spectrum of a strongly interacting condensate is further modified by beyond mean-field effects related to the correction derived by Lee, Huang, and Yang [47, 46, 158].

As mentioned earlier in this thesis, one of the goals of our new ^{85}Rb BEC machine was to be able to make large, stable ^{85}Rb condensates in a system with plenty of optical access that would allow more sophisticated probes of a strongly interacting BEC. The experiments described in this chapter represent the realization of this goal. By adding a pair of counter-propagating laser beams to our science cell we are able to probe the excitation spectrum of our ^{85}Rb gas through Bragg spectroscopy. Since we have access to the ^{85}Rb Feshbach resonance, we can continuously tune the scattering length into the strongly interacting regime. This allows us to probe the onset of corrections to the mean-field theory of a condensate. Our measurements of the excitation spectrum of a strongly interacting BEC near a Feshbach resonance have revealed some very interesting physics. In the case of large momentum excitations, we have observed that the excitation energy of the condensate is significantly *smaller* than what is expected from a mean-field theory. Our observation of a smaller than expected excitation energy is in qualitative agreement with the free-particle regime predictions of Refs. [160, 161], which are related to the LHY beyond mean-field corrections. However, our experiments were not performed completely in the free-particle regime. That regime is characterized by $k\,\xi \gg 1$ where k is the wave vector of the excitation and ξ is the healing length of the condensate. Our experiments were performed with a wave vector such that $k\,\xi \geq 2$. To understand what we expected for our strongly interacting condensate, we have collaborated with S. Ronen and J. Bohn who have predicted the excitation spectrum using existing theories that include many-body effects [160, 161].

In this chapter we describe experiments designed to probe beyond mean-field corrections to the excitation spectrum of a BEC. Bragg spectroscopy is used to record the excitation spectrum over a wide range of scattering length. Bragg spectroscopy has several advantages over measurements of collective excitations, including a measurement time much shorter than the radial trapping period and the ability to access different momentum regimes. To date our experimental focus has been on acquiring and understanding the large momentum excitations of a strongly interacting BEC. In this regime, the excitation energy is larger than the chemical potential of the condensate. In future experiments it may be possible to study excitations with smaller momentum, and therefore with energy less than the chemical potential. A particularly interesting regime to study is where the wave vector of the excitation is approximately equal to the inverse of the interparticle spacing. It is in this regime that the roton minimum of ^{4}He appears.

7.2 The excitation spectrum of a BEC

The excitation spectrum of a homogeneous BEC in mean-field theory is given by the well-known Bogoliubov formula, which states that the excitation energy ($\hbar\,\omega(k)$) as

a function of the momentum $\hbar\, k$ is given by

$$\hbar\,\omega(k) = \sqrt{\frac{\hbar^2 k^2}{2m}\left(\frac{\hbar^2 k^2}{2m} + 2\,g\,n\right)} \tag{7.1}$$

where $g = 4\pi\hbar^2\, a/m$, a is the s-wave scattering length and n is the average condensate density. The excitations of an interacting quantum fluid differ significantly from a gas described by Maxwell-Boltzmann statistics with free particle excitations at all momenta. In particular at small values of k condensate excitations are phonon-like and the energy is approximately $\epsilon_k \approx c\,\hbar\,k$ with $c = \sqrt{\frac{g\,n}{m}}$. For large k, condensate excitations are free-particle-like except with a shift in energy due to the interactions; the energy is given by $\epsilon_k \approx \hbar^2 k^2/(2m) + g\,n$. The gradual crossover from the phonon regime to free-particle regime is indicated by the condensate healing length $\xi = 1/\sqrt{8\,\pi\,n\,a}$. Figure 7.1 shows the excitation energy of a condensate and the free-particle excitation energy as a function of momentum.

The excitation spectrum of a trapped BEC is qualitatively similar to the homogeneous case. The spectrum is calculated by averaging the Bogoliubov energy over the inhomogeneous density of the trapped condensate. In the large momentum regime, averaging the excitation spectrum over the Bogoliubov energies again predicts a constant shift due to interactions.

So far only weak atom-atom interactions in the condensate have been considered. The Bogoliubov excitation spectrum is valid only in the limit that the condensate is dilute ($n\,a^3 \ll 1$) and two-body scattering is independent of momentum ($k\,a \ll 1$). With our apparatus we can achieve experimental conditions of density and scattering length under which neither of these conditions are met. Since we have chosen to create large momentum excitations with Bragg spectroscopy, even at a modest scattering length of 900 a_0 we have $k\,a = 0.8$. As we will see later in this chapter, we set the density of the condensate to be large to enhance beyond mean-field effects due to $n\,a^3$ physics with respect to the momentum-dependent scattering physics.

7.3 Bragg spectroscopy of a BEC

In our experiments we use Bragg spectroscopy to precisely probe the excitation spectrum of a condensate. Bragg spectroscopy is performed by driving stimulated two-photon transitions with two independent laser beams that are directed onto the condensate. The interference pattern of the two laser beams creates a small-amplitude, spatial oscillation in the BEC wave function. The energy and momentum associated with the wave function oscillation are given by the frequency difference and wave vector difference between the two lasers. We can detect the effect of Bragg spectroscopy by measuring the number of atoms that make a two-photon transition. Since the majority of atoms in the condensate have zero momentum prior to Bragg spectroscopy, the excitation of the BEC can be probed with good resolution.

Bragg spectroscopy of a condensate was first demonstrated at MIT in 1999.[1] In their original work large momentum excitations of a Na condensate were studied, and the energy shift due to condensate interactions was directly observed [163]. They

[1] The Phillips group at NIST also demonstrated two-photon Bragg transitions in a Na BEC [162].

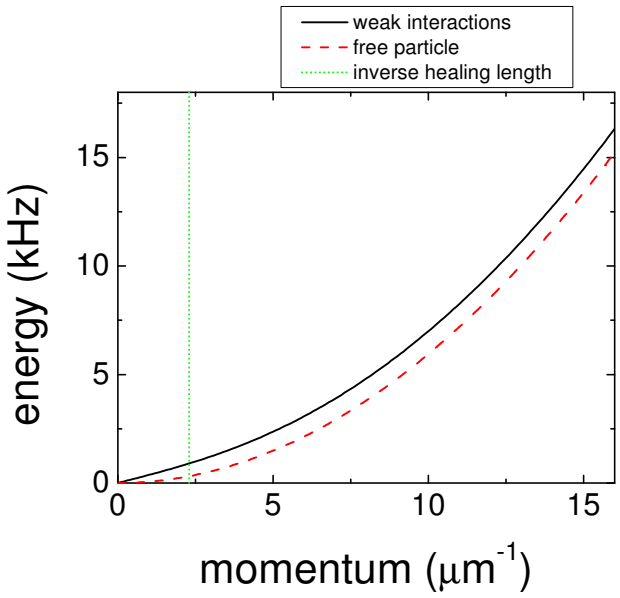

Figure 7.1: Bogoliubov excitation spectrum (Eqn. 7.1) for a condensate (black curve) and the free particle energy (red curve) as a function of momentum. The black curve has $n = 10^{14}$ cm^{-3} and a scattering length of 150 a_0. The green vertical line represents the inverse healing length of the condensate and the crossover to free-particle excitations.

also observed that the coherence length of the BEC is larger that its size, since Bragg spectroscopy reveals the momentum distribution of the gas. In later work they studied excitations in the phonon regime. In particular they were able to observe a suppression of the Bragg response for low-momentum excitations [164]. This suppression is caused by the presence of correlated atom pairs with momentum $\pm\mathbf{p}$. Bragg spectroscopy at low momenta is a superposition of two events, scattering from the $-\mathbf{p}$ states into the condensate and scattering from the condensate into a state with momentum $\mathbf{p}$. If the momentum change due to Bragg spectroscopy is very small, the two events occur with equal probability and the Bragg response is suppressed. These two experiments each studied the excitation spectrum at a single value of momentum. In 2002, the Davidson group measured the excitation spectrum over a wide range of momentum, spanning the phonon and free-particle regimes. Excellent agreement between their data and the Bogoliubov spectrum was observed. Our Bragg spectroscopy work builds upon these observations by studying condensate excitations over a very wide range of interaction strength. Since we have access to a Feshbach resonance, we are able to explore the excitation spectrum in a regime of interactions where beyond mean-field corrections are important.

Our experiments are initiated by creating a pencil-shaped ^{85}Rb BEC in an optical dipole trap. For these experiments the 46 micron waist optical trap is used. The radial trap frequency was measured to be $2\,\pi \times 129(2)$ Hz and the axial frequency was measured to be $2\,\pi \times 2.9(1)$ Hz.[2] A Helmholtz pair of coils provides a magnetic field of up to 700 G; the curvature of the field enhances confinement along the axial direction of the optical trap.

Two-photon Bragg transitions change the energy and momentum of an atom without changing the internal spin state. The energy and momentum imparted to the condensate is calibrated via the frequency and wave vector difference of the two laser beams. The momentum imparted to the BEC via Bragg scattering is given by $q = \hbar\, k\, \sin(\theta/2) = 2\,\hbar k_L\, \sin(\theta/2)$ where $k_L = \frac{2\,\pi}{780\,nm}$ is the magnitude of the wave vector of the laser beams and θ is the angle between the two beams. A significant advantage of Bragg spectroscopy is that the energy and momentum imparted to the condensate is well calibrated. Therefore the energy and momentum of the excitation does not need to be directly determined from the atoms that undergo Bragg transitions.

In our system the condensate is illuminated by the Bragg spectroscopy light for a duration t_p. A pair of counter-propagating Bragg laser beams are oriented along the axis of the condensate. The motivation of this choice will be discussed in the next section. Figure 7.2 shows the optics and beam paths in the science cell area. The Bragg light is delivered to the science cell area with a pair of polarization-maintaining optical fibers. The Bragg light is aligned along the axis of the trapped condensate onto the atoms by overlapping the beams with the optical trap light.

The laser light for Bragg spectroscopy is derived from an external cavity diode laser located on a different optical table from the main apparatus. The laser frequency is stabilized to the ^{87}Rb $F = 2 \rightarrow F' = 2/F' = 3$ crossover line in the saturated-absorption spectrum, which is detuned 133.5 MHz from the cycling transition. Approximately 20 mW of total light is available from the laser. For Bragg spectroscopy we require two phase stable, independently steerable laser beams with a precisely tunable frequency

[2] Note that the frequency of breathing motion along the elongated direction of the condensate is approximately 1.6 ω_z [23].

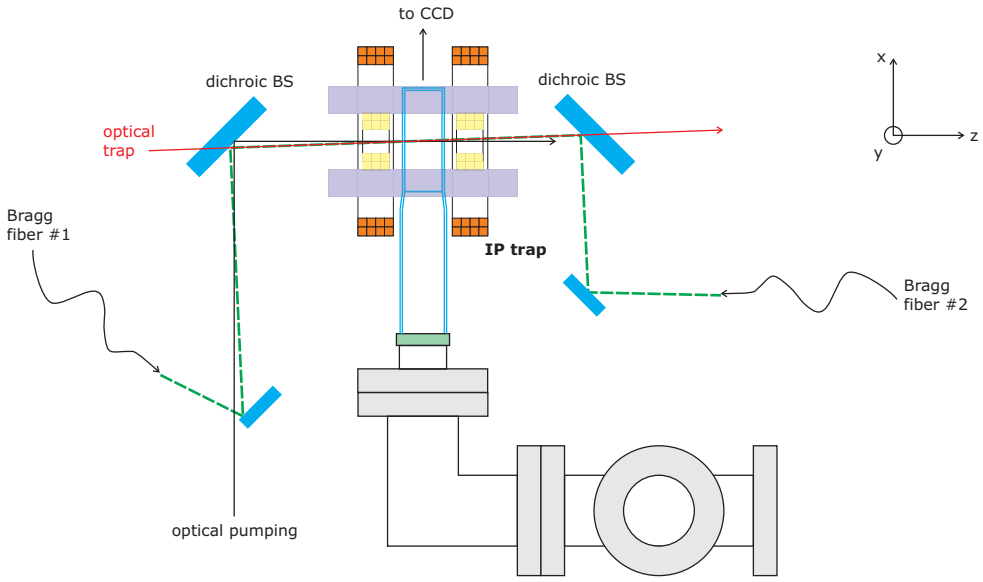

Figure 7.2: Simplified schematic of the science cell area including the Bragg laser beams, the science cell optical pumping light, and the optical trapping beam. The Bragg beams (shown as a dashed green line) are delivered by two optical fibers. The Bragg light is overlapped with the optical trapping beam to assure that Bragg excitations are along the axis of the condensate. The optical pumping and Bragg light are misaligned by a few degrees so that the beams do not need to be combined with a beamsplitter. The Bragg beam diameter is a few mm at the center of the science cell.

difference. The light from the Bragg laser is split into two beams with a polarizing beamsplitter cube. Each beam is passed through an 80 MHz AOM. One of the AOMs is set exactly at 80 MHz and the other AOM frequency is tunable. For simplicity we use a pair of synthesized frequency generators to create the 80 MHz signals sent to the AOMs. In addition to controlling the relative frequency of the Bragg beams, the AOMs are used to generate short duration pulses of the light.

7.4 Obtaining Bragg spectra with strongly interactions

This section describes the technique we use to detect the signal of Bragg spectroscopy in the strongly interacting regime. Two-photon Bragg transitions in our experiment cause atoms to be scattered from the condensate into a momentum state with a velocity of 1.2 cm/s. The total momentum of the scattered atoms is the signal for Bragg spectroscopy. The standard method for determining the total momentum is to count the number of atoms scattered after they exit the BEC. Since the Bragg laser beams are oriented along the axial direction in our experiments, it takes approximately 20 ms for the scattered atoms to completely exit the BEC. During that 20 ms, collisions between the Bragg scattered atoms and the condensate occur. Eventually enough collisions occur that none of the Bragg scattered atoms are observed to cleanly exit the BEC. Using the ^{85}Rb Feshbach resonance we can minimize the collision rate in the condensate so that few collisions occur during the 20 ms it takes for the Bragg scattered atoms to exit the BEC. Figure 7.3 (a) shows an absorption image acquired 40 ms after the Bragg light was applied. For this measurement, immediately after the Bragg light is switched off the scattering length is ramped in 0.2 ms to less than 10 a_0. The condensate appears on the left hand side of the image and the Bragg scattered atoms are on the right. We can cleanly obtain Bragg spectra using this sequence as long as the scattering length during the Bragg pulse is below about 300 a_0. For comparison, Figure 7.3 (b) shows an absorption image under the same conditions as in (a), except the scattering length was not ramped after the pulse. As is observed in the image, collisions severely compromise the signal for Bragg spectroscopy.

Unfortunately, the successful method described above, in which the scattering length is lowered to minimize collisions between the Bragg scattered atoms and the condensate, only works if the scattering length during the Bragg pulse is smaller than approximately 300 a_0. If the scattering length is higher, collisions during the pulse are rapid enough that our signal for Bragg spectroscopy is severely compromised. So we use another technique to extract a signal for Bragg spectroscopy, which works equally well even at large a. We exploit collisions between the quasiparticles and the condensate to measure the momentum imparted to the BEC [165, 166]. Related experiments have been performed with a strongly interacting Fermi gas by C. Regal. For this technique immediately after the Bragg beams are extinguished, we ramp the ^{85}Rb scattering length to 900 a_0 to increase the elastic collision cross section. The quasiparticles excited by the Bragg pulse then rapidly collide with the condensate and deposit momentum along the optical trap axis. The total momentum generated by Bragg spectroscopy causes a center-of-mass (COM) oscillation in the condensate axial position. We detect the momentum by monitoring the amplitude of the condensate COM oscillation as a function of time; an example of the oscillation is shown in Figure 7.4. We fit the data to a sine wave in order to extract the oscillation period and amplitude.

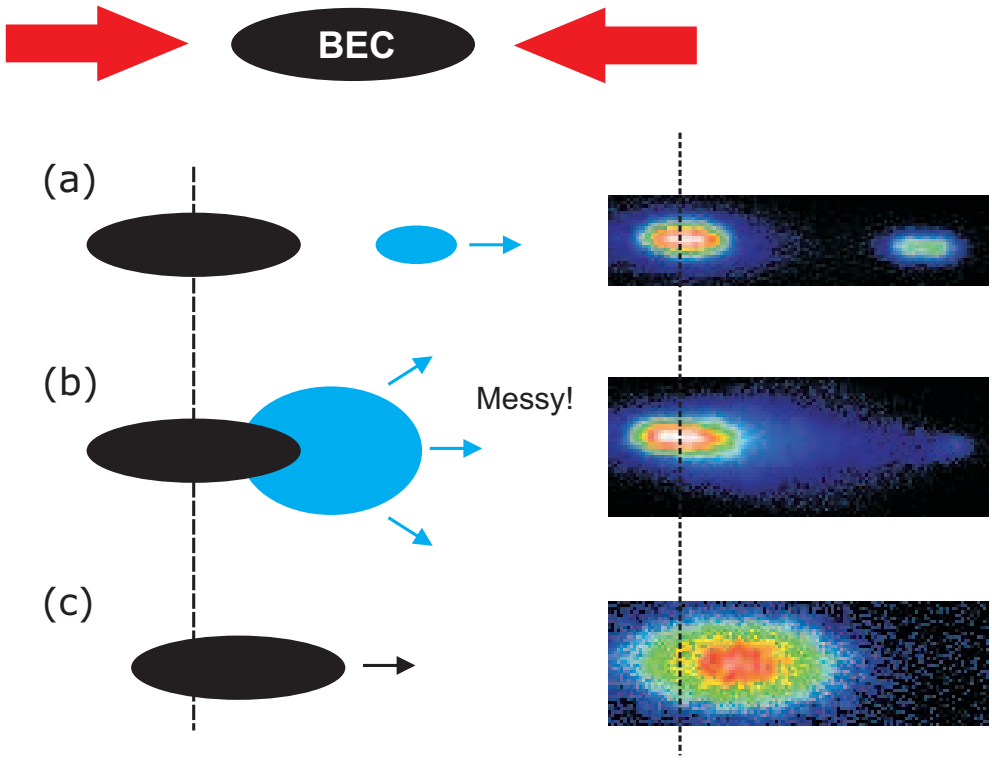

Figure 7.3: A comparison of different Bragg spectroscopy detection techniques. (a) The number of Bragg scattered atoms is directly counted after the atoms exit the BEC. The scattering length was set to 150 a_0 during the Bragg pulse. For this technique to be successful collisions between the Bragg scattered atoms and the BEC must be minimized. Immediately following the Bragg pulse the scattering length is tuned close to zero. (b) The scattering length was not tuned toward zero after the Bragg pulse. Many collisions occurred between the Bragg scattered atoms and the condensate, and our signal is diminished. (c) Our method for Bragg spectroscopy in which all the Bragg scattered atoms collide many times with the BEC. The momentum is deposited into the condensate which generates a COM oscillation. The amplitude of this oscillations is our signal. The center position of the condensate in (c) is clearly offset from the condensate on the left hand side of (a) and (b).

We studied the signal-to-noise ratio of our Bragg spectroscopy signal. Since our signal is the amplitude of condensate COM oscillations, we must detect the position of the BEC along its axis with high precision. We optimized the probe beam intensity for our absorption imaging to produce the lowest noise per pixel in the processed absorption image. We determined that the lowest noise is obtained when the intensity is set such that the fluctuations in each pixel is primarily due to shot noise. Naturally, we also found that the axial size of the condensate is important in determining the center position of the cloud. We acquired our Bragg spectroscopy data when the phase of the axial breathing motion is such that the size of the cloud is smallest.

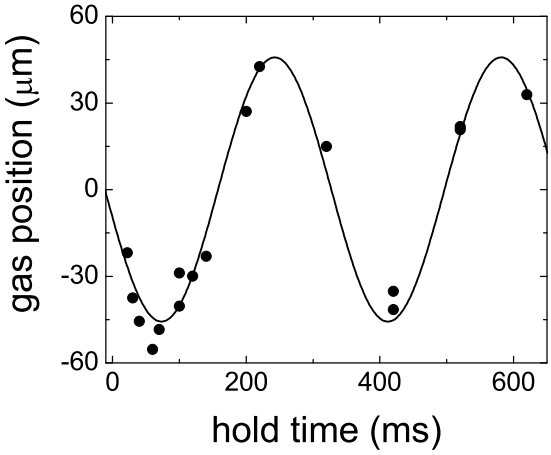

Figure 7.4: A center-of-mass condensate oscillation along the axial direction of the optical trap induced by two-photon Bragg transitions. The amplitude of this motion is our signal for Bragg spectroscopy. Bragg spectra are obtained by monitoring the condensate position at 230 ms.

Our technique for Bragg spectroscopy requires a stable condensate position between repeated runs of the experiment. Since the Bragg beams are aligned along the axis of the condensate, the stability in that direction is critical. In particular, we observe residual COM motion in the axial direction of the trap due to a slight misalignment during the optical trap load from the magnetic trap.[3] [4] This "sloshing" motion appears as a Doppler shift of the Bragg resonance, and the slosh amplitude and phase is not perfectly repeatable from run-to-run of our experiments. To solve this problem, we applied an rf field to the atoms that was only resonant with the edges of the cloud along its axis. The rf damps the amplitude of the sloshing motion by selectively removing the most energetic atoms from the optical trap. For the optimum removal of slosh, rf fields were applied at frequencies near both the ^{85}Rb and ^{87}Rb resonances. The rf effectively

[3] Due to the details of our system we are not able to correct this misalignment.

[4] The COM motion does not fully decay during the evaporation since the contribution of anharmonic terms to the axial potential is small. The optical trap evaporation primarily removes energy along the radial direction of the trap and therefore the COM motion remains throughout the cooling.

damps the sloshing motion, at the end of evaporation the position stability of the ^{85}Rb condensate is better than 2.5 μm (standard deviation). Typically the size of our Bragg signal is 60 μm.

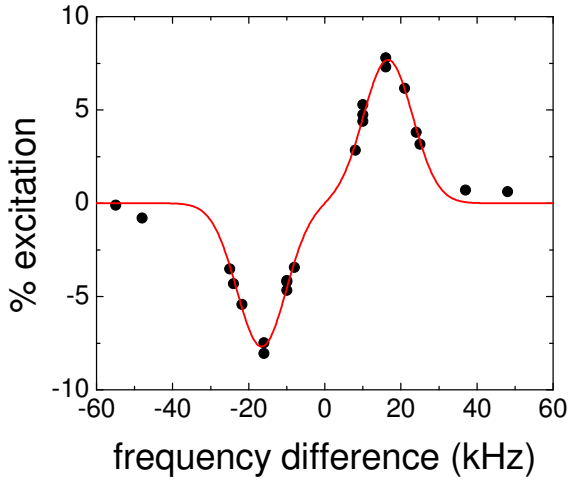

Figure 7.5: A typical Bragg spectrum acquired at a scattering length of 900 a_0, with $n\,a^3 = 0.01$. The Bragg pulse duration was 0.087 ms. We extract the center position and width of the Bragg spectrum by fitting the data to the difference of two gaussians. Since our data is anti-symmetric about zero, the gaussian fit is performed with only a single value of the amplitude, the center position, and the width.

To record the Bragg resonance of a condensate we monitor the amplitude of the condensate oscillation as we vary the frequency difference between the two laser beams. For each frequency difference, we measure the position after a 230 ms hold in the optical trap at which time the oscillation amplitude is largest. Figure 7.5 shows a typical Bragg spectrum for a strongly interacting condensate. From the measured Bragg resonance we extract the linewidth and line shift of the resonance by fitting the spectrum to the difference of two gaussians. Here we define the Bragg line shift as the difference of the measured center frequency and the free-particle energy $\frac{\hbar^2\,k^2}{2\,m}$.

7.5 Momentum signal for a weakly interacting gas

Our signal for Bragg spectroscopy is the amplitude of the condensate center-of-mass oscillation along the axis of the optical trap. The on-resonance signal size depends on the Bragg laser power, the pulse length, and the detuning from the atomic resonance. We extract the total momentum excited from the oscillation amplitude based on knowledge of the harmonic trapping frequency. The total momentum per atom imparted to the condensate is

$$P = 2\,\hbar\,k\,\gamma \tag{7.2}$$

where γ is the fraction of the condensate excited. It is useful to note that our Bragg spectroscopy signal does not explicitly depend on the absolute number of atoms in the BEC. Following the analysis of Refs. [167, 168] the fraction of the condensate that undergoes a two-photon Bragg transition is given by

$$\gamma = \sqrt{\frac{\pi}{2}} \frac{\Omega_R^2 \, t_p}{2 \, \sigma} \tag{7.3}$$

where t_p is the length of the Bragg pulse, σ is the RMS width of the Bragg response lineshape, and $\Omega_R = \frac{\Gamma^2}{4\Delta} \frac{\sqrt{I_1 \, I_2}}{I_{sat}}$ is the two-photon Rabi frequency and Δ is the detuning of the Bragg laser beams from atomic resonance.[5] This formula is only valid when the fraction of the condensate excited is small, the duration of the Bragg pulse is short compared to the trap oscillation time but long compared to the inverse of the frequency difference between the Bragg laser beams, and the momentum of the excitations is large ($k\,\xi \gg 1$).

Figure 7.6 shows the fraction of a ^{85}Rb condensate excited by two-photon Bragg transitions as the Bragg laser power and pulse length are varied. The fraction excited scales quadratically with the Bragg pulse duration, and it scales linearly with the product of the two laser beam intensities. In the figure, the solid lines represent the prediction of Eqn. 7.2 for the total momentum per atom imparted to the condensate by Bragg spectroscopy. The measured Bragg spectra presented in this chapter were all obtained with a combination of intensity and pulse length such that the number of atoms excited were in the range of 5% to 10%. We expect that this means the Bragg scattering process does not dramatically alter the properties of the condensate. Furthermore, our signal for Bragg spectroscopy, namely the amplitude of condensate COM oscillations, does not saturate until the excitation fraction is much larger than 10% (Fig. 7.6).

7.6 Bragg lineshape function for a trapped BEC

To understand the expected dependence of the line shift and linewidth of the Bragg resonance on atom-atom interactions, we have modeled the Bragg resonance lineshape using existing theories. Here the Bragg resonance refers to the amount of momentum imparted to the condensate as a function of the excitation energy; an example was shown in Fig. 7.5.[6] To theoretically understand a lineshape such as this, we calculate the rate of Bragg scattering which determines the momentum imparted. The Bragg scattering rate can be separated into the product of two terms; the rate is given by [169]

$$\Gamma_{Bragg} = \frac{2\,\pi}{\hbar} \, \frac{\left(\hbar \, \Omega_R\right)^2}{4} \times S(\vec{k}, E) \tag{7.4}$$

where $\vec{k}$ is the wave vector of the excitation and E is the energy of the excitation. In Eqn. 7.4 the term on the left ($\left(\hbar \, \Omega_R\right)^2$) depends only on the laser beams and the single atom-photon coupling, while the right hand term ($S(\vec{k}, E)$) depends only on the properties of the condensate, such as the excitation spectrum, chemical potential, size, *etc.* The dynamic structure factor $S(\vec{k}, E)$ has been studied extensively for the case of a weakly

[5] In this formula we have assumed that the excitations are free-particle-like and the static structure factor of the condensate is unity. See the next section for details of the structure factor.

[6] Experimentally the excitation energy is the frequency difference of the Bragg laser beams.

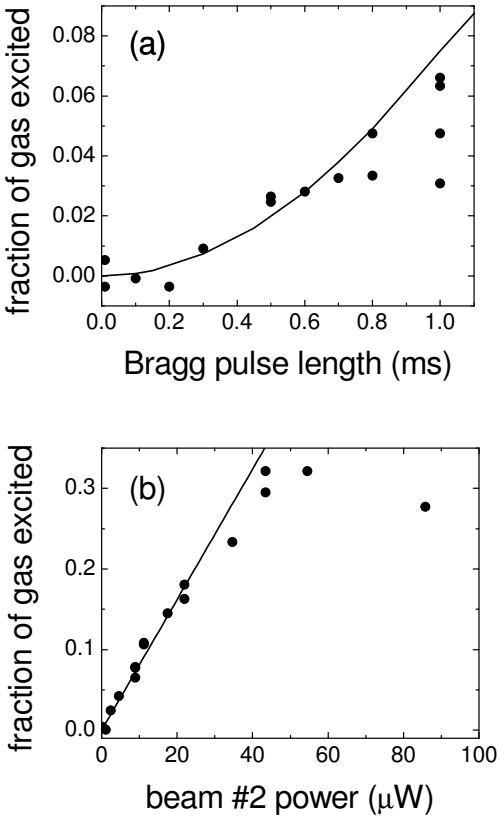

Figure 7.6: (a) Fraction of the condensate excited as a function of Bragg pulse length. The Bragg laser powers were fixed at 35 μW and 2.5 μW and the beam $1/e^2$ radii are approximately 2.3 mm and 1.3 mm, respectively. The data points at 1 ms are noisy since the linewidth of the Bragg resonance is so narrow. (b) Fraction of the condensate excited as a function of Bragg laser power. The pulse length was fixed at 0.5 ms and one of the laser beams had a power of 35 μW while the other power was varied. The solid lines are the prediction for the fraction of the condensate excited from Eqn. 7.2.

interacting Bose-Einstein condensate. In particular modifications of $S(\vec{k}, E)$ due to the inhomogeneous density of a trapped condensate have been considered [170, 169, 167]. Since the Bragg scattering rate is proportional to $S(\vec{k}, E)$, the line shift and linewidth can be calculated directly from $S(\vec{k}, E)$. In this section we present the dynamic structure factor calculated in two approximation schemes: the impulse approximation (IA) and the local density approximation (LDA).

In the impulse approximation (IA), which can be applied when the excitation momentum ($\hbar\,\vec{k}$) is very large, the form of the dynamic structure factor is dominated by Doppler broadening. Here Doppler broadening refers to the fact that Bragg scattering is sensitive to the momenta of the trapped atoms. Due to the finite size of a trapped condensate, there is a distribution of atomic momenta that tends to broaden the Bragg resonance. The distribution of momenta is given by the Fourier transform of the spatial density distribution; a small-sized BEC has a large spread in momentum. For the IA case, $S(\vec{k}, E)$ is given by [170]

$$S(\vec{k}, E)_{IA} = \frac{m}{\hbar k} \int dp_x\, dp_y\, n_z(p_x, p_y, p_z) \tag{7.5}$$

where $n_z(p_x, p_y, p_z)$ is the momentum distribution of the condensate which is integrated along the two directions that are perpendicular to the Bragg beams and $p_z = \frac{m}{\hbar k}(E - E_r(k))$ with $E_r(k) = \frac{\hbar^2 k^2}{2\,m}$ is the energy of the excitation. For fixed momentum in the IA, the width in energy of $S(\vec{k}, E)$ scales as $\hbar k/R_z$ where R_z is the size of the condensate. As shown in Figure 7.2, the Bragg light is aligned along the axis of the condensate, in the direction where the BEC is larger than 0.1 mm. The contribution from the IA is very small in our experiments with a typical value of 30 Hz, since the size R_z is typically on order of 0.1 mm.

In the local density approximation (LDA), the form of the dynamic structure factor is dominated by the condensate density profile. For the LDA case, $S(\vec{k}, E)$ is given by [170]

$$S(\vec{k}, E)_{LDA} = \frac{1}{\hbar} \int d\vec{r}\, n(\vec{r})\, \delta(E - \hbar\,\omega(n(\vec{r}), k)) \frac{(\hbar k)^2}{2\,m\,\hbar\,\omega(n(\vec{r}), k)} \tag{7.6}$$

where $n(\vec{r})$ is the density distribution of the BEC and $\hbar\,\omega(k)$ is the Bogoliubov excitation energy (Eqn. 7.1) evaluated at the local density $n(\vec{r})$. Our experiments are performed under conditions in which the condensate dynamic structure factor is described by the LDA. This approximation is used below to calculate the excitation spectrum of a trapped BEC with inhomogeneous density.

7.6.1 Line shift

The Bragg line shift is defined here to be the difference in the condensate excitation energy ($E(k)$) and the free-particle energy ($E_r(k)$). Since we are only interested in changes to the condensate excitation spectrum due to interactions, we subtract the free particle energy from $E(k)$ to obtain the Bragg line shift.

7.6.1.1 The weakly interacting case

The center of the Bragg resonance for a trapped BEC in the weakly interacting regime is calculated by averaging the Bogoliubov excitation spectrum (Eqn. 7.1) over

the inhomogeneous density of the condensate. By applying the Thomas-Fermi approximation for the condensate density, the excitation energy for any value of k is given by [170, 168]

$$E(k) = \sqrt{(c(k))^2\ \hbar^2 k^2 + \left(\frac{\hbar^2 k^2}{2\,m}\right)^2} \tag{7.7}$$

where $c(k)$ is a complicated function of momentum and the condensate chemical potential. For small k in the phonon regime ($k\,\xi \ll 1$) $c(k) = \frac{32}{15\pi}\sqrt{\mu/m}$, and in the free-particle regime ($k\,\xi \gg 1$) $c(k) = \sqrt{\frac{4}{7}\mu/m}$. Here μ is the chemical potential of the condensate given by $\mu = g\,n_0$ where n_0 is the density at the center of the condensate and $g = \frac{4\,\pi\,\hbar^2}{m}\,a$.

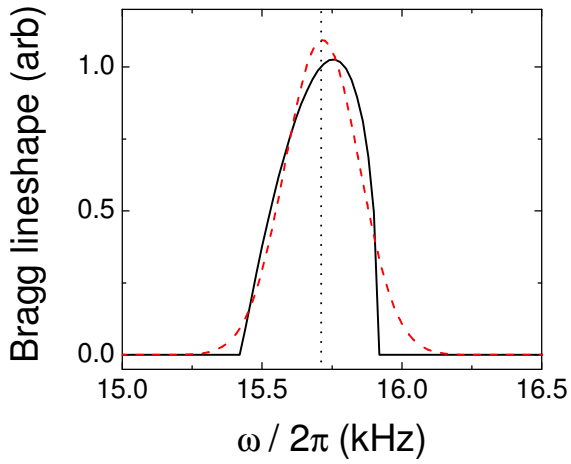

Figure 7.7: The solid black line is the calculated Bragg lineshape plotted as a function of the frequency $\omega/2\pi$. The lineshape is asymmetric due to the Thomas-Fermi density. The vertical dotted line indicates the mean excitation energy of the condensate. The red dashed line shows a gaussian fit to the Bragg lineshape which accurately determines the mean excitation energy.

Using the Thomas-Fermi approximation for the condensate density, the Bragg lineshape is given by the dynamic structure factor

$$S(\vec{k}, E)_{LDA} = \frac{15}{8\,\hbar}\frac{E^2 - E_r^2}{E_r \mu^2}\sqrt{1 - \frac{E^2 - E_r^2}{2\,E_r\,\mu}}. \tag{7.8}$$

The Bragg lineshape is plotted in Figure 7.7 as a function of the frequency E/h. The center of the Bragg resonance is the mean value of this function. The Bragg lineshape is asymmetric due to the Thomas-Fermi profile. However, it is interesting to note that a gaussian fit to the asymmetric shape still yields the correct mean value of the

distribution. In the free-particle regime the mean energy is given by

$$E(k) = E_r(k) + \frac{4}{7}\mu. \tag{7.9}$$

The second term, which is independent of k, is the condensate mean-field contribution to the excitation energy. This formula for the excitation energy is valid in the limit that the chemical potential is small compared to the free-particle energy or that $k\xi \gg 1$.

7.6.1.2 Estimates of the Bragg line shift with strong interactions

In this section we present calculations of the excitation spectrum of a strongly interacting homogeneous condensate using existing theories.[7] Later on in this chapter we compare the predictions of these theories to our measured Bragg spectra of strongly interacting ^{85}Rb condensates. When the atom-atom interactions in the condensate are strong, the excitation spectrum is not accurately described by the Bogoliubov formula. In particular, when na^3 is no longer small beyond mean-field effects are expected to be important, and when $k\,a$ is no longer small two-body scattering in the condensate is expected to be momentum dependent. Beliaev has derived two corrections to the Bogoliubov excitation spectrum of a homogeneous BEC using perturbation theory with the small parameter na^3 [171, 160]. Note that Beliaev's theory may be applied to excitations with any value of $(k\,\xi)$. The calculations are somewhat similar in nature to those performed by Lee, Huang, and Yang to obtain the first-order correction to the condensate chemical potential which scales as $\sqrt{n\,a^3}$. In the first correction the condensate is assumed to be dilute with $na^3 = 0$, but $k\,a$ may take on any value and the excitation spectrum is given by [160]

$$E(k) = \sqrt{\left(E_r + \frac{8\,\pi\,\hbar^2}{m}\,n\,\Re(f_s(k/2)) - n\,g\right)^2 - n^2\,(f_s(k))^2} \tag{7.10}$$

where $\Re(f_s)$ is the real part of the symmetrized s-wave scattering amplitude that is discussed in Section 7.6.3. [8] It is useful to think of $\Re(f_s(k/2))$ as a scattering length that depends on the momentum wave vector. The first Beliaev correction tends to reduce the excitation energy of the condensate since excitation-condensate interactions via two-body scattering are reduced as $k\,a$ is increased. This reduction is related to the famous Ramsauer-Townsend effect in which a very large scattering phase shift associated with strong interactions actually *suppresses* the $s-$wave elastic cross section [48]. In the limit that $k\,a \ll 1$, $f_s(k/2) \to a$ and the Bogoliubov formula (Eqn. 7.1) is recovered.

The Beliaev second order correction to the Bogoliubov theory considers beyond mean-field effects by allowing na^3 to take on a finite value. However in this second approximation it was assumed that $k\,a = 0$ so that two-body scattering is independent of momentum. The excitation energy in the second approximation is given by the poles of Eqn. (5.17) in [160]. Analytical results for the excitation energy in the second Beliaev approximation were obtained for the limiting cases of low-momentum phonon

[7] We thank Shai Ronen and John Bohn for helping us understand the theory presented here.

[8] Shai Ronen and John Bohn have calculated that $f_s(k) \approx 4\,\pi a$ to a few percent for the experiments presented in this chapter.

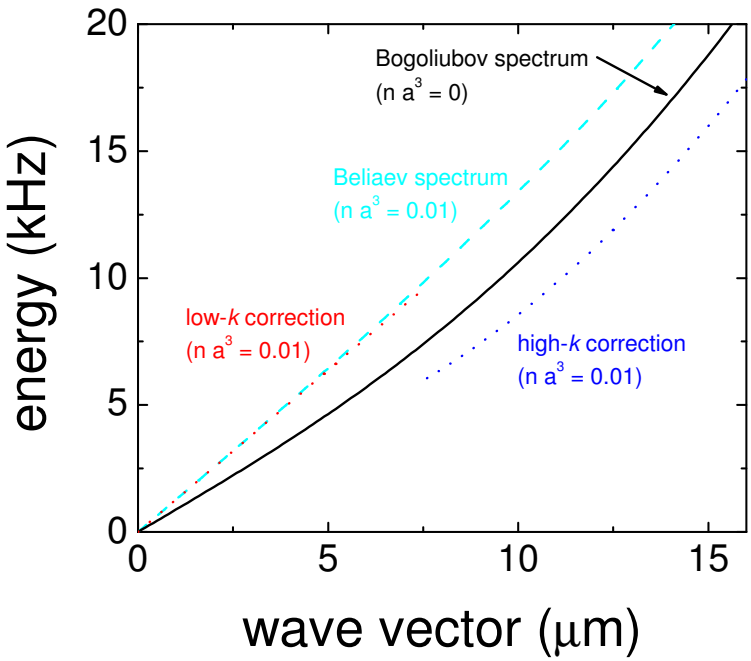

Figure 7.8: Excitation energy as a function of the wave vector k. The black curve is the Bogoliubov spectrum for weak interactions. The red and blue curves are the respectively low-k and high-k limits of the excitation energy including the $n\,a^3$ correction. The scattering length is 900 a_0 and the density is 10^{14} cm^{-3}. The red and blue curves were arbitrarily broken at 9 μm^{-1}. For each theory line shown here we assume that $k\,a = 0$.

excitations and large-momentum free-particle excitations. For small k, the excitation energy is

$$E(k) = \sqrt{\frac{g\,n}{m}}\,\hbar\,k\left(1 + \frac{8}{\sqrt{\pi}}\sqrt{na^3}\right). \tag{7.11}$$

For large k excitations in the free particle regime, the energy is expected to be smaller than the mean-field prediction, but the correction factor also scales as $\sqrt{n\,a^3}$. The result for large k is

$$E(k) = E_r(k) + g\,n\,\left(1 - \frac{32}{3\sqrt{\pi}}\sqrt{na^3}\right). \tag{7.12}$$

Equations 7.12 and 7.11 are plotted as a function of the wave vector k in Figure 7.8 for a strongly interacting ^{85}Rb condensate with a density of 9×10^{13} cm^{-3} and a scattering length of 900 a_0. Shai Ronen and John Bohn have used the Beliaev second order approximation to calculate the excitation spectrum of a condensate for excitations with an arbitrary wave vector k. This allows us to connect the small-k and large-k limits. For comparison, their calculation of the condensate excitation energy is also shown in Fig. 7.8. Note that for the range of wave vector that is plotted, the predicted excitation energy has not yet reached its large-k limiting value. All of the experiments described in this chapter were performed with wave vector of 16.1 μm^{-1}. At this value, the Beliaev theory with $k\,a = 0$ and finite na^3 predicts that the excitation energy is *larger* than the Bogoliubov prediction.

The free-particle excitation energy of a strongly interacting BEC can also be obtained using Hartree-Fock-Bogoliubov (HFB) theory. The HFB energy is given by [172]

$$E(k) = E_r(k) + 2\,g\,n - \mu. \tag{7.13}$$

The second term represents interactions between the condensate and the excitations generated by Bragg scattering, including both direct and exchange interactions. The third term is the chemical potential of the condensate. As shown in Eqn. 7.13, the HFB is only valid in the limit that $k\,a = 0$ and $na^3 = 0$. We have modified the HFB picture to include momentum-dependent two-body scattering and beyond mean-field effects. The energy of direct and exchange interactions between the condensate and the excitations is modified to be $\frac{8\pi\hbar^2}{m}\,n\,f_s(k/2)$. We also include the first-order LHY correction to the condensate chemical potential due to strong interactions given by $\mu = g\,n\,\left(1 + \frac{32}{3\sqrt{\pi}}\sqrt{na^3}\right)$. The energy of large-$k$ excitations is given by

$$E(k) = E_r(k) + \frac{4\,\pi\,\hbar^2\,n}{m}\left(2\,\Re(f_s(k/2)) - a\,\left(1 + \frac{32}{3\sqrt{\pi}}\sqrt{na^3}\right)\right). \tag{7.14}$$

In Figure 7.9 we have plotted the predicted Bragg resonance line shift from the different theories presented here as a function of scattering length. Since the theories discussed here are for a homogeneous gas, the results shown in the figure are for the mean density of our trapped condensate. The top axis of the figure shows the size of the LHY correction to the condensate chemical potential as a function of scattering length. At 900 a_0 the LHY correction is 0.6 indicating the importance of beyond mean-field effects.

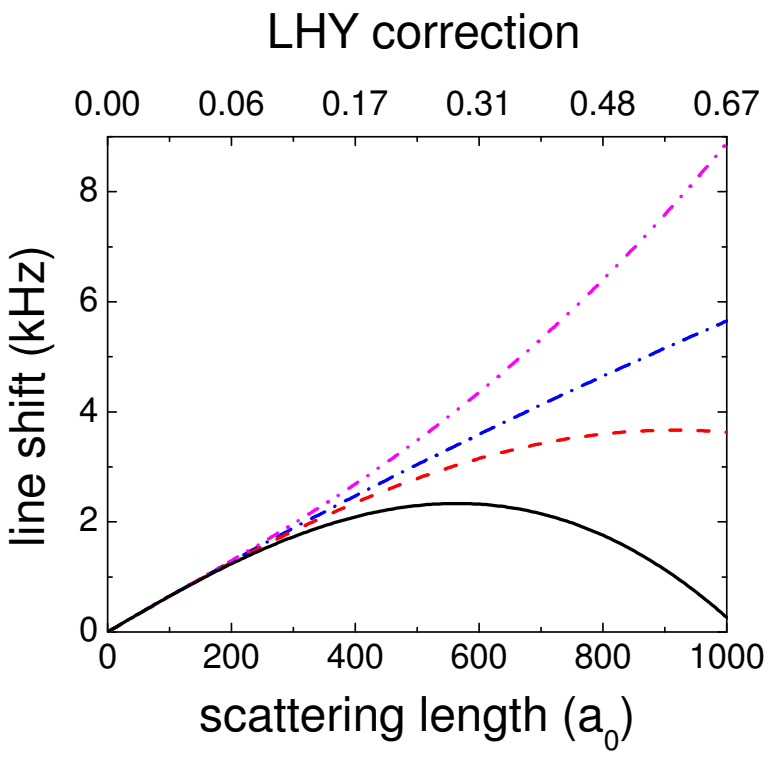

Figure 7.9: (a) Theoretical Bragg line shift of a homogeneous condensate as a function of scattering length. The curves, in order of smallest to largest shift, correspond to the following theories: Hartree-Fock-Bogoliubov (solid black), Beliaev first approximation (dashed red), Bogoliubov (dash-dot blue), and Beliaev second approximation (dash-dot-dot magenta). Calculations were performed with a mean density of 8.5×10^{13} cm^{-3} and an excitation momentum of $2\,\hbar\,k_L$. For reference the top axis shows the size of the LHY correction to the condensate chemical potential.

7.6.2 Linewidth

In order to accurately measure the Bragg resonance line shift, it is important to quantitatively understand the width of the Bragg resonance in our experiments. In this section we present predictions of the Bragg resonance width using existing theories. Later on in this chapter we will compare these predictions to our experimental data. The width of the Bragg resonance depends on several contributions, including the duration of the Bragg pulse, the distribution of momenta in the inhomogeneous condensate, and collisions during the Bragg pulse. We model the lineshape of each contribution separately. To understand the composite lineshape that includes each of these contributions, we calculate the convolution of the contributing lineshapes. For further detail on calculating composite lineshapes see, for example, Ref. [83]. A gaussian fit to the convolution extracts the total linewidth. Since our measured Bragg spectra are also fit to a gaussian, we can directly compare our measurements with the model.

The lineshape associated with the duration of Bragg spectroscopy is a sinc^2-function, and the lineshape due to the inhomogeneous density of the condensate is the asymmetric function shown in Figure 7.7. The convolution of these two lineshapes is shown in Figure 7.10. Since it is similar to a gaussian, we can extract the total width with a fit. The gaussian width σ of the convolution is

$$\sigma = \sqrt{\left(\frac{0.36}{t_p}\right)^2 + \left(\sqrt{\frac{8}{147}}\frac{\mu}{h}\right)^2} \tag{7.15}$$

where t_p is the duration of the Bragg pulse and $\sqrt{\frac{8}{147}}\frac{\mu}{h}$ is the frequency width due to the inhomogeneous density of the condensate. The linewidth of the Bragg resonance might be increased due to beyond mean-field effects. For example the contribution due to the inhomogeneous density might be increased in the strongly interacting regime since the LHY chemical potential is larger than the mean-field value.

Collisions between the condensate and the quasiparticle excitations created by Bragg scattering tend to broaden the Bragg resonance. Beliaev first studied the decay of quasiparticles due to collisions in Ref. [160]. He showed that the excitation spectrum has an imaginary component equal to the quasiparticle-condensate collision rate that should be interpreted as the energy width of the spectrum. We note that this imaginary component only appears in the result of Beliaev's second approximation where finite $n\,a^3$ is considered but the limit that $k\,a = 0$ is assumed. The lineshape associated with quasiparticle-condensate collisions is a lorentzian that is characterized by a full width at half maximum (FWHM) $\gamma = \frac{1}{2\,\pi\,\tau}$. Here $\frac{1}{\tau}$ is the collision rate in the gas given by $\frac{1}{\tau} = \langle n\rangle \sigma_{el}(k) \langle v_{rel}\rangle$ where $\sigma_{el}(k)$ is the elastic collision cross section, $\langle n\rangle$ is the average density, and $\langle v_{rel}\rangle = \hbar\,k/m$ is the mean relative speed. At low momentum, the elastic cross section for quasiparticle-condensate collisions is suppressed due to energy and momentum conservation; this suppression has already been observed via Bragg spectroscopy of a ^{87}Rb condensate [165]. Shai Ronen and John Bohn have calculated the elastic cross section for quasiparticle-condensate collisions based on Ref. [160]. We have used their result to predict the lorentzian FWHM.

We are able to determine the expected width of the Bragg resonance by calculating the convolution of all three lineshapes (pulse duration, inhomogeneous density, and quasiparticle-condensate collisions) and performing a gaussian fit. Figure 7.11 shows

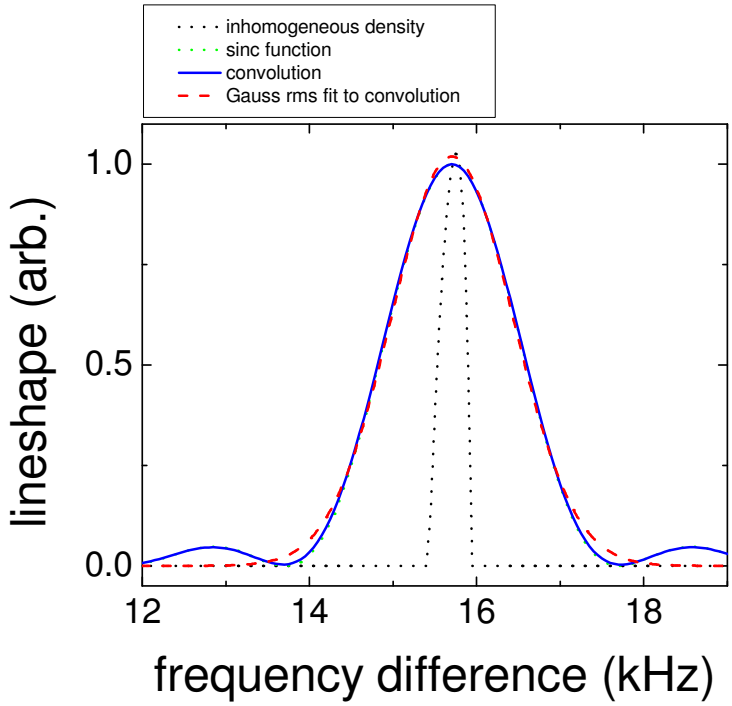

Figure 7.10: A comparison of the lineshape due to the inhomogeneous density of the condensate (black dotted line) and the sinc-function lineshape of the Bragg pulse (green dotted line). The convolution of these two function is the blue solid line. We extract the total width from a gaussian fit (red dashed line) to the convolution.

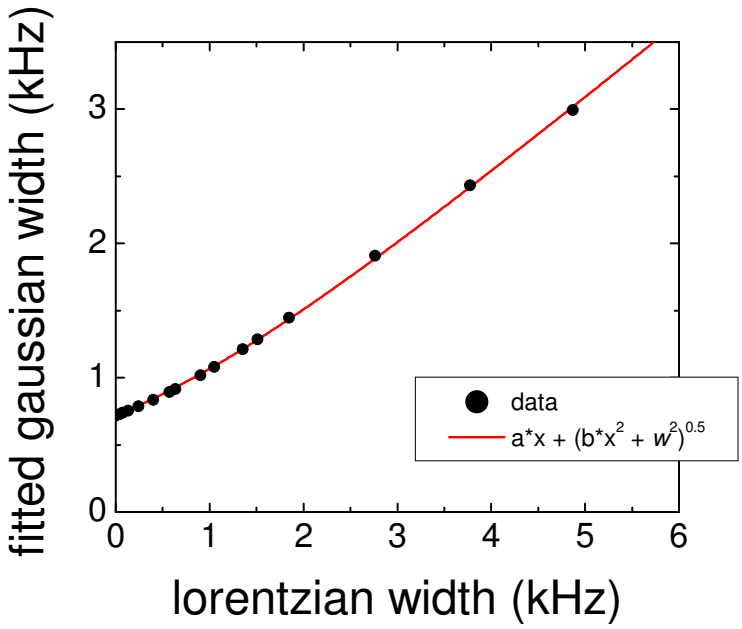

Figure 7.11: Gaussian width from a fit to the convolution of the three lineshape functions versus the lorentzian width γ. The data are fit to the function $a\,\gamma + \sqrt{b\gamma^2 + w^2}$ to extract the parameters a and b. This fitting function resembles that which is used to understand the total width of a Voigt profile [2]. A Voigt profile is the convolution of a gaussian and a lorentzian.

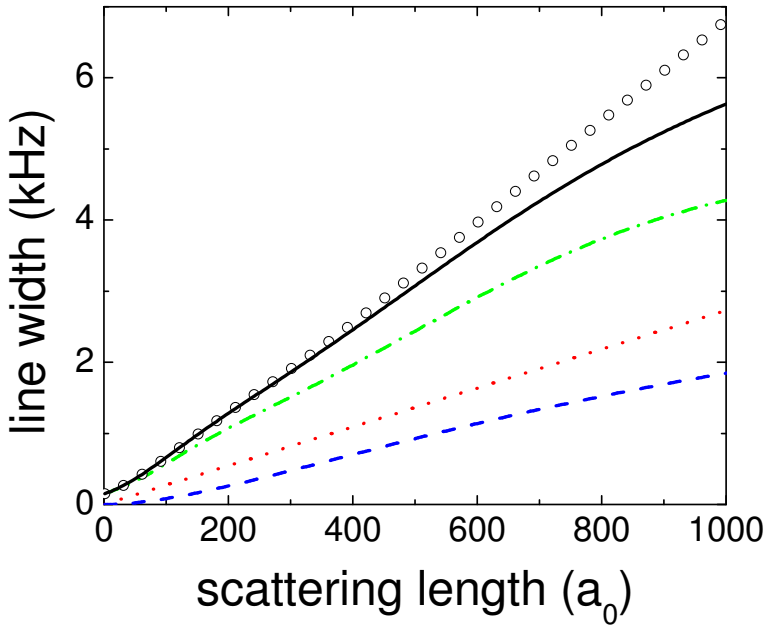

Figure 7.12: Prediction of the Bragg resonance width as a function of scattering length. The dotted lines correspond to different contributions to the total RMS width including the lorentzian FWHM width due to condensate-excitation collisions (blue dashed line), the gaussian RMS widths due to the inhomogeneous density (red dotted line), and the pulse duration (green dash dotted line). The solid black line is the prediction for the total width of the Bragg resonance based on a convolution of the profiles for each contribution. To get an idea of the size of beyond mean-field effects on the width, the black open circles are the predicted total width including the LHY chemical potential in the inhomogeneous density contribution. Calculations were performed with a mean density of 8.5×10^{13} cm^{-3} and an excitation momentum of $2\,\hbar\,k_L$.

the calculated gaussian width as a function of the lorentzian width. For this simulation we fixed the Bragg pulse duration to 0.25 ms; the lorentzian width and inhomogeneous density width were simultaneously varied by changing the scattering length.[9] The gaussian width σ of the Bragg resonance based on our convolution modeling is given by

$$\sigma = a\,\gamma + \sqrt{b\,\gamma^2 + \left(\frac{0.36}{t_p}\right)^2 + \left(\sqrt{\frac{8}{147}}\frac{\mu}{h}\right)^2} \tag{7.16}$$

where the numerical factors $a = 0.287$ and $b = 0.089$ were determined from a fit to the data points in Figure 7.11. In general the lorentzian width γ is added to a series of gaussian widths w_i via

$$\sigma = a\,\gamma + \sqrt{b\,\gamma^2 + \sum_i w_i^2}. \tag{7.17}$$

In Figure 7.12 we have plotted the contributions to the Bragg resonance linewidth as a function of scattering length. Also shown in the figure is the combined linewidth which is obtained from a convolution of the three contributing lineshapes. To get an idea of how large beyond mean-field effects on the resonance width might be, the black open circles in the figure show the total width in which the inhomogeneous density contribution includes the LHY chemical potential instead of only the mean-field chemical potential. Since the theories discussed here are for a homogeneous gas, the results shown in the figure are for the mean density of our trapped condensate.

7.6.3 Two-body scattering physics for $k\,a \sim 1$

In this section we review the two-body scattering physics necessary to predict the line shift and linewidth of Bragg spectroscopy in the regime with $k\,a \sim 1$. In particular, we will calculate the dependence of the symmetrized s-wave scattering amplitude ($f_s(k/2)$) on the momentum wave vector of a quasiparticle-condensate collision. This quantity depends on the zero-energy scattering length. Near the ^{85}Rb Feshbach resonance, the zero-energy scattering length is given by $a(B) = a_{bg}(1 - \frac{\Delta}{B - B_{peak}})$ with $\Delta = 10.71(2)$ G, $B_{peak} = 155.041(18)$ G, and $a_{bg} = -443(3)a_0$. A significant advantage of our system is the detailed knowledge of the Feshbach resonance parameters which is available from previous work in the Wieman group [5] and other groups [135]. In experiments performed at 900 a_0 the B-field was set to 158.6 G, nearly 4 G from the peak of the Feshbach resonance.

Following the basic scattering theory in the quantum mechanics text by Sakurai [48], the scattering amplitude is calculated in a partial-wave expansion. Here we consider only s-wave scattering and k_{cm} refers to the relative wave vector of the collision in the center-of-mass frame. The scattering amplitude is given by

$$f = \frac{1}{k_{cm}\cot(\delta) - i\,k} \tag{7.18}$$

which includes the unitarity limit. The scattering phase shift δ is given in the effective range approximation as

$$k_{cm}\cot(\delta) = -\frac{1}{a} + \frac{1}{2}r_e {k_{cm}}^2 \tag{7.19}$$

[9] We verified that this analysis is the same over the range of pulse lengths used in our experiments.

and the effective range parameter r_e was determined analytically in Refs. [173, 174] to be

$$r_e/\beta_6 = \left(\frac{2}{3\chi_e}\frac{1}{(a/\beta_6)^2}\right)\{1 + [1 - \chi_e(a/\beta_6)]^2\} \tag{7.20}$$

with $\beta_6 = (mC_6/\hbar^2)^{1/4}$, $C_6 = 4707(10)$ a.u. for ^{85}Rb [5], and $\chi_e = \Gamma(1/4)^2/2\pi$ where Γ is the Euler-Gamma function. The dependence of the real part of the k-dependent scattering amplitude on the phase shift is given by

$$\Re(f_s(k)) = -\frac{\sin(2\delta)}{2k}. \tag{7.21}$$

We can also determine the dependence of the elastic collision cross section ($\sigma(k/2)$) on the momentum wave vector. It is useful to understand how much the elastic cross section is modified by the unitarity limit and the effective range of the scattering potential. But here we do not consider the suppression of the elastic cross section for low-k quasiparticle-condensate collisions.[10] The elastic collision cross section for quasiparticle-condensate collisions is given by

$$\sigma(k) = \frac{8\pi}{k^2}\sin^2(\delta) \tag{7.22}$$

which is also obtained from the optical theorem result $\mathrm{Im}(f) = k\,\sigma/\,8\pi$. The rate of quasiparticle-condensate collisions is increased by a factor of two due to correlation effects. Both the elastic cross section and the k-dependent scattering amplitude are plotted in Fig. 7.13 as a function zero-energy scattering length. In this analysis the relevant momentum and energy of a collision are given in the center-of-mass frame by $p_{cm} = \hbar\,k_{cm} = \hbar\,k_L$ and $E_{cm} = \frac{p_{cm}^2}{m} = 370$ nK.

We compared the predictions of our analytic formulae for the elastic collision cross section (Eqn. 7.22) and the real part of the scattering amplitude (Eqn. 7.21) to the exact results from a coupled-channels calculation supplied by Chris Greene's group [3]. The k-dependent scattering length (Eqn. 7.21) and the elastic collision cross section (Eqn. 7.22) are shown in Figure 7.13 as a function of the zero-energy scattering length. The excellent agreement between our model and the exact calculation is an indication that the effective range approximation we use is accurate.

7.7 Simulations of the BEC density

A comparison of our experimental Bragg spectra to theory requires a knowledge of the condensate density. For a static condensate the density is extracted from a measurement of the atom number and knowledge of the harmonic trap frequencies using the Thomas-Fermi approximation. However many of our Bragg spectra are obtained with non-static condensates in which the size is changing. We use a variational solution of the Gross-Pitaevskii (GP) equation to model the density based on a knowledge of the scattering length during our experiments [4].

We performed a simple experiment to test our understanding of the time dependent condensate density. A large condensate density oscillation was created by quickly

[10] To our knowledge, no theoretical predictions exist for the cross section of phonon-like quasiparticles interacting with a condensate when $k\,a$ may take on any value.

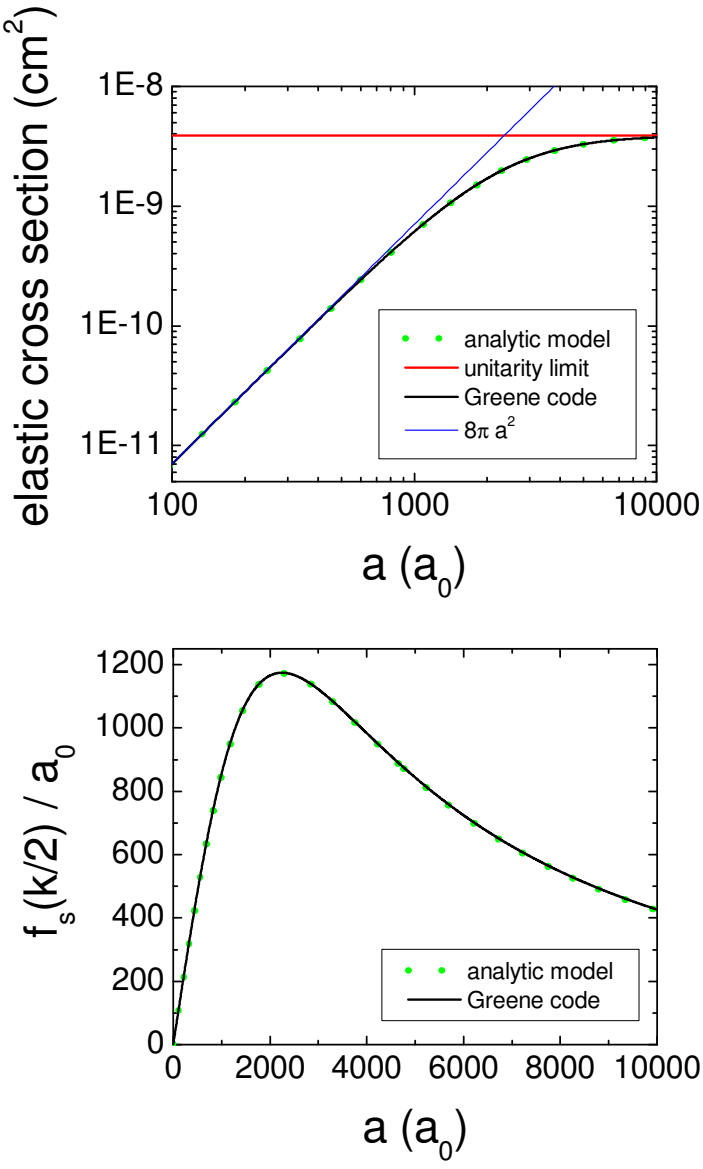

Figure 7.13: (Top) The elastic collision cross section for quasiparticle-condensate collisions with wave vector k_{cm}. (Bottom) The k-dependent scattering length derived from the real part of the scattering amplitude with wave vector k_{cm}. Several quantities are plotted on each graph. The red line is the unitarity limit, the blue line is $\sigma = 8\pi a^2$, the black line is from Ref. [3], and the green dotted line is our analytic results given by Eqn. 7.22 and Eqn. 7.21.

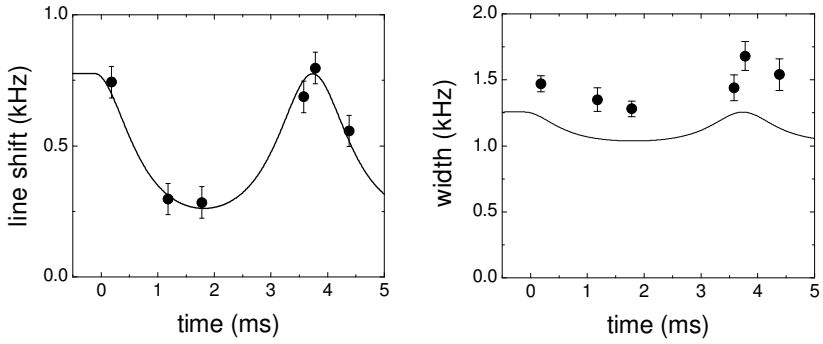

Figure 7.14: Measured Bragg line shift (left) and width (right) as a function of time. A large density oscillation was excited in the condensate, and we detected that oscillation with Bragg spectroscopy. The solid lines are a theoretical prediction based on the model of Ref. [4] for the time-dependent condensate density.

ramping the scattering length from 144 a_0 to 500 a_0 in 0.15 ms. We acquired Bragg spectra as a function of time immediately following the scattering length ramp. A Bragg pulse was applied for 0.25 ms, a duration much less than the radial breathing period of the condensate. The measured Bragg resonance line shift and width are shown in Figure 7.14 as a function of time. We subtracted the free-particle energy $E_r(k)$ from each measurement of the center to obtain the Bragg line shift. In the figure the solid lines represent the theoretical prediction for the line shift (Eqn. 7.9) and the width (Eqn. 7.16) including the results from our time-dependent simulations of the density. There is excellent agreement between the measured line shift and the theory indicating an accurate understanding of the condensate density for some range of parameters. The measured Bragg width is consistently 200 Hz larger than the prediction, and this discrepancy is on order of our typical line shift uncertainty based upon a gaussian fit. As discussed previously, it is important that we understand the Bragg lineshape in order to accurately measure the center position of the resonance and extract the Bragg line shift.

7.8 Bragg spectra of a strongly interacting ^{85}Rb BEC

We have acquired Bragg spectra over a very wide range of scattering length to probe the excitation spectrum of a strongly interacting BEC. To begin the experiment, we create a weakly interacting ^{85}Rb BEC in which the scattering length is 150 a_0. The gas has a mean density of 2.1×10^{13} cm^{-3} and a condensate fraction greater than 85%. We then apply a time-dependent sequence of scattering length ramps (Fig. 7.15 (a and b)) to increase the condensate density (Fig. 7.15 (c and d)) prior to the Bragg spectroscopy pulse. We exploit the aspect ratio $\nu_z/\nu_\rho = 0.022$ of the optical trap to semi-independently control the radial and axial size of the gas, where ν_ρ (ν_z) is the radial (axial) trapping frequency. By lowering the scattering length to 30 a_0 quickly compared to ν_z^{-1}, a condensate axial size oscillation is excited which transiently increases the density. Along its axis the condensate size shrinks by a factor of 2.2 in 120 ms. To further increase the density the scattering length is ramped quickly compared to ν_ρ^{-1}. First the radial size is expanded by increasing to 200 a_0 in 3.7 ms, then the scattering length is ramped to the value a_{evolve} in 0.2 ms and held there for 1 ms. The radial size rapidly shrinks by approximately a factor of two in the final few ms of the sequence. We model the time-dependent condensate density (Fig. 7.15 (c and d)) using a variational solution to the Gross-Pitaevskii (GP) equation [4].

We measured the condensate size as a function of time during the scattering length sequence to monitor the compression; the results are shown in Figure 7.16. In these data the final few milliseconds of the sequence were omitted to study only the axial portion of the compression. Measurements were obtained after a 20 ms ballistic expansion from the optical trap. The curves in the figure are the result of the GP-equation simulation (Section 7.7) including the expansion from the trap. The excellent agreement between our data and the simulation indicates the success of the compression sequence with respect to the axial direction of the condensate. To estimate the uncertainty in condensate density we performed simulations assuming slightly different conditions. The results for a 30% higher or lower density are shown by the dashed lines in the figure. We have separately verified the success of the condensate compression during the final few milliseconds of the sequence by performing a similar experiment.

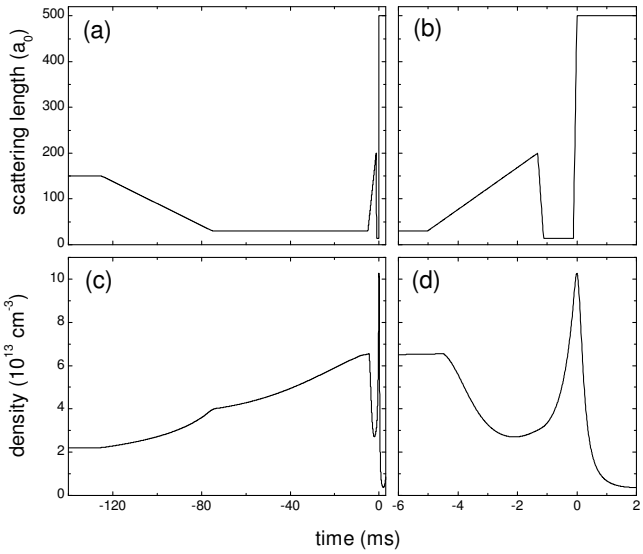

Figure 7.15: (a) Scattering length sequence to increase the condensate density. Knowledge of the scattering length is derived from measurements of the magnetic-field and a previous experimental calibration of the ^{85}Rb Feshbach resonance [5]. The Bragg pulse is initiated at 0 ms immediately following a rapid (0.12 ms) increase to a_{Bragg}. Not shown is the Bragg pulse timing, the ramp to 890 a_0 to excite a condensate center-of-mass oscillation, and the scattering length ramps used during absorption imaging. (b) Expanded view of the scattering length ramps near 0 ms. The radial size of the BEC is lowered by setting the scattering length to a_{evolve}. (c, d) Calculated time-dependent density during the scattering length sequence based on Ref. [4].

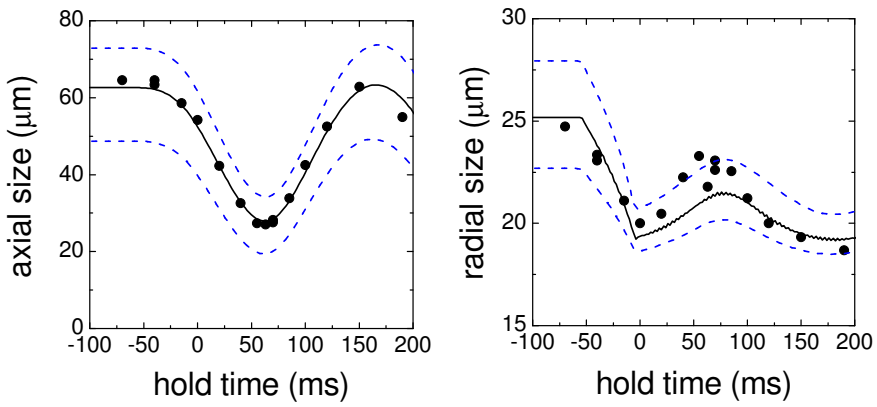

Figure 7.16: Measurements of the condensate axial size (left) and radial size (right) as a function of time during the compression sequence. The solid curves are the result of the GP-equation modeling of the condensate size. The dashed curves indicate the expected sizes if the density were 30% higher or lower. See the main text for more details.

Following the compression of the condensate density, the scattering length is ramped in 0.12 ms to a value between 50 a_0 and 900 a_0. The rate of this magnetic-field ramp does not exceed 17 μs/G. The ramp is designed to be slow compared to typical many body time scales as determined by $\hbar/E_b$, where $E_b = \frac{\hbar^2}{m\,a^2}$ is the two-body binding energy associated with the Feshbach resonance. This ensures that the condensate remains in its many-body ground state throughout our measurements. For each value of scattering length, the compression sequence is optimized so that the predicted average density during the Bragg pulse is 8.5×10^{13} cm^{-3}. Immediately following this scattering length ramp the Bragg spectroscopy pulse is initiated. Since the condensate size rapidly expands after the scattering length is set, the Bragg pulse duration is set so that only a 30% change in the predicted condensate density occurs during the pulse.

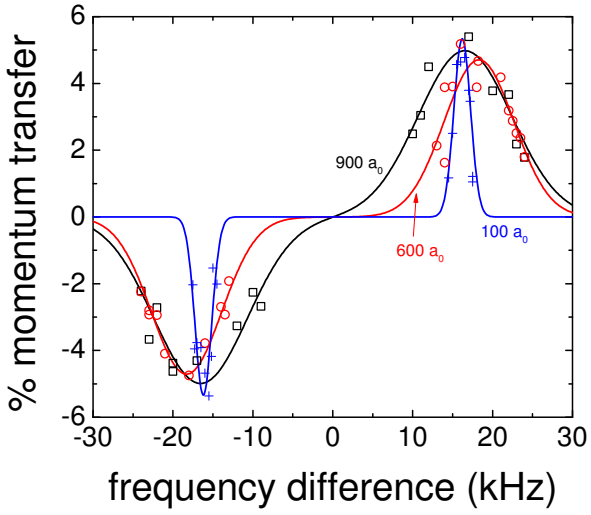

Figure 7.17: Typical Bragg spectra at a scattering length of 100 a_0 (blue crosses), 600 a_0 (red circles), and 900 a_0 (black squares). Lines are fits of the data as described in the text.

Figure 7.17 shows measured Bragg spectra for three values of scattering length. As interactions are increased from zero, mean-field theory predicts a continuous increase in the line shift. A comparison of our data at 600 a_0 and 900 a_0 displays a *decreasing* shift with stronger interactions. This reversal in the line shift trend reflects the onset of strong interactions in the condensate. It is important to note that the character of the condensate excitations also changes with increasing scattering length. At small a the excitations are free-particle-like with $k\,\xi \gg 1$, but at 900 a_0 the character of the excitations is intermediate of the free particle and phonon limits with $k\,\xi = 2$. Theoretical predictions of the line shift in our system must account for this fact. As we increase the strength of interactions, the Bragg pulse duration is shorter and we observe a larger width. The large width of the resonance makes a determination of the center less certain. The plot shown here demonstrates the typical quality of our measured Bragg spectra in the strongly interacting regime.

We have studied the Bragg resonance of a ^{85}Rb condensate (Fig. 7.18) as a function of scattering length from the regime of weak interactions into the strongly interacting regime. The measured Bragg line shift shown in Fig. 7.18 (a) exhibits a linear dependence on the scattering length below approximately 300 a_0, which is in excellent agreement with Bogoliubov theory. However as the scattering length is increased further, the Bragg resonance line shift deviates significantly from the Bogoliubov prediction. This deviation reflects the onset of beyond mean-field corrections to the excitation spectrum. The line shift is observed to saturate near 600 a_0 and then it slightly *decreases* as the scattering length is raised further. Our line shift data shown in Fig. 7.18 (a) exhibits a systematic dependence on the temperature of the sample which cannot be neglected [167]. A small number of non-condensed ^{85}Rb atoms in the optical trap also respond to the Bragg pulse, *i.e.* momentum is transferred to the non-condensed gas as well. This is because the Bragg resonance width of the condensate and the non-condensed atoms becomes comparable beyond 500 a_0, therefore the response of the non-condensed atoms at the condensate is approximately the same. We varied the temperature of the condensate to characterize this effect; a small correction is applied to our data to represent the expected line shift (black circles in Fig. 7.18 (a)) at zero temperature. This temperature dependence is discussed in more detail in Section 7.9.

To understand how our observations compare to the theories of the Bragg line shift discussed earlier in this chapter, we have also plotted these theoretical predictions in Fig. 7.18 (a). Instead of evaluating the theories at the mean density of the trapped condensate, a local density approximation is used in which we average the excitation energy over the density profile of the condensate. Here we assume the density of the condensate is given by a Thomas-Fermi profile. These predictions of the line shift also account for observed number losses during our experiments, which are approximately consistent with the previously observed three-body recombination rate of ^{85}Rb [12]; For more details see Section 7.9. Note that our observed Bragg resonance line shift is significantly smaller than the Bogoliubov prediction (blue upward triangles) when the scattering length is larger than 600 a_0. Both the first Beliaev approximation, in which $n\,a^3 = 0$ but $k\,a$ and $k\,\xi$ may take on any value, and the Hartree-Fock-Bogoliubov theory, in which $n\,a^3$ and $k\,a$ may take on any value but $k\,\xi \gg 1$, predict a reduced Bragg line shift. In particular, the HFB theory predicts the smallest line shift and it appears to be in reasonable agreement with our data even though that theory should only be applied to the case of free-particle excitations. Our data disagrees with the prediction of the Beliaev second approximation, in which $n\,a^3$ and $k\,\xi$ may take on any value but $k\,a = 0$. A simple estimate of the size of a momentum-dependent correction to the second approximation, given by the difference between Bogoliubov theory and the first Beliaev approximation (red open boxes in Fig. 7.18 (a)), does not appear to explain the discrepancy.

The measured Bragg linewidth (Fig. 7.18 (b)) increases continuously as a function of scattering length. This trend is what we expect based on the predictions shown in Fig. 7.12. The primary reason for the increase is that a shorter Bragg pulse duration must be used at larger a, since the condensate size rapidly expands. We expect that there are two other significant contributions to the Bragg linewidth, the inhomogeneous density of the condensate and collisions during the Bragg pulse. The dashed curves in Fig. 7.18 (b) indicate the relative size of the different expected contributions to the width. The solid curve is a combination of the three contributions based on our

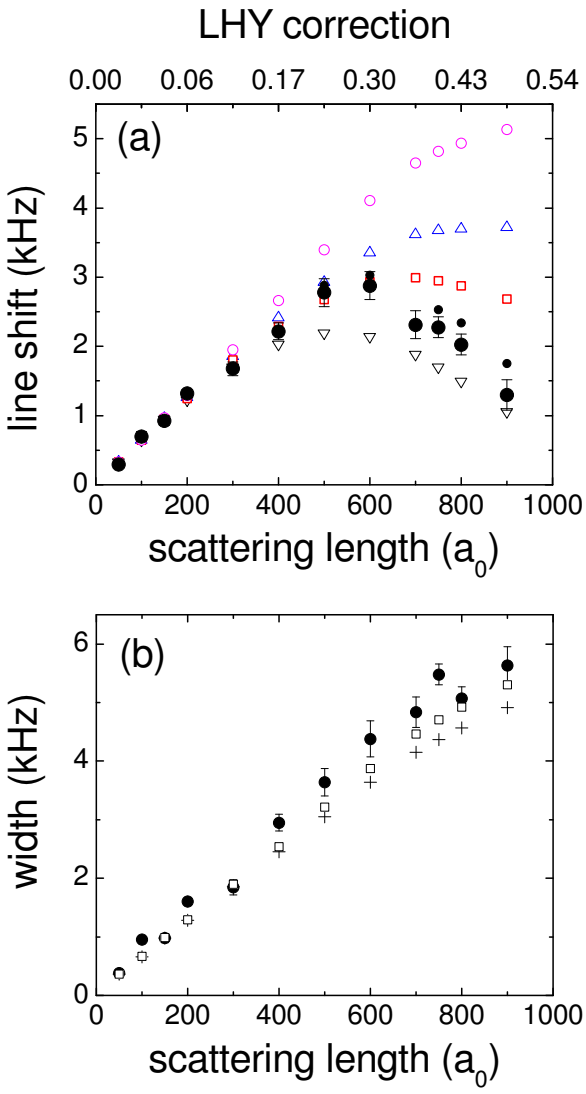

Figure 7.18: (a) Bragg line shift and (b) width extracted from a gaussian fit to the Bragg resonance as a function of scattering length. The points are our observations and the error bars represent standard deviations of the fit. The mean density during the measurements ranges from 6×10^{13} cm^{-3} to 8.5×10^{13} cm^{-3} due to three-body recombination during the Bragg pulse. In (a) the theory points, in order of smallest to largest shift, correspond to the following theories calculated for our trapped gas using a local density approximation: Hartree-Fock-Bogoliubov with $n\,a^3$ and $k\,a$ finite but $k\,\xi \gg 1$ (black downward triangles), Beliaev first approximation with $k\,a$ finite, $n\,a^3 = 0$ and $k\,\xi$ any value (red boxes), Bogoliubov with $n\,a^3 = 0$ and $k\,a = 0$, but $k\,\xi$ any value (blue upward triangles), and Beliaev second approximation with $n\,a^3$ finite, $k\,a = 0$, and $k\,\xi$ any value (magenta open circles). For reference the top axis shows the size of the LHY correction to the condensate chemical potential. In (b) the crosses represent a theoretical prediction for the resonance width under the conditions of our experiments. The open squares represent the predicted width when the LHY chemical potential is used to calculate the inhomogeneous density contribution.

convolution analysis (Eqn. 7.16). At small scattering length there is reasonable theoretical agreement with our data indicating that the relevant physics is included in our model. At large scattering length our observed Bragg linewidth is slightly smaller than our expectation for the total linewidth. The discrepancy is approximately 0.5-1 kHz and we do not currently understand its origin in detail. The open black boxes in Fig. 7.18 (b) represents a preliminary estimate for beyond mean-field effects on the total linewidth. For this line the LHY chemical potential is used instead of the mean-field value in calculating the contribution of the condensate inhomogeneous density. While the total width including the beyond mean-field correction does appear to agree better with the data, the uncertainty of our data is not adequate to differentiate between the different theoretical predictions shown.

At the time of this writing our understanding of the data and theory presented here is still incomplete. Please see our forthcoming paper for the final details and conclusions of these measurements.

7.9 Systematic effects on the Bragg line shift

The data in Section 7.8 appears to demonstrate the onset of beyond mean-field effects to the condensate excitation spectrum. The observed Bragg line shift is significantly smaller than Bogoliubov theory predicts. A less interesting alternative explanation of the data is that the density was not as large as expected, and therefore a smaller mean-field shift accounts for our observations. We performed a number of experiments designed to test the condensate density in the strongly interacting regime. As discussed below, we investigated the rate of inelastic losses and condensate heating. We also used Bragg spectroscopy to monitor the effects of condensate heating. Finally, we studied the temperature dependence of our Bragg resonance line shift.

7.9.1 Measurements of BEC fraction from absorption images

We have experimentally characterized ^{85}Rb condensate melting and atom number loss due to inelastic collisions during Bragg spectroscopy at an average density of 8.5×10^{13} cm^{-3}. The same experimental sequence described in Section 7.8 is used to compress the condensate density. We then increase the scattering length to some value between 50 a_0 and 900 a_0 in 0.12 ms. Instead of applying a Bragg pulse, we release the atoms from the optical trap to let the gas expand, and then take an absorption image. We fit the image to a two-component gaussian to extract the number of atoms in the condensate and the non-condensed gas. The results of this experiment are shown in Figure 7.19. Prior to any compression of the condensate density, the fraction of the total gas in the condensate was greater than 85%. We verified that the condensate fraction does not change during the density compression sequence.

The absorption images clearly show that a bimodal distribution of condensate and thermal gas always exists, even with $a = 900\ a_0$. This means that a large fraction of the remaining atoms are a part of the condensate following the hold in the strongly interacting regime. However, the reduction in BEC fraction at large a is disturbing. A loss of particle number in the condensate during Bragg spectroscopy would lead to a lower density, which might explain our observations of a smaller line shift. The measured atom number loss shown here is included in the theoretical predictions that

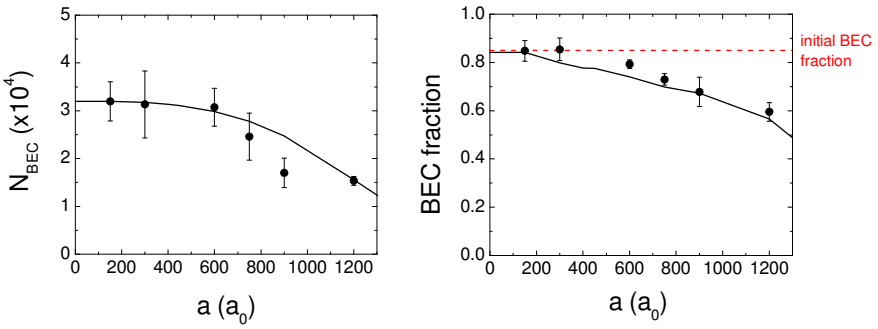

Figure 7.19: (Left) Measured atom number and (Right) measured condensate fraction after the condensate density compression and scattering length ramp for the Bragg pulse as a function of a. The solid line is the predicted atom number loss based on the measured three-body recombination rate of ^{85}Rb in Ref. [6]. The measured atom number loss is used to estimate the density during the Bragg pulse for the experiments shown in Fig. 7.18.

are compared to our data is Fig. 7.18. The amount of atom loss that occurs during the Bragg pulse is roughly consistent with previous observations [6], but the loss is not large enough the explain the discrepancy between the Bogoliubov theory and our observations.

We discovered another small factor the limits the density of the condensate during the compression sequence. The detailed shape of the magnetic-field ramps is important in achieving the largest compression. There are small discrepancies between the desired field ramps and what actually happens due to the finite bandwidth of the bias coil servo electronics. A small scattering-length dependent correction to the density of less than 9% has been applied.

7.9.2 Bragg spectra after ramping to large a

We have used Bragg spectroscopy to directly probe the condensate momentum distribution after the scattering length is set for Bragg spectroscopy. The density of a ^{85}Rb condensate is compressed using the sequence of scattering length ramps described in Section 7.8. Following the density compression, the scattering length is quickly ramped to either 600 a_0 or 900 a_0, under these conditions the condensate is strongly interacting. For each of these scattering lengths we acquired Bragg spectra as a function of time after the scattering length ramp is complete. The condensate density immediately begins to drop once the scattering length ramp is initiated and the Bragg spectra reflect the lower density with a line shift close to zero. In particular, we are interested in the width of the Bragg resonance since this quantity should be sensitive to any unexpected energy generated in the strongly interacting regime. We will refer to this unexpected energy as heating but we note that there is likely not enough time for the gas to rethermalize.

Figure 7.20 shows the measured Bragg linewidth as a function of time immediately following the scattering length ramp. In each plot of the figure there are two theoretical predictions for the Bragg width based on Eqn. 7.16. The blue curves represent the predicted Bragg width in the absence of any heating, and the red curves represent the predicted width in addition to some heat. We varied the amount of heat so that the model fit the data. For the 600 a_0 (900 a_0) data 6 nK (20 nK) of heat was required to make our model fit well. At the shortest times the data is somewhat more consistent with the zero-heating model, while at longer times the Bragg width clearly indicates that some energy has been generated in the gas. Since we lack a detailed understanding of the Bragg lineshape in the strongly interacting regime it is difficult to conclusively assign a cause to the extra width observed in the Bragg lineshapes.

In a related experiment we attempted to characterize the extra energy observed in the Bragg spectra. The density of the condensate was increased using our standard sequence and the scattering length was ramped to 900 a_0 in 0.12 ms. The scattering length was held at this value for 0.1 ms before it was lowered to 150 a_0 in 0.1 ms. Bragg spectroscopy was performed at this smaller scattering length to test for heating effects during the 0.1 ms hold at 900 a. In particular we are interested in the Bragg width which was measured to be 1.65 kHz. If no heating occurs during the hold at 900 a_0, then the width should be approximately 1.1 kHz.

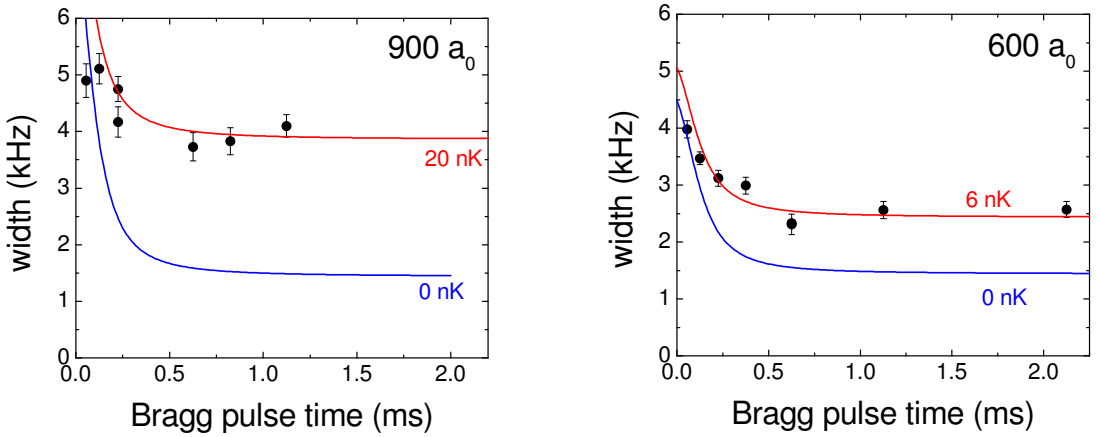

Figure 7.20: Measured Bragg linewidth as a function of time after the scattering length was increased to 900 a_0 (left) and 600 a_0 (right). The blue curves are a prediction based on our model for the Bragg width, and the red curves add some condensate heating to the prediction.

7.9.3 The temperature dependence of the Bragg line shift

We studied the temperature dependence of the Bragg line shift in a regime of density and scattering length in which beyond mean-field effects are important. At finite temperature a condensate has two components, the gas of atoms not in the condensed state which are characterized by a temperature, and the gas of atoms which all occupy the lowest quantum state of the trapping potential. Both of these components are sampled by Bragg spectroscopy. Therefore our measured Bragg spectra are actually a combination of the two components. Bragg scattering from the thermal gas experiences no mean-field shift and the Bragg resonance is centered at the free particle energy of ^{85}Rb , *i.e.* the line shift is zero. Obviously there is a line shift for the condensate component. If the fraction of atoms in the condensate is small, the thermal gas response to the Bragg light should systematically shift the Bragg resonance towards the free-particle energy. So far in this chapter, we have made predictions for the Bragg lineshape based on a zero temperature BEC. In this section we estimate the systematic shift of the Bragg resonance caused by the thermal gas.

To model the effects of finite temperature on our measured Bragg spectra, we simulated the Bragg lineshape of the condensate and the thermal gas with gaussians of different center and width.[11] The width of the thermal gas gaussian is related to the temperature of the gas,[12] while the width of the condensate gaussian is estimated from our experimental data. The thermal gas gaussian is centered at the free-particle energy of ^{85}Rb. We combine the two gaussians and fit the result to extract the combined center position. If the condensate fraction is very small, the combined center should be close to the free-particle energy. For large condensate fraction the opposite limit applies.

Figure 7.21 shows the measured Bragg resonance center position as a function of condensate fraction.[13] Here the condensate fraction is measured after Bragg spectroscopy so that the value quoted is a lower limit. The data was acquired with a density of approximately 10^{14} cm^{-3} and at a scattering length of 500 a_0. The curve in the figure is the result of our of a fit to the data based on the simulation described above. The reasonable agreement between our data and the model is encouraging. It indicates that the size of the systematic correction to our measured Bragg line shift is small compared to the correction of the Bogoliubov excitation spectrum due to beyond mean-field effects. In particular, we find that the line shift is typically changed by less than 1 kHz as the condensate fraction increases from 0.5 to 1. In Figure 7.18 the data points shown as small filled circles indicate an estimate of the zero temperature Bragg line shift.

[11] In our model we assume that the response of the thermal gas to the Bragg scattering pulse is the same as that of the condensate. This seems to be a reasonable assumption since the Bragg width of the thermal gas is smaller than the free particle energy. If the Bragg width of the thermal gas were on order or larger than the free-particle energy we would expect a significant reduction in the thermal gas response.

[12] The Bragg width of a thermal gas is $\frac{k}{2\pi}\sqrt{k_B\,T/m}$.

[13] We produce the largest values of condensate fraction in our experiments by stopping the optical trap evaporation very close to the bottom of the trap. In addition we typically hold the optical trap depth at a very low value for a few hundred ms following evaporation to let thermal atoms fall out of the trap.

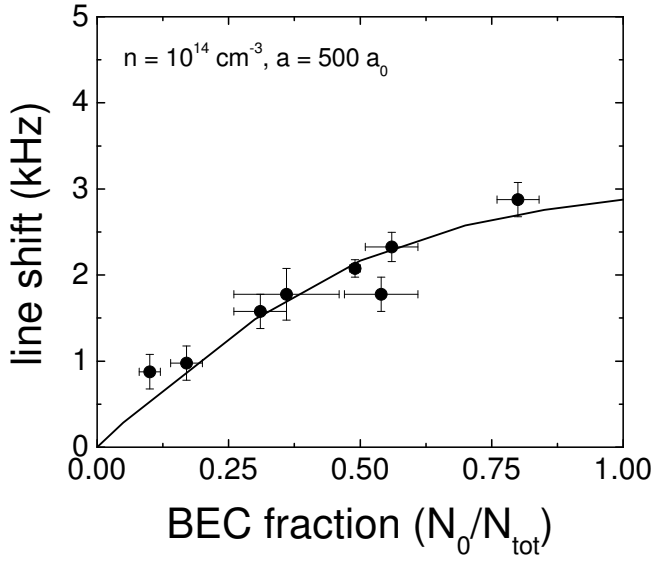

Figure 7.21: Measured Bragg line shift as a function of the condensate fraction. We the fraction is zero the temperature of the gas is slightly below the transition temperature. Our data indicate a significant increase in the Bragg lineshift as the condensate fraction is increased. The curve represents the prediction of our model where the lineshift at 100% condensate fraction is 18.3 kHz.

7.10 Bragg spectra at lower density

We have also acquired Bragg spectra over an even wider range of scattering length, but for these measurements the density of the condensate was lower. A ^{85}Rb BEC was created with an static average density of 2.0×10^{13} cm^{-13} and a scattering length 144 a_0. To perform Bragg spectroscopy the scattering length was quickly increased in 0.12 ms to a value in the range 144 a_0 to more than 3000 a_0. The condensate density begins to drop as soon as the scattering length is changed. Therefore the Bragg duration was set to be 0.25 ms. The average density during the Bragg pulse is calculated using the GP-equation model. The character of the excitations ranges from free-particle-like at small a ($k\,\xi = 12$ at 100 a_0) to intermediate between phonon-like and free-particle-like at large a ($k\,\xi = 2.5$ at 2500 a_0). Figure 7.22 shows the measured Bragg line shift and width as a function of scattering length. Also in the figure we show a set of theoretical predictions for the Bragg line shift and the width. The same theory that has been described above is used, but with this data we can compare over a larger range of scattering length.

There are three potential problems with this data related to entering the strongly interacting regime. At a scattering length of 2000 a_0 or greater we observe atom number loss during Bragg spectroscopy. A possible source of this loss may be a projection of correlated atoms pairs into molecules near the peak of the Feshbach resonance. Also beyond 2000 a_0 the two-body molecule binding energy associated with the Feshbach resonance is less than 10 kHz. With this small binding energy, the scattering length ramp may not be slow enough compared to the timescale of many-body physics in the condensate. Finally, our measurements of the Bragg resonance width exceed the predicted value based on the known density and scattering length.

7.11 Future work

A variety of future experiments might be possible with the our system. It might be interesting to study the effects of the molecular state associated with the Feshbach resonance on the Bragg spectrum. This could be accomplished by driving two-photon Bragg transitions between a pair of colliding condensate atoms and a bound Feshbach molecule. Since Bragg transitions conserve both energy and momentum, the resonance condition for a Bragg transition is modified by the molecule binding energy to be $E(p) = p^2/2\,M - \frac{\hbar^2}{2\,M\,a^2} + V_{int}$ where M is the reduced mass, p is the momentum of the molecule, and V_{int} represents the effect of atom-molecule interactions. These atom-molecule Bragg spectra would represent a different way to create Feshbach molecules and it might allow the interactions between atoms and Feshbach molecules to be studied.

It might also be interesting to study the excitation spectrum of a condensate for smaller momentum excitations than we have done so far. One complication of studying these low momentum excitations is that the size of our signal for Bragg spectroscopy is reduced. Since the total momentum imparted to the condensate is smaller, the amplitude of condensate COM oscillations in the trap is reduced. The signal-to-noise ratio of the measurements presented in this chapter may be large enough to perform initial measurements of phonon-like excitations. It is also possible to detect the momentum imparted to the condensate by directly counting the the number of photons scattered from the Bragg laser beams [175]. By dramatically lowering the intensity of one Bragg beam, and increasing the other by a corresponding amount, the change in photon number that

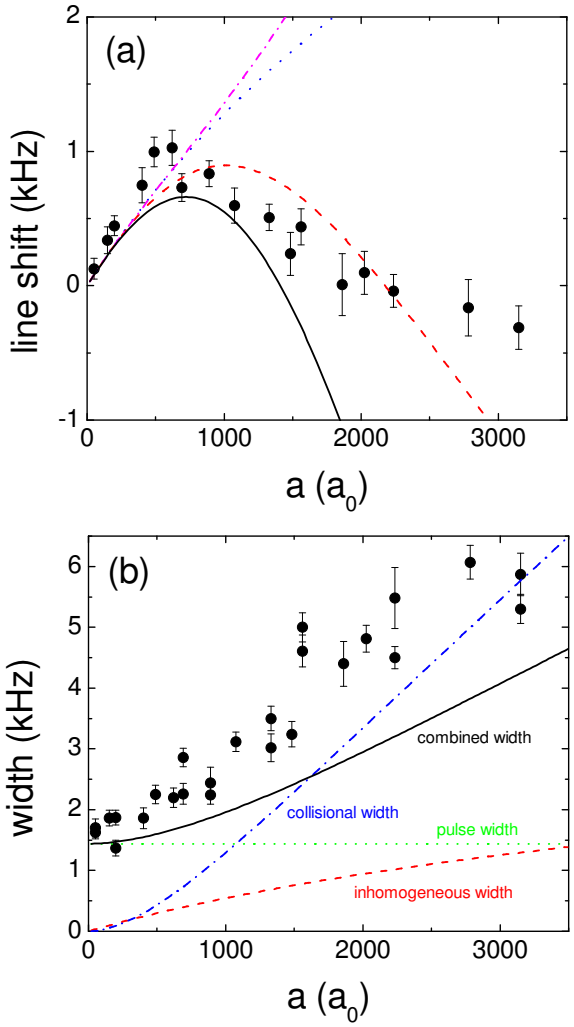

Figure 7.22: (a) Bragg line shift as a function of scattering length with an average density of approximately 2.0×10^{13} cm^{-3}. The theory lines, in order of smallest to largest shift, correspond to the following theories calculated for our trapped gas using a local density approximation: Hartree-Fock-Bogoliubov with $n\,a^3$ and $k\,a$ finite but $k\,\xi \gg 1$ (black solid line), Beliaev first approximation with $k\,a$ finite, $n\,a^3 = 0$ and $k\,\xi$ any value (red dashed line), Bogoliubov with $n\,a^3 = 0$ and $k\,a = 0$, but $k\,\xi$ any value (blue dotted line), and Beliaev second approximation with $n\,a^3$ finite, $k\,a = 0$, and $k\,\xi$ any value (magenta dash-dotted line). (b) Bragg width as a function of scattering length at a density of 2.0×10^{13} cm^{-3}. The lines show the contributions of the pulse duration (green dashed line), the inhomogeneous density of the condensate (red dashed line), and the width due to collisions during Bragg spectroscopy (blue dshed line). The black solid line is a combination of three contributions following Eqn 7.16.

corresponds to the number of atoms that make a Bragg transitions can be detected. We expect that the signal-to-noise ratio of this method could be approximately 20.

Chapter 8

Conclusion

This thesis has presented my work with an ultracold gas of ^{85}Rb and ^{87}Rb atoms. The second and third chapters of this thesis are dedicated to describing the new apparatus that was constructed. In designing and assembling the system, I tried to make the apparatus as robust and versatile as possible. I hope this will enable a wide range of new experiments using quantum-degenerate Bose gases with tunable interactions to be performed. Where relevant I have tried to write this thesis in such a way that pieces of the apparatus can be reproduced in other quantum gas experiments at JILA.

The fourth chapter contains a recipe for robust creation of ^{85}Rb condensates with up to 80,000 atoms, a significant improvement over the previous record. We are further able to create either a singles species ^{87}Rb condensate or a dual BEC of the two species. This has required a thorough study of sympathetic and simultaneous cooling of ^{85}Rb and ^{87}Rb. Our versatile system has opened the door to a variety of experiments utilizing widely tunable interactions.

I have had the chance to perform a set of experiments using the tunability of interparticle interactions via magnetic-field Feshbach resonances. These include studies of the first heteronuclear Feshbach molecules [155], of tunable phase separation in a two-species BEC [176], and of the excitation spectrum of a strongly interacting ^{85}Rb condensate using Bragg spectroscopy [177]. The Bragg spectroscopy work has been the most exciting physics to work on; we have seen initial evidence of long-sought beyond mean-field corrections to the excitation energy of a superfluid. And I hope the work described in this thesis represents only the start of a series of experiments that will elucidate strongly correlated Bose gases.

Bibliography

[1] J. James Patrick Burke, Theoretical Investigation of Cold Alkali Atom Collisions, Ph.D. thesis, University of Colorado, 1999.

[2] J. J. Olivero and R. L. Longbothum, Empirical fits to the Voigt line width: A brief review, *Journal of Quantitative Spectroscopy and Radiative Transfer* **17**, 233 (1977).

[3] C. Greene, http:
fermion.coloraod.edu/ chg/Collisions (unpublished).

[4] V. M. Pérez-García, H. Michinel, J. I. Cirac, M. Lewenstein, and P. Zoller, Dynamics of Bose-Einstein condensates: Variational solutions of the Gross-Pitaevskii equations, *Phys. Rev. A* **56**, 1424 (1997).

[5] N. R. Claussen, S. J. J. M. F. Kokkelmans, S. T. Thompson, E. A. Donley, E. Hodby, and C. E. Wieman, Very-high-precision bound-state spectroscopy near a ^{85}Rb Feshbach resonance, *Phys. Rev. A* **67**, 060701(R) (2003).

[6] J. L. Roberts, Bose-Einstein condensates with tunable atom-atom interactions: the first experiments with ^{85}Rb BECs, Ph.D. thesis, University of Colorado, 2001.

[7] S. L. Cornish, N. R. Claussen, J. L. Roberts, E. A. Cornell, and C. E. Wieman, Stable ^{85}Rb Bose-Einstein condensates with widely tunable interactions, *Phys. Rev. Lett.* **85**, 1795 (2000).

[8] J. L. Roberts, N. R. Claussen, S. L. Cornish, E. A. Donley, E. A. Cornell, and C. E. Wieman, Controlled collapse of a Bose-Einstein condensate, *Phys. Rev. Lett.* **86**, 4211 (2001).

[9] E. A. Donley, N. R. Claussen, S. L. Cornish, J. L. Roberts, E. A. Cornell, and C. E. Wieman, Dynamics of collapsing and exploding Bose-Einstein condensates, *Nature* **412**, 295 (2001).

[10] E. A. Donley, N. R. Claussen, S. T. Thompson, and C. E. Wieman, Atom-molecule coherence in a Bose-Einstein condensate, *Nature* **417**, 529 (2002).

[11] I. Bloch, M. Greiner, O. Mandel, T. W. Hänsch, and T. Esslinger, Sympathetic cooling of ^{85}Rb and ^{87}Rb, *Phys. Rev. A* **64**, 021402(R) (2001).

[12] J. L. Roberts, N. R. Claussen, S. L. Cornish, and C. E. Wieman, Magnetic field dependence of ultracold inelastic collisions near a Feshbach resonance, *Phys. Rev. Lett.* **85**, 728 (2000).

[13] J. P. Burke, Jr., J. L. Bohn, B. D. Esry, and C. H. Greene, Prospects for Mixed-Isotope Bose-Einstein Condensates in Rubidium, *Phys. Rev. Lett.* **80**, 2097 (1998).

[14] H. K. Onnes, On the sudden rate at which the resistance of mercury disappears, *Akad. van Wetenschappen* **14(113)**, 818 (1911).

[15] P. Kapitza, Viscosity of liquid helium at temperatures below the lambda point, *Nature* **141**, 74 (1938).

[16] J. F. Allen and A. D. Misener, Flow of liquid helium II, *Nature* **141**, 75 (1938).

[17] J. Wilkes, *The Properties of Liquid and Solid Helium* (Clarendon Press, Oxford, UK, 1967).

[18] R. P. Feynman and M. Cohen, Energy Spectrum of the Excitations in Liquid Helium, *Phys. Rev.* **102**, 1189 (1956).

[19] A. Griffin, *Excitations in a Bose-Condensed Liquid* (Cambridge University Press, Cambridge, England, 1993).

[20] M. H. Anderson, J. R. Ensher, M. R. Matthews, C. E. Wieman, and E. A. Cornell, Observation of Bose-Einstein condensation in a dilute atomic vapor, *Science* **269**, 198 (1995).

[21] K. B. Davis, M.-O. Mewes, M. R. Andrews, N. J. van Druten, D. S. Durfee, D. M. Kurn, and W. Ketterle, Bose-Einstein condensation in a gas of sodium atoms, *Phys. Rev. Lett.* **75**, 3969 (1995).

[22] C. C. Bradley, C. A. Sackett, J. J. Tollett, and R. G. Hulet, Evidence of Bose-Einstein Condensation in an Atomic Gas with Attractive Interactions, *Phys. Rev. Lett.* **75**, 1687 (1995), *ibid.* **79**, 1170 (1997).

[23] F. Dalfovo, S. Giorgini, L. P. Pitaevskii, and S. Stringari, Theory of Bose-Einstein condensation in trapped gases, *Rev. Mod. Phys.* **71**, 463 (1999).

[24] M. R. Andrews, C. G. Townsend, H.-J. Miesner, D. S. Durfee, D. M. Kurn, and W. Ketterle, Observation of Interference Between Two Bose-Einstein Condensates, *Science* **275**, 637 (1997).

[25] M. R. Matthews, B. P. Anderson, P. C. Haljan, D. S. Hall, C. E. Wieman, and E. A. Cornell, Vortices in a Bose-Einstein Condensate, *Phys. Rev. Lett.* **83**, 2498 (1999).

[26] M. Greiner, O. Mandel, T. Esslinger, T. W. Hänsch, and I. Bloch, Quantum phase transition from a superfluid to a Mott insulator in a gas of ultracold atoms, *Nature* **415**, 39 (2002).

[27] T. Kinoshita, T. Wenger, and D. S. Weiss, Observation of a One-Dimensional Tonks-Girardeau Gas, *Science* **305**, 1125 (2004).

[28] B. DeMarco and D. S. Jin, Onset of Fermi Degeneracy in a Trapped Atomic Gas, *Science* **285**, 1703 (1999).

[29] A. G. Truscott, K. E. Strecker, W. I. McAlexander, G. B. Partridge, and R. G. Hulet, Observation of Fermi pressure in a gas of trapped atoms, *Science* **291**, 2570 (2001).

[30] C. A. Regal, M. Greiner, and D. S. Jin, Observation of resonance condensation of fermionic atom pairs, *Phys. Rev. Lett.* **92**, 040403 (2004).

[31] M. W. Zwierlein, C. A. Stan, C. H. Schunck, S. M. F. Raupach, A. J. Kerman, and W. Ketterle, Condensation of pairs of fermionic atoms near a Feshbach resonance, *Phys. Rev. Lett.* **92**, 120403 (2004).

[32] C. A. Regal, Experimental realization of BCS-BEC crossover physics with a Fermi gas of atoms, Ph.D. thesis, University of Colorado, 2006.

[33] M. Greiner, C. A. Regal, and D. S. Jin, Emergence of a molecular Bose-Einstein condensate from a Fermi gas, *Nature* **426**, 537 (2003).

[34] S. Jochim, M. Bartenstein, A. Altmeyer, G. Hendl, S. Riedl, C. Chin, J. H. Denschlag, and R. Grimm, Bose-Einstein condensation of molecules, *Science* **302**, 2101 (2003).

[35] M. W. Zwierlein, C. A. Stan, C. H. Schunck, S. M. F. Raupach, S. Gupta, Z. Hadzibabic, and W. Ketterle, Observation of Bose-Einstein condensation of molecules, *Phys. Rev. Lett.* **91**, 250401 (2003).

[36] B. D. Esry, C. H. Greene, and H. Suno, Threshold laws for three-body rescombination, *Phys. Rev. A* **65**, 010705(R) (2001).

[37] D. S. Petrov, Three-body problem in Fermi gases with short-range interparticle interaction, *Phys. Rev. A* **67**, 010703(R) (2003).

[38] D. S. Petrov, C. Salomon, and G. V. Shlyapnikov, Weakly bound dimers of fermionic atoms, *Phys. Rev. Lett* **93**, 090404 (2004).

[39] J. P. D'Incao and B. D. Esry, Scattering Length Scaling Laws for Ultracold Three-Body Collisions, *Phys. Rev. Lett.* **94**, 213201 (2005).

[40] E. Hodby, S. T. Thompson, C. A. Regal, M. Greiner, A. C. Wilson, D. S. Jin, E. A. Cornell, and C. E. Wieman, Production efficiency of ultracold Feshbach molecules in bosonic and fermionic systems, *Phys. Rev. Lett.* **94**, 120402 (2005).

[41] S. Dürr, T. Volz, A. Marte, and G. Rempe, Observation of molecules produced from a Bose-Einstein condensate, *Phys. Rev. Lett.* **92**, 020406 (2004).

[42] K. Xu, T. Mukaiyama, J. R. Abo-Shaeer, J. K. Chin, D. E. Miller, and W. Ketterle, Formation of Quantum-Degenerate Sodium Molecules, *Phys. Rev. Lett.* **91**, 210402 (2003).

[43] J. Herbig, T. Kraemer, M. Mark, T. Weber, C. Chin, H.-C. Nagerl, and R. Grimm, Preparation of a pure molecular quantum gas, *Science* 1088876 (2003).

[44] C. J. Pethick and H. Smith, *Bose-Einstein condensation in dilute gases* (Cambridge Univ. Press, Cambridge, UK, 2002).

[45] R. K. Pathria, *Statistical Mechanics*, second edition ed. (Butterworth Heinemann, Woburn, MA, 1996).

[46] T. D. Lee and C. N. Yang, Many-Body Problem in Quantum Mechanics and Quantum Statistical Mechanics, *Phys. Rev.* **105**, 1119 (1957).

[47] T. D. Lee, K. Huang, and C. N. Yang, Eigenvalues and Eigenfunctions of a Bose System of Hard Spheres and Its Low-Temperature Properties, *Phys. Rev.* **106**, 1135 (1957).

[48] J. J. Sakurai, in *Modern Quantum Mechanics*, edited by S. F. Tuan (Addison-Wesley, Reading, Massachusetts, 1994).

[49] J. R. Taylor, *Scattering Theory: The Quantum Theory of Nonrelativistic Collisions* (Robert E. Krieger Publishing Company, Malabar, FL, 1987).

[50] G. F. Gribakin and V. V. Flambaum, Calculation of the scattering length in atomic collisions using the semiclassical approximation, *Phys. Rev. A* **48**, 546 (1993).

[51] U. Fano, Effects of Configuration Interaction on Intensities and Phase Shifts, *Phys. Rev.* **124**, 1866 (1961).

[52] H. Feshbach, A unified theory of nuclear reactions. II, *Ann. Phys.* **19**, 287 (1962).

[53] E. Tiesinga, B. J. Verhaar, and H. T. C. Stoof, Threshold and resonance phenomena in ultracold ground-state collisions, *Phys. Rev. A* **47**, 4114 (1993).

[54] C. Chin, Simple mean-field model for condensates in the BEC-BCS crossover regime, *Phys. Rev. A* **72**, 041601 (2005).

[55] K. Góral, T. Köhler, S. A. Gardiner, E. Tiesinga, and P. S. Julienne, Adiabatic association of ultracold molecules via magnetic-field tunable interactions, *J. Phys. B* **37**, 3457 (2004).

[56] T. Kohler, K. Goral, and P. S. Julienne, Production of cold molecules via magnetically tunable Feshbach resonances, *Rev. Mod. Phys.* **78**, 1311 (2006).

[57] I. Bloch, J. Dalibard, and W. Zwerger, Many-Body Physics with Ultracold Gases, *arXiv:0704.3011v2* (2007).

[58] N. R. Claussen, Dynamics of Bose-Einstein condensates near a Feshbach resonance in ^{85}Rb, Ph.D. thesis, University of Colorado, 2003.

[59] C. J. Myatt, , Ph.D. thesis, University of Colorado, 1997.

[60] C. J. Myatt, N. R. Newbury, R. W. Ghrist, S. Loutzenhiser, and C. E. Wieman, Multiply loaded magneto-optical trap, *Opt. Lett.* **21**, 290 (1996).

[61] M. Greiner, I. Bloch, O. Mandel, T. W. Hänsch, and T. Esslinger, Exploring Phase Coherence in a 2D Lattice of Bose-Einstein Condensates, *Phys. Rev. Lett.* **87**, 160405 (2001).

[62] H. Lewandowski, Simplified System for Creating a Bose-Einstein Condensate, *J. Low Temp. Phys.* **132**, 309 (2003).

[63] J. H. Moore, C. C. Davis, and M. A. Coplan, *Building Scientific Apparatus* (Perseus Books, ADDRESS, 1989).

[64] J. F. O'Hanlon, *A User's Guide to Vacuum Technology* (Wiley, ADDRESS, 2003).

[65] C. G. Townsend, N. H. Edwards, C. J. Cooper, K. P. Zetie, C. J. Foot, A. M. Steane, P. Szriftgiser, H. Perrin, and J. Dalibard, Phase-space density in the magneto-optical trap, *Phys. Rev. A* **52**, 1423 (1995).

[66] H. J. Metcalf and P. van der Straten, *Laser Cooling and Trapping* (Springer-Verlag, New York, NY, 1999).

[67] C. G. Townsend, N. H. Edwards, K. P. Zetie, C. J. Cooper, J. Rink, and C. J. Foot, High-density trapping of cesium atoms in a dark magneto-optical trap, *Phys. Rev. A* **53**, 1702 (1996).

[68] M. G. Peters, D. Hoffmann, J. D. Tobiason, and T. Walker, Laser-induced ultracold $\mathrm{Rb}(5S_{1/2})$+$\mathrm{Rb}(5\mathrm{P}_{1/2})$ collisions, *Phys. Rev. A* **50**, R906 (1994).

[69] L. G. Marcassa, G. D. Telles, S. R. Muniz, and V. S. Bagnato, Collisional losses in a K-Rb cold mixture, *Phys. Rev. A* **63**, 013413 (2000).

[70] A. Gallagher and D. E. Pritchard, Exoergic collisions of cold Na^*-Na, *Phys. Rev. Lett.* **63**, 957 (1989).

[71] W. Petrich, M. H. Anderson, J. R. Ensher, and E. A. Cornell, Behavior of atoms in a compressed magneto-optical trap, *J. Opt. Soc. Am. B* **11**, 1332 (1994).

[72] D. Sesko, T. Walker, C. Monroe, A. Gallagher, and C. Wieman, Collisional Losses from a Light-Force Atom Trap, *Phys. Rev. Lett.* **63**, 961 (1989).

[73] J. Smith, Efficient Transfer of Cold Atoms Over Large Distances, Ph.D. thesis, University of Colorado, 2003.

[74] H. Lewandowski, Coherences and correlations in an ultracold Bose gas, Ph.D. thesis, University of Colorado, 2002.

[75] W. Petrich, M. H. Anderson, J. R. Ensher, and E. A. Cornell, Stable, Tightly Confining Magnetic Trap for Evaporative Cooling of Neutral Atoms, *Phys. Rev. Lett.* **74**, 3352 (1995).

[76] M.-O. Mewes, M. R. Andrews, N. J. van Druten, D. M. Kurn, D. S. Durfee, and W. Ketterle, Bose-Einstein Condensation in a Tightly Confining dc Magnetic Trap, *Phys. Rev. Lett.* **77**, 416 (1996).

[77] T. Bergeman, G. Erez, and H. Metcalf, Magnetostatic trapping fields for neutral atoms, *Phys. Rev. A* **35**, 1535 (1987).

[78] D. M. Pozar, *Microwave Engineering* (Wiley, Hoboken, NJ, 1998).

[79] R. Grimm, M. Weidemüller, and Y. B. Ovchinnikov, Optical dipole traps for neutral atoms, *Adv. in AMO Phys.* **42**, 95 (2000).

[80] K. L. Corwin, A Circularly-Polarized Optical Dipole Trap and Other Developments in Laser Trapping of Atoms, Ph.D. thesis, University of Colorado, Boulder, 1999.

[81] K. W. Miller, Trapping and Cooling Rubidium in Far-off-resonant Optical Dipole Traps, Ph.D. thesis, University of Colorado, Boulder, 2004.

[82] W. Ketterle, D. S. Durfee, and D. M. Stamper-Kurn, in *Proceedings of the International School of Physics - Enrico Fermi*, edited by M. Inguscio, S. Stringari, and C. E. Wieman (IOS Press, ADDRESS, 1999), p. 67.

[83] W. Demtröder, *Laser Spectroscopy* (Springer-Verlag, New York, 1998).

[84] C. E. Wieman and L. Hollberg, Using diode lasers for atomic physics, *Rev. Sci. Instrum.* **62**, 1 (1991).

[85] T. P. Dinnen, C. D. Wallace, and P. L. Gould, Narrow linewidth, highly stable, tunable diode laser system, *Opt. Commun.* **92**, 277 (1992).

[86] H. Patrick and C. E. Wieman, Frequency stabilization of a diode laser using simultaneous optical feedback from a diffraction grating and a narrowband Fabry–Perot cavity, *Rev. Sci. Instrum.* **62**, 2593 (1991).

[87] B. C. Young, F. C. Cruz, W. M. Itano, and J. C. Bergquist, Visible Lasers with Subhertz Linewidths, *Phys. Rev. Lett.* **82**, 3799 (1999).

[88] A. D. Ludlow, X. Huang, M. Notcutt, T. Zanon-Willette, S. M. Foreman, M. M. Boyd, S. Blatt, and J. Ye, Compact, thermal-noise-limited optical cavity for diode laser stabilization at 1×10^{-15}, *Opt. Lett.* **32**, 641 (2007).

[89] M. Notcutt, L.-S. Ma, A. D. Ludlow, S. M. Foreman, J. Ye, and J. L. Hall, Contribution of thermal noise to frequency stability of rigid optical cavity via Hertz-linewidth lasers, *Phys. Rev. A* **73**, 031804 (2006).

[90] K. L. Corwin, Z.-T. Lu, C. F. Hand, R. J. Epstein, and C. E. Wieman, Frequency-Stabilized Diode Laser with the Zeeman Shift in an Atomic Vapor, *Appl. Opt.* **37**, 3295 (1998).

[91] B. DeMarco, Quantum behavior of an atomic Fermi gas, Ph.D. thesis, University of Colorado, 2001.

[92] J. L. Roberts, N. R. Claussen, J. P. Burke, Jr., C. H. Greene, E. A. Cornell, and C. E. Wieman, Resonant magnetic field control of elastic scattering of cold ^{85}Rb, *Phys. Rev. Lett.* **81**, 5109 (1998).

[93] R. V. E. Lovelace, C. Mehanian, T. J. Tommila, and D. M. Lee, Magnetic confinement of a neutral gas, *Nature* **318**, 30 (1985).

[94] H. F. Hess, Evaporative cooling of magnetically trapped and compressed spin-polarized hydrogen, *Phys. Rev. B* **34**, 3476 (1986).

[95] O. J. Luiten, H. G. C. Werij, I. D. Setija, M. W. Reynolds, T. W. Hijmans, and J. T. M. Walraven, Lyman-α Spectroscopy of Magnetically Trapped Atomic Hydrogen, *Phys. Rev. Lett.* **70**, 544 (1993).

[96] O. J. Luiten, M. W. Reynolds, and J. T. M. Walraven, Kinetic theory of the evaporative cooling of a trapped gas, *Phys. Rev. A* **53**, 381 (1996).

[97] K. B. Davis, M.-O. Mewes, M. A. Joffe, M. R. Andrews, and W. Ketterle, Evaporative cooling of sodium atoms, *Phys. Rev. Lett.* **74**, 5202 (1995).

[98] W. Petrich, M. H. Anderson, J. R. Ensher, and E. A. Cornell, in *Fourteenth International Conference on Atomic Physics (ICAP XIV)* (Unknown, ADDRESS, 1994), Chap. 1M, p. 7.

[99] E. A. Cornell and C. E. Wieman, Nobel Lecture: Bose-Einstein condensation in a dilute gas, the first 70 years and some recent experiments, *Rev. Mod. Phys.* **74**, 875 (2002).

[100] M. Holland, J. Williams, K. Coakley, and J. Cooper, Trajectory simulation of kinetic equations for classical systems, *Quantum Semiclass. Opt.* **8**, 571 (1996).

[101] B. DeMarco, S. B. Papp, and D. S. Jin, Pauli blocking of collisions in a quantum degenerate atomic Fermi gas, *Phys. Rev. Lett.* **86**, 5409 (2001).

[102] G. Delannoy, S. G. Murdoch, V. Boyer, V. Josse, P. Bouyer, and A. Aspect, Understanding the production of dual Bose-Einstein condensation with sympathetic cooling, *Phys. Rev. A* **63**, 051602 (R) (2001).

[103] J. P. Burke and J. L. Bohn, Ultracold scattering properties of the short-lived Rb isotopes, *Phys. Rev. A* **59**, 1303 (1999).

[104] E. A. Burt, R. W. Ghrist, C. J. Myatt, M. J. Holland, E. A. Cornell, and C. E. Wieman, Coherence, Correlations, and Collisions: What One Learns about Bose-Einstein Condensates from Their Decay, *Phys. Rev. Lett.* **79**, 337 (1997).

[105] K. B. Davis, M.-O. Mewes, and W. Ketterle, An analytical model for evaporative cooling of atoms, *Appl. Phys. B* **60**, 155 (1995).

[106] C. J. Myatt, E. A. Burt, R. W. Ghrist, E. A. Cornell, and C. E. Wieman, Production of Two Overlapping Bose-Einstein Condensates by Sympathetic Cooling, *Phys. Rev. Lett.* **78**, 586 (1997).

[107] F. Schreck, L. Khaykovich, K. L. Corwin, G. Ferrari, T. Bourdel, J. Cubizolles, and C. Salomon, Quasipure Bose-Einstein condensate immersed in a Fermi sea, *Phys. Rev. Lett.* **87**, 080403 (2001).

[108] Z. Hadzibabic, C. A. Stan, K. Dieckmann, S. Gupta, M. W. Zwierlein, A. Görlitz, and W. Ketterle, Two species mixture of quantum degenerate Bose and Fermi gases, *Phys. Rev. Lett.* **88**, 160401 (2002).

[109] G. Roati, F. Riboli, G. Modugno, and M. Inguscio, Fermi-Bose quantum degenerate ^{40}K-^{87}Rb mixture with attractive interaction, *Phys. Rev. Lett.* **89**, 1804 (2002).

[110] J. Goldwin, S. Inouye, M. Olsen, B. Newman, B. D. DePaola, and D. S. Jin, Measurement of the interaction strength in a Bose-Fermi mixture with ^{87}Rb and ^{40}K, *Phys. Rev. A* **70**, 021601 (2004).

[111] S. Aubin, S. Myrskog, M. H. T. Extavour, L. J. LeBlanc, D. McKay, A. Stummer, and J. H. Thywissen, Rapid sympathetic cooling to Fermi degeneracy on a chip, *Nat Phys* **2**, 384 (2006).

[112] B. D. Esry and C. H. Greene, Low-lying excitations of double Bose-Einstein condensates, *Phys. Rev. A* **57**, 1265 (1998).

[113] K. Dieckmann, Bose-Einstein Condensation with High Atom Number in a Deep Magnetic Trap, Ph.D. thesis, Universiteit van Amsterdam, 2001.

[114] K. M. O'Hara, M. E. Gehm, S. R. Granade, and J. E. Thomas, Scaling laws for evaporative cooling in time-dependent optical traps, *Phys. Rev. A* **64**, 051403 (2001).

[115] L. Guttman and J. R. Arnold, The Nonparticipation of He^6 in the Superfluidity of He^4, *Phys. Rev.* **92**, 547 (1953).

[116] D. S. Hall, M. R. Matthews, J. R. Ensher, C. E. Wieman, and E. A. Cornell, Dynamics of Component Separation in a Binary Mixture of Bose-Einstein Condensates, *Phys. Rev. Lett.* **81**, 1539 (1998).

[117] J. Stenger, S. Inouye, D. M. Stamper-Kurn, H.-J. Miesner, A. P. Chikkatur, and W. Ketterle, Spin domains in ground-state Bose-Einstein condensates, *Nature* **396**, 345 (1999).

[118] G. Modugno, M. Modugno, F. Riboli, G. Roati, and M. Inguscio, Two Atomic Species Superfluid, *Phys. Rev. Lett.* **89**, 190404 (2002).

[119] T.-L. Ho and V. B. Shenoy, Binary Mixtures of Bose Condensates of Alkali Atoms, *Phys. Rev. Lett.* **77**, 3276 (1996).

[120] P. Ao and S. T. Chui, Binary Bose-Einstein condensate mixtures in weakly and strongly segregated phases, *Phys. Rev. A* **58**, 4836 (1998).

[121] B. D. Esry, C. H. Greene, J. P. Burke, Jr., and J. L. Bohn, Hartree-Fock Theory for Double Condensates, *Phys. Rev. Lett.* **78**, 3594 (1997).

[122] E. Timmermans, Phase Separation of Bose-Einstein Condensates, *Phys. Rev. Lett* **81**, 5718 (1998).

[123] H. Pu and N. P. Bigelow, Properties of Two-Species Bose Condensates, *Phys. Rev. Lett.* **80**, 1130 (1998).

[124] R. A. Barankov, Boundary of two mixed Bose-Einstein condensates, *Phys. Rev. A* **66**, 013612 (2002).

[125] T. Busch, J. I. Cirac, V. M. Pérez-García, and P. Zoller, Stability and collective excitations of a two-component Bose-Einstein condensed gas: A moment approach, *Phys. Rev. A* **56**, 2978 (1997).

[126] R. Graham and D. Walls, Collective excitations of trapped binary mixtures of Bose-Einstein condensed gases, *Phys. Rev. A* **57**, 484 (1998).

[127] M. Trippenbach, K. Góral, K. Rzążewski, B. Malomed, and Y. B. Band, Structure of binary Bose-Einstein condensates, *J. Phys. B* **33**, 4017 (2000).

[128] F. Riboli and M. Modugno, Topology of the ground state of two interacting Bose-Einstein condensates, *Phys. Rev. A* **65**, 063614 (2002).

[129] D. M. Jezek and P. Capuzzi, Interaction-driven effects on two-component Bose-Einstein condensates, *Phys. Rev. A* **66**, 015602 (2002).

[130] E. G. M. van Kempen, S. J. J. M. F. Kokkelmans, D. J. Heinzen, and B. J. Verhaar, Interisotope Determination of Ultracold Rubidium Interactions from Three High-Precision Experiments, *Phys. Rev. Lett.* **88**, 093201 (2002).

[131] C. A. Regal, C. Ticknor, J. L. Bohn, and D. S. Jin, Creation of ultracold molecules from a Fermi gas of atoms, *Nature* **424**, 47 (2003).

[132] J. M. Sage, S. Sainis, T. Bergeman, and D. DeMille, Optical Production of Ultracold Polar Molecules, *Phys. Rev. Lett.* **94**, 203001 (2005).

[133] D. DeMille, Quantum Computation with Trapped Polar Molecules, *Phys. Rev. Lett.* **88**, 067901 (2002).

[134] J. J. Hudson, B. E. Sauer, M. R. Tarbutt, and E. A. Hinds, Measurement of the Electron Electric Dipole Moment Using YbF Molecules, *Phys. Rev. Lett.* **89**, 023003 (2002).

[135] D. J. H. E. G. M. van Kempen, S. J. J. M. F. Kokkelmans and B. J. Verhaar, Interisotope Determination of Ultracold Rubidium Interactions from Three High-Precision Experiments, *Phys. Rev. Lett.* **88**, 093201 (2002).

[136] J. Y. Seto, R. J. L. Roy, J. Verges, and C. Amiot, Direct potential fit analysis of the $X^1\ \Sigma_g^+$ state of Rb_2: Nothing else will do!, *J. Chem. Phys.* **113**, 3067 (2000).

[137] W. Kolos, K. Szalewicz, and H. J. Monkhorst, New Born–Oppenheimer potential energy curve and vibrational energies for the electronic ground state of the hydrogen molecule, *J. Chem. Phys.* **84**, 3278 (1986).

[138] A. J. Kerman, J. M. Sage, S. Sainis, T. Bergeman, and D. DeMille, , *Phys. Rev. Lett.* **92**, 033004 (2004).

[139] D. Wang, J. Qi, M. Stone, O. Nikolayeva, H. Wang, B. Hattaway, S. Gensemer, P. Gould, E. Eyler, and W. Stwalley, , *Phys. Rev. Lett* **93**, 243005 (2004).

[140] M. Mancini, G. Telles, A. Caires, V. Bagnato, and L. Marcassa, , *Phys. Rev. Lett.* **92**, 133203 (2004).

[141] J. Cubizolles, T. Bourdel, S. J. J. M. F. Kokkelmans, G. V. Shlyapnikov, and C. Salomon, Production of long-lived ultracold Li_2 molecules from a Fermi gas of atoms, *Phys. Rev. Lett* **91**, 240401 (2003).

[142] S. Jochim, M. Bartenstein, A. Altmeyer, g. Hendl, C. Chin, J. H. Denschlag, and R. Grimm, Pure gas of optically trapped molecules created from fermionic atoms, *Phys. Rev. Lett.* **91**, 240402 (2003).

[143] K. E. Strecker, G. B. Partridge, and R. G. Hulet, Conversion of an atomic Fermi gas to a long-lived molecular Bose gas, *Phys. Rev. Lett.* **91**, 080406 (2003).

[144] S. T. Thompson, E. Hodby, and C. E. Wieman, Ultracold molecule production via a resonant oscillating magnetic field, *Phys. Rev. Lett.* **95**, 190404 (2005).

[145] N. R. Claussen, E. A. Donley, S. T. Thompson, and C. E. Wieman, Microscopic dynamics in a strongly interacting Bose-Einstein condensate, *Phys. Rev. Lett.* **89**, 010401 (2002).

[146] S. Inouye, J. Goldwin, M. L. Olsen, C. Ticknor, J. L. Bohn, and D. S. Jin, Observation of Heteronuclear Feshbach Resonances in a Mixture of Bosons and Fermions, *Phys. Rev. Lett.* **93**, 183201 (2004).

[147] C. A. Stan, M. W. Zwierlein, C. H. Schunck, S. M. F. Raupach, and W. Ketterle, Observation of Feshbach Resonances between Two Different Atomic Species, *Phys. Rev. Lett.* **93**, 143001 (2004).

[148] C. Ticknor, C. A. Regal, D. S. Jin, and J. L. Bohn, Multiplet structure of Feshbach resonances in nonzero partial waves, *Phys. Rev. A* **69**, 042712 (2004).

[149] S. T. Thompson, E. Hodby, and C. E. Wieman, Spontaneous dissociation of ^{85}Rb Feshbach molecules, *Phys. Rev. Lett.* **94**, 020401 (2005).

[150] T. Köhler, E. Tiesinga, and P. S. Julienne, , *Phys. Rev. Lett.* **94**, 020402 (2005).

[151] S. J. J. M. F. Kokkelmans and E. G. M. van Kempen, personal communication (unpublished).

[152] J. L. Bohn, personal communication (unpublished).

[153] J. E. Williams, N. Nygaard, and C. W. Clark, , *cond-mat/0511011* (2005).

[154] J. F. Bertelsen and K. Mølmer, , *Phys. Rev. A* **73**, 013811 (2006).

[155] S. B. Papp and C. E. Wieman, Observation of Heteronuclear Feshbach Molecules from a [sup 85]Rb–[sup 87]Rb Gas, *Phys. Rev. Lett.* **97**, 180404 (2006).

[156] J. P. Gaebler, J. T. Stewart, J. L. Bohn, and D. S. Jin, p-Wave Feshbach Molecules, *Phys. Rev. Lett.* **98**, 200403 (2007).

[157] C. A. Regal, C. Ticknor, J. L. Bohn, and D. S. Jin, Tuning p-wave interactions in an ultracold Fermi gas of atoms, *Phys. Rev. Lett.* **90**, 053201 (2003).

[158] T. D. Lee and C. N. Yang, Low-Temperature Behavior of a Dilute Bose System of Hard Spheres. II. Nonequilibrium Properties, *Phys. Rev.* **113**, 1406 (1959).

[159] A. Altmeyer, S. Riedl, C. Kohstall, M. J. Wright, R. Geursen, M. Bartenstein, C. Chin, J. H. Denschlag, and R. Grimm, Precision Measurements of Collective Oscillations in the BEC-BCS Crossover, *Phys. Rev. Lett.* **98**, 040401 (2007).

[160] S. T. Beliaev, Energy-spectrum of a non-ideal Bose gas, *Sov. Phys. JETP* **34**, 299 (1958).

[161] F. Mohling and A. Sirlin, Low-Lying Excitations in a Bose Gas of Hard Spheres, *Phys. Rev.* **118**, 370 (1960).

[162] M. Kozuma, L. Deng, E. W. Hagley, J. Wen, R. Lutwak, K. Helmerson, S. L. Rolston, and W. D. Phillips, Coherent Splitting of Bose-Einstein Condensed Atoms with Optically Induced Bragg Diffraction, *Phys. Rev. Lett.* **82**, 871 (1999).

[163] J. Stenger, S. Inouye, A. P. Chikkatur, D. M. Stamper-Kurn, D. E. Pritchard, and W. Ketterle, Bragg Spectroscopy of a Bose-Einstein Condensate, *Phys. Rev. Lett.* **82**, 4569 (1999).

[164] D. M. Stamper-Kurn, A. P. Chikkatur, A. Görlitz, S. Inouye, S. Gupta, D. E. Pritchard, and W. Ketterle, Excitation of Phonons in a Bose-Einstein Condensate by Light Scattering, *Phys. Rev. Lett.* **83**, 2876 (1999).

[165] N. Katz, J. Steinhauer, R. Ozeri, and N. Davidson, Beliaev Damping of Quasiparticles in a Bose-Einstein Condensate, *Phys. Rev. Lett.* **89**, 220401 (2002).

[166] A. P. Chikkatur, A. Grlitz, D. M. Stamper-Kurn, S. Inouye, S. Gupta, and W. Ketterle, Suppression and Enhancement of Impurity Scattering in a Bose-Einstein Condensate, *Phys. Rev. Lett.* **85**, 483 (2000).

[167] A. Brunello, F. Dalfovo, L. Pitaevskii, S. Stringari, and F. Zambelli, Momentum transferred to a trapped Bose-Einstein condensate by stimulated light scattering, *Phys. Rev. A* **64**, 063614 (2001).

[168] J. Steinhauer, R. Ozeri, N. Katz, and N. Davidson, Excitation Spectrum of a Bose-Einstein Condensate, *Phys. Rev. Lett.* **88**, 120407 (2002).

[169] R. Ozeri, N. Katz, J. Steinhauer, and N. Davidson, Colloquium: Bulk Bogoliubov excitations in a Bose-Einstein condensate, *Reviews of Modern Physics* **77**, 187 (2005).

[170] F. Zambelli, L. Pitaevskii, D. M. Stamper-Kurn, and S. Stringari, Dynamic structure factor and momentum distribution of a trapped Bose gas, *Phys. Rev. A* **61**, 063608 (2000).

[171] S. T. Beliaev, Application of the Methods of Quantum Field THeory to a System of Bosons, *Sov. Phys. JETP* **34**, 289 (1958).

[172] A. Griffin, Conserving and gapless approximations for an inhomogeneous Bose gas at finite temperatures, *Phys. Rev. B* **53**, 9341 (1996).

[173] H. Fu, Y. Wang, and B. Gao, Beyond the Fermi pseudopotential: A modified Gross-Pitaevskii equation, *Phys. Rev. A* **67**, 053612 (2003).

[174] V. V. Flambaum, G. F. Gribakin, and C. Harabati, Analytical calculation of cold-atom scattering, *Phys. Rev. A* **59**, 1998 (1999).

[175] M. Saba, T. A. Pasquini, C. Sanner, Y. Shin, W. Ketterle, and D. E. Pritchard, Light Scattering to Determine the Relative Phase of Two Bose-Einstein Condensates, *Science* **307**, 1945 (2005).

[176] S. B. Papp, J. M. Pino, and C. E. Wieman, Studying a Dual-Species BEC with Tunable Interactions, *in preparation* .

[177] S. B. Papp, J. M. Pino, R. J. Wild, S. Ronen, J. L. Bohn, D. S. Jin, C. E. Wieman, and E. A. Cornell, Bragg Spectroscopy of a Strongly Interacting ^{85}Rb BEC, *in preparation* .